Insulating properties of materials for Medium Voltage Direct Current applications

Igor Silva

THÈSE

Pour obtenir le grade de

DOCTEUR DE L'UNIVERSITÉ GRENOBLE ALPES

École doctorale : EEATS - Electronique, Electrotechnique, Automatique, Traitement du Signal (EEATS)
Spécialité : Génie électrique
Unité de recherche : Laboratoire de Génie Electrique

Propriétés des matériaux isolants pour application dans les appareillages moyenne tension à tension continue

Insulating properties of materials for Medium Voltage Direct Current applications

Présentée par :

Igor SILVA

Direction de thèse :

Pascal RAIN PROFESSEUR DES UNIVERSITES, Université Grenoble Alpes	Directeur de thèse

Rapporteurs :

Gilbert TEYSSEDRE
DIRECTEUR DE RECHERCHE, CNRS DELEGATION OCCITANIE OUEST
Petru NOTINGHER
PROFESSEUR DES UNIVERSITES, Université de Montpellier

Thèse soutenue publiquement le **26 juin 2024**, devant le jury composé de :

Gérard MORTHA, PROFESSEUR DES UNIVERSITES, Grenoble INP - UGA	Président
Pascal RAIN, PROFESSEUR DES UNIVERSITES, Université Grenoble Alpes	Directeur de thèse
Gilbert TEYSSEDRE, DIRECTEUR DE RECHERCHE, CNRS DELEGATION OCCITANIE OUEST	Rapporteur
Petru NOTINGHER, PROFESSEUR DES UNIVERSITES, Université de Montpellier	Rapporteur
Sébastien PRUVOST, PROFESSEUR DES UNIVERSITES, INSA Lyon	Examinateur

Abstract

Recent advancements in direct-current technology from the high-voltage transport and low-voltage consumption have brought medium-voltage DC (MVDC) to the forefront. This thesis delves into the insulating DC properties of two commonly used materials in distribution equipment: epoxy filled with silica and silicone rubber.

In a monolayer configuration, each material underwent extensive investigation, focusing on water sorption characteristics and electrical conduction. Current measurements were conducted to analyze conduction under various fields, temperatures, and water uptake conditions. Additionally, the Laser Pressure Pulse (LIPP) method was employed for space charge measurements as a complementary technique. The study extended to a bilayer configuration, combining both materials, with insights from monolayer experiments informing the properties of the bilayer and predicting field distribution.

The DC conduction in epoxy exhibited high dependence on water absorption, with moisture influencing non-linearity and altering the conduction mechanism. Conversely, silicone demonstrated electrode-limited conduction, with current variations tied to water sorption through a saturation-limited mechanism. In a hypothetical bilayer configuration, where epoxy represents a type-C bushing and silicone serves as the cable termination, the field is expected to concentrate in the epoxy in dry environments, shifting to silicone as humidity increases. The thesis concludes with discussions on material selection strategies and the design of multi-layer configurations.

Keywords: epoxy resin, silicone rubber, MVDC, medium-voltage, direct current, conductivity, conduction,space charge, water sorption.

Résumé

Les récentes avancées dans la technologie du courant continu, du côté du transport à haute tension et de la consommation à basse tension, ont propulsé le courant continu de moyenne tension (MVDC) au premier plan. Cette thèse explore les propriétés isolantes en courant continu de deux matériaux couramment utilisés dans l'équipement de distribution : de l'époxy chargé en micro-silice et le silicone elastomère.

Dans une configuration monocouche, chaque matériau a fait l'objet d'une enquête approfondie, mettant l'accent sur les caractéristiques de sorption d'eau et la conduction électrique. Des mesures de courant ont été effectuées pour analyser la conduction dans divers niveaux de champs, à différentes températures et conditions d'absorption d'eau. De plus, la méthode Laser Pressure Pulse (LIPP) a été utilisée pour des mesures de charge d'espace en tant que technique complémentaire. L'étude s'est étendue à une configuration bicouche, combinant les deux matériaux, nous permettant ainsi de confirmer un modèle prédisant les propriétés du multicouche et sa distribution de champs en fonction des valeurs des monocouches.

La conduction en courant continu dans l'époxy a montré une forte dépendance à l'absorption d'eau, l'humidité influençant la non-linéarité et modifiant le mécanisme de conduction. À l'inverse, le silicone a démontré une conduction limitée par l'électrode, avec des variations de courant liées à la sorption d'eau par le biais d'un mécanisme limité par saturation. Dans une configuration bicouche hypothétique, où l'époxy représente un manchon et le silicone sert de terminaison de câble, le champ est censé se concentrer dans l'époxy dans des environnements secs, passant au silicone à mesure que l'humidité augmente. La thèse se conclut par des discussions sur les stratégies de sélection des matériaux et la conception de configurations multicouches.

Mots-clés : résine époxy, caoutchouc de silicone, MVDC, moyenne tension, courant continu, conductivité, conduction, charge d'espace, sorption d'eau.

To my mother, Denise.
To the memory of my father, Hélcio.

But nature is always more subtle,
more intricate, more elegant than
what we are able to imagine.

Carl Sagan
The Demon-Haunted World:
Science as a Candle in the Dark

Acknowledgements

Completing a Ph.D. is a challenging endeavor, and I am deeply fortunate to have crossed a path adorned with countless enriching experiences, made possible by the remarkable individuals who have surrounded and collaborated with me. These individuals provided me with the support, knowledge, generous amounts of their time, high expectations, patience, and above all, the kindness I needed.

Firstly, I would like to express my sincere thanks to Mr. Pascal Rain and Mr. François Gentils, my advisors, for accepting my application three years ago, welcoming me, providing me with a lot of assistance and advice, for all the scientific discussions, and for supporting me in exploratory experiments, hypotheses, and ideas.

I am also grateful for my reviewers, Mr. Gilbert Teyssedre and Mr. Petru Nothinger, for accepting to evaluate this manuscript and for the valuable advice during the review; and to the examiners, Mr. Gerard Mortha and Mr. Sébastian Pruvost, for contributing to my defense and engaging in discussions during and after it.

Most of the work has been done in the G2Elab (Grenoble Electrical Engineering Laboratory), in the Dielectric Materials and Electrostatics team[1], in which I had the good fortune to be supported by an incredible technical team: Mr. Sebastien Flury[2], Mr. Christophe Pollet [3], Mr. Enzo Cuilla[4]; and Mr. Jean-Luc Palanzuela at the first year of my thesis. I also express my gratitude to Mr. Olivier Lesaint for sharing valuable knowledge and equipment.

I am also grateful to my friends in the lab for being the driving force behind the enriching experiences that have colored these days: the "adults" team (including Nelly Bonifaci, Rachelle Hanna, and Alain Sylvestre), my colleagues who shared the office with me at times (Simon-Emannuel Haim, Simon Soulié, Enrique Quesada, Gwenn Monvezen, and Nathalie Moubarak), and the colleagues from the team: Francis Boakye-Mensah, Jonathan Ranucci, Marwa Gassab, Hissam Karim; and especially to Chencho Dorji for his friendship.

Another part of this work was executed in the Technopole of Schneider Electric,

[1] In french, Matériaux Diélectrique et Electrostatique: MDE, the best team of the *MonDE*

[2] Current-voltage test bench and climatic chamber life-saver

[3] Cabling and LIPP life-saver

[4] Water jet and laser cut life-saver

involving most of the physical characterizations and molding of materials.

Starting from Christophe Prévé, and Pavel Novak, for supporting and following this work; to Yvon Scremin [5]; for the team at the Mendeley's lab, specially Marie-Helène Tiertant[6]; to the Material's expertise team, within or outside the DC squad: Laurent, Damien, Mehrdad, Lucas, Léo, Jacques-Armel, and Stephane; to the team from Saint-Geoirs factory, specially Bruno [7]. For all the colleagues that I encountered during my stays in the office: Diana, Lorenzo, Nicolas, Ignacio, Marilia, Suzie, Naëlle, Laurène, Adrien, Yara. And lastly, but not the least, to Mr. Lou Lacquement, the first intern I was charged to co-supervise, and that helped me with interesting experiments and analysis.

Finally, I would like to express my sincere gratitude to my family and friends from Brazil. It was not easy to my mother having me so far away during these years, as it was not easy from my side to deal with all the *saudade* and the memories. I am engaged to make these efforts worth it.

[5]For sharing a valuable expertise on molding epoxy plates

[6]For all our SEM sessions, cracking sample under liquid nitrogen, and burning silicone rubber at 900°C!

[7]Giving continuity on the molding of plates, and even answering my calls during his vacation (sorry!).

Contents

Abbreviations and acronyms ii

Symbols iii

Introduction v

1 Literature review 1
1.1 Industrial context and challenges . . . 2
1.1.1 The emergence of MVDC . . . 2
1.1.1.1 The basement of the actual power system. . . . 3
1.1.1.2 The silent evolution of HVDC transmission. . . . 4
1.1.1.3 Environmental policies gain prominence. . . . 5
1.1.1.4 Is the future belonging to DC? . . . 6
1.1.2 Switchgear: Power and safety . . . 7
1.2 Theoretical background . . . 9
1.2.1 Generalities about polymeric materials and composites . . . 9
1.2.2 Epoxydic systems . . . 11
1.2.3 Silicone rubber systems . . . 15
1.2.4 Generalities about water sorption in polymers . . . 18
1.2.4.1 Terminology . . . 19
1.2.4.2 Time-dependent sorption: Diffusion mechanisms . . . 20
1.2.4.3 Steady-state sorption: Isotherm models . . . 22
1.2.5 Electrical properties of polymers under static fields . . . 26
1.2.5.1 Generalities and DC events . . . 26
1.2.5.2 Charge carriers and space charge . . . 28
1.2.5.3 Space charge density and field distortion measurement 30
1.2.5.4 Charge transport and energy: Band theory . . . 32
1.2.5.5 Charge transport and time: Transient current . . . 34
1.2.5.6 Charge transport and voltage: Steady-state currents 37
1.3 State-of-the-art of the systems of this work . . . 45
1.3.1 Epoxy composites and related subjects . . . 45
1.3.1.1 Water diffusion into the epoxy-silica system . . . 45

1.3.1.2 Charge transport and space charge events in epoxy-silica system . . . 47
1.3.2 Silicone rubbers: water sorption, and electrical properties . . . 49
1.3.2.1 Water diffusion into the silicone-silica system . . . 49
1.3.2.2 Charge transport and space charge events in silicone-silica system . . . 51
1.3.3 Multi-layer with focus to the epoxy and silicone rubbers interface 53
1.3.3.1 Current measurements and space charge on bilayer samples: . . . 53
1.4 Thesis objectives . . . 56

2 Materials characterization and methods 58
2.1 Physicochemical methods . . . 58
2.1.1 Differential Scanning Calorimetry (DSC) . . . 58
2.1.2 Thermodynamic Mechanical Analysis (DMTA) . . . 59
2.1.3 Fourier-tranform Infrared Spectroscopy (FT-IR) . . . 59
2.1.4 Scanning Electronic Microscopy (SEM) . . . 59
2.1.5 Weight measurements (Gravimetric method) . . . 60
2.1.6 Thermogravimetric Method (TGA) . . . 60
2.2 Materials of the study . . . 61
2.2.1 Epoxy resin . . . 61
2.2.1.1 Formulation . . . 61
2.2.1.2 Characterization . . . 62
2.2.2 Silicone rubber . . . 66
2.2.2.1 Formulation . . . 66
2.2.2.2 Characterization . . . 66
2.3 Sample preparation and conditioning . . . 73
2.3.1 Shaping . . . 74
2.3.2 Drying . . . 74
2.3.3 Hydration . . . 75
2.3.4 Sputter deposition . . . 76
2.4 Electrical measurements . . . 78
2.4.1 Current-voltage measurements . . . 78
2.4.1.1 Set-up . . . 78
2.4.1.2 Installation and cell preparation . . . 79
2.4.1.3 Measurement parameters and program . . . 80
2.4.2 Space charge measurements . . . 80
2.4.2.1 Set-up . . . 80
2.4.2.2 Data acquisition and treatment . . . 81
2.5 Questionning sample preparation and measurement protocols: some answers provided by the experiments. . . . 86
2.5.1 Why should we care about sample fabrication? . . . 86
2.5.2 Why discharge the sample prior to the electrical test? . . . 87
2.5.3 Why control the water content? . . . 87
2.5.4 Why care about electrode material? . . . 88
2.5.5 How much strict should we be about temperature and RH control? . . . 89
2.5.5.1 The ambiguity of room temperature: . . . 89

2.5.5.2 The risk of testing a meta stable sample 90
2.5.5.3 The risk of a negative sum of currents 91
2.5.6 Is the 1 hour-1 hour test the best time length? 92
2.5.7 Are the conduction current values repeatable? 93
2.5.8 Additional details that has to be highlighted 93
2.5.8.1 Evaluating the off-set: 93
2.5.8.2 The discrepancy of digital filtering and smooth: . . . 94
2.5.8.3 The challenges of testing at extreme conditions: . . . 95
2.6 Partial conclusions & perspectives 96

3 The monolayer of epoxy composite 98
3.1 Water Sorption of the Epoxydic System 98
3.1.1 Results 98
3.1.1.1 Temporal Weight Gain 98
3.1.1.2 Steady-state Weight Gain 98
3.1.2 Discussion 100
3.1.2.1 Diffusion mechanisms 100
3.1.2.2 Water sorption isotherms 101
3.1.2.3 Investigating the abnormal increase at higher temperatures 103
3.2 Electrical tests in the Epoxydic System 108
3.2.1 Results 108
3.2.1.1 Current-voltage tests 108
3.2.1.2 Space-charge profile 110
3.2.2 Discussion 114
3.2.2.1 The limits of the ohmic conduction 114
3.2.2.2 Exploring the super-ohmic mechanisms 116
3.2.2.3 The impact of the temperature and its implications . 122
3.2.2.4 Comment about the space charge measurements . . . 123
3.3 Partial conclusions and perspectives 125

4 The monolayer of silicone rubber 127
4.1 Water Sorption of the Silicone System 127
4.1.1 Results 127
4.1.1.1 Temporal Weight Gain 127
4.1.1.2 Steady-state Weight Gain 128
4.1.1.3 Water absorption in the complementary silicone rubber 129
4.1.2 Discussion 129
4.1.2.1 Diffusion mechanisms 129
4.1.2.2 Water sorption isotherms 130
4.2 Electrical tests in the Silicone System 135
4.2.1 Results 135
4.2.1.1 Current-Voltage profiles 135
4.2.1.2 Space-charge profiles 138
4.2.1.3 Complementary results: exploring a second silicone rubber free of fillers 139
4.2.2 Discussion 143
4.2.2.1 An electrical conduction model based on water adsorption 143

4.2.2.2 Determining the linearity threshold . . . 146
4.2.2.3 Exploring the current mechanisms and charge transport . . . 146
4.2.2.4 Exploratory reasoning to explain the conduction mechanisms . . . 153
4.2.2.5 Exploring the filler-free silicone rubber . . . 158
4.3 Partial conclusions & perspectives . . . 161

5 The multilayer and practical considerations 163

6 Conclusions & Perspectives 164
6.1 Perspectives . . . 166

A Molding procedure of epoxy composite plates 167

B Selecting and preparing an alternative LSR silicone rubber 168
B.1 Motivation . . . 168
B.2 Fabrication procedure . . . 168

C Dielectric spectroscopy: Theory and application in the materials of the study 170
C.1 Motivation . . . 170
C.2 Theoretical background . . . 170
C.3 Materials and methods . . . 173
C.3.0.1 Set-up . . . 173
C.3.0.2 Measurement program . . . 173
C.4 Study case 1: Epoxy composite . . . 174
C.5 Study case 2: Industrial silicone rubber . . . 176

Abbreviations and acronyms

AC Alternating-current
AIS Air-insulated switchgear
ASTM American Society for Testing and Materials
ATH Alumina trihydrate
ATR Attenuated total reflectance
BPA Bisphenol A
DC Direct-current
DSC Differential Scanning Calorimetry
DEGBA Diglycidyl ether of bisphenol A
DMTA Thermodynamic Mechanical Analysis
EDX Dispersive X-ray spectroscopy
EN European Standard
FT − IR Fourier-tranform Infrared Spectroscopy
G2Elab Grenoble Electrical Engineering Lab
GIS Gas-insulated switchgear
HCR High consistency rubber or Heat curing rubber
HOMO Highest occupied molecular orbital
HV High-voltage
HVDC High-voltage direct-current
IEC International Electrotechnical Commission
ISO International Organisation for Standardisation
LIPP Laser induced pressure pulse
LSR Liquid silicone rubber
LUMO Least unoccupied molecular orbital
MVAC Medium-voltage alternating-current
MVDC Medium-voltage direct-current
MVQ Methyl-vinyl-siloxane
MTHPA Methyltetrahydrophthalic anhydride
PDMS Polydimethylsiloxane
PDC Polarization-depolarization currents
PWP Pressure-wave-propagation
RH Relative humidity
RTV Room-temperature vulcanized rubber
SCLC Space charge limited current
SEM Scanning Electronic Microscopy
SiR Silicone rubber
SSIS Shielded Solid Insulation Switchgear
SMALT *Sectionneur mis à la terre*: Earthed Disconnect Switch
TGA Thermogravimetric Method
Tg Glass transition temperature
Tm Melting temperature

Symbols

Starting by greek letter:

α absorption coefficient (Langmuir's diffusion)
β desabsorption coefficient (Langmuir's diffusion)
β_s Schottky constant
β_{PF} Poole-Frenkel constant
ϵ Permittivity
ϵ_r Relative permittivity
ϵ_0 Vacuum permittivity
ϵ_s Static permittivity
θ Sorbed concentration, or fractional sorption
θ_T Trap concentration
λ Jump distance
λ_d Field reinforcement/attenuation parameter
μ Charge carrier mobility
μ_{eff} Effective mobility
χ Insulation susceptibility
ρ_c Charge density (encountered)
σ Electrical conductivity
σ_{app} Apparent conductivity
σ_{real} Intrinsic material conductivity ("real")
$\sum_s$ Charge concentration at the interface
τ Relaxation time
τ_{MW} Relaxation time according to Maxwell-Wagner theory
ϕ Work function
ϕ_{eff} Effective barrier energy
ϕ_h Barrier height
ϕ_m Metal work function
ϕ_s Insulation work function
Φ Volume fraction

Starting by lowercase letter:

b Langmuir's isotherm constant
c Concentration
c_b Concentration of bounded sorbant (Diffusion)
c_f Concentration of free sorbant (Diffusion)
d Sample thickness
i Electrical current
i_{abs} Absorption current
i_{res} Resorption current
i_{sum} Sum of absorption and resorption currents
i_c Conduction current
i_d Depolarization current
i_p Polarization current
i_{sc} Space-charge current

k Boltzmann constant
m Mass
m_0 Initial mass
$m(t)$ Mass intake at a given time t
m_∞ Mass intake at equilibrium at $t = \infty$
m_e^* Effective mass
n Concentration of charge carriers
q Unit electrical charge
t Time
$tan\delta$ Loss factor
v_d Drift velocity

Starting by capital letter:

A Richardson constant
D Diffusion constant
D_0 Maximum diffusion coefficient at an infinite temperature
D_{Fick} Diffusion constant (Fickian diffusion)
$D_{Langmuir}$ Diffusion constant according to Langmuir's model
E Electric field
E_a Activation energy
E_{app} Applied electric field
E_d Contact field
E_f Fermi level
E_{Fm} Fermi level of the metal
E_{Fs} Fermi level of the insulation
E_t Trap level
E_{T0} Deepest trap level
H Henry's isotherm constant
I Electrical current
J Electrical current density
J_Ω Ohmic current
J_θ Single-level SCLC
J_l SCLC with exponential distribution of traps
J_s Current density according to Schottky injection
J_{PF} Current density according to Poole-Frenkel
J_{FN} Current density according to Fowler-Nordheim injection
J_{HOP} Current density according to hopping mechanism
J_0 Current density as reference
J_d Diffusion flux
L Exponential trap level parameter
N_A Avogadro number
N_c Total amount of charges participating in the conduction
N_t total amount of traps, trap density
P Vapour (partial) pressure
P_0 Saturation vapour (partial) pressure
Q Adsorption heat
R Gas constant
T Temperature
T_t Trapping temperature
V Voltage
V_d Voltage at the contact
V_{th} Voltage threshold
V_{app} Applied voltage

Introduction

The landscape of power distribution is on the edge of transformation. It is facing an impact from multiple fronts: high-voltage direct-current (HVDC) from the left, low-voltage direct-current (LVDC) from the right, environmental regulations from above, and economic policies from below.

Traditionally, the distribution system operates using alternating current (AC), connecting AC power sources to AC loads via AC transmission lines. But advancements in HVDC transmission have revolutionized long-distance bulk transmission, significantly enhancing efficiency: a single DC cable has the capacity to replace a three-phase AC link, resulting in a valuable reduction in material usage, which is particularly significant in the context of climate change and resource depletion! At the moment I'm writing this manuscript, there are approximately 200 gigawatts (GW) of operational HVDC cables covering a distance of 58,000 kilometers worldwide, and almost the double of the power is forecasted to be installed in the upcoming years. The rise of specific renewable energy sources, such as photovoltaic panels and wind platforms, which typically generate or convert energy into direct current (DC), has significantly increased DC generation.

Consumer profiles are also evolving. When Nikola Tesla and George Westinghouse designed the first AC power plant at Niagara Falls in 1896, daily life was not yet influenced by data centers and the large use of batteries in computers, mobile cellphones, vehicles, and machines. Additionally, DC circuit breakers and switches were not available at that time. Now, thanks to developments in power electronics, access to these components is widely spread.

The Medium Voltage networks, which is related to voltage levels between 1 kV and 52 kV, are still quasi exclusively in AC but MVDC grids are being built locally, in particular to connect photovoltaic generation or other platforms. They are expected to multiply in the near future. To do so, the development of reliable MVDC switches and circuit breakers are necessary, so as the insulation system.

The first challenge concerns the material's selection for the insulation: they have to be compared based on properties that better describe their responses to DC stresses. These are the DC conductivity and the space charge accumulation. These properties merit to be measured at different conditions of temperature and relative humidity, in order to give the broad picture about how they would behave under different environments. This will be one of the focus of the thesis.

The materials selected for this study were the epoxy composite, and the silicone rubber. These materials vary significantly one from another. Epoxy, with over fifty years of application in HV electrical engineering, has a well-established history of traceable tests and validations. In contrast, silicone rubber remains relatively unexplored, with many of its features yet to be thoroughly examined. In addition, both of them are applied together in in-series configuration commonly found when connecting equipment to cable, or between the connection of two or more equipment.

Therefore, an interdisciplinary approach is proposed, gathering together elements from electrical and materials engineering, along with insights from chemistry and physics. The thesis defended by this work can be articulated in this direction:

> To select, to validate, and to improve the robustness of a (MV)DC insulation system, a thorough examination of the structure-property relationship is imperative. This involves conducting a comprehensive characterization encompassing DC conductivity and space charge build-up, considering environmental and operational parameters such as voltage stress, temperature, and relative humidity. It is crucial to account for the influence of these factors on the insulating materials to ensure the overall structural integrity, whether in individual or multi-layer configurations.

The thesis is organized as it follows:

Chapter 1, which is the literature review, is divided in four main parts: (1) The context about the MVDC technology and Schneider's applications; (2) Theoretical background about polymers and composites, water sorption mechanisms, and electrical properties under DC stresses; and (3) State of the art targeting epoxies and silicone rubbers under DC stresses. At the end (4), the gaps in the literature review are discussed, and the thesis objectives are stated.

Chapter 2 has a progressive approach that culminates in the electrical characterization protocol of the systems of the work. In a first part, the chemical, structural, thermal, and mechanical characterizations are outlined. In a second part, these characterizations are applied to examine the materials under study. The aim is to provide a comprehensive overview of the target materials, going beyond the information provided in the supplier's data sheet. In a third step, the chapter elaborates on how to prepare samples; and more importantly, how to test their electrical properties taking into account their particular structures and microstructures. In a fourth and latter part, we critically examine and contextualize the various investigations, comparisons, failures, and efforts that contributed to the formulation of the electrical test protocol discussed in the third section.

Chapter 3 delves into the epoxy resin, presenting results and discussions on water sorption first, followed by results and discussions on electrical current and space charge measurements. Similarly, in Chapter 4, the same approach is employed for the silicone rubber. As the samples used in these investigations are single flat discs, we refer to them as "monolayers" since they consist of a single composite material. Nevertheless, it is important for the reader to understand that a composite material comprises more than one material. In this case, we have a mixture of an organic polymer (epoxy) or inorganic polymer (silicone) and an inorganic filler (silica), resulting in a material with multiple phases and interphases, with final properties that differs from their individual components.

These chapters adopt a scientific focus, aiming to evaluate the impact of key environmental parameters (relative humidity and temperature) on the physical properties and chemical structures of these materials. These findings are then cross-referenced with the results of electrical tests. Ultimately, the goal is to gather sufficient information to establish a more precise structure-electrical property relationship. Put differently, once these materials are stressed by DC fields, we want to understand "what is going on".

In Chapter 5, the epoxy and silicone rubber are tested together in an in-series configuration, hereafter named "bilayer" configuration. First, we want to know to what extent the results of the bilayer samples can be deduced from the monolayer results. Finally, the practical implications of all the results of Chapters 3, 4, and 5 are discussed: in which material the electric field will be enhanced? Can the field ping-pong from one material to another during application? If so, when and in which conditions? What can we infer about the interface? Which risks does it implies?

At the end, all the conclusions, learnings, and recommendations are resumed in Chapter 6, as well as the many possibilities and perspectives that were opened during the development of this work.

1 Literature review

This literature review is divided into four main sections:

In section 1.1, the industrial context is developed from a historic perspective (1.1.1). The specific technology and challenges of MVDC switchgears are introduced in subsection 1.1.2.

In section 1.2, the fundamental theoretical background is presented. Insulating materials applied in those switchgears are described in subsection 1.2.1 with respective to their special structures, microstructures, and general properties. The different mechanisms of water sorption as a function of time and vapour pressure are described in subsection 1.2.4. The heart of this work, the dielectric properties, supported by the main fundamental theories behind the conductivity and electrical events under DC fields, is explored in section 1.2.5.

In section 1.3, these previous sections are connected: the latest research about electrical properties of those materials is investigated, as an attempt to correlate the material's (micro)structure and its electrical properties, and to forecast their behaviours under stresses commonly found in switchgears. These conclusions will draft the guidelines for this research.

These guidelines are postulated in section 1.4, in which the contributions and objectives will be unveiled.

1.1 Industrial context and challenges

1.1.1 The emergence of MVDC

This thesis deals with direct-current (DC). It embodies a continuous flow of electricity in a single direction, traveling from a region of high potential to a region of lower potential (from positive to negative poles). It is not the only way energy can be generated, transmitted, and utilized: there is also the alternating current (AC) in which electricity undergoes cyclical changes in direction at regular intervals [1]. Both modes are represented in Figure 1.1.1. It is just a formal representation, since real DC currents, when we look closer, can present some small (sometimes insignificant) AC component [2, 3].

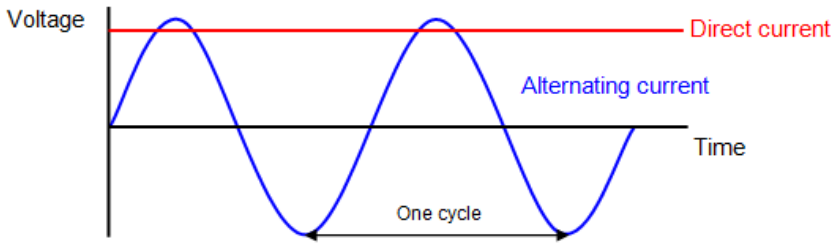

Figure 1.1.1: Comparison between alternating current (AC) and direct current (DC).

These two conduction modes were developed together tracing back to the late 1800s when many important electric inventions became popular. This was also the time when the first electric power plants and distribution centers appeared. Back then, the common choice was to use direct current (DC), which Thomas Edison favored. He even built the Pearl Street steam-electric plant in New York in 1882, a significant achievement. [4, 5].

However, the use of both DC and AC for transmitting electricity across long distances was marked by inefficiencies and limitations [6]. The choice between one of them would rely on the safety and reliability[1] of the system, ensured by two major operations:

- The control of voltage levels.
- The possibility to open/close the circuit when necessary, provided by circuit breakers and switches[2].

The absence of a current zero-crossing point in DC mode has always posed concerns; the arc generated by the mechanical separation of conductors could not be naturally extinguished. At this item, the AC was in advance [7]. A pivotal turning point emerged with the introduction of the AC transformers, developed in parallel by George Westinghouse (in the United States), and Zipernowsky, Blathy, and

[1] Ability of a network or system to consistently perform its intended functions without interruption or failure.

[2] There is a technical difference between switches and circuit breakers. The first one just open or close an electrical circuit, but the second one should also provides overcurrent protection, when it detects a fault or excessive current, thereby preventing damage to the circuit and equipment.

Déri (in Hungary). This breakthrough allowed for the effective transmission of alternating current (AC) over vast geographical expanses to power remote homes and businesses. The transformer, which enables gradual voltage reduction at specific stages, addressed these safety concerns, minimizing energy losses, and ensuring compatibility with a wide range of electrical equipment.

Although some people were still unsure about the safety and reliability of former AC[3], the prominent engineer Nikola Tesla, ancient Edison's pupil, strongly supported it. A confrontation between Tesla and Edison started and progressively became public as the name of "war of currents"[4]. But Tesla rapidly made important improvements to Westinghouse's AC transformers, which were used in the Niagara Falls hydroelectric power plant in 1896. The success of this plant and others like it built in the early 1900s led to a network of connected AC power systems. These systems, which we now call major power grids, established AC as the dominant choice over DC [4].

1.1.1.1 The basement of the actual power system.

This thesis also deals with medium voltage for electric distribution, represented by the green lines in Figure 1.1.2, which is a scheme that illustrates the fundamental components of an electrical system. The process begins with generation, where energy is generated within power plants through various sources such hydraulic action, solar radiation, wind power, or geothermal sources. This energy undergoes transformation at the power station, converting into high-voltage (HV) electrical energy. It is then transported over extensive distances via transmission lines until it reaches remote substations. At these substations, the voltage is reduced to enhance efficient delivery to consumers. Just then, the energy is distributed to end consumers who receive it at medium-voltage levels and subsequently adjust it to match commercial or residential voltage standards, typically at 110 V or 220 V.

Most of the network is three-phase, having naturally 3 conductors, a neutral, and sometimes a ground. Two voltages can be distinguished, the phase-to-phase, and the phase-to-neutral. The voltage level is often described with the phase-to-phase reference. In France, for example, they are divided in four groups, as seen in Table 1.1.1.

Nomination	Acronym	Scale	Voltage range
Very high voltage	HTB2	Long distance	$>$ 100 kV
High voltage	HTB	Regions/local	400 / 225 kV
Medium voltage	HTA	Local distribution	15 / 30 kV
Low voltage	BT	Small lines	230 / 400 V

Table 1.1.1: Typical phase-to-phase voltage levels (based on [8])

According to IEC 38 [9], medium voltage spans from 35 kV to 1 kV. Some sources point to the range between 52 kV and 1 kV [10, 11]. The distribution net-

[3]Critics argued that AC's ability to reach higher voltages in transmission could lead to more dangerous accidents if someone came into contact with a live conductor.

[4]Edison was the owner of dozens of DC technology patents.

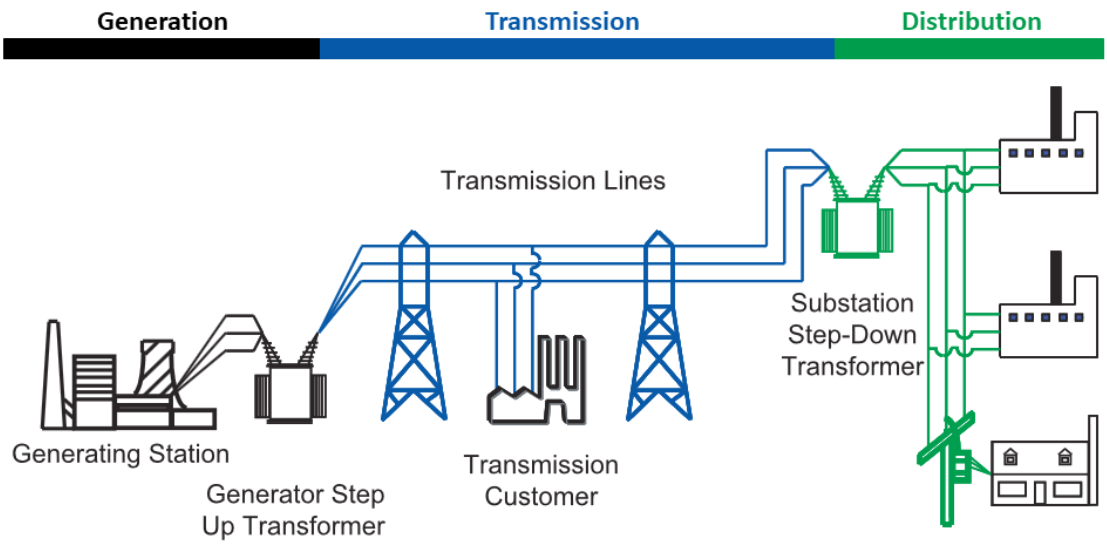

Figure 1.1.2: Electric system overview

work bonds the transmission system (primary voltage[5]) and consumers (secondary voltage). From the perspective of the transformer, primary and secondary voltages can also be understood as the input and output voltages, respectively.

1.1.1.2 The silent evolution of HVDC transmission.

The technology employed in this thesis comes from high-voltage direct-current (HVDC) technology. One big short-come of AC has always been its reactive power, which increases losses and makes overhead transmission at distances over 100 km challenging because of excessive line charging[6]. In 1930's, a mercury-arc device playing the role of rectifier (AC-DC convertor) was developed, and applied at a big scale for the first time in 1954 [12]. This project, called Gottland 1 ($\pm$ 100 kV, 20 MW, 96 km line cables), was the first "modern" HVDC commercial link put into operation, associating the Baltic Sea of Gottland to the Swedish mainland.

This enabled the power transmission at long distances. In the next decades, the HVDC would survive focusing on certain specialized high voltage long-distance transmissions applications world-wide, as transmission via overhead lines[7] or submarine cables (point-to-point), or for connections of asynchronous AC lines via back-to-back installations[8].

As long more HVDC lines have been installed, the technology behind it has also developed, pushing the limits of power supply. In the 1970's, solid-state thyristor[9] appeared with higher voltage ratings, opening the development of current source converters (CSCs). In the 1980's, the Insulated-Gate Bipolar Transistor (IGBT) valves were developed. They were able to improve the efficiency of AC-DC and

[5]The voltage output resulting from converting high-voltage to medium-voltage at a transformer substation.

[6]For submarine cables, a distance of some tens of kilometers can already present issues.

[7]Network of elevated cables that we can see running along roads, railways, and open areas.

[8]Conversion of a AC line to DC, and DC back again to AC, useful to link two AC lines with different frequencies or phase angles, i.e., to connect two isolated asynchronous AC lines.

[9]Semiconductor device that acts as an electrically controlled switch.

DC-AC conversion, so as the voltage control. In the 1990's, various types of power converters, particularly voltage source converters (VSCs) IGBT-based started to be available commercially.

1.1.1.3 Environmental policies gain prominence.

This thesis is the product of its time. In 2015, 196 nations signed the Paris Agreement, which states low-carbon energy transition as the key support to reach the "well below 2°C" goal. At the same year, the United Nations adopted the 2030 Sustainable Development Goals (SDGs) placing the affordable and clean energy on the hot spot. Meeting all these environmental policies and new demand consumption encompassed investments related to DC current.

Clean energy is related to sources that emit little to no greenhouse emissions, including renewable and carbon-free sources. Solar and wind power are the biggest representatives of renewable energies. But solar panels naturally produce energy in DC. [13]. Wind turbines generate asynchronous current which is often converted to DC[10]. Additionally, the DC would represent economy in materials and more energy efficiency:

- **About the conductors:** there is no skin effect. In AC, the charge carriers are pushed to the surface of the conductor, while in DC, the bulk also contributes to the energy transport. In consequence, less conductor can be used to provide the same power (or more power can be transmitted with the actual amount of conductors).
- **About the insulating materials:** there is no dielectric loss (no $tan\delta$ [11] because no frequency). Energy is not lost by dielectric heating, and much less reactive energy is involved since there is no capacitive current (in steady-state conditions).
- **Operating mode**: no phase shift, or asynchronous currents, and only two polarities possible (positive and negative). One DC monocable is able to replace a tree-phase AC link, leading again to an economy of materials.

According to many energy agencies, the combined share of solar panels and wind farms on the global electricity generation should rise from 8% in 2019 to 30% in 2030, and to 60% in 2050. Following to Paris Agreement, many nations have set their own goals at the medium and long-term. The European Union and the United States, for example, search to achieve carbon neutrality up to 2050; and China in 2060 [14].

On the other hand, electrical vehicles (EVs), laptops, smartphones (i.e. any battery-based equipment), and data centers all consume DC energy. In the particular case of EVs, the worldwide inventory of electrical vehicles (EVs) is supposed to increase by 800 times from its total stock of 2015. [6, 15].

As schematised in Figure 1.1.3, the actual situation involves enhancing both the generation and transportation of DC energy on one hand, while witnessing

[10]Back-to-back conversion. If the wind turbines are installed far from the consumers, as in offshore windfarms, DC is special interesting to transport with lower losses.

[11]The $tan\delta$ is a property of the material related to the energy that is lost due to cycling stresses coming from alternating voltage. The complex relative permittivity $\epsilon^* = \epsilon' - i\epsilon''$ related to the ability of the material to stock charges, $tan\delta = \frac{\epsilon''}{\epsilon'}$.

a growing demand for DC low-voltage and medium-voltage systems on the other hand. This dynamic has sparked discussions about a significant aspect: the gap in DC distribution networks.

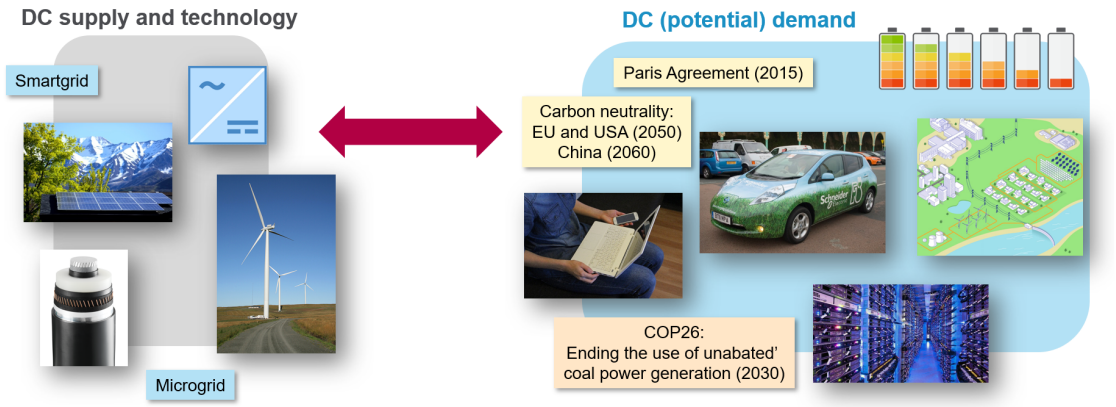

Figure 1.1.3: The MV-LVDC gap: we are generating and transporting HVDC energy from one side, and increasing the demand of DC energy on the other.

1.1.1.4 Is the future belonging to DC?

The DC can be implemented in hybrid mode with the AC, but a fundamental work on the reduction of conversions seems necessary, since the energy lost on DC/AC and AC/DC conversions can become no negligible. Nowadays, about half of the energy wasted on commercial buildings and data centers are from AC to DC conversions and the rest from stepping down DC voltage to DC conversions. It is estimated that the elimination of multiple conversions could prevent energy losses up to 35%.

Another strategy consist of total-dedicated DC systems. It has been developed mostly in DC power microgrids, "islands" that can operate independently of the bulk power grid and very useful for commercial buildings, neighborhoods, data centers, electrical charge of vehicles or ships having with their own generation power system (from photovoltaic cells to batteries, for example). For both macro or micro, in this approach, the energy has to be distributed by MVDC networks.

But besides the interest on MVDC, its usage still face some challenges. The first one is related to the cost. Apart from the economy with less materials and more energy efficiency, DC terminal stations are usually expensive due to the fact that they need to perform multiple conversions, which includes costly filters, capacitors and other sophisticated equipment for protection against short-circuits [16, 17, 18]. A compromise between cheaper transmission and costly accessories is determined by the "break-even-distance" from which DC will give lower costs towards AC networks (Figure 1.1.4) [19, 17]. This logic, valid for transmission, can be also valid for distribution. Without competitive costs, only strong choices made by private companies and governments (so, ultimately, the civil society) could make MVDC accessible.

The second challenge is related to the technology in power electronics. Reliable, efficient and low-cost converters (DC/DC and AC/DC) need to meet high voltage ratios to be utilized for MVDC grids [20, 18]. In addition, high performance circuit-breakers lack on the market (actual power losses during normal operation are still too high) [20, 21, 17, 22]. The third one is related to the insulating materials.

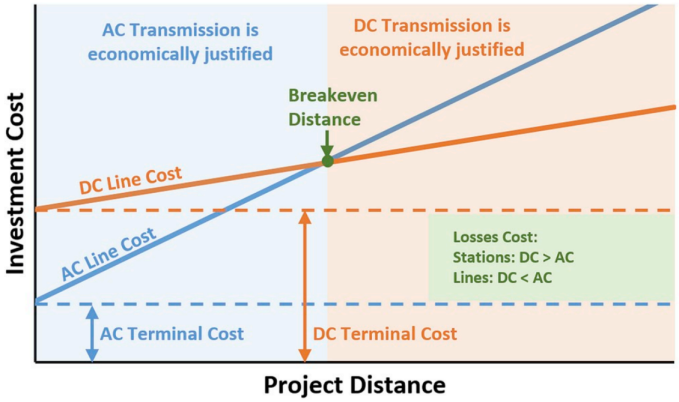

Figure 1.1.4: The break-even-distance that justifies economically the employment of DC technology [17]

The behavior of such materials under DC fields isn't clear. There are no obvious criteria to select materials for DC applications, and even the performance of actual AC insulating materials under DC stresses are still unknown. The domain suffer of a notorious lack of standards, or ambiguous one (as the ASTM D257-14 or IEC 62631). Because of it, many working groups and standard revisions having been settled worldwide. This point will be explored later in sections 1.2.5 and 1.3.

Besides all these adversities, the techno-scientific community is very optimistic. The expectation is so high that some specialists, like Francisco de Léon, the editor-in-chief of IEEE Transactions on Power Delivery, anticipates that "Edison will beat Tesla after all" [23].

1.1.2 Switchgear: Power and safety

The materials studied in this work are already applied to isolate switchgears.

Switchgear is a specialized equipment designed to fulfill various essential functions within an electrical network, including control, measurement, protection, and regulation. Its primary purpose is to isolate and to switch (on or off) generators, transmission or distribution lines, or other electrical equipment (as circuit breakers, fuses, and off-load isolators). A secondary purpose consists of fault detection and clearance (as a short-circuit) and disconnect the unhealthy section [1, 24]. Additionally, provision must be made for metering, control, and data functionalities.

Figure 1.1.5 illustrates some models in the market. This thesis focuses on those bonding the medium voltage range (primary ones, connecting the HTA to HTB, or secondary ones, associating HTA to BT; see Table 1.1.1). There are three main categories of switchgears: Air Insulated Switchgear (AIS), Gas Insulated Switchgear (GIS), and Solid Insulation Switchgear (SIS) [25].

The normal service conditions for the installation and use of actual AC switchgears are specified in the IEC 62271-1 standard. The ambient air temperature must range between 40°C and -5°C (some equipment can withstand -50°C in very cold climates, and +55°C in very hot ones) [26]. The manufacturers assume that there is not pollution from dust, smoke, corrosive and/or flammable gases, vapours or salts; humidity associated with condensation should be avoided. To do so, the average value of relative humidity and vapour pressure over 24 hours cannot exceed 95% and 2.2 kPa, respectively. In one month, theses limits decrease to 90% and 1.8 kPa, respectively

Figure 1.1.5: Examples of Schneider switchgears. GIS Schneider Electric GHA up to 40.5kV (a), MCset Air Insulated Switchgear (b), and SIS Schneider Electric PREMSET (c).[25]

[10].

Within the switchgear cubicle, electrical current travels through plug-like connectors, metal bars, disconnectors, or various other devices, and exits through additional metal bars linked to other cubicles. These connections and supports are constructed over insulating materials. The specific component utilized to insulate and secure the entry and exit connections is known as a "bushing." The bushing's role extends beyond electrical isolation; it also ensures mechanical stability and, in certain instances, serves as a seal, protecting the cubicle from moisture, contaminants, or gases. As an illustration, Figure 1.1.6 is showing a disconnector earthing switch function in an SF6 free GIS together with cable and extensibility bushing. The entry connector is called type-C bushing, and the exiting one is extensibility bushing (because they can connect one cubicle with another, extending its functions).

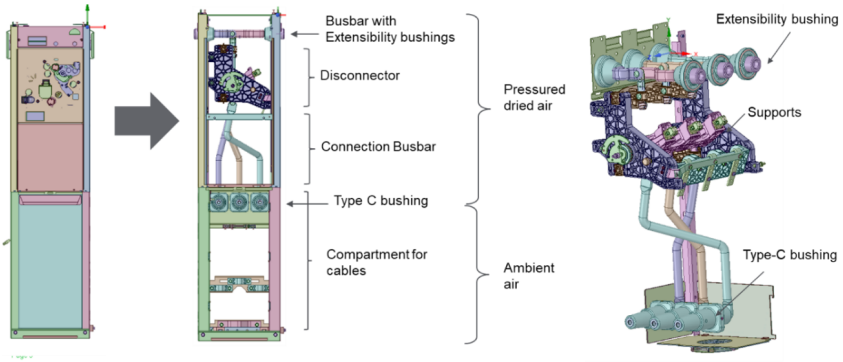

Figure 1.1.6: Configuration of MVDC switchgear, and details to insulating system.

1.2 Theoretical background

1.2.1 Generalities about polymeric materials and composites

This section provides the fundamental building blocks necessary to understand the types of materials that will be investigated later. Before introducing them, a key concept that requires clarification is the notion of the *Materials Tetrahedron*, pictured in Figure 1.2.1.

As seen there, materials are selected based on their *performances* (cost, resistance, durability, processability, etc). These performances are determined from some *properties*. The physical and chemical properties are derived from both the material's *composition* and its *microstructure*. The former is linked to the chemical elements that make up the material and their interrelationships, while the latter encompasses what we observe under a microscope, such as morphology, phase separation, and fiber orientation. Both of these aspects are influenced by the *manufacturing process*, and some of them can be altered by factors like storage conditions, and electrical/mechanical/thermal stresses, i.e. the entire history of the material.

Despite its apparent simplicity, this concept will be revisited and emphasized throughout this thesis because the conductivity, once measured, will reflect the structure and microstructure of the sample, which can vary not only across different works worldwide but also over time and in response to various stresses.

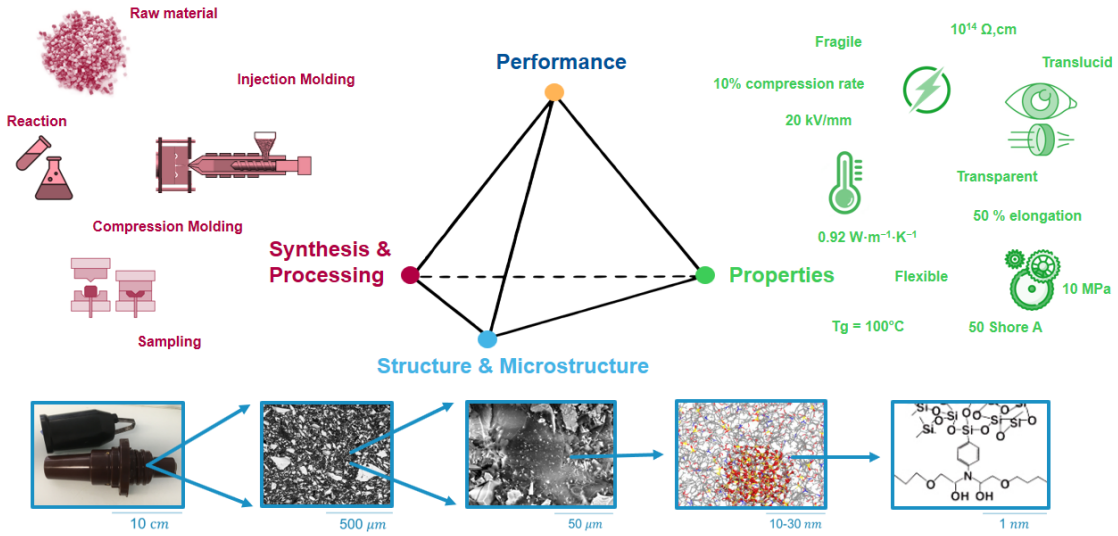

Figure 1.2.1: Materials Tetrahedron. Scheme made by the author, the main concept coming from [27]

The insulating materials under investigation here are classified as polymers or polymeric composites. Polymers are long-chain molecules of very high molecular weight. They are macromolecules formed by linking together large numbers of simple chemical units (*structural units*) covalently bonded. The starting molecule giving birth to the structural unit is called monomer (just one repeating unit) [28]. A couple of monomers associated together produce a bigger molecule composed already of structural units, the *oligomer* (oligo = *some* in Greek). As the quantity of structural units increases (some sources suggest tens of thousands of repeating units [29]), the oligomer becomes a polymer, having the properties we are used to study.

Solid polymers are generally categorized into three main groups based on their mechanical behavior [30, 28]:

- **Thermoplastics:** These polymers can soften and flow when subjected to higher temperatures and pressure, returning to a solid state when the conditions are reduced. They are not studied in this thesis.

- **Thermosets:** They cannot soften or flow with temperature changes because they have undergone curing. This curing process involves creating a three-dimensional network structure with the monomers connected by covalent bonds, typically facilitated by a cross-linking molecule, also known as a hardener. The curing is irreversible, resulting in a rigid solid [31]. In this study, this class is represented by the epoxy resin, widely used as an insulating material in electrical engineering. Its features are presented in section 1.2.2.

- **Elastomers or Rubbers :** Elastomers are polymers that can deform at room temperature and return to their original shape once the force is removed. This property is often achieved through a low density of cross-linking reactions among oligomers or thermoplastics [32]. Cable terminations and connections frequently employ elastomers. In this study, our focus is on silicone rubber as a representative elastomer. It is detailed in section 1.2.3.

When a polymer is combined with another material, the resulting product is known as a composite. A composite is precisely defined as the combination of two or more materials to create a unique set of properties that differs from those of the individual raw materials. These distinctive properties must be a result of their combination. Composites encompass a broad range of materials, including metal alloys, plastic co-polymers, minerals, and wood. However, the term "composite" is most commonly associated with the incorporation of reinforcing fibers, particulates, or whiskers into a matrix resin [33]. This reinforcing material is often referred to as a *filler* and typically possesses dimensions in the micron range (on the order of 10^{-6} meters). If they are in the nano range (10^{-9} m), it characterises a nanocomposite; and in the middle, a mesocomposite.

The size of the filler is a critical factor in determining the composite's properties. Smaller fillers result in larger contact surfaces, and the contribution of the filler material varies accordingly. The surface properties of the filler can significantly differ from those of the bulk material, leading to specific enhancements in the composite's characteristics.

In addition to a matrix and a filler, industrial compounds incorporate a variety of additives within a complex formulation. These additives serve different purposes, such as enhancing the material's characteristics for specific fabrication processes, storage, applications, recycling, and reutilization. Some common additives include plasticizers, antioxidants, fire-resistant agents, pigments, dyes, demolding agents, anti-static agents, voltage stabilizers, and many others. These additives are not limited to influencing just one property of the material; they often have multifaceted effects. Due to the intricate nature of these compound formulations, the materials studied in this thesis are regarded as *systems*. The final properties, including electrical conductivity, represent the specific response of these systems to electrical stress and are influenced by the interplay of various additives and components within the material.

1.2.2 Epoxydic systems

Definition: Rigorously speaking, epoxy is the ring-shaped functional group represented in Figure 1.2.2 [34], also known as oxirane group. Etymologically, "ep" means "between" in ancient Greek, while "oxy" refers to oxygen. "Epoxy resin" is a general (and sometimes misleading) term that involves both any prepolymer (monomer or oligomer) containing an oxirane and the cured resins formed from this oxirane-containing prepolymer.

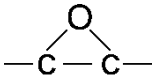

Figure 1.2.2: Molecular structure of the epoxy group.

Synthesis: Many routes can be taken to produce the prepolymer. One classical method, known as the *Taffy process*, involves:

1. An addition reaction between epichlorohydrin (containing the epoxy group) and a compound containing an active hydrogen.

2. Dehydrogenation using a base, removing the chlorine.

Figure 1.2.3 provides examples of this process with the prepolymer DGEBA (diglycidyl ether of bisphenol A) obtained from Bisphenol A (BPA) and epichlorohydrin. DGEBA is the most commonly used thermoset in electrical applications, and it is employed in this work. The prepolymer is typically a viscous liquid containing DGEBA at room temperature. The viscosity of the prepolymer can be controlled by adjusting the number (n) of additional monomers or the degree of polymerization. According to Ellis [34], 88% of commercial raw materials consist of prepolymers without additional monomers (n = 0). May [35] informs that commercial grades can have n ranging from 0 to 12.

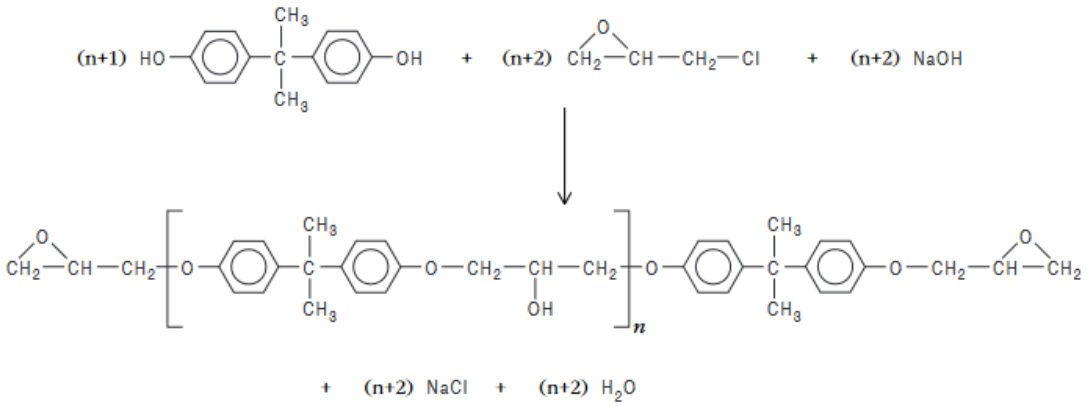

Figure 1.2.3: Synthesis of DGEBPA prepolymer.

The curing process: The prepolymer is mixed to a hardener to give the final thermoset through a curing (or cross-linking) reaction. Because the curing reaction will outcome the cross-linked macromolecule, it is indeed a polymerization. The curing temperature, and the reactional mechanism, will closely depend on the hardener selected for the curing, which can drive a homopolymerization (catalytic hardners), or participate as a reactant to drive a copolymerization (co-reactive hardeners). Other cross-linking agents include nitrogen compounds (urea, melanine, hydrazine), boric nitrogen compounds (borates, metaborates), salts of metals and oxydes.

In this work we are using the methyltetrahydrophthalic anhydride (MTHPA) as hardener, as seen in Figure 1.2.4, and a quaternary ammonium halide salt as catalyser.

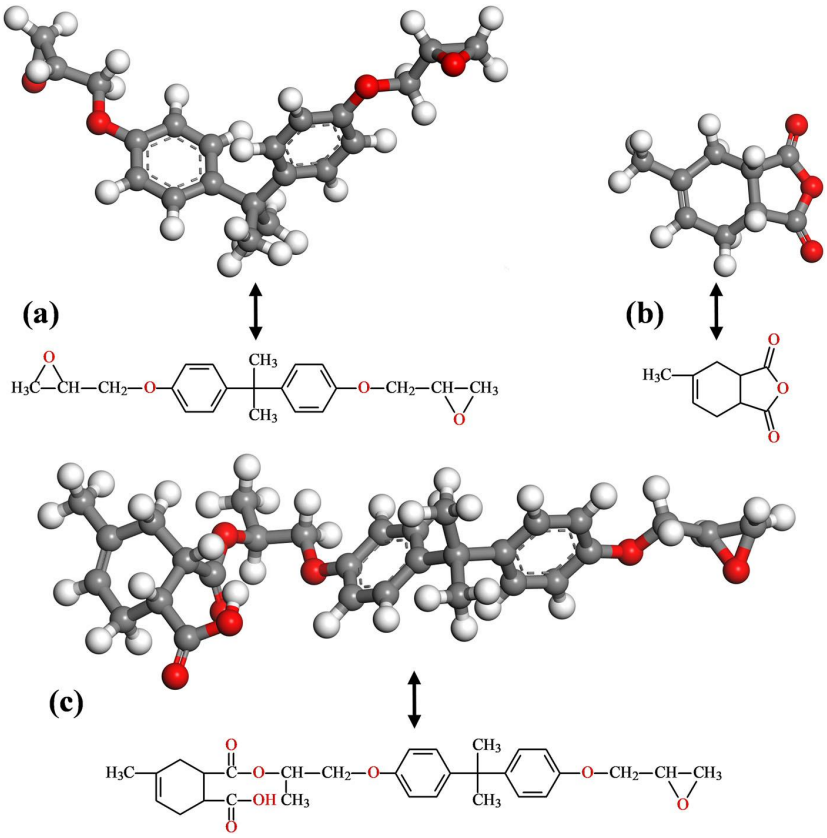

Figure 1.2.4: Molecular strucure of the DGEBA (a), MTHPA (b), and cured resin (c). [36]

We do not intent to describe in details the curing mechanisms. We can not either describe all the possibilities, otherwise the list of mechanisms would be long and non-exhaustive. As many mechanisms have been described by renowned references, as for example May [35] and Ellis [34], and similar resins/hardener have been studied by Le Huy [37] and Dureault [38], there are some clues and standard steps that should be expected.

- **Initiation:** The MTHPA, being an anhydride, acts as a Bronsted acid and becomes active at temperatures typically exceeding 80°C. It can undergo direct interaction with DGEBA through esterification (where anhydride cycles are opened by $-OH$). Alternatively, different DGEBA molecules may interact with each other through homopolymerization involving etherification. In

the presence of a basic catalyst, such as the tertiary amine R_3N, which also serves as a low-temperature curing agent and can be employed as accelerator, an anhydride-amine complex forms. This complex functions as an anionic initiator, as illustrated in Figure 1.2.5 for the case of a phtalic anhydride.

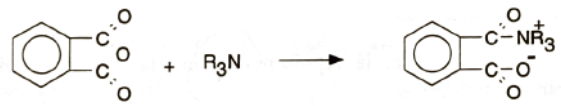

Figure 1.2.5: Example of possible initiation with a tertiary amine as catalyser resulting in an carboxylate ion

- **Propagation:** The reaction undergo through sterification between the epoxy groups of uncured DGEBA and carboxylate ions, as Figure 1.2.6 shows.

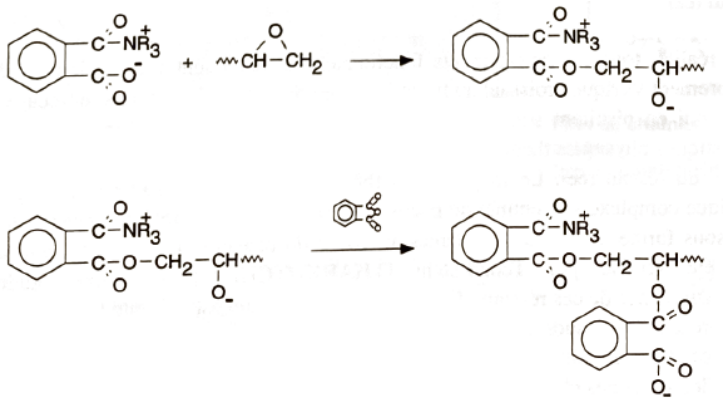

Figure 1.2.6: Examples of possibles propagation by sterification

- **Termination:** when two propagation centers meet each other, the reaction ceases, and the catalyser is reconstituted (Figure 1.2.7).

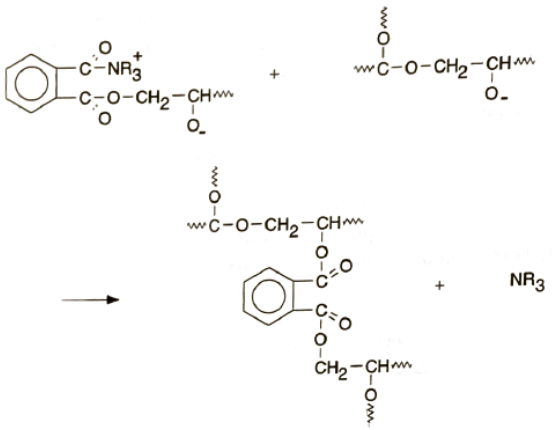

Figure 1.2.7: Example of possible termination and catalyser restitution

When concentration of catalyser is well dosed, there is no homopolymerization, as discussed by Le Huy [37]. However, the excess of DGEBA can induce homopolymerization and "hopolymer" regions in the chain. Alternativelly, an excess of MTHPA

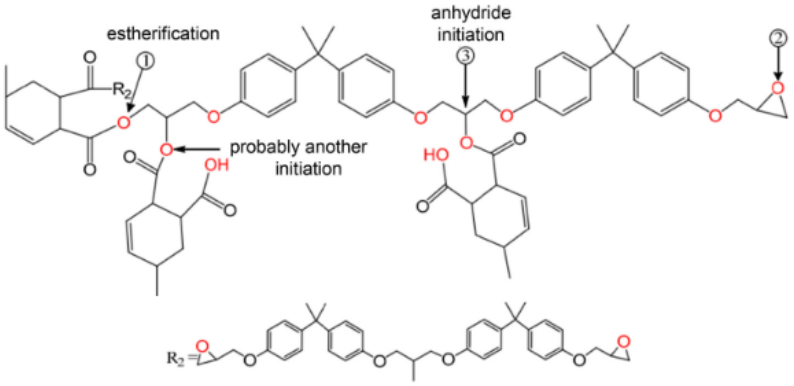

Figure 1.2.8: Example of network scheme for anhydride-hardened DGEBA.

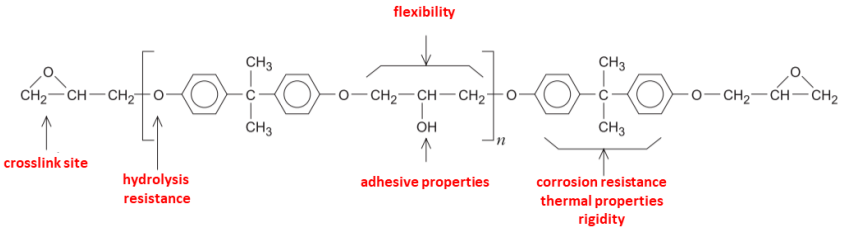

Figure 1.2.9: Structural unity of the DGEBA prepolymer. Adapted from [39]

would promote acid end chains formation. At the end, the curing process outcomes a 3D network like the one in Figure 1.2.8.

Structure-property relationships: The properties of a cured epoxy is directly related to epoxy monomer and the curing agent. The strength, extensibility, and toughness below Tg are mostly associated with short-segment motion derived from the monomeric chemistry, while at temperatures through and above Tg, mechanical properties depend on the crosslink density and molecular weight between crosslinks [35].

Looking closely to the structural unity of the DGEBA (Figure 1.2.9), the different functional groups give insights about the final properties: phenyl groups are often associated with rigidity. Evidences relate them to antioxidant action, which leads to improvements in corrosion and degradation resistance. Hydroxils, on the other hand, participate in hydrogen bonding, and generate either positively or negatively charged ion. The alcohol-like behaviour enabled by hydroxides enhance the solubility in water. The alkyl group bounded to the $-OH$ present a rotational chain movements, giving some flexibility. Ether groups are very polar and can also participate in hydrogen bonding, whereas they is highly stable, making the cleavage unlike in absence of specialized reagents, as strong basic agents.

Comment about the filler: Fillers are often added to the epoxy to improve their mechanical properties and impact resistance. It can also reduce the expansion coefficient and the shrink during molding. In terms of electrical properties, at least under AC, they often increase the dielectric strength of the composite. The epoxy of the study forms a composite with silica. Many studies ([40, 41]) confirmed that the silica does not affect considerably the curing mechanism, and the overall Tg.

The chemical structure of silica can be seen two SiO_4 tetrahedra bridged together by a shared oxygen. [42]. This oxygen, if not bonded, can be the site of hydrogen bonds coming from water molecules or from the matrix (if any). Silica flour can contain amorphous silica and eventually crystalline structures, as quartz. The quartz presents piezoelectric properties because the center of dipole moment does not coincide with the centre of the cubicle cell. As a consequence, it can mechanically deform with an electrical stress; and a mechanical deformation can generate polarization. This can be particularly problematic for space charge measurement methods that encompasses some pressure feature, as the pressure pulse method used in this thesis, since the piezoelectric effect will produce spurious signals [43].

1.2.3 Silicone rubber systems

Definition: Silicone rubbers (SiR), also known as poly(siloxane), are elastomers composed of an inorganic siloxane backbone ($-Si-O-$ chain) associated with organic groups [44]. The silicon atom is able to establish four chemical bonds, so thus silicone rubbers are often abbreviated by the letter Q (*quaternary group*)[45]. Bounded to the silicon atom, methyl groups (-CH_3), abbreviated by M, give origin to the polydimethylsiloxane (PDMS, or simply MQ), which is the most simple and common silicone rubber available.

Classification according to the structure: Many commercial grades have some methyl groups replaced by other groups [46, 47]:

- The vinyl ($-CH=CH_2$), abbreviated by V (thus MVQ), reduces the compression set and it gives a preferred cross-linking sites though its reactive insaturations. The vinyl content ranges of about from 0,5 to 4,5%.
- The phenyl ($-C_6H_5$), abbreviated by P (thus MPQ or MPVQ) is voluminous and increases the free space between chains, which decreases the Tg and increases the flexibility at lower temperatures. Because of the stability of phenyl groups, these materials are usually temperature resistant.
- The trifluoropropyl ($-CH_2-CH_2-CF_3$), abbreviated by F (providing FVQ structures), is polar. It decreases the swelling with aliphates, but increases swelling with acetones. It is also oil resistant, once many oils found in the market are apolar.

Structure-property relationship: The structure of a uncured MVQ silicone chain is presented in Figure 1.2.10

The $Si-O$ bond is very polarized because of the lower electronegativity of silicon (1.8) in comparison with carbon (2.5). It leads to a highly ionic and large bond energy of 452 kJ/mol (108 kcal/mol) resistant to homolytic scission and responsible for the chemical and thermal stability of silicone rubbers. The methyl groups ($-CH_3$) bounded around the inorganic backbone gives hydrophobicity to the material as the same time it leads to low intermolecular interactions (mainly composed of London-van der Waals interactions). As the main consequences, a high free volume appears and results in highly solubility and diffusion of gases, i.e. high permeability. The free volume is also due to the bond angle $Si-O-Si$ that vary from 105° to 180°,

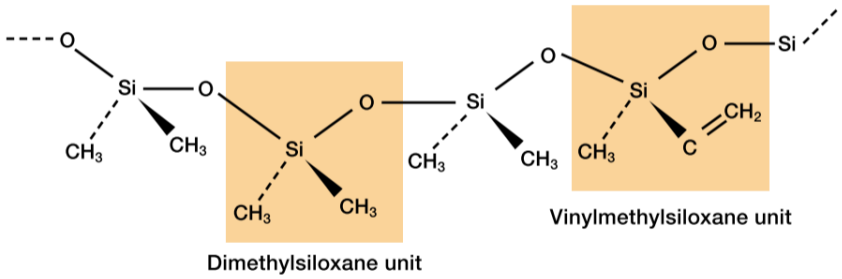

Figure 1.2.10: Chemical structure of an uncured silicone chain (MVQ type) [45]

.

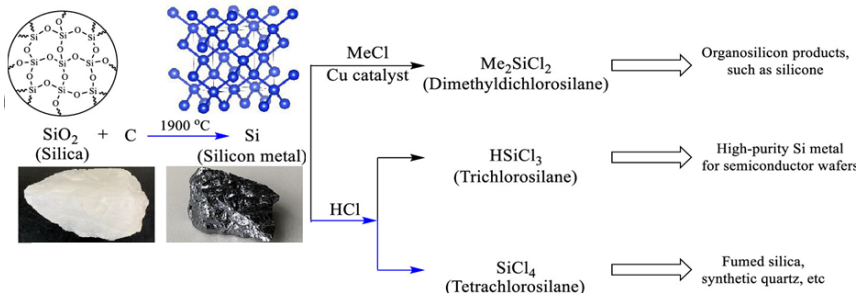

Figure 1.2.11: Transformation of quartz to many silicone rubber precursors. Adapted from [50]

which is very rotational. All this justifies a very low glass transition temperature (Tg near -125°C), a low melting temperature (T_m near -50°C), and permeability to oxygen, nitrogen and water vapour [44, 48, 49].

Synthesis: The precursor of silicone is quartz ($Si0_2$), which is converted to silicon metal (Si_{metal}), then to chlorosilanes, which are hydrolysed, producing silanols or hydroxysilanes [50]. An overview of this process can be seen in Figure 1.2.11. Note that this process is the same to produce fumed silica, which is the most common filler found in silicone elastomers. The conversion of silicon metal to chlorosilanes is a catalytic reaction and compounds with different functionalities can be produced. The possibility to produce bigger molecules (oligomers) by polycondensation, enabled by the control of the final viscosity through a balance of hydroxysilanols with different functionalities, explains why many physical states of silicones can be found in the market: liquids, oils, pastes or greases, and gums [44, 51]..

Classification according to processing: The physical states of silicone elastomers raw materials are classified into solids (high consistency rubber, HCR), or liquids (liquid silicone rubber, LSR). Not just the physical state differs, but many routes can be used to vulcanize/cure the oligomers. If the curing agent is activated by moisture at room temperature, the final silicone is classified as RTV (room temperature vulcanized). Others will require temperature to be activated, being classified as HTV (high temperature vulcanized). Some sources treat HTV and HCR as synonyms, since HCR is also an acronym for *Heat Curing Rubber*. But LSR can also be vulcanized at high temperatures, and in some extend they are HTV too. Other sources consider RTV as a class itself, separated from HCR and LSR, and

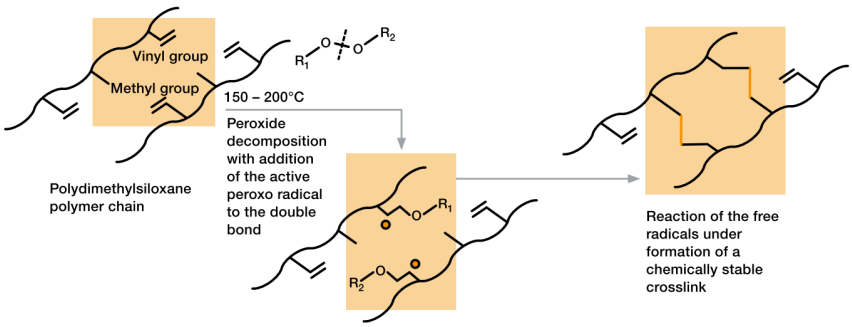

Figure 1.2.12: Scheme of HCR curing via peroxide condensation reaction. [45]

subdivided in RTV-1 (adding), and RTV-2 (condensation).

Curing: The curing strategy is associated with the physical state of the raw material. Here, we are focusing on two of them:

1. **Condensation reactions of HCR provided by peroxides:** Peroxide molecules ($R_1 - O - O - R_2$) undergo thermal dissociation, giving rise to peroxide radicals ($R_1 - O\cdot$ and $\cdot O - R_2$). These radicals are capable of attracting hydrogen atoms from methyl groups or adding to double bonds in vinyls, resulting in the formation of macroradicals, specifically radical centers on elastomers. Subsequently, these macroradicals recombine, leading to the formation of carbon-carbon cross-links [52]. In this process, the R groups from the departing peroxides can be substantial enough to adhere to the matrix, serving to inhibit or reduce potential exudation. This makes the curing agent particularly suitable for High Consistency Rubber (HCR). A schematic representation of this curing process is provided in Figure 1.2.12.

2. **Adding reactions of LSR provided by platinum-based catalysts:** At elevated temperatures, typically around 160°C, platinum (typically present in a concentration of 10-15 ppm) catalyzes the cleavage of double bonds in vinyls. Consequently, these vinyls form bonds with hydrides from another polymer chain. The hydride source is often a short-chain polyorganosiloxane, serving as a cross-linking agent. This process is illustrated in Figure 1.2.13. Liquid Silicone Rubber (LSR) kits generally consist of two components: one containing the base polymer and the catalyst, and the other containing the base polymer, the cross-linking agent, and a cross-link inhibitor.

   The inhibitor's role is crucial in preventing premature curing and volatilization at high temperatures. Inhibitors may include short polymer chains with end groups, such as ethynyl cyclohexanol, or acetylenic alcohols, hydroperoxides, alkenyl-containing maleates, or isocyanurates. These inhibitors play a vital role in maintaining the stability of the LSR mixture until it is ready for controlled curing processes.

Comment about the filler: Commercial grades often incorporate fumed silica, also known as pyrolized or pyrogenic silica, a distinct form of silica that differs from the microsilica discussed in Section 1.2.2. Fumed silica is a synthetic product created through the hydrolysis of silicon tetrachloride in a hydrogen flame, resulting in

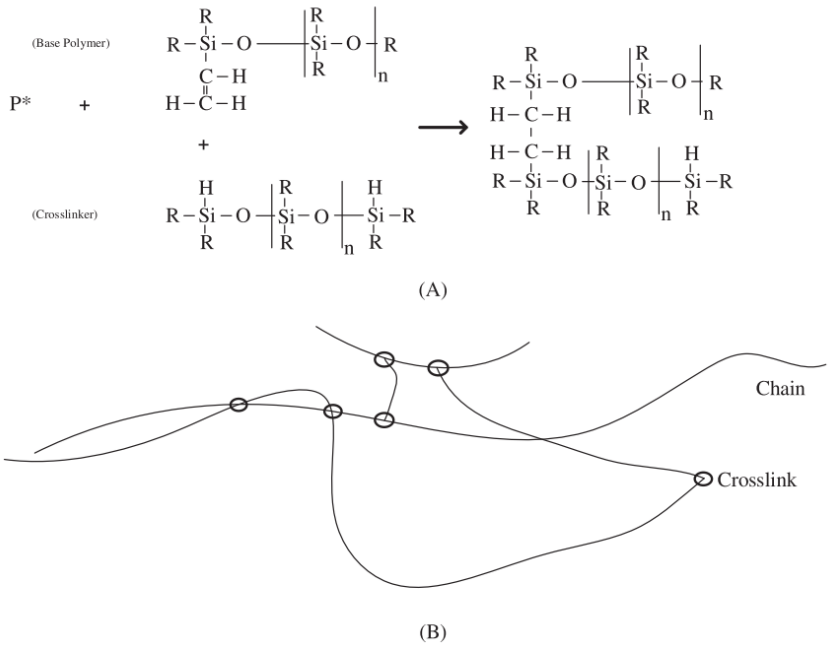

Figure 1.2.13: Adding curing reaction between a base polymer, a crosslinker, and a catalyst (A); and a scheme of a random crosslink structure (B). From [53]

the production of steam and HCl as byproducts [54]. The silicon tetrachloride is illustrated in Figure 1.2.11. Alternatively, precipitated silica, produced from a solution containing silica salts, can also be utilized. Both forms of silica are amorphous. The addition of silica is primarily aimed at improving mechanical and electrical properties [55], typically constituting around 20-30% of the material's weight.

Each particle of pyrogenic silica typically ranges in diameter from 7 to 40 nm [54]. These particles have the potential to form aggregates, and these aggregates can further agglomerate into structures measuring up to 200 nm. In the agglomerated form, a porosity is also expected [56]. These structures have the capability to interact with the matrix through hydrogen bonds with silanol groups. However, if the silica is not silanized and the matrix lacks hydroxyl groups, only weak Van der Waals interactions will occur [57, 58].

Comment about degradation: In the process of degradation, the oxidation of silicone chains transforms the inorganic backbone into silica; it is said that the polymer is "ceramised". Simultaneously, methyl substituents undergo oxidation, resulting in the formation of carbon monoxide, carbon dioxide, formaldehyde, hydrogen, and water [59]. In other words, the primary degradation product of silicone rubbers is expected to be silica, which itself is a dielectric material. This is the basis for the assertion by many suppliers that silicone rubbers yield a dielectric ash during electrical degradation.

1.2.4 Generalities about water sorption in polymers

An integral aspect of this thesis is the meticulous regulation of water absorption by the dielectrics and the assessment of electrical properties in relation to this uptake. Consequently, gaining essential insights into the sorption kinetics and mechanisms

becomes imperative. Only a summary about the subject is presented, since the literature concerning such events is huge and further considerations about the kinetics, thermodynamics, and sorption mechanisms are far beyond the scope of this thesis.

The relative humidity (RH) : We remember that the relative humidity (RH) is the relation of the vapour pressure of the environmental water P and the temperature-dependent saturation pressure P_0 (Equation 1.2.1).

$$RH = \frac{P(T) * 100}{P_0(T)} \tag{1.2.1}$$

Since the RH can be measured by test probes, and since the temperature is stabilized during electrical tests, the partial pressure of water vapour can be obtained if we considered the saturation vapour pressure as the theoretical one provided by the standard ISO 13788:2012, showed in Equation 1.2.2 in which T representing the temperature in ^oC. The pressures are in Pa.

$$P_0 = 610.5exp\left(\frac{17.269T}{237.3+T}\right) \tag{1.2.2}$$

1.2.4.1 Terminology

A simplified diagram is presented in Figure 1.2.14 to illustrate the various species and interactions involved in a sorption process. This visual aid is complemented by a list of definitions.

Sorption: General term used to describe the penetration and dispersal of penetrant molecule in a polymeric matrix to form a mixture [60].

Sorbate and sorbent: Sorbate is the species that is going to be attached, and sorbent is the material that will receive the species.

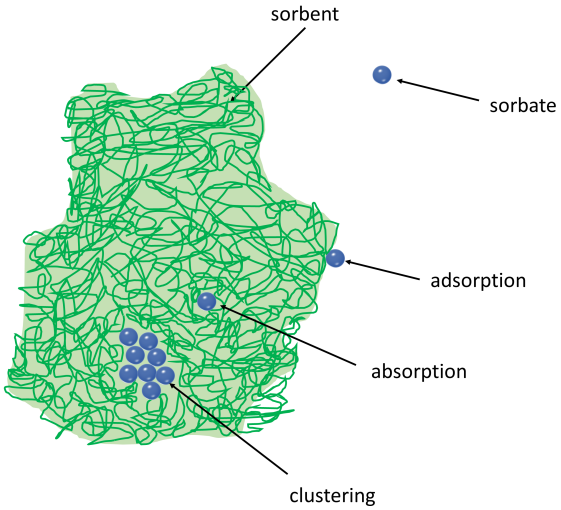

Figure 1.2.14: Schematic illustration of a very simplistic case of a hypothetical sorbent and a hypothetical sorbate, here represented as spheres, and some of possible interactions (adsorption, absorption, and clustering)

Absorption: The process of one material being retained by another[61]. Here, it is mostly related to the penetration of water molecules into the bulk of polymers [60]. The water absorption is possible because, once polymers have a high molecular motion, they are permeable, whilst ceramics, glasses, and metals are not [60]. As water permeates, it can attach to the material, ultimately changing its properties. The bulk material is the absorbent, and the molecule species that penetrates it is the absorbate.

Adsorption: The increase in the concentration of a molecular species at the interface of a condensed phase due to surface forces [61]. The condensed phase (the solid) is the adsorbent and the molecular species (the water, for example) adhering to it the adsorbate. The polymeric matrix can also be seen as adsorbed on the silica surface, and an adhesion between them should exist. It is a challenging task to differentiate absorption and adsorption: still because the flexibility of polymer chains, the sorbed material can penetrate into the mass in such a way that the sorption mechanism may comprises both adsorption and absorption components[62]. In addition, the composite itself has many interfaces (some consider them as interphases) in which water can be allocated.

Physisorption or Physical adsorption: when the adsorption mechanism is described in terms of weak intermolecular forces, as Van der Waals interaction. It alters the the surface structure of polymers. It is very fast unless limited by mass transport rates in the gas phase or porous adsorbent, and it is also reversible [63].

Chemisorption: when the adsorption energy is large enough to be comparable to chemical bond energies. It modifies the adsorbent and restructures the surface. It has a higher chemical specificity and the adsorbate is difficult to remove. It is expected to be limited to a monolayer, although physisorption can comprehend multilayers, possibly even above a chemisorbed layer. A gas can be physically adsorbed at first, and then, slowly, participate in a chemical reaction [63].

1.2.4.2 Time-dependent sorption: Diffusion mechanisms

Numerous models exist to describe the diffusion of water molecules into polymers [64]. Commonly, two primary mechanisms are applied: the Fickian and the pseudo-Fickian. These mechanisms are often graphically represented by the mass uptake as a function of the square root of time, known as the "reduced sorption curve." Both mechanisms are illustrated in Figure 1.2.15. Daviaud [65] further subdivides the pseudo-Fickian into two classes: Langmuir's model and anomalous diffusion. The latter does not adhere to either the Fickian or Langmuirian theories.

The Fick's model The simplest mechanism of diffusion is described by Fick's one-dimensional law. This law posits that the sorbate is free to diffuse into the sorbent based on the concentration gradient of the sorbate between the environment and the bulk of the sorbent. The first and second laws of Fick are expressed in Equations 1.2.3 and 1.2.4, respectively. Whilst the first law describe the sorbate density flow J_d merely as a function of the gradient concentration ∇c, the second law takes into account the time and the diffusion kinetics. In these equations, D denotes

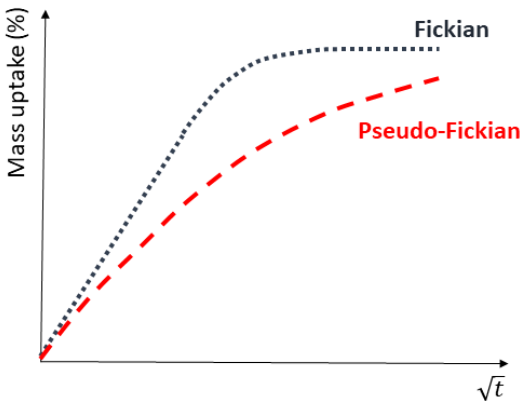

Figure 1.2.15: Reduced sorption curves of a Fickian and a pseudo-Fickian diffusional mechanisms

the diffusion coefficient, and it may depend on the temperature T, pressure P of diffusive species, the concentration, and porosity of the diffusion media.

$$J_w = -D.\nabla c \tag{1.2.3}$$

$$\frac{\partial c}{\partial t} = \nabla(D\nabla c) \tag{1.2.4}$$

In the case of diffusion in solids, the diffusion coefficient D follows an Arrhenius law, such as in equation 1.2.5, in which D_0 is a maximum diffusion coefficient at an infinite temperature, and E_a is an activation energy. The D here still represents a simple case of one-dimensional diffusion for a homogeneous and isotropic media without any bounding of diffusive species.

$$D = D_0 exp\left(\frac{E_a}{RT}\right) \tag{1.2.5}$$

By solving Equations 1.2.3 and 1.2.4 the mass uptake in weight (m(t)) can be calculated as shown in Equation 1.2.6 where m_∞ is the total mass ingress at equilibrium, and d is the sample thickness [64].

$$\frac{m(t)}{m_\infty} = 1 - \frac{8}{\pi^2}\sum_{n=0}^{\infty}\frac{1}{(2n+1)^2} exp\left(-\frac{D(2n+1)^2\pi^2 t}{(2d)^2}\right) \tag{1.2.6}$$

As can be seen in Figure 1.2.15, the first part of the Fickian model curve is a linear curve. Thus, equation 1.2.6 can be simplified to Equation 1.2.7 considering that, at the beginning, the mass uptake is linear . It facilitates the determination of the diffusion coefficient D.

$$m(t) = m_\infty \frac{4}{d\sqrt{\pi}}\sqrt{Dt} \tag{1.2.7}$$

The Langmuir's model This model is also known as diffusion in two phases as has been initially one way to describe an anomalous water uptake [64]. Regardless Fick's diffusion model that considers species free on space, so the diffusion is governed only by concentration gradient, in Langmuir's model the water uptake can be

attached to the bulk[66]. Thus, we assume that there will be c_f free mobile water molecules per unit volume that will diffuse with D_L as the diffusion coefficient and become bound at a rate αc_f. Alternatively, there will be c_b bound water molecules that become mobile at the rate βc_b. At equilibrium, these α and β coefficients are related and depend upon the RH (Equation 1.2.8).

$$\alpha c_f(RH) = \beta c_b(RH) \tag{1.2.8}$$

The first and second Fick's laws can be adjusted to bears bonding and debounding events. The Equations 1.2.9 and 1.2.9 represent them.

$$D_L \frac{\partial^2 c_f}{\partial x^2} = \frac{\partial c_f}{\partial t} + \frac{\partial c_b}{\partial t} \tag{1.2.9}$$

$$\frac{\partial c_b}{\partial t} = \alpha c_f - \beta c_b \tag{1.2.10}$$

As done for the Fickian model, both equations can be solved to describe the total moisture uptake in an initially dry slab as a function of the time. The approximated solution is detailed in Equations 1.2.11 and 1.2.12.

$$\frac{m(t)}{m_\infty} = \frac{\beta}{\alpha+\beta} exp(-\alpha t) y(t) + 1 - exp(-\beta t) + \frac{\beta}{\alpha+\beta}[exp(-\beta t) - exp(-\alpha t)] \tag{1.2.11}$$

with

$$y(t) = 1 - \frac{8}{\pi^2} \sum_{n=0}^{\infty} \frac{1}{(2n+1)^2} exp[-\frac{D(2n+1)^2 \pi^2 t}{(2d)^2}] \tag{1.2.12}$$

Again, if the exposure time is small enough, i.e. for an exposure time smaller than $0.7h^2/\pi^2 D_L$, the equation 1.2.11 can be simplified to Equation 1.2.13.

$$m_\infty \approx \frac{4}{\pi^{3/2}} \left(\frac{\beta}{\alpha+\beta} m_\infty \right) \sqrt{\frac{\pi^2 D_L t}{d^2}} \tag{1.2.13}$$

1.2.4.3 Steady-state sorption: Isotherm models

The transport behavior of penetrants in polymers is elucidated by analyzing isotherm curves and their corresponding physical interpretations. These curves are obtained in stable conditions (temperature and pressure). A stabilisation in water sorption quantity (as the weight, for example), is an indication that a saturation level has been achieved for that temperature/RH couple [67]. This saturation level indicates that the water is uniformly distributed through the bulk.

These isotherms were initially developed to describe adsorption mechanisms [63], involving the plotting of a parameter θ against the vapor pressure P of the sorbate species. Here, θ represents the sorbed concentration, or fractional sorption, and it is ratio of the total surface covered (S_1) to the entire surface (S), expressed as $\theta = S_1/S$. Comyn [60] applies these isotherms interchangeably, whether the process under consideration is adsorption or absorption. Such equality should be treated carefully, since adsorption and absorption are different *phenomena*.

Subsequently, θ has been further investigated in terms of mass uptake or concentration of sorbed species in the sorbent phase [68, 69, 70]. In order to be coherent with the initial concept of θ, two main hypothesis are made:

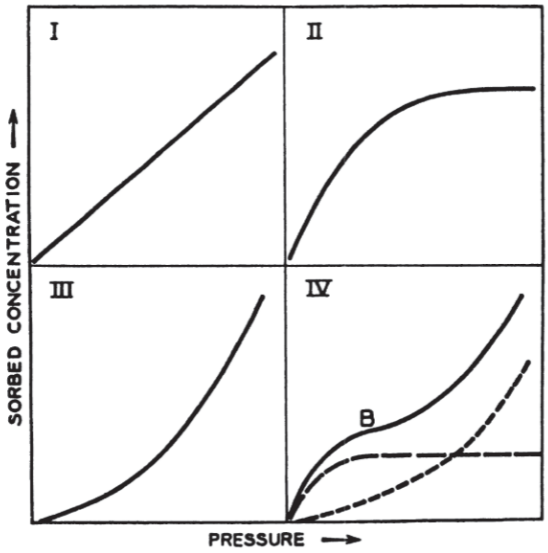

Figure 1.2.16: Typical isotherm plots [60]

Type	Law's name	Physical description
I	Henry	Ideal-dilute solution: case of penetrant randomly dispersed within the polymer matrix.
II	Langmuir	Initial sorption on some kind of specific sites, as hydrophilic sites in the matrix or sorption on dispersed high-area inorganic filler particle.
III	Flory-Huggins	The first molecules sorbed tend to loosen the polymer structure locally and make it easier for subsequent molecules to enter (plasticization of the polymer)
IV	BET	Combination of types II and III. At low pressures, water is sorbed in polar sites. At high pressures, there is the predomination of relative vapour pressure solution or clustering process.

Table 1.2.1: Sorption isotherm types and description

- The surface covered is correlated to the total amount of water sorbed, so the weight gain is considered; i.e. weight of a sample m less the weight of the dry sample m_0.

- The total surface that can be covered is related to the total amount of water that the sample is able to sorb at a constant temperature; i.e. the sample's weight under stabilization at $RH = 100\%$ less the dry sample m_0.

Assuming these hypothesis true, the ration of water sorbed becomes the Equation 1.2.14 (for a constant temperature). It agrees with the concept of θ presented by Do [70].

$$\theta = \frac{m_{sorbed}}{m_{saturation}} = \frac{m - m_0}{m_{(RH=100\%)} - m_0} \tag{1.2.14}$$

Comyn [60] categorizes four distinct isotherm types for sorption in polymers. These patterns are visually depicted in Figure 1.2.16. The corresponding nomenclatures and physical interpretations are succinctly summarized in Table 1.2.1.

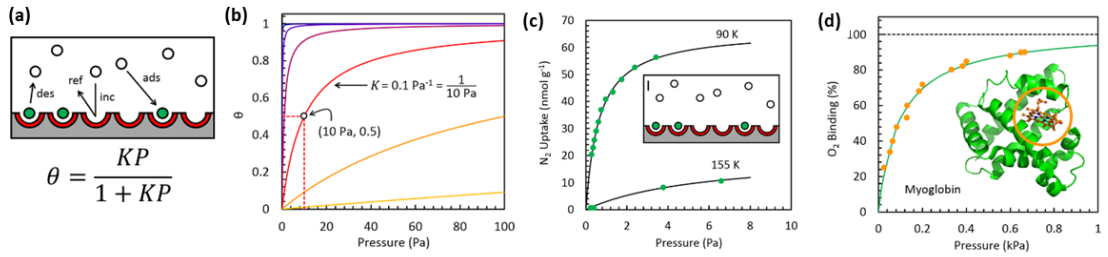

Figure 1.2.17: (a) Langmuir's kinetic model of adsorption of four processes occuring between gas in equilibrium with a surface: incidence (inc), reflection (ref), adsorption (ads), and desorption (des). In the equation, K represents a temperature-dependent constant. [68] (b) Dependence of the Langmuir isotherm on the Langmuir binding constant K as a function of pressure. [68] (c) Equilibrium desorption measurements of N_2 on mica at 90 and 155 K showing a single-site Langmuir (SSL) adsorption character. [68] (d) Equilibrium O_2 binding on myoglobin showing a single-site Langmuir (SSL) character. [68]

The Henry's isotherm According to Henry's equation for ideal-dilute gases in a liquid, the vapour pressure of a component P and the ratio θ of such component in the sorbent are associated by a constant of proportionality which is not the vapour pressure of the pure substance, but a new parameter named later as Henry's constant H [71].The Equation 1.2.15 is propose to resume such idea.

$$P = H\theta \tag{1.2.15}$$

The Henry's constant H is a temperature-dependent parameter, generally increasing with temperature. Experimental curves of θ against P generally does not correspond to Henry's law, but it is therefore a limiting law achieving a reliability when θ goes to zero. Thus, Henry's law is the tangent of the experimental curve at $\theta = 0$.

The Langmuir's isotherm According to Langmuir's adsorption model, the total amount of vapour adsorbed, υ, is related to the pressure of the gas phase P, through the total amount of vapour adsorbed under saturation, υ_m, and a factor $b = k_2/k_1$, with k_1 and k_2 being constants associated to the rate of evaporation and condensation, respectively. The rate of sorbed species θ can be obtained according to Equation 1.2.16 [72, 68].

$$\theta = \frac{\upsilon}{\upsilon_m} = \frac{bP}{1+bP} \tag{1.2.16}$$

Examples of many surface interactions, as the theoretical patterns of Langmuir's adsorption model can be seen in Figure 1.2.17(a) and (b). There, the K parameter is an old notation for the b. Practical examples of N_2 adsorption on mica, and O_2 uptake on myoglobin can be seen in Figure 1.2.17(c) and (d).

The b is also known as affinity constant, and is an indicator of how strong and adsorbate molecule is attracted onto a surface. It can be described as a relation between a pre-exponential factor b_∞ inversely proportional to the square root of the molecular weight, the adsorption heat Q equivalent to the activation energy of desorption, and the Boltzmann constant k (Equation 1.2.17).

$$b = b_{\infty}.exp(Q/kT) \tag{1.2.17}$$

During the modelling of the Langmuir's law of diffusion, Carter [66] proposes an equation for the fraction of moisture at equilibrium with the RH (Equation 1.2.18). This equation associated both Langmuir theories and suggest an isotherm as a function of bounded and debounded water molecules (c_{β} and c_{α} respectively), the molecular weight of water M_w, the Avogadro number N_A, and the density of the dry resin d_{dry}

$$m_{\infty}(RH) = \frac{100 M_w}{N_A d_{dry}}[c_{\alpha}(RH) + c_{\beta}(RH)] \tag{1.2.18}$$

The Flory-Huggins isotherm This model was not developed by Flory and Huggins, but derived from their polymer-monomer solution theory, and has been applied for liquid phase adsorption cases. There are two main assumptions [73]:

- The adsorption layer behaves like an athermal lattice interfacial solution because of the supposed big difference in sizes between sorbed and sorbent species.
- The coordination number z of the adsorption (number of neighboring adsorbed gas molecules that directly interact with a central adsorbed gas molecule) tends to infinity.

The isotherm equation that the fraction amount adsorbed θ is related to the equilibrium liquid phase concentration C (thus, the concentration of sorbed species in the environment, here often denoted by P or RH) according to the Equation 1.2.19. There are three parameters in this equation: b, which is an equilibrium constant (as for Langmuir's isotherm), k which is associated with interactions between adsorbed material, and n that is a molecular size ratio or the area ratio parameter.

$$bC = \frac{\theta}{(1-\theta)^n} exp(-k\theta) \tag{1.2.19}$$

It can be observed that, if $k = 0$ and:

- $n = 1$, the equation can be converted to a Langmuir's isotherm.
- $n = 0$, the equation becomes the Henry's law.
- $n \neq 1$ and $n \neq 0$, it becomes the Freundlich's law.

Thus, Flory-Huggins isotherm is surrounded by numerous pitfalls, and its application requires meticulous attention and care [69].

The BET isotherm The BET model (Brunauer, Ellet, and Teller's work), an extension of Langmuir's model comprising multilayer adsorption, is a tentative of generalization of adsorption isotherms. The main assumption is that the Langmuir equation 1.2.16 applies to each layer, just the heat of adsorption of the first layer (Q_1) is different from the others, which should be the same as the heat of condensation of the liquid adsorbate (Q_v). Additionally, the condensation has to occur only from or on exposed surfaces. It has also been identified in many high energy powdered

solids, as for precipitated silica [74]. The BET equation is described in equation 1.2.20. The x represents the ratio of the the pressure of the gas phase P and the pressure of saturation or condensation P^0 ($x = P/P^0$). The constant c, on the other hand, is related to the difference of energy of adsorption of additional layers on the first monolayer (as in equation 1.2.21).

$$\theta = \frac{\upsilon}{\upsilon_m} = \frac{cx}{(1-x)[1+(c-1)x]} \tag{1.2.20}$$

$$c \simeq e^{(Q_1 - Q_\upsilon)/RT} \tag{1.2.21}$$

1.2.5 Electrical properties of polymers under static fields

If there is a material property that characterizes a material under DC stresses as significantly as ϵ_r and tan_δ are important for AC, it is the conductivity σ. In the following sections, our focus is on determining how materials behave under DC stresses, identifying the charge carriers responsible for such conduction, understanding how conduction evolves with time, voltage, temperature, and humidity, and pinpointing other crucial DC properties for characterizing a dielectric material in DC applications. It is worth noting that we exclusively consider volumetric properties (and potentially interfacial ones); surface conductivity and other electrical events on the surface, as well as degradation and life-time estimations, are deemed sufficiently complex to warrant exploration in a dedicated thesis.

1.2.5.1 Generalities and DC events

Material selection often involves the comparison of specific representative properties or relationships, known as a "merit index", carefully chosen in advance. Thus, in DC applications, the first step should the the seek of a proper merit index, which should primarily reflect insulating characteristics under static fields, i.e. what makes an insulation isolates the conductor.

An insulating material is one that exhibits extremely high resistivity when subjected to a DC electric field, indicating its ability to impede the flow of electrical current. Thus, this definition is not based on the chemical structure, but in a property: the *resistivity* (ρ), or its reciprocal, the *conductivity* ($\sigma = 1/\rho$).

In addition of the evaluation of the resistivity, there are special events particular to DC stresses that merit equal attention [75]:

- **Accumulation of space charges:** Storage of free charge carriers able to distort the electrical field distribution and lead to failures. The field generated by the space charge follows the Poisson's equation 1.2.22 relating the charge density encountered by a Gaussian surface ρ_c and the dielectric permittivity ϵ:

$$\vec{\nabla}\vec{E} = \frac{\rho_c}{\epsilon} \tag{1.2.22}$$

- **Field inversion:** The conductivity is proportional to the temperature increase. If an insulation is exposed to a temperature gradient caused by the heat of the inner conductor, the electric field strength in layers next to the heat source can be reduced in such a way that the field, previously pointing out to the conductor, invert in the opposite direction.

- **Thermal runaway:** As the conductivity is temperature-dependent, at higher temperatures the direct current through the insulation can increase and heat even more the dielectric until a thermal breakdown.

- **Multi-layer distribution:** in a multi-layer configuration, if one dielectric present a resistivity much higher than others do, the electric field will slowly dislocate to it and increase the possibility of field inversion and space charge accumulation.

In a more classical and practical approach, the merit index is simply the conductivity or the resistivity under different fields. It involves a thorough comprehension of how conductivity may vary with environmental factors. That's the approach of this thesis. Another approach consists of taking the current measure out of the focus, since it risks to average the mechanisms and is often very low, and focus directly on space charge profile in order to have insights of charge carries and evaluate directly the presence, the nature, and the quantity of space charge accumulated. The density of space charges could be, itself, a merit index. In this thesis, this approach will be considered in certain moments.

The principle behind the resistivity is the Ohm's law, represented in a most general case by equation 1.2.23, in which dV is the voltage applied in a material's slab, R is the resistance of this slab to the passage of a current I that is crossing the surfaces of the layer.

$$R = \frac{dV}{I} \tag{1.2.23}$$

The resistance itself does not represent a property of the material because it's embedded of geometrical parameters. The extraction of them, possible if a measure is performed in a well defined geometry, give access to the volumetric resistivity. However, it is much more convenient to obtain the conductivity according to another form of Ohm's law presented in equation 1.2.24. Here, J represents the current density (in A/m^2) that achieves an electrode (with surface S) and E the electric field (V/m).

$$J = \sigma E \tag{1.2.24}$$

In experiments, when two parallel flat electrodes enclose a flat insulating polymeric sample, and when a static field is created (because of the application of a step voltage in one of the electrodes), a current can be measured in the counter-electrode. Immediately after the application of the voltage, a transient current appears (subsection 1.2.5.5), that will converge after a more or less considerable time to a steady-state current (subsection 1.2.5.6). In metals, the conduction current represents the flow of electrons that collides with ions of the lattice. In ceramics and polymers, the literature diverges, but it's acceptable that the electron, in the case of electronic conduction, will jump from a potential energy to another (subsection 1.2.5.4). With the steady-state current in hand, the current density can be calculated dividing it by the surface of the counter-electrode. If this experiment is performed for many voltage levels, a linear relationship between J and E should be found in such a fashion that the slope of them, as seen in equation 1.2.24, is the conductivity of the media.

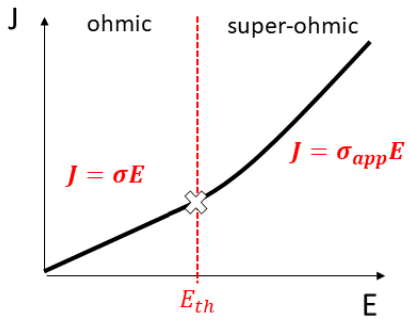

Figure 1.2.18: Relationship between the current density J as a function of the electric field E, and the separation of two *regimen*, the ohmic and the super-ohmic.

This conductivity is defined as a relation among the quantity of charge carriers n, their mobility μ and the charge of the carrier q, as in equation 1.2.25.

$$\sigma = n\mu q \tag{1.2.25}$$

The mobility itself (equation 1.2.26), in $m^2V^{-1}s^{-1}$, represents the drift velocity v_d (the velocity coming as a consequence of the momentum gain from electric force qE). In the case of metals, it also gives a relationship between the charge carrier mass and the mean time between collisions in the lattice τ, sometimes entitled relaxation time. For insulators, one can relate τ with the time spent by the charge carrier in localized energy levels (see section 1.2.5.4) but this straightforward relationship is not completely evident.

$$\mu = \frac{v_d}{E} = \frac{q\tau}{m} \tag{1.2.26}$$

Nonetheless, there is often a voltage threshold (V_{th}) after which the conductivity is not linear anymore (Figure 1.2.18, with $E_{th} = V_{th}/d$); the increase of current is usually higher than the increase of voltage, it's a *super-ohmic* conduction. Many mechanisms have been studied to explain why the super-ohmic conduction exist (1.2.5.6), the majority of them converges to the accumulation of space charge. As a matter of fact, space charges can be also accumulated in the ohmic voltage levels, they are just not strong enough to alter significantly the current profile. In engineering applications, the Ohm's law has been used to compute a relationship between J and V_{app} even for super-ohmic regions; we have been calling the result as an apparent conductivity σ_{app}, but has to bear in mind that the σ_{app} is dependent of the field E.

1.2.5.2 Charge carriers and space charge

Figure 1.2.20 provides examples illustrating the diverse range of charge carriers generated and transported within a dielectric under an electric field E which turns the electrical contacts into a cathode (electron source) and an anode (electron sink).

Space charge: Positive or negative charges originated from electrons or ions, located in the insulators, occupying a volume in which they are not neutralized; ultimately causing field distortion according to Poisson's equation.

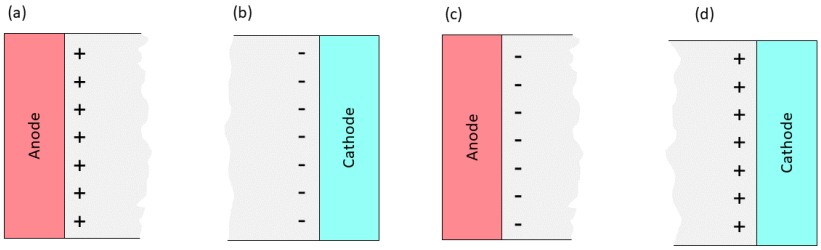

Figure 1.2.19: Positive homocharges (a), negative homocharges (b), negative heterocharges (c), and positive heterocharges (d).

Induced charges: Additional charges appearing on the electrodes as a compensation of space charge accumulated in the insulator.

Homocharges and heterocharges: Charge carriers generated at the electrode interface possessing the same polarity as the electrode are termed *homocharges*; those with an opposite polarity are referred to as *heterocharges*, as seen in Figure 1.2.19.

In simple terms, negative charges at the interface with a cathode and positive charges at the interface with an anode are homocharges, extending the source or sink zones, attenuating the field on the interface, and reinforcing in the bulk. Conversely, positive charges at the interface with a cathode and negative charges at the interface with an anode are heterocharges, reinforcing the field in the contacts and attenuating in the volume.

Intrinsic and extrinsic charges: Charge carriers can be categorized as intrinsic (originating within the material) or extrinsic (coming from external sources). They may be generated through processes such as dissociation, ionization, and injection from the electrodes, and extinguished through recombination, absorption, and ejection (extraction).

Immediately after the application of voltage, intrinsic species within the material of all levels, including atoms, molecules, and interfaces, polarize. These species contribute to a polarization current, wherein charge is transported based on dipole movement aligning with the electric field. Dipoles play a crucial role in capacitive current in AC applications, and under static fields, their impact on current is expected to be neglected if given sufficient time to stabilize according to their relaxation time τ_p.

Ions (and protons) present in the structure or created by electrodissociation and ionization are considered intrinsic, while ions generated with the assistance of species from the electrodes, gaseous plasma, or particle/electron beams are considered extrinsic. The intrinsic or extrinsic nature of OH^- and H^+ created by water dissociation is debated; while water typically comes from external sources, once absorbed by the material, it can be viewed as a component of the system, akin to additives and fillers. Due to its easy removal, water may be considered extrinsic. Ions, being larger and heavier than electrons and holes, exhibit lower mobility, leading to skepticism about their influence on measured current. Moreover, a flow of ions can contribute to time-limited ionic conduction and space charge accumulation if not neutralized.

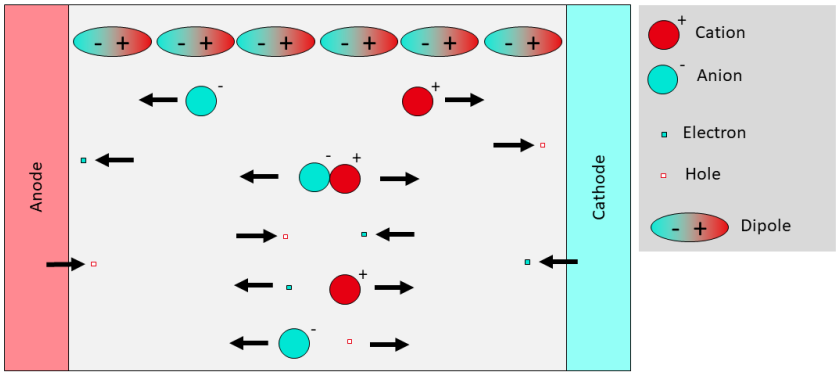

Figure 1.2.20: Scheme with different charge carriers generated and transported within a dielectric. Adapted from Laurent [76].

In steady-state fields, electron conduction is generally attributed to the measured current, although the presence and impact of holes should not be disregarded. While electrons have an effective mass m_e^*, a hole is typically defined as an entity with an effective mass of $-m_e^*$.

Any transport of charges induces local polarization in the surrounding media, disturbing dipoles and the overall structure. This combined charge and polarization transport is referred to as a *polaron*, which can be seen as charge carriers too.

Energy required for the generation and movement of these species is not solely provided by the electric field; temperature also contributes to this process. It is acknowledged that electrons can be excited by *phonons*, aiding them in overcoming energy barriers.

1.2.5.3 Space charge density and field distortion measurement

Detecting space charge: There are a plenty of different techniques that can be used to detect space charge accumulated within a sample [77, 78, 76, 79]. Many of them have spatial resolution, i.e. they enable the analysis of charge density as a function of position. It consists of some excitation (thermal of acoustic) followed by the measurement of the material's response to such excitation converted to a function of the time in a form of an electric signal. Understanding the propagation of such excitation throughout the sample enables the data conversion of the time-dependent signal to the positional-dependent charge density. Thus, these measurements are always somewhat associated with the thermal, or acoustic, or mechanical properties of the material. At this instance, the laser induced pressure pulse (LIPP) is applied in this work following a past history of studies, improvements and developments of such technique in the G2Elab team and partners [80, 81, 82, 83].

The LIPP principle: for this technique, a short light pulse from a laser illuminates the surface of an electrode; such surface has been coated by graphite ink. The light pulse heats the upper layer of the graphite to temperatures above the boiling point, causing an ablation that launches the desired pressure pulse. The pressure propagates throughout the sample based on the velocity of sound of the material's media. It generates a current $I(t)$ that can be measured in short-circuited [84, 85, 86]. This current, indicated by equation 1.2.27, enables the direct determination of

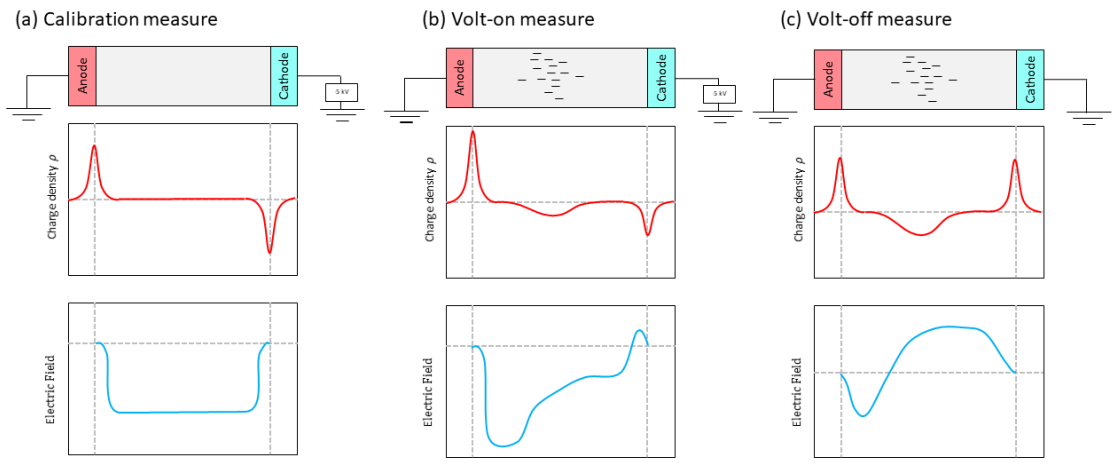

Figure 1.2.21: Example of the charge density spatial distribution and electric field distribution of an hypothetical sample immediately after the application of -5 kV (a), Volt-on measure after some time under voltage, with negative packet charge accumulated in the bulk (b), Volt-off measure obtained immediately after a short-circuit (c) . Adapted from [87, 76, 81]

the charge density in the dielectric. It is related to the material's compressibility χ, the compacity C, the factor $G(\epsilon)$ sensible to the pressure $P(z,t)$, and the field obtained from deconvolution $E(z)$ in the direction z [76, 83]. One of the advantages of this technique is that the signal obtained from the oscilloscope has the same profile as the charge density profile, leading of a directly verification of the quality of the measurement.

$$I(t) = \chi C G(\epsilon) \int_0^d E(z) \frac{\partial P(z,t)}{\partial t} dz \tag{1.2.27}$$

Illustrations of measurement results: Immediately after the application of a voltage, no space charge is expected to be present. In Figure 1.2.21(a), a schematic example illustrates a neutral sample just after the application of -5 kV. The sample polarizes to compensate for the applied voltage, resulting in identifiable input and output peaks. Integration, based on Gauss's law, allows the obtaining of the field distribution profile. This measurement is conducted under the name of calibration and is utilized to determine charges generated in the electrodes.

If space charges accumulate over time under voltage, they will manifest in a second measurement (referred to as the volt-on measure, as the voltage is still applied, 1.2.21(b)) as a distortion of the charge density and field profile at a specific position. Typically, another measurement is performed by turning off the voltage (1.2.21(c)). Under these conditions, any peaks identified at the electrodes indicate induced charges resulting from space charge accumulation.

A comprehensive explanation about the data treatment leading to such profiles are described in chapter 2, section 2.4.2.

1.2.5.4 Charge transport and energy: Band theory

The energy band structure, rooted in molecular dynamics and solid-sate physics, and primarily developed to explain semiconductors and poly-crystalline materials, often fail to describe polymeric insulation, whenever it is amorphous, or semi-crystalline. Nevertheless, it is the more applied and studied theory to explain conduction events in solid dielectrics. Even if they do not provide a complete picture, it has been the basis of a lot of important research, and merit some attention.

In single atoms, one electron (or a pair of electrons with opposite spins, according to the *Pauli exclusion principle*) occupies the highest orbital. These electrons become available for conduction when excited to higher energy levels. When two different atoms form a covalent bond, they can share one or more electrons, causing their most energetic levels to interact and create a degenerate energy state different from the original orbital. Many atoms interacting to form a molecule create numerous degenerate states. These states, closely spaced, can be treated as a continuum, referred to as a "band." The quantity of states $N(E)$ per energy level is known as the density of states, denoted as $D(E) = dN(E)/dE$. Valence electrons reside in the valence band.

In metals at $0K$, the valence band is half-occupied, and the probability of finding charge carriers ($P(E)$) up to this half is 100%, dropping to null just above it (Figure 1.2.22(a)). With increasing temperature, charge carriers gain sufficient energy (through the absorption of photons or phonons) to occupy higher energy levels. At room temperature, many charge carriers exist in these higher energy levels, making them available for conduction. These carriers are termed thermal carriers because they are in the conduction band due to thermal energy (Figure 1.2.22(b)).

In semiconductors, a gap separates valence charge carriers in the valence band from higher energy states assembled in theso-called conduction band. The edge of the valence band is the $HOMO$ (highest occupied molecular orbital), often corresponding to the valence energy E_v, while the lower energy level of the conduction band is the LUMO (least unoccupied molecular orbital), corresponding to the conduction band energy E_c. For an electron or hole to be available for conduction, it must be excited enough to jump from HOMO to LUMO. This gap typically ranges from 0.2 eV to 2 eV and is called the band gap. The midpoint of this gap represents the Fermi level E_f, usually equivalent to the $HOMO$ for metals at $0K$, or the energy level at which $P(E)$[12] at higher temperatures is equal to 50%. In a perfect insulator, the configuration is similar, but the gap is larger than 2 eV, rendering conduction unlikely.

However, this theory was originally developed for ideal cases. In real polymeric insulators, chemical and structural disorders are abundant. Polymer chains exhibit non-periodic sequences, large lateral groups causing structural distortions, chain ends, additional vibrations from plasmons and phonons, and the presence of additives and impurities. All these chain imperfections, and external disorder components contribute to the creation of localized states within the forbidden band. These states act as traps, capturing electrons and holes, holding them in place and requiring additional energy to release them (detrap). Traps situated near the edges of any band are referred to as "shallow traps," while those around the Fermi level are termed "deep traps", as illustrated by Figure 1.2.23(b) which has been inspired

[12]Some authors apply the notation $f(E)$, but the $P(E)$ will be preferred in this work.

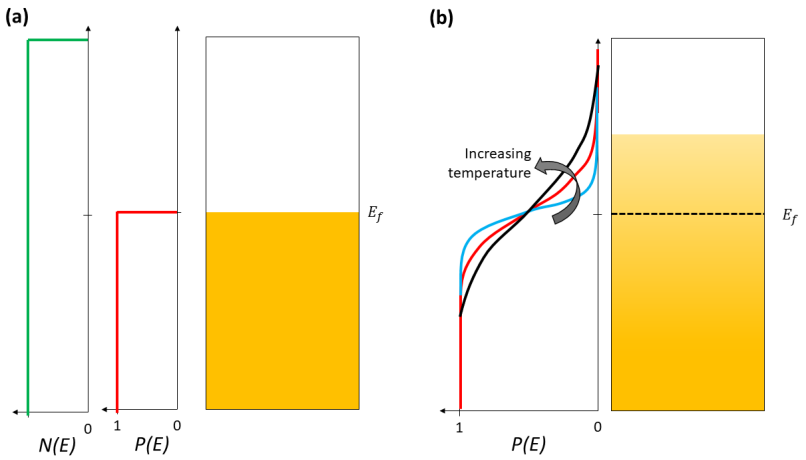

Figure 1.2.22: The Fermi function P(E) and the density stated N(E) describing the relative filling energy levels for a metal at 0 K (a); at T > 0 K, with P(E) indicating the promotion of some electrons above E_f (b). Adapted from Shackelford [88] and Dissado [89]

in the Gaussian-like profile commonly associated to polyethylene.

The quantity of traps can be significant, sometimes forming a band of their own. Most often, conduction in insulating polymers involves charge transport between shallow traps and the LUMO. Trap levels above E_f are seen acceptorlike electron traps, whereas those below E_f are donorlike hole traps. In a thermal equilibrium, traps above E_f are empty, and those below E_f are accupied [87].

When the voltage level escalates to high values, it induces a shift in the equilibrium of the system, causing the Fermi level to rise. This newly established Fermi level, resulting from the altered equilibrium under high voltage conditions, is denoted as the quasi-Fermi level $F(x)$. Indeed, any perturbation in the energy band diagram—such as when interfaces are established, like those between the matrix and additives, impurities, or metallic electrodes—will induce band bending, with the potential to generate a $F(x)$. Consequently, there always exists a $F(x)$, and it is precisely within the region encompassing the original thermal E_f and $F(x)$ where significant trapping phenomena occur [87].

The presence of traps is inevitable, necessitating their consideration to some extent. For simplicity, the trap band is approximated to a single energy state level, denoted as E_t, positioned adjacent to the LUMO. In this approximation, only the influence of a shallow trap energy state is taken into account, as the schematic representation Figure 1.2.24 for the case of a single set of shallow trap state. Here, the concentration of charge carrier n is just a fraction of the one suggested by the ideal case of equation 1.2.25; being this fraction the rate θ (Equation 1.2.28), which represents the relationship between the charge carrier concentration (n_c) and the concentration of trapped charge carriers (n_t). This relationship is analogous to the Fermi-Distribution and involves factors such as the effective density of states in the conduction band (N_c), the concentration of traps (N_t), and the degeneracy factor (g).

Given that trapped carriers spend more time in the trap state than in the conduction band, θ_T also represents the ratio of the time spent in the conduction band (τ_c) to the time spent trapped (τ_t). Consequently, it also represent the relationship

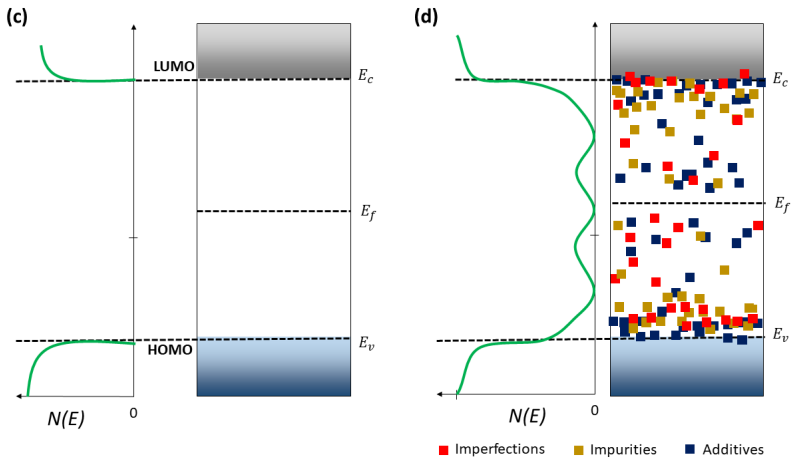

Figure 1.2.23: Model of the energy band structure for a perfect insulator (a), and a real insulator in which some chemical imperfections are denoted as localized energy levels, or traps (b). Adapted from Shackelford [88], Dissado [89], and Teyssedre [90]

of mobilities (μ_c/μ_t).

$$\theta_T(T) = \frac{n_c}{n_t} = \frac{\tau_c}{\tau_t} = \frac{\mu_c}{\mu_t} = \frac{N_c}{gN_t} exp\left(\frac{E_t - E_c}{kT}\right) \tag{1.2.28}$$

At high voltages the concentration of injected charges becomes close to N_t, rising the Fermi level to a level above E_t. In this case, that single set of trap level now is considered deep, thus being fully occupied, and the current immediately rises at a voltage V_{TFL}, which corresponds to a trap-filled limit, after which the insulator is considered free of traps. This configuration can be seen in the scheme of Figure 1.2.24 as TFL (trap-filled limited) problem. It's worth noting that this issue is rarely encountered in traditional polymers used in high voltage insulation. The energy required to reach this level is often considered higher than the breakdown threshold, making it an aspect not further explored in this thesis.

The single set of trap energy level is a good approximation for single-crystal materials of high chemical and structure purity, but vitreous or amorphous structures associated to chemical and structural disorders is more likeable to be described by a broad smearing out of this trap level. Among possibles representations of the smearing out of E_t there is the exponential and the uniform distribution of trap energy states at energy levels above Fermi, both illustrated in Figure 1.2.24.

1.2.5.5 Charge transport and time: Transient current

When a flat insulating sample is installed under two flat electrodes, if a voltage is applied in one side (Volt-on condition), an electric field will cross the sample, and a current is about to be collected in the counter-electrode. This current as a function of the time, which can be seen almost as a monotonic decrease, usually follow the shape of Figure 1.2.25(a), which is often related to an exponential function 1.2.29, also known as Curie's law, with a a parameter that can be time-dependent, and n as constant:

$$i(t) = a.t^{-n} \tag{1.2.29}$$

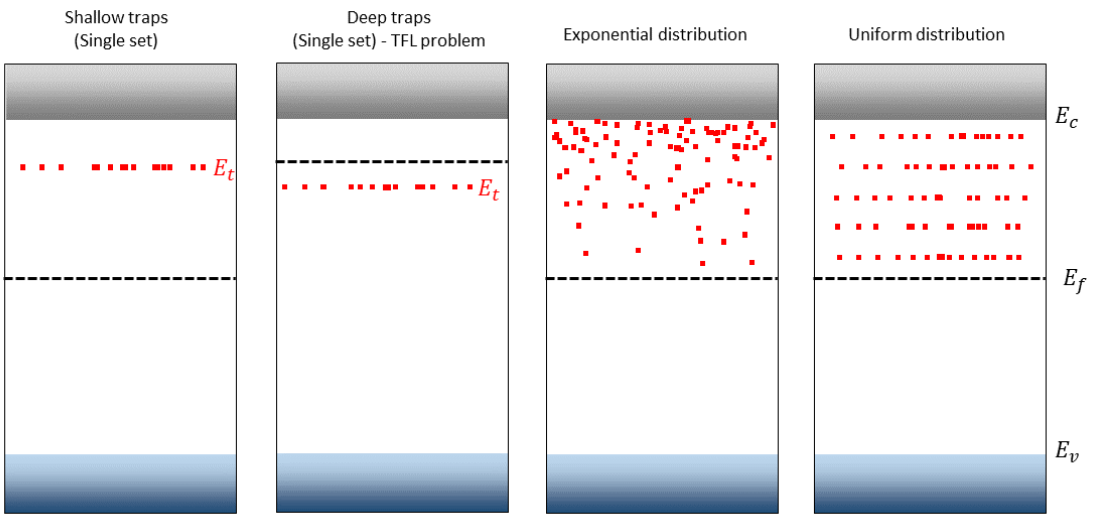

Figure 1.2.24: Scheme of different trap states and distributions for space charge limited current models based on the descriptions found in Lampert [91]

At the beginning, the current is relatively high due to polarization current, but as enough time higher than the relaxation time is given, the current is about to be constant and achieve a stead-state condition, in which it is named conduction current i_c. The time to achieve the i_c can be long enough as some minutes, hours, days, or much more. Coelho [92] states that the current will never be stable for reasons yet unknown in his time.

This current as a function of the time is called absorption current. It is the sum of the polarization current i_p, which is a capacitive current; the conduction current i_c. , and finally an abnormal or residual current, here referred as i_1'. The i_p is related to the electric flux density $\vec{D}$, which is embedded of a displacement portion $\frac{\partial(\epsilon_0 \vec{E})}{\partial t}$ and the polarisability $\vec{P}$. In the equation system 1.2.30, S represents the surface of collecting electrode, and $\vec{j}$ simply as the current density.

$$\begin{cases} i_{abs} = i_p + i_c + i_1' \\ i_p = S.\vec{j_p} = S(\frac{\partial(\epsilon_0 \vec{E} + \vec{P})}{\partial t}) \\ i_c = S.\vec{j_c} = S(\sigma.E) \end{cases} \tag{1.2.30}$$

Within i_1' we can have a space-charge current i_{sc}, associated with the accumulation of space charge as stated by the equation of continuity. The derived form of the equation of continuity is written in the equation 1.2.31; it asserts that points of changing charge density are sources of current density. The integral form, complementary, says that any change of charge in a region comes with a flow of charge in a surface surrounding this region.

$$\vec{\nabla} \vec{J} = \frac{-\partial \rho_v}{\partial t} \Leftrightarrow \oint_s \vec{J} \vec{ds} = \frac{-d}{dt} \int_v \frac{\rho_v}{dv} \tag{1.2.31}$$

The i_1' can also be related to ionic transport, if any, leading to a i_{sc}. Wintle [93] adds the tunneling to empty traps and electrode polarization, while the trapping of charges can be considered, indeed, a space charge event.

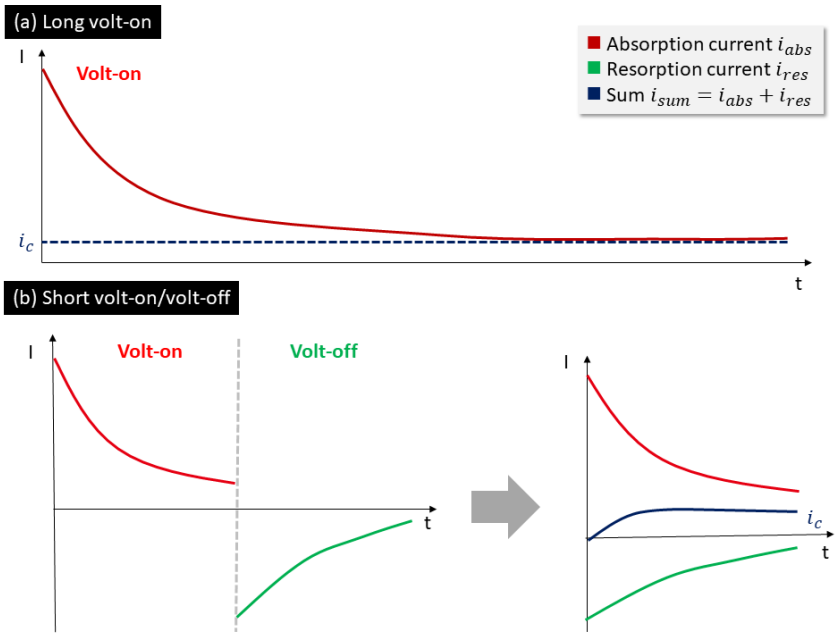

Figure 1.2.25: Scheme of the current as a function of the time when an insulating sample is exposed to a voltage for a longtime (a); Volt-on and Volt-off strategy to obtain the conduction current in a shorter time (b).

If a short-circuit is established, the opposite shape should be found under Volt-off, but no conduction current should occur, leading the current to be null after a certain time, as illustrated by Figure 1.2.25(b). This current, called resorption current i_{res}, should represent all the other process in a reversible manner, as the depolarisation current $i_d = -i_p$, and any residual current here referred as i'_2.

$$i_{res} = i_d + i_{displ} + i'_2 \tag{1.2.32}$$

For reversible systems, in which $i'_1 = -i'_2$, the i_c is able to be found according to the sum i_{sum}, showed in equation 1.2.33.

$$i_{sum} = i_{abs} + i_{res} = i_c + (i'_1 + i'_2) \tag{1.2.33}$$

As a consequence, i_c could be obtained in shorter times through absorption and resorption tests, as illustrated in Figure 1.2.25(b). This can be done by synchronous tests of charging and discharging, volt-on/volt-off cycles, starting by lower voltages, and increasing in electrical stress at each Volt-on step. There is no standard or pattern in order to set the time-length for each test: many perform 1h/1h tests, or 8h/8h tests, and even the 1h/2h have been suggested as a manner to make sure of fully discharge prior to the following volt-on. The higher the temperature, the faster the current stabilisation, and the faster can be the cycles.

The complexity of analysing transient currents does not rely only on the variety of mechanisms that are responsible, collectively, to the current decrease, but by the influence of irreversible or abnormal process that makes $i'_1 \neq -i'_2$, as the ionic and space charge currents, or simply asynchronous process (as different rates of trapping and detrapping). In such case, the i_{sum} does not give the i_c directly because there will be always a residual current.

Besides, many reports of nonmonotonic decreases can be found on literature. Notingher [79] highlights that, at high fields, electronic conduction, initially negligible, increases over time until stabilization. However, it can become so significant that it surpasses the polarization current, ultimately creating a peak-like profile or an undershoot in the i(t) curve. Many and Rakavy [94] theorized the i(t) profile of space-charge-limited transient as a function of trapping time for insulating crystals, verifying also an undershoot when no trapping, and a longtime stabilization when trapping occur. Iwamoto [95] provided insights about the ionic conduction which could, indeed, cause an undershoot, due to space charge accumulation and accommodation.

1.2.5.6 Charge transport and voltage: Steady-state currents

Ohmic mechanism with a single set of shallow traps The Ohm's law in the equation 1.2.24 and 1.2.25 represent a perfect trap-free insulator with thermal free carriers, which is such an idealization. Taking into consideration the trapping theory, the ohmic conduction can be represented as a function of θ, according to equation 1.2.34.

$$J_\Omega = \theta_T n e \mu E \tag{1.2.34}$$

Non-linearity according to space charge theory At low voltage levels, the mechanism is usually ohmic, but as the voltage increases, charges are injected inside the polymer, which are responsible for space charge accumulation. These injected charges $n_{injected}$ can eventually dominates the J-V profile. The measured current would be the sum of J_Ω and the J provided by $n_{injected}$ [89, 91].

Space-charge-limited model with a single set of shallow traps: Being the space charge defined by an accumulation of charges in a particular given volume which obeys the Poisson's equation, an equation of conduction for space charges accumulation can be found by replacing the quantity of charge carriers n in equation 1.2.34 by a dn/dx provided by Poisson's, followed by further simplifications [89, 91]. As the main requirements, only the current in one dimension is considered, as just one charge carrier, a constant mobility is considered, and no diffusion or displacement currents because of the since steady-state condition. The resulting equation 1.2.35 represent the Space-Charge Limited-Current (SCLC) with a single set of shallow traps J_θ.

$$J_\theta = \frac{9}{8}\theta_T \epsilon_0 \epsilon_r \mu \frac{V^2}{d^3} \tag{1.2.35}$$

Space-charge-limited model with an exponential distribution of traps: When a distribution of traps is considered, it is usually accounted by changing the total amount of traps N_t in the θ equation (1.2.28). In the case of a exponential distribution (Figure 1.2.24) the N_t is obtained by the integration of an equation that describes that quantity of traps per energy level exponentially related to the energy levels below E_c. The integration is conducted between the Fermi level, and a quasi-Fermi E_{qf}. The final equation of current for an exponential distribution of traps J_l

is detailed in equation system of equation 1.2.36, also known as the $(l+1)$-power law.

$$\begin{cases} J_l = L(\epsilon_0\epsilon_r)^l \mu \frac{V^{(l+1)}}{d^{(2l+1)}} \\ L = N_c e^{(1-l)} \left[\frac{l}{N_t(l+1)}\right]^l \left(\frac{2l+1}{l+1}\right)^{(l+1)} \\ l = T_t/T \end{cases} \tag{1.2.36}$$

Here, the l is a thermal rate between the temperatures T and a T_t. The physical meaning of T_t is not clear, it seems to characterize the trap distribution; so as it may be related to the structural and chemical disorder, while T is the temperature of the test (at isothermal conditions), related as the lattice temperature by Lampert [91].

If $T_t > T$, as $l > 1$, most of the traps between the E_c and the quasi-Fermi E_{qf} may have an influence in the conduction. It has been assumed that the "push" of the Fermi level (or the excursion of E_{qf} away from E_f) is lower than kT_t. In the case of large excursion, or very large $T_t > T$, we have $l >> 1$, and the problem can be regarded as the case of uniform distribution in which the quantity of traps per energy level is a constant, roughly schematised by Figure 1.2.24.

If large $T_t < T$, in such a way that $l \approx 0$, a free-trap with thermal carriers situation is achieved, and J_l is transformed in J_Ω with practically no trapping ($\theta = 1$).

Finally, if $T_t \approx T$ and such a way that $l \approx 1$, the empty traps on the top of the distribution and close to E_c are about to dominate, reducing the situation to the single-set of shallow traps J_θ.

Non-linearity according to traverse mechanisms of energy potential barriers The space-charge model anticipates charge injection but falls short in explaining how this injection occurs. Furthermore, it addresses charge transport through the bulk but lacks details on the actual transfer process. To unravel these intricacies, we turn to energy potential barrier models, as illustrated in Figure 1.2.26. The injection mechanisms and bulk transports presented in the figure succinctly capture these dynamics, all summarized by the comprehensive concept of "traverse mechanisms".

The initial assumption involves the existence of an energy barrier that charge carriers must overcome to move from one site to another. The dynamics of the charge carriers depend on the thermal energy imparted to them: with ample thermal energy, they can hop to the top of the barrier; without thermal energy, they must traverse the barrier directly through tunneling and field emission at the Fermi level; and with some but insufficient thermal energy, they will eventually tunnel, but at levels above the Fermi level (thermionic emission). In all the assumptions, the energy barrier height is lowered (and "bent") by the field; the higher the field, the more pronounced the bend.

In Figure 1.2.26, injection mechanisms occurring at the metal-insulation interface and bulk transport are depicted side by side. Each is subdivided according to the traverse strategy. Despite distinct assumptions for injection and bulk transport (while the injection involves a barrier created by surface and contacts, the transport in the bulk can be seen as a detrapping process), the mechanisms at the same strategy share striking similarities, making it challenging to distinguish between injection and bulk transport based solely on their $J - E$ profiles.

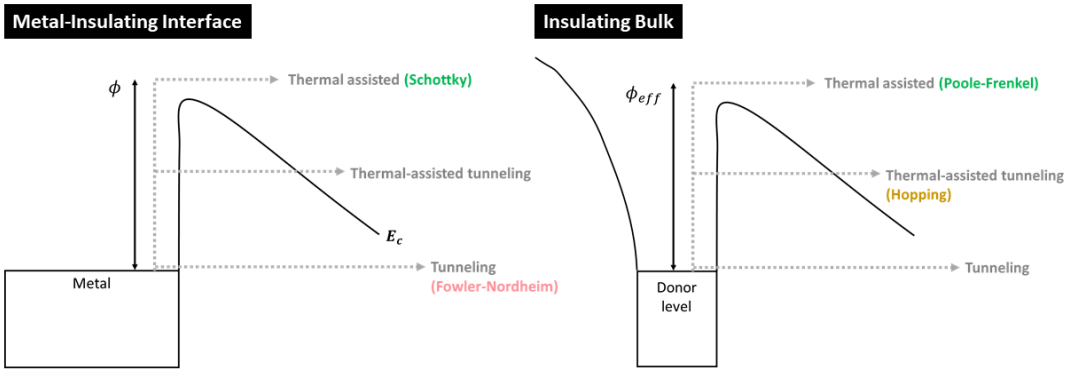

Figure 1.2.26: Scheme of traverse mechanisms according to the position (contact metal/insulation, or bulk) and energy, or traverse strategy (tunneling, thermal assisted, and thermal-assisted tunneling). Adapted from Laurent [76], Dissado [89], Coelho [92], and Teyssedre [90].

Understanding the interface: The physical quantities characterizing the interface are associated with the energy levels formed when a material comes into contact with the vacuum, as illustrated in Figure 1.2.27. In metals, the highest energy levels are denoted by the Fermi level E_{Fm}. Removing an electron from the metal involves overcoming a potential barrier from E_{Fm} to the vacuum level, known as the metal work function in the vacuum, denoted as ϕ_m. Conversely, insulating materials possess their own energy barrier between their Fermi level E_{Fs} and the vacuum level, termed the insulator's work function, denoted as ϕ_s. The potential barrier between the edge of its conduction band and the vacuum is referred to as the susceptibility χ. Figure 1.2.27(b) illustrates an insulator with traps in thermal equilibrium: all traps below E_{Fs} are occupied, functioning as donors, while those above E_{Fs} are empty, serving as acceptors.

Additionally, it merits to be highlighted that the density function of trap states at the interface differs from that in the bulk due to various factors: increased surface imperfections, exposure to external environments, potential alterations upon the adsorption of foreign materials, and modifications during the metallization process. Consequently, the trap density N_t is typically higher, as the scheme of Figure 1.2.27(c). These distinctive states on the surface are known as *surface states*. They facilitate both the tunneling and thermionic emission of charges, enabling them to access the conduction band through thermal activation. The distribution of these surface states can extend as deep as 300 $\mathring{A}$. In the case of polyethylene, it is recognized that a significant injection of electrons into these surface states can occur until the traps gradually become saturated, at which point bulk transport mechanisms come into play.

As already suggested by Figure 1.2.28(c), when a metal and an insulator come into contact, a new equilibrium can be reached to align their Fermi levels through the exchange of charge carriers. This flow of charge carriers results in the accumulation of space charge at the interface, forming an electric double layer that gives rise to a contact potential V_d, as described by Equation 1.2.37. This potential barrier is influenced by the work functions of both the metal and the insulator. It is

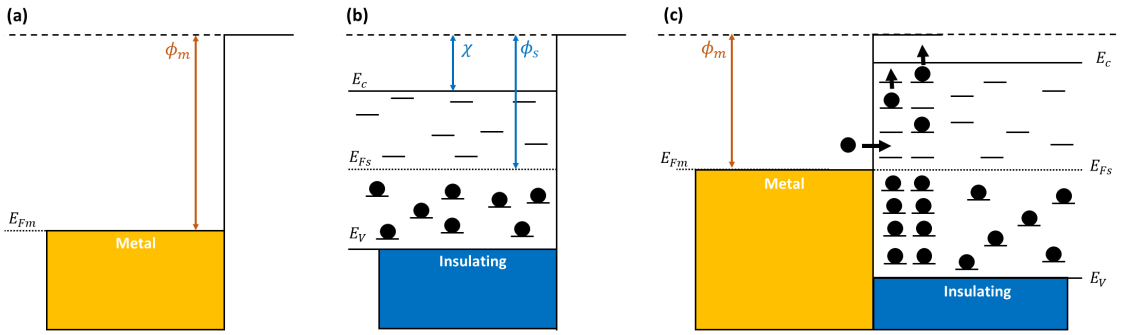

Figure 1.2.27: Scheme of a contact between a metal of and vacuum (a), between an insulator with traps and the vacuum (b), and a simplification of the contact between a metal and an insulator with distribution of traps of surface and bulk without voltage application. Adapted from Kao [87].

temperature-dependent and significantly affected by the presence of impurities.

$$V_d = \frac{1}{q}(\phi_m - \phi_s) = \frac{1}{q}[\phi_m - \chi - (E_c - E_f)] \tag{1.2.37}$$

The possibility and rate of charge exchange and the magnitude of the contact potential will depend on the relationships of the metal/insulator work functions, which can be used to differentiate the type of the contact. Before the contact, three configurations can be found, illustrated with the help of Figure 1.2.28 that shows the multitude of configurations before contact:

- $\phi_m = \phi_s$: the metal and insulator correspondent Fermi levels are already at the same level; once in contact, there is no net flow of charges and no space charge near the interface; the contact is referred as *neutral*.

- $\phi_m < \phi_s$: once in contact, the bands will bind; electrons will flow from the metal to the insulator, no net flows of holes; the electrons may get stuck on the interface and leave a negative charge region called *depletion region*, and the contact receives the name of *blocking for holes*. If the bulk is less resistive than the interface, and if the metal behaves as an ideal cathode (infinite reservoir of electrons), those electrons will vanish and a continuously flow of electrons will leave the metal; the contact is said *ohmic for electrons*.

- $\phi_m > \phi_s$: if in contact, energy will bind too; holes may flow from the insulator to the metal (no net electron flow is observed), leaving a positive space charge region; the contact is called *blocking for electrons*. If the bulk is less resistive than the interface, and the anode behaves ideally, those holes will vanish, and a continuous flow of holes is promoted; making the contact *ohmic for holes*.

Thermionic emission (Schottky injection): The Schottky emission has been primarily modeled for a semiconductor without traps and dopants, in which thermal energy is given in a quantity enough to make the charge carrier surpass a potential barrier height ϕ_h . The height is usually lower than the vacuum level because of the image force and external electric force biased by a DC voltage application. In the

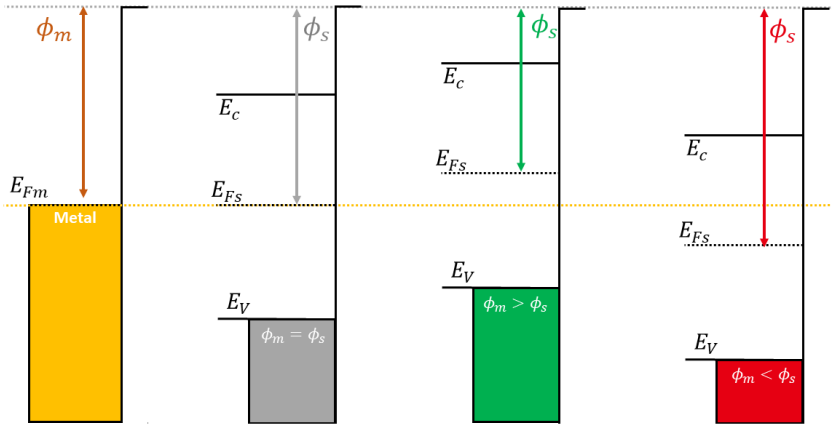

Figure 1.2.28: Comparative schemes of contacts between the vacuum and a metal (a), a dielectric material with $\phi_m = \phi_s$ (b), with $\phi_m > \phi_s$ (c), and with $\phi_m < \phi_s$ (d), taking as reference the Fermi level of the metal. Adapted from Kao [87].

particular case of dielectrics, the barrier is further reduced to account the polymer susceptibility χ.

For a material relatively conductive, with a mobility independent of the field, and without band bending when voltage is applied, the current flow tends to be ohmic at low voltage levels; the contact is ohmic. The current increases up to a saturation J_0 beyond which the contact become blocking, and the conduction became electrode-limited. The current in which all electrons thermionically emitted are carried away in the conduction band of the insulator without any effect of space charge or traps are represented by J_s in the equation system 1.2.38 of the Schottky injection. In this system, V is the applied voltage, T is the temperature, k is the Boltzmann constant, q is the electric charge. The saturation current J_0 depends on the Richardson-Schottky coefficient equals to 120 A/cm^2K^2 and dependent on the carrier mass m, the barrier height ϕ_h (which, itself, is a relation between the metal work function ϕ_m and the polymer susceptibility χ), a parameter named Schottky constant β_s, and the contact field E_d.

$$\begin{cases} J_s = J_0 \left[exp\left(\frac{qV}{kT}\right) - 1 \right] \\ J_0 = AT^2 exp\left[-\frac{(\phi_h - \beta_s E_d^{1/2})}{kT} \right] \\ A = \frac{4\pi qmk^2}{h^3} = 1,2.10^6 A/m^2K^2 \\ \phi_h = \phi_m - \chi \\ \beta_s = \left(\frac{q^3}{4\pi\epsilon}\right)^{1/2} \end{cases} \tag{1.2.38}$$

Often the full equation of J_s is approximated to J_0, and the Schottky injection is usually identified from a data fitting of $J(\sqrt{E})$ or indeed $J/T^2(\sqrt{E})$, being the slope β_s/kT, and the interception the ϕ_h. Nevertheless, this procedure demand a lot of precaution because literally all parameters involving J_0 may be impacted when a polymeric insulation is considered:

- **Richardson-Schottky coefficient** A^*: the value of 120 A/cm^2K^2 is only valid under vacuum. For isotropic insulating materials, it may be corrected according to the effective mass m^* of the charge carrier.

- **The effective energy barrier** ϕ_{eff}: the barrier height increases with increasing forward bias. On the other hand, the same barrier may be importantly reduced due to the surface state. Electrons thermally activated can tunnel to the localized states, which are necessarily at lower states than ϕ_h.

- **Contact field** E_d: the contact field is created by the V_d and may differ significantly from the V applied. Notingher [79] suggests to approximate E_d it to $\lambda_d E$, being λ_d a temperature-dependent constant indicating a field reinforcement.

- **The value of** ϵ: ideally, the ϵ in question should represent the static permittivity ϵ_s obtained under DC field; however, in the vicinity of the contact, a lower ϵ should be expected. Rigorously speaking, it is neither the ϵ_s, neither the ϵ at 50 Hz that is usually found in material's data sheets.

Field emission (Fowler-Nordheim injection): The field emission is defined as the quantum-mechanical tunneling of electrons through a potential barrier; as illustrated in Figure 1.2.26. It is characteristic of low temperatures, in which most of electrons tunnel at the Fermi level. The modeling for such injection in solids without defects involves considering the current of injection as a function of D_T, that is the quantum mechanical transmission function for the transmission probability, and the Fermi-Dirac distribution $P(E)$. Defects are introduced considering rate trapping in the case of electron-injecting contact towards empty trap levels, forming homocharges.

The net current density J_{FN} is presented in equation 1.2.39 in which h is the Planck constant, m^* is the effective mass, m_0 is the rest mass of the electron, $\phi_b(t)$ is the effective potential barrier at the electron injection contact, and $E_d(t)$ is the effective field at the electron-injecting contact. The variable t here is not the time, but an indicative of the trapping consideration.

$$J_{FN} = \frac{q^2 m_0 E_d^2}{16\pi^2 h m^* [q\phi_b(t)]} exp\left(\frac{4(2m^*)^{1/2}[q\phi_b(t)]^{3/2}}{3hqE_d(t)}\right) \tag{1.2.39}$$

Poole-Frenkel transport: It is analogous to the Schottky effect in bulk transport, wherein field-enhanced thermal excitation leads to the detrapping of electrons or holes. The model suggests that the applied field lowers the energetic barrier, enabling an electron to escape and encounter a positive trap. Therefore, if the trap is empty, it must carry a positive charge to generate sufficient Coulomb forces; otherwise, the model will not be applicable.

As indicated by the equation system 1.2.40, the current density J_{PF} is similar to J_s, but the potential barrier is twice that of the Schottky barrier. Consequently, the Poole-Frenkel constant β_{PF} is equal to twice the value of β_s. It is a refined version present in [79].

$$\begin{cases} J_{PF} = J_0.exp\left(-\frac{E_{T_0}-\beta_{PF}E^{1/2}}{kT}\right) \\ J_0 = n\mu_0 qE \\ \beta_{PF} = \frac{q^{3/2}}{(\pi\epsilon_0\epsilon_r)^{1/2}} = 2\beta_s \end{cases} \tag{1.2.40}$$

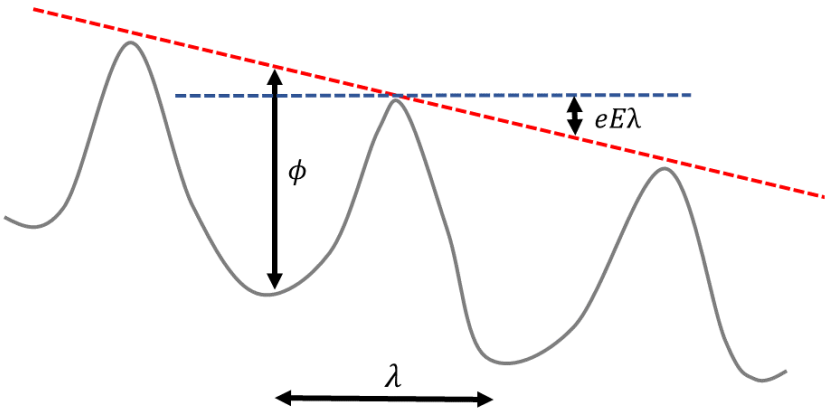

Figure 1.2.29: Scheme of charge transport via hopping. Adapted from Mott and Gurney ([97]) and Guillermin ([96]).

From J-V curves, the Schottky or Poole-Frenkel (PF) model can be discerned by analyzing the extracted ϵ from the slope of $lnJ - E^{1/2}$. Kao [87] recommends comparing this ϵ with values obtained at high frequencies through dielectric spectroscopy. However, the fit frequently fails to provide accurate values of ϵ due to the potential influence of multiple mechanisms simultaneously. Our conclusion is that relying solely on J-V plots for differentiation may not be a reliable strategy.

Hopping transport: It is the mechanism in which an electron hop from on site to another, as from a molecule or atom to a neighboring molecule or atom overcoming a potential barrier via thermal excitation, and schematized in Figure 1.2.29. The distance between sites (λ) must be larger than 10 Å, otherwise the tunneling is favored [87]. On the other hand, if distances are too large (as for a low concentration of traps) the PF is favored [96] .

This kind of mechanism has been initially developed for Ionic mobility within crystalline structures, and has roots in atomic diffusion. The mobility μ_{HOP} in diffusion follows the Einstein relation, related to the charge carrier q and a diffusion coefficient D, which is itself related to the probability of hopping transition W_H and the λ. The W_H, on its turn, is associated with the attempt-to-scape jump frequency ν and is an Arrhenius-like equation 1.2.41.

$$\begin{cases} \mu_{HOP} = \frac{q}{kT} D \\ D = W_H \lambda^2 \\ W_H = \nu . exp(-E_a/kT) \end{cases} \tag{1.2.41}$$

Because such Arrhenius-like behavior, some authors describe the conductivity ([89, 92, 98]) as a merely relationship with the temperature, as the equation 1.2.42 relating σ with a variable n comprised between $1/4$ and $1/2$ for amorphous materials. The A and B are constants.

$$\sigma_{HOP} = A . exp\left(\frac{-B}{T^n}\right) \tag{1.2.42}$$

Mott and Gurney ([97]) obtained theoretically the equation 1.2.43 based on the diffusion of lattice defects. Further, many authors applied such equations to describe polymers, as for example the polyethylene [99], epoxy [100, 101], and PEEK [102].

$$J_{HOP} = J_0 exp\left(\frac{-E_a}{kT}\right) sinh\left(\frac{q\lambda E}{2kT}\right) \tag{1.2.43}$$

The advantage of this equation is that the distance between sites λ can be extracted from $J - E$ curves. Another feature comes from the use of hyperbolic sinus; for low values of field, the current can be approximated to the equation inside the parenthesis; being, thus, proportional to the field0.

Comment about the diversity of conduction mechanisms and modeling: The mechanisms and the equations presented in the last sections are often applied to investigate the conduction mechanism of polymers, but they are not the only equations possible to represent such mechanisms, neither represent all the mechanisms that we can find in literature; otherwise, the list of equations would be non exhaustive. As additional mechanisms, we can cite the double Schottky [103], that considers indeed an energy barrier for extraction of charge carrier and permit the comparison of different barrier heights; and the Onsager conduction [104], which is rooted on the probability of an electron to be neutralized through recombination when a field is applied.

During the development of the last section, it was implicit that only a single polarity charge carrier has been considered. Another approach to deal with current and space charge accumulation modeling consists of considering both electrons and holes on equationing, what has given birth to bipolar charge transport (BCT) models in the literature. In such approach, equations representing the flow of charge injection, extraction, transport, trapping, detrapping, recombination, and more, are defined for each charge carrier and computed numerically [105, 106]. Here, the variety of models are still non-exhaustive, with models defined to take into account temperature and field gradient ([107]), AC-DC combined electric field ([108]), surface roughness ([109]), crystallinity evolution ([110]), and so on [111, 112, 90].

1.3 State-of-the-art of the systems of this work

In this section, we aim to endeavor the latest or notable works that encountered either the materials of this work, or other materials in similar contexts. The first and second subsections are dedicated to the epoxy (1.3.1) and silicone (1.3.2) separately, in which both water absorption and electrical characteristics are explored. The last section deals with multi-layer configuration (1.3.3).

1.3.1 Epoxy composites and related subjects

1.3.1.1 Water diffusion into the epoxy-silica system

The epoxy matrix has hydrophilic sites, so as the surface of the silica. Thus, in a (micro)composite, we consider that most of the water is absorbed by the matrix, with only a minor fraction on the silica. The evidences of these sorptions, and the events consequent to them, are presented as it follows.

The epoxydic matrix: According to Daviaud [65], the diffusion mechanism in epoxy is highly dependent of the hardener applied: the DGEBA cured with diaminodiphenyl sulfone presents a Fickian diffusion, with the dicyandiamide has a Langmuir's diffusion, and with the phthalic anhydride an anomalous one. Brun [113] has found a Fickian diffusion when curing DGEBA with acid anhydride.

The diffusion also depends on the microstructure: Pham Hong [114] investigated a laminated structure of glass cloth and mica, both binded together by the DGEBA cured with polyester acid, and a superposition of two different Fickian mechanisms has been attributed for the epoxy phase and the interphases between epoxy and fillers.

The Fick's diffusion can be seen as a limiting case of Langmuir's mechanism in which the highly hydrophilic sites, as specific electronegative atoms, are abundant. According to Verdu [67], electronegative oxygen atoms provided by the carbonyl group ($C = O$), hydroxides ($-OH$) , and some partial electronegativity coming from the siloxane ($-Si-O-$) and polyesters ($-CO-O-$), the last ones being less electronegative, may account for hydrogen bond sites.

Apicella [115] observed that the water absorption in DGEBA cured with triethylenetetramine followed the Henry's isotherm. The equilibrium moisture sorption showed highly temperature and humidity history dependencies: at high humidity, the total amount of water increased with temperature. It was attributed to a synergistic temperature-water effect that would cause microcavitational damage in the form of water crazing, but no proof was given for that. On the other hand, a decay on Tg up to 47 K (from 135°C to 88°C) was identified when a dry sample has been saturated at 45°C, thus arguing in favor of a plasticizing process [116]. Paradoxically, if saturated at 75°C, the Tg decay was smaller (of 27K). The hypothesis of Apicella is that the microcavities, if formed, may disappear through an annealing process, which imply saying that the damage is reversible. Later on [117], the author explained this reversibility by the fact that the epoxy network would be formed by highly cross-linked nodules immersed in an inter-nodular matrix of lower curing degree, and it would be these low density regions that may concentrate water and expand or contract. If an irreversible damage happens, as in hydrolysis, this would be iden-

tified by the increase of water uptake during time after the saturation achievement. Such increase is credited to the propagation of defects into the form of cracks [67].

Verdu [67], and Woo [118] propose the Equation 1.3.1 to represent the mass ratio of water within a polymer at equilibrium with the RH. The Equation 1.3.1 has two parameters: a constant κ that represents the mass ratio of water at saturation and depends on the nature of the polymer and the temperature, and an exponent γ. If γ is close to the unity, the Equation 1.3.1 can be approximated to the Henry's law, and the H constant can be deduced.

$$water(\%) = \kappa(RH)^{\gamma} \tag{1.3.1}$$

In the specific case of epoxies, the parameter κ typically remains constant or may exhibit a slight decrease with temperature [67]. If γ is not equal to unity, the equation transforms into a power-law form, resembling the Freundlich law [119] (Equation 1.3.2). This modified form better accommodates experimental curves and is interpreted as a local Langmuir isotherm model. This equation better fit with the findings of Lutz [120, 121], that argues that there is not exactly a saturation level of water absorption as a function of RH: the relationship between the water uptake and the RH is always a monotomic increasing temperature-dependent function.

$$P^a = H\theta \tag{1.3.2}$$

The microsized silica: As per Beyer [122], when filled with silica flour, the composite absorbs less water then the unfilled system, even if the silica can adsorb water on its surface [123]. Imai et al [124] observed that the microcomposite of DGEBA with 5 wt% of silica absorbed 0.3% less water than the pure resin, independently if the silica had been treated with silane agents or not. Zou [125] identified for the DGEBA cured with acid anhydride and 60% of silica flour a decrease of water absorbed of around 1.5% at 25°C and 75% RH when compared to the pure resin.

The water adsorbed can be relevant if the filler has porosity. This porosity comes from particles aggregation (if loosely attached to each other), agglomeration (if rigid attached), or if the filler is loosely attached to the matrix, creating a space between filler and matrix than can allocates water coming from capillarity forces. This is widely studied in the field of Earth Sciences and Mineralogy for the case of soils, grains, and sands [126, 127, 128].

Once silica flour is present, the water absorbed can generate ions by dissociation of electrolytic impurities as carbonates of calcium, aluminum, magnesium, and iron [122]. Furthermore, the surface of the silica and eventual oxides, as iron oxide, may provide favorable sites for OH^- accommodation, shifting the equilibrium constant of the water towards its ionization, liberating H^+ or H_3O^+ for conduction [129].

According to Zou [130] and Gonon [131], most of the water absorbed may be attached to the matrix, and not the microsilica or the microsilica interface. A similar feature has been found in the case of epoxy filled with alumina [132]. Brun [113] suggests that for longer times of water exposition, a threshold percolation may be achieved even for microcomposites under degradation mechanisms having the increase of water uptake during time as signature.

1.3.1.2 Charge transport and space charge events in epoxy-silica system

The impact of water in the overall electrical conduction: Lovell [133] compared the steady-state electrical currents at 40°C of a dried and an undried butanediol diglycidyl ether based epoxy filled with silica (10 % in volume) and cured with triethyl tetra-amine over many applied fields (from 5 to 100 MV/m). A decrease of one order of magnitude was observed when unconditioned samples had been dried for 8 days at 50°C under vacuum conditions. The author developed the hypothesis of having electronic hopping conduction during the transient current, and an ionic current under steady-state condition of humid samples.

The DGEBA cured with phtalic anhydride and filled with quartz tested by Apicella et al [117] showed an increase in apparent conductivity of two orders of magnitude between their driest and the more humidified sample (for $E_{app} = 1\ kV/mm$). They performed the same measurement and sample preparation with a polyurethane cured with polyol, and a increase of six orders of magnitude has been found.

Lutz [120] investigated a "mineral filled aromatic epoxy resin" having the water absorption mechanism coinciding with the Fick's diffusion and Henry's isotherm, and an increase of apparent conductivity of seven orders of magnitude was found between the driest specimen and the sample conditioned at 99% RH at ambient temperatures (for $E_{app} = 1\ kV/mm$). But in this case, the drop in conductivity started only at relative humidity ranges above 93%. He explains it with the enhancement of ionic conduction issued from dissociated water or ions from impurities dissociated by the absorbed water. The drop above 93% RH is interpreted as a percolation phenomenon as at the filler/matrix interphase leading to conductive water channels, as also found by Gonon [131].

There are two contradictions that the interpretation of Lutz and Lovell has to face: first, even if water favor ionization and dissociation of species, and provide a media that facilitates their mobilities, ionic conduction would mean a transport of matter which is necessarily non permanent, as pointed out by Ieda [134]. Second, even if Gonon et al [131] had also found an increase of seven orders of magnitudes correlated with a percolation process, they studied a material with a very special and particular microstructure that should not be taken directly as reference: the alternating plies of epoxy, mica paper and glass studied by Pham Hong [114].

The impact of microsized silica in the overall conduction process: Guillermin [135] studied the impact of the silica (filled 60 wt%) on conduction mechanisms of DGEBA cured with anhydride. Using a round-roller sample, he had identified that the silica introduction decreases the conductivity and shifts the voltage threshold to lower voltage levels. If the conduction takes place in the matrix, it sounds logic that the introduction of dielectric particles may reduce the conductivity because there will have less media to transport electrical charges. But these conclusions contrast with Castellon [136] that identified the opposite behaviour for cycloaliphatic resin cured with anhydride : the increase in the current density with the introduction of microsized silica. This increase has been correlated to a field reinforcement at the cathode due to heterocharge build-up there. This conclusion agrees with other works [137, 138] that focused on the influence of others ceramic fillers, as zinc oxide and aluminum oxide. Both of them observed an increase in the measured current and a decrease of the voltage threshold with the introduction of fillers.

The heterocharge formation at the cathode has also been identified by Guillermin in another work [101] at 80°C (above the Tg) and was credited to H^+ coming from the dissociation of organic acids ($R-COOH$), by-product, antioxidants reactions, and water ionisation ($H_2O \rightarrow H^+ + OH^-$). When his sample was degassed, and all the volatile extracted, the heterocharge build-up decreased. When enough time was given to humidify the sample, they reappeared. As presented in 1.3.1.1, the presence of the silica can increase the quantity of ionic species because it provides ionic impurities and enhance the water ionisation.

The conduction mechanisms and the temperature effect: In terms of temperature, below the Tg, there is general agreement that an ohmic mechanism predominates up to electric field levels around 5 kV/mm, after which it appears a super-ohmic conduction attributed to SCLC, or Schottky, or hopping. Despite some conditioning process, none of the references strictly controlled the water content, but there is the suspicion that those who tested microcomposite systems that were most probably dry may have found a non-linear mechanism in accordance with the SCLC with exponential levels of traps [135], whereas a single-level SCLC is about to happen for pure resins or when the microcomposite network may has some water content [136, 139, 140]. Besides, those who explored the Schottky mechanism considering a field reinforcement (which are, coincidentally, those that we believe have probably tested humid samples) have found a field reinforcement at the cathode, indicating heterocharge build-up. The evidences are detailed as it follows:

- Testing the filler-free resin:
  - Guillermin [135] observed two regimen: an ohmic one, up to 7 kV/mm, and another one associated with the single-level SCLC, despite of acceptable correlations with hopping and Schottky injection.
  - It agrees with the pure resin tested by Castellon [136] at 25°C, and Desmars [140] at 60°C.
- When silica particles are introduced at 60-65 wt%:
  - Both authors have found a conduction mechanism transition at the same voltage threshold, but Guillermin has found a SCLC with exponential distribution of traps at higher voltage levels, and Castellon observed a single-level SCLC. Yahyaoui [141] and Desmars [140] tested similar resins but with different fillers, and a single-level SCLC was also obtained. Because Guillermin tested round-rollers, and all the other tested plates, we believe that the samples of Guillermin were dry or driest in relation to the others.

At 80°C (above the Tg) no standard mechanism were capable to explain neither the slope smaller than the unity neither a slope between the unity and 2 in the log(J) versus E plot, with a threshold at around 5 kV/mm. It was the same independently of the filler's content.

Space charge build-up: Below the Tg, and at 'non-ohmic' voltage levels, there is a convergence in the literature about homocharge build-up on both sides of the cathode and the anode, for many DGEBA-based systems, filled or not, controlled in water or not [101, 142, 143, 144] with the solely difference that systems filled with industrial silica may contain quartz, which is piezoelectric and can produce spurious signals that demand a more refined data treatment [43].

Liu et al [145] took care on preparing dry epoxydic systems, and they observed that the homocharge accumulation was better noticeable when the field and the temperatures have increased (at 20°C and 10 kV/mm, almost no homocharge build-up was visible after one hour of poling). There was a temperature threshold after which the quantity of homocharges became strong (next to 60°C).

At higher temperatures (close or higher to the Tg), or higher electric fields, or if the test is executed for very long times ($>$ 40 hours under voltage) there is heterocharge build-up. Li et al [146] observed that epoxy-anhydride systems without evident strict control of water content and apparently without mineral fillers have not presented clear space charge accumulation up to 80 kV/mm and 140°C, after which positive heterocharge appears at the vinicity of the cathode. A similar event have been identified by Gallot-Lavallée [142] and Guillermin [101] for the filled resin at lower voltages and temperatures. In addition, the quantity of charge accumulated seems to depend on the electrode material.

Gallot-Lavallée [142] justified the heterocharge build-up by the migration of those previous homocharges towards the opposite electrode. Guillermin [101], on the other hand, defended the hypothesis of intrinsic charge carriers generation by ionisation and dissociation processes. It would justify why there is heterocharge apparition in the cathode first, and just then heterocharge in the anode: the H^+ has a higher mobility than anions like OH^- or $COOH^-$. This interpretation is in agreement with Li [146]. Anyway, as pointed out by Gallot-Lavallée [142], once heterocharges were identified, the dielectric breakdown is imminent.

1.3.2 Silicone rubbers: water sorption, and electrical properties

1.3.2.1 Water diffusion into the silicone-silica system

The siloxane matrix and industrial formulations: The siloxane chain has two contrasting features: it is highly permeable to gases and vapours, but it is also highly hydrophobic, and it is not expected that water can be absorbed by the matrix. Under oxidation during exposing to corona discharges in air, radiofrequency plasma treatments, salt-fog environments, surface pollution, or long-term immersion in water, the surface hydrophobicity can be lost in a first time, but recovered in a second moment. The reasons for hydrophobicity recovery, as stressed by Hillborg [48], can be numerous, and may account for migration of low molar mass species from the bulk to the surface, or reorientation of polar groups at the surface, or changes in surface roughness.

Water absorption has been detected in industrial grades. Gubbels [147] highlights that water, either present on the surface of at the form of clusters, may provide a media to ionic diffusion. But silicones may still be considered more effective as corrosion protectives than epoxies because the quantity of water uptake

under saturation is ten times lower. Cheng [148] identified a Langmuir's diffusion mechanism for an external insulating HTV silicone rubber, but the formulation of the silicone was not detailed.

Gao et al [149] studied the impact of ATH content in water uptake (samples immersed in deionized water at 50°C) and permittivity of PDMS filled with silica. The increase of ATH concentration from 80 to 120 parts per hundred parts of rubber was related to the increase of water intake from 1% to 1.5% of weight gain. As main consequence, capacitance also increased two unities. The weight gain curve also fitted well with Langmuir's diffusion law.

The nanosized silica: Because many silicone rubbers are filled with pyrolysed, or pyrogenic, or fumed silica (these therms are often used interchangeably) that are frequently part of the fabrication process of silicone rubbers [57], and because these special silica particles are often presented in nanosized or mesosized dimensions, there is a chance that industrial silicone rubber composites may be framed as nanocomposite materials, and the mechanisms of water absorption, as well as the effects in the insulating properties, are very different from a microcomposite to a nanocomposite.

The impact of nanosized properties in the insulation performance has been extensively studied in the literature [150]. Tanaka [151, 152] proposed a multi-core model to explain nanodielectrics based on "interaction zones" around the filler, their electrical double-layer and triboelectricity characteristics: there would exist a first bounded layer of a nanometer or less, a second bound layer of about 2 to 9 nanometers, and a third loose layer of about some tens of nanometers. According to them, the polymer structure varies across layers, so as the charge carriers traps, with predominance of deep traps in inner layers due to ionic and covalent bonds, and shallow traps in the third layer. In addition, based on the triboelectricity series, it is noted that the silicone elastomer has more tendency to give up electrons than the quartz, but more tendency to attract electrons than the glass (quartz $(+) >$ silicone $(+) >$ glass $(+)$).

Zou [125] studied the impact of water uptake in epoxy-based systems filled with nanosilica. The water layer next to the filler surface may be firmly bounded to it, but the external layer will be bounded by Van der Wals forces and surrounded by water diffusing freely in the bulk, all the layers together creating an aqueous core-shell structure around the nanofiller. Because these water layers are larger than those from micro particles, channels can be created after a percolation threshold is achieved [153] in a similar manner as proposed by Gonon [131]. They have been found that the water uptake can increase from 1 to 4% according to the RH and the nature of filler.

From what concerns the surface of the fumed silica, Lange [74] posits that two types of adsorbed water may be present: physically adsorbed water, and hydrogen-bonded water to silanol groups ($SiOH$), the last aligning with Langmuir's adsorption isotherm. The coexistence of these types implies a predominant monolayer coverage. Silanols, which are, then, adsorption sites on amorphous fumed silica surfaces, may be randomly distributed [154, 155].

Water adsorbed in silica can generate charge carriers, with Bascom [129] noting proton and hydronium exchange between adsorbed water and surface hydroxyls, resulting in water dissociation. Prigogine et al. [156] support the notion of charge

transfer associated with the unsaturated character of silicon atoms. They propose two adsorption sites, one acting as an electron acceptor (proton donor) and another as an electron donor (proton acceptor), creating a duality akin to an acid-base relationship. Observations on pure silica powder indicate water clustering around $SiOH$ groups, redistributing electronic density and imparting basic-like character to neighboring oxygen.

1.3.2.2 Charge transport and space charge events in silicone-silica system

The current and conduction mechanisms of polysiloxane-based insulators: Niedik and collaborators investigated polarization and depolarization currents of a LSR at 45°C at voltages ranging from 2 to 20 kV/mm [157]. A non-linear current-time behavior with a deviation near 1000s appeared for E $<$ 10 kV/mm. Rising the field strength also reduced the deviation suggesting that it could be caused by space charge accumulation associated with trapping and transport mechanism happening in the range of 6 kV/mm – 15 kV/mm. They also studied the impact of different metals on the deviations of apparent currents in comparison with the main value. Titanium-based electrodes showed better reliability against aluminum and copper, which oxidize faster.

Further works of the same team [158] went deep on repeatability and in thermal and electric field analysis of silicone compounds. In total 48 samples were tested at 45°C and 10 kV/mm and a maximum repeatability deviation ranging from 13.56% to 60.25% was found. The authors also tested with different polarities and previously applied voltage stresses and no significant influences were measured. In another work [159], a reasonable fit based on hoping conduction described both thermal and field dependencies of conductivity.

Alam et al [160] conducted similar tests with two different grades of HTV SR filled with silica and ATH. Flat samples 0.3mm thick were tested at ambient conditions (22°C and RH of 50-60%) from 300 V to 1 kV. Step voltages were applied without depolarizing, and to achieve steady-state current each voltage lasted 14-28h to samples filled with ATH and 22-50h for free-filler samples. At the end, the filler-free samples presented a slope close to the unity (corresponding to the Ohmic behavior) but filled samples deviated from linear fit at higher fields, suggesting the possibility to charge injection and accumulation.

The liquid-solid conduction ambiguity: If the silicones of Alam [160] presented an ohmic or super-ohmic conduction mechanisms, as usual solid dielectrics, it was not always the case for another group of authors:

- Nguyen [82] investigated a RTV PDMS under different temperatures (from 20°C to 100°C) and for all temperatures higher than 20°C, his silicone presented a sub-ohmic behavior. Three hypothesis were considered:
  - The electric field "clean" the sample evacuating electrons and ionised impurities, as suggested by Das-Gupta [161].
  - Blocking electrodes due to imperfections in the metal-insulator contact, as suggested by Garton with thin films of insulating liquids [162].

  - His own hypothesis: charge injection followed by a field attenuation.

- Mourad [163] observed the same sub-ohmic mechanism and, crossing them with space charge measurements, this was related to homocharge accumulation leading to field attenuation due to blocking electrodes.

Zink [164] investigated the absorption currents of a silicone rubber composite at temperatures ranging from 20°C to 90°C, and the polarisation patterns were attributed to those of dielectric liquids. If we look closely to the absorption current patterns from the silicones of Nguyen [82], Niedik [157], and Freye [165, 158], or the polypropylene of Das-Gupta [161] at 100°C, or the polyethylene terephthalate of Montanari [166] at 120°C, the same conclusion arises: it looks like an ionic process similar to those of dielectric liquids. Coincidentally, all of them observed such feature at temperatures above the Tg of their materials.

The conduction in dielectric liquids is attributed to the migration of ions coming from impurities. This diffusion results in a random walk, with the field merely superimposing the random path [167]. The current-voltage characteristics is usually divided into three regions: at low fields, an ohmic-liquid conduction can result from the the dissolution of impurities; at middle fields, the current is controlled by the dissociation kinetics, and the slope either decreases or achieves a plateau; and at high fields, space charge can be generated and the slope increases again, potentially being super-ohmic.

Because of the diffusional component, the conduction mechanism at the steady-state in dielectric liquids can be non-ohmic, specially from middle fields. However, such diffusion requires a viscous media.

The viscous media may be present if the material has been tested at temperatures above the Tg. Put differently, the molten amorphous phase can eventually provide viscous paths at which the DC field may be reinforced. If the field reinforces on the molten phase, the current-time or current-voltage plot could mimetize a dielectric liquid one.

Space-charge build-up in silicone rubbers: There is a consensus in the literature regarding the accumulation of homocharge in pure or filled resins under steady-state conditions, accompanied by the presence of negative space charges in the bulk when similar electrodes are employed. However, under shorter durations, lower temperatures, or reduced voltage levels, some authors have reported instances of heterocharge on either side [168, 169], or even the absence of bulk charges altogether [170]. Notably, the role of external and internal interfaces appears to be more pronounced in silicone compared to epoxy. This influence is so substantial that it introduces considerable complexity in distinguishing between surface and bulk properties [171, 172, 173].

The evidences are listed and connected as it follows:

- Rain [168] tested a PDMS filled with silica (35 wt%), manufactured in a round roller sample incorporating aluminum electrodes. It was noted the heterocharge build-up at low stress condition, that was surpassed by homocharge formation at more stressful conditions (temperatures, fields, or time). In addition, the positive homocharge zone appeared first, and a density larger than the negative homocharge.

- The same material and sample was tested by Nguyen [82] who pointed out the identification of a zone with a null electric field in the volume under discharge measurements. It was this zone that justified, according to him, the theory of blocking electrodes induced by injected space charge [170]. The work of Mourad [163] reinforced this interpretation, as another silicone rubber has been tested, and the same behaviour identified.

- The interpretations of Rain [168] align with the findings of Liang, who conducted experiments on silicone rubber filled with TiO_2 and manufactured plates with distinct electrode configurations—aluminum on one side and copper on the other, as documented in [172]. It was noticed that the polarity of the space charge in the bulk depended on the polarity of the electrode having the lower work function. In this particular case, the polarity of the bulk space charges depended on the polarity of the aluminum side: if in the cathode, negative injection and accumulation was privileged; if in the anode, positive injection and accumulation.

- Wang et al [171] stressed that the silica, especially if nanosized, may introduce deep traps to the pure resin. Deep traps were interpreted by them as strong dipole moments, with the silica acting as an impurity particle highly polarizable. Besides, it was identified a low injection threshold, correlated by the amorphous nature of the elastomer that would help an electronic injection via tunnel effect.

- Alam et al [174] studied five different silicone rubber formulations, all of them having silica, some of them having ATH. Their surface potential decay sounded to be dominated by their bulk conduction, as the conductivity calculated from results agreed with the Poole-Frenkel transport model.

- Zhang et al [169] prepared an LSR composite and tested it under 15 minutes at increasing voltage steps, reproducing fields from 800 V/mm to 4 kV/mm. Consistent with earlier studies, the results revealed easy injection and the accumulation of negative space charge. Notably, in this investigation, heterocharge was observed to accumulate at the anode, while homocharge continued to predominate at the cathode.

1.3.3 Multi-layer with focus to the epoxy and silicone rubbers interface

Looking at the epoxy-silicone interface: When epoxy and silicone are in contact, and an electrical field is applied, the epoxy seems to concentrate the stress, as evidenced by the eroded surface observed by Andersson [175] and by the electrical trees found by Beca [176]. Some deterioration can, indeed, be observed in the silicone layer, which were attributed by Andersson to oxidative cross-link reactions caused by electrical discharges and ozone .

1.3.3.1 Current measurements and space charge on bilayer samples:

In a subsequent study, Andersson et al. [177] performed current-time measurements on epoxy-silicone bilayer samples and their respective monolayers. The samples

were either unconditioned or subjected to prolonged boiling in water. Due to the silicone's higher water absorption compared to the epoxy, with the latter exhibiting minimal water absorption under an environment close to 100% RH, the current density of the silicone increased by over one order of magnitude from unaged to boiled conditions. In contrast, the conductivity of the epoxy remained unchanged after boiling. Consequently, the unconditioned bilayer replicated the behavior of the silicone, while the boiled bilayer mirrored that of the epoxy. Notably, only a thin layer on the epoxy side, near the surface, showed some degradation.

Bodega [178, 179, 180] conducted a series of conduction and space charge measurements of XLPE/EPR bilayers, and the same feature of field reinforcements in one or another layer has been found (naturally, because a bilayer is an in-series resistance). This report of field reinforcement changed accordingly to the temperature. The time to achieve a steady electric field distribution was calculated based on Maxwell-Wagner theory (equation 1.3.3, with d as the thickness of layers A and B), that represents a relaxation time and may depend, as the equation suggests, to space charge formation in the interface.

$$\tau_{MW} = \frac{d_A\epsilon_A + d_B\epsilon_B}{d_A\sigma_B + d_B\sigma_A} \tag{1.3.3}$$

Vu et al. [181, 182, 183] undertook similar investigations concerning the XLPE/EPDM interface. The methodology involved: (i) conducting current measurements on EPDM and XLPE separately at various temperatures and electric fields; (ii) predicting the polarity of charge accumulation at the interface using Equation 1.3.3; (iii) simulating the field distribution and charge accumulation under steady-state conditions for all temperatures and electric fields; and (iv) performing space charge measurements with PEA to compare simulations with experimental results. Both XLPE and EPDM exhibited non-linear conductivity with an evolving electric field threshold.

Subsequently, interfacial charge was predicted based on the continuity condition of the electrical displacement normal to the surface, derived from Gauss's law (Equation 1.3.4).

$$\begin{cases} \epsilon_A E_A = \epsilon_B E_B + \sum_s \\ \sum_s(t) = \frac{d_A\epsilon_B - d_B\epsilon_A}{d_A\sigma_B + d_B\sigma_A}.V_{app}(1 - e^{-t/\tau_{MW}}) \end{cases} \tag{1.3.4}$$

The prediction of the electric field distribution was further accomplished by considering the conservation of current density and the boundary condition of the potential, as expressed in Equation 1.3.5; both predictions aligned well with the experimental results. At low fields, XLPE is expected to exhibit greater resistivity than EPDM, justifying the higher fields within this layer. However, due to the non-linear conductivity response to the electric field, an inversion occurs at higher fields, making EPDM more resistive. Consequently, at elevated fields, homocharges concentrate in EPDM near the interface. Moreover, at higher temperatures, heterocharges are also concentrated in XLPE near the interface.

$$\begin{cases} \sigma_A(E_A)E_A = \sigma_B(E_B)E_B \\ d_A E_A + d_B E_B = -V_{app} \end{cases} \tag{1.3.5}$$

Stancu et al [184] conducted experiments with XLPE/EPDM multi-layer samples

thermally aged, and it was noted that the surface charge density was firstly reduced at the beginning of the aging, but then it increased, leading to relevant field at the interfaces, with charges in the bulk and at the internal interfaces contributing to the heterocharge build-up.

1.4 Thesis objectives

Understanding the behavior of insulating materials under DC stresses is crucial for the development of safe and reliable power equipment. This is not a brand new field, because DC fields have always been a matter of interest in the science and in the industry. However, the materials employed in MVDC applications, even if derived from MVAC tools, may undergo changes in formulation and design compared to those used in HVDC applications.

Based on the literature review, one of the main property to evaluate was obviously the electrical conductivity. However, the determination of this property is still a challenge:

- There is no uniformity in performing the current measurement. The standards are not respected probably because they only provide a polarization index instead of some value close to the steady-state materials resistivity. In addition, different protocols are applied worldwide, making the comparison of reported experiments sometimes difficult.

- The correlation of the dielectric's structure and electrical properties is not clear, and maybe it is related to the lack of uniformity in sample preparation found in the literature.

These considerations justified the establishment of the first objective for this thesis, which is stated as it follows:

> **Objective 1:** Designing a measurement protocol that is efficient enough to provide all the information we need, and that considers the structural and microstructural nature of the material, so as the sample's stabilization prior and during the test.

The information we seek is the electrical conductivity, considering its dependence on electric field, temperature, and water content. Notably, water content, often underestimated, plays a significant role. While numerous studies delve into the effects of water absorption on the structure, microstructure, and mechanical properties of epoxy and silicone rubber, the control of water content is not consistently verified when measuring electrical properties.

On the other hand, much information has been collected from reports on epoxy resins, since this material has been applied for more than fifty years in power insulation, and many correlations between the conduction mechanism and space charge build up were able to be crossed from the literature.

The situation is distinct for silicone rubber, recognized as the third generation of elastomeric material commonly used in joints and terminations. The existing literature presents conflicting information on various aspects of silicone rubber behavior: it may be hydrophobic but it can absorb more water than epoxy, it may accumulate heterocharges under high voltages but it depends more on the electrode system than the insulation itself, it may behave as a dielectric liquid even in the solid state, etc. The uncertainties in these characteristics underscore the complexity and the need for a thorough investigation into the properties and performance of silicone rubber in various conditions.

Bearing all of this on mind, the second objective is announced as it follows:

Objective 2: Exploring the individual behaviour under DC fields of an industrial epoxy resin and silicone rubber currently applied in MVAC systems, as a function of environmental parameters, such as temperature and relative humidity. Given our emphasis on comprehending the electrical response, our exploration involves a systematic integration of physico-chemical experiments and correlations throughout the study.

Studying individual components is important to isolate mechanisms, but technological developments also involve going one step further and testing samples that represent better the complexities of the applications. Thus, the third objective is precised as it follows:

Objective 3: Understanding how epoxy and silicone rubber function together as multi-layer insulators within the system, inferring their behaviour from those of the individual components, and consolidating the main practical implications derived from these findings.

We believe that collectively pursuing these objectives will provide valuable support to enhance the comprehension of these insulation materials under MVDC stresses.

2 Materials characterization and methods

This chapter organizes all the information about the materials studied in this thesis, and the methods applied to test them. It has five progressive sections:

In section 2.1, the techniques applied to characterize the materials are detailed.

In section 2.2, we want to "hack" the insulating materials prior to the electrical tests. They are first described according to initial appearances and supplier's information. Then, the techniques listed in the proceding section are applied to investigate and go deep in their structures and the microstructures.

Section 2.3 is dedicated to the sample conditioning process, considered here as a step as important as the electrical test itself.

Electrical tests set-up and their protocols are announced in section 2.4 as they ended to be, after many attempts, fails, and questions raised during the seek of repeatability on results, summarized in section 2.5.

At the end, conclusions and perspectives are envisaged.

2.1 Physicochemical methods

2.1.1 Differential Scanning Calorimetry (DSC)

Prior to electrical tests, it is important to verify phase transitions, residual curing reactions, effects of plasticizers, and potentially the identification of mixtures. These features will change the material and ultimately change the conductivity, and the DSC is the most versatile technique to do it.

The technique consist in measuring the heat flux between two samples: a reference sample and the sample of interest (of around 10 mg). Since they both heat at the same rate, the temperature difference of them is proportional to the enthalpy variation of the sample[185, 186].

Experiments have been executed with the Texas Instruments Q10 under nitrogen. Samples have been cooled at -20°C and heated at 150°C with the rate of 10°C/min (and sometimes 20°C/min in order to increase the resolution). They remained at 150°C for 15 minutes to finish some reticulation reaction, if any. Then, they were cooled again at -20°C and heated again, in a second cycle. Data extracted from the first cycle give information about the molding and storage; it tells about the mechanical history of the sample. The second cycle tells about the material itself, and is more suitable to compare different materials.

In this thesis, the Tg is determined based on the middle-set of the second-run curve, i.e. the middle of the transition.

2.1.2 Thermodynamic Mechanical Analysis (DMTA)

Because the epoxy of this study has glass transition around 110°C, there is a chance that tests will be conducted around sub-Tg transitions (20°C to 80°C, and sometimes 100°C). The DSC hasn't the sensibility to identify sub-Tg transitions, but the DMTA has.

This technique assesses the deformation of a sample subjected to a sinusoidal load while undergoing a programmed temperature change. The resulting data can be analyzed in terms of time, frequency, or temperature [186].

The experiments were conducted using a TA Instruments' DMA Q800 V21.3 instrument. For the tests, we employed a 3-point bending setup with samples measuring 1 mm in thickness and having a rectangular shape of 50 x 10 x 1 mm^3. These samples were obtained from casting plates, shaped using a water jet, and conditioned under the same parameters as the electrical test samples. The tests were performed at a fixed frequency of 1 Hz, and the temperature ranged from -40°C to 150°C, with a heating rate of 3°C per minute.

2.1.3 Fourier-tranform Infrared Spectroscopy (FT-IR)

The quality of the molding process, the robust adhesion between the filler and matrix, and any potential degradation reactions stemming from conditioning or electrical tests can manifest through the formation or cleavage of covalent bonds. Some of these bond changes can be readily identified using infrared spectroscopy.

Fundamentally, infrared spectroscopy serves as a valuable tool for structural identification. The methodology employed in this thesis leverages the Attenuated Total Reflectance (ATR) accessory.

Within this particular technique and using the ATR accessory, an infrared radiation (IR) beam, ranging in frequencies from 10^{-13} Hz to 10^{-12} Hz, is directed through a crystal and then reflected off a surface in contact with a solid sample. The evanescent wave, a result of resonance in the dipole moments of chemical bonds associated with molecular vibrations, permeates and is absorbed by the sample. Subsequently, the beam is collected at the crystal's terminus by a detector, facilitating the analysis of the sample's properties [187, 188].

The primary advantage of this technique lies in its ability to analyze solid materials without requiring additional preparation. However, it's important to note that the depth of penetration (d_p) into the sample is restricted to 2 μm. As a result, the obtained results are inherently representative of the surface condition of the specimen. While this technique has been predominantly used to gain insights into the material's structure, it is crucial to approach the analysis of results with caution and consideration.

2.1.4 Scanning Electronic Microscopy (SEM)

The morphology of the composite is explored with the Scanning Electron Microscopy (SEM) technique (Thermo Scientific's Quattro S), with a resolution of 1 nm at high vacuum (30 kV), and 1.3 nm (30 kV) or 3 nm (3 kV) at low vacuum up to 200 Pa.

The sample is irradiated by an incident electron beam, generated by an electron gun. Fractions of the electrons are absorbed or reflected by the sample, depending on the composition of the irradiated portion. Electrons also excite back-scattered and secondary electrons from the sample, which detection and recording yield high brightness from examining rough surfaces [189].

The equipment utilized is dotted of energy dispersive X-ray spectroscopy (EDX) tool which enables to elemental composition characterization. Prior to the test, samples are covered by a conductive layer of gold if low vacuum is operated. Aiming to have a view of the bulk, samples are also cut and broken under liquid nitrogen (cryogenic conditions).

2.1.5 Weight measurements (Gravimetric method)

Prior to the electrical test, samples undergo a drying and conditioning process in climatic chambers, detailed in sections 2.3.2 and 2.3.3, respectively. The water content in each sample is assessed by measuring weight variations before, during, and after these procedures using an analytical balance (Ohaus Explorer) with a readeability of 0.1 mg, and maximum capacity of 64g. It's worth noting that with a typical sample weight of around 6 g, this resolution results in a sensitivity of 0.017%.

It is possible that some samples were still warm during the gravimetric test. We know that weighing hot objects can lead to inaccuracies in sample mass due to air buoyancy effects—specifically, the tendency of air to rise. When a hot sample is placed in the balance cell, the air above it warms and expands, becoming less dense and creating an upward convection motion [190]. As the air density decreases, the force applied to the balance panel also decreases, resulting in an underestimation of weight [191]. To address this inaccuracy, dry hot epoxy samples (which have low kinetics absorption, as discussed in Chapter 3) at 20°C are compared with dry samples at 40°C, 60°C, and 80°C. A deviation is then calculated based on the weight difference, and the weights of the hot samples are corrected accordingly.

Comparing measurements taken at 20°C as the standard, an underestimation of 0.02% was observed at 40°C, 0.05% at 60°C, and 0.08% at 80°C.

2.1.6 Thermogravimetric Method (TGA)

A thermogravimetric analysis was conducted exclusively for the silicone rubber. It was used a TGA Setaram 16, equipped with mass spectrometry for the examination of released materials (TGA-MS). The procedure involved stabilizing a 32 mg sample at 20°C under a 300 ml/min flow of inert gas (argon). The weight was then measured using a microbalance as the temperature increased at a rate of 10°C/min. Upon reaching 680°C, oxygen was introduced into the flow to complete the degradation process under an oxidized atmosphere. Simultaneously, the mass spectrometer examined the gas evolved through electron bombardment. The gas evolved underwent ionization, filtration, and detection based on the mass/energy ratio [192].

2.2 Materials of the study

2.2.1 Epoxy resin

2.2.1.1 Formulation

The epoxy system of this study is the [redacted] (DGEBA) with [redacted] (MTHPA as hardener), and [redacted]. The Tg is around 110-120°C. Silica flour ([redacted]) is added to the raw material in order to provide the composite. It dried and stored in a oven at 60°C.

This flour presents a large particle size distribution, as suggested by figure 2.2.1 provided by the supplier. It ranges from 130 μm to around 2μm, and the D50[1] is around 40 μm. Only 20% of the particles has more than 80 μm.

In addition, traces of other minerals can be found, with maximum quantities measured by chemical analysis and provided by [redacted]: Fe_2O_3 (180 ppm), Al_2O_3 (4000 ppm), TiO_3 (150 ppm), CaO (100 ppm), and K_2O (90 ppm).

Details about the home-made fabrication of single layers of such composite are presented in Annex A. It involves a cast molding by gravity of mixed raw materials, followed by curing and post-curing steps. The final proportions of resin, hardener, and filler is 100 pbw, 80 pbw, and 270 pbw respectively.

The composite has (at 23°C) dielectric permittivity of 4 (50 Hz, IEC 60250), volume resistivity at the order of $10^{15}\Omega cm$ when measured at 1000 V following the standard IEC 60093, and AC breakdown strength near 20 kV/mm (IEC 60243-1).

[1] 50% of the particles are smaller or bigger than the D50

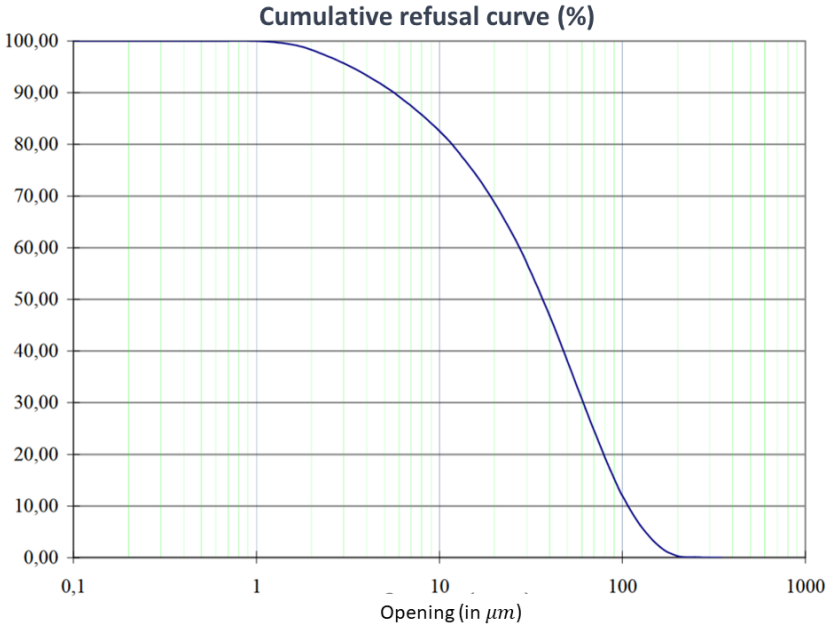

Figure 2.2.1: Particle size analysis provided by [redacted]. The Y-axis represents the cumulative percentage of particles that are smaller than or equal to a specific size.

2.2.1.2 Characterization

The dispersion of silica particles was evaluated based on SEM micrographs. While this method provides an approximation, it may not be the most optimal for estimating size distribution. X-ray diffraction would be a more suitable strategy; however, the presented results aim to offer an approximate overview and support insights into the particles used.

SEM samples were prepared using the drop-casting method, where a small portion of silica was dispersed in an ethanol solution and then dropped onto a silicon stub substrate.

Figures 2.2.2-a, -b, and -c display the resulting micrographs, particle selection from the figures, and particle distribution, respectively. The scale, equivalent to 1 mm, is considered large, enabling the examination of larger particle sizes. After acquiring an image, particle surfaces were determined through contrast differences, counted, and their respective surfaces calculated. Assuming an approximate round shape, equivalent diameters were obtained, referred to here as particle size. All distributions were asymmetrically unimodal, skewed towards smaller particles.

At this scale, the modal value is 3 μm in diameter, with a mean value around 6 μm. Scaling down to 50 μm to examine smaller particles (Figures 2.2.2-d, -e, and -f) reduces the modal value to 0.5 μm, with a mean around 0.75 μm.

These values differ from those in Figure 2.2.1, but it is not excluded that the results in 2.2.2 may have been influenced by the sampling procedure. Nevertheless, it provides insights into the broad distribution and irregularity of particle sizes typical in industrial silica. Particles less than 2 μm, and even in the meso range, cannot be ruled out.

The micrographs of figures 2.2.3 and 2.2.4 suggest a good dispersion and distribution of particles in the thermoset matrix, so as the variability of filler sizes (from mesoparticles to 100 μm).

Because the dispersion of sizes of the silica flour is broad, it is expected that bigger particles will decant, producing a layer of sediments at the bottom of the plate due to drag effects, and causing a gradient of silica concentration thorough the plate length, so as among different samples. In order to evaluate the variability of silica concentrations, thermogravimetric analysis have been performed for different samples extracted from the top and the bottom of the plate, and a difference of 11,5% has been found between the opposite extremities of the plate.

The completion of cross-link is verified through DSC thermograms with samples collected from different spots of different plates. The absence of an exothermic peak during the initial heating, as illustrated in Figure 2.2.5, has indicated that residual cross-link did not occur. There was a difference of 7°C of Tg between the first and second cycles. In the absence of evidence for incomplete cross-link, the interpretation suggests a potential plasticizing process. Upon closer examination of the Tg region, a post-Tg relaxation peak has been systematically found. This peak is generally associated to supplementary movements and molecular rearrangements of the chemical structure, often attributed to a physical ageing associated to the fabrication history and storage. Insights of the chemical structure were given by infrared measurements with ATR accessory, as seen in Figure 2.2.6 for a piece of the plate after molding. The attribution of peaks and bands have been compiled by referencing the works of Dureault [38], Le Huy [37], and Brun [113] and can be seen in Table 2.2.1.

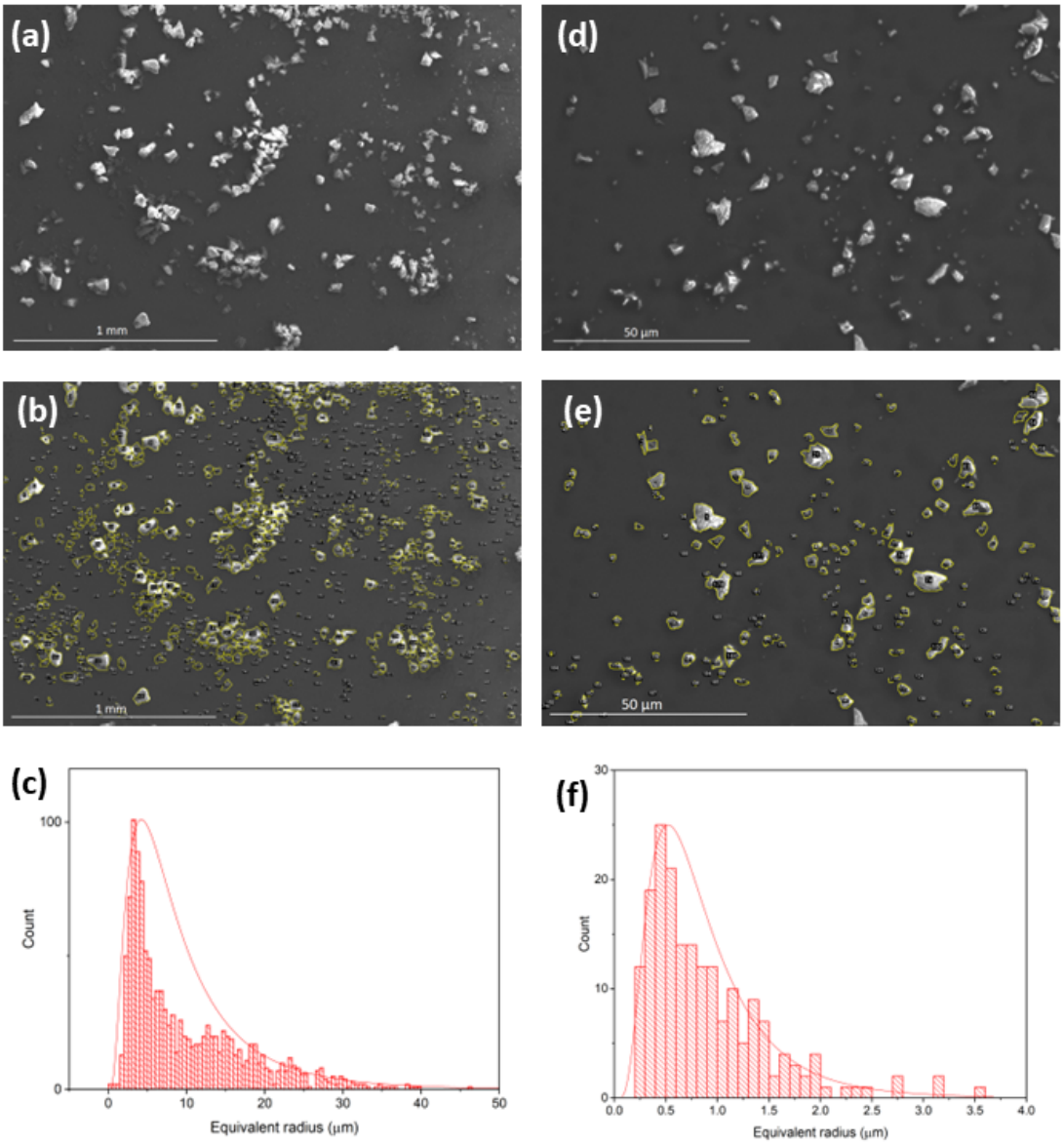

Figure 2.2.2: Dispersion of microsilica based on SEM images. (a) Micrograph with secondary electron detector at high vacuum and 10 kV, (b) identification of particle sizes, and (c) respective disperstion. (d) Another micrograph in the same conditions but different region and scale, (e) identification of particle sizes, and (f) respective dispersion. Granulometry determined with the open-source software *ImageJ*.

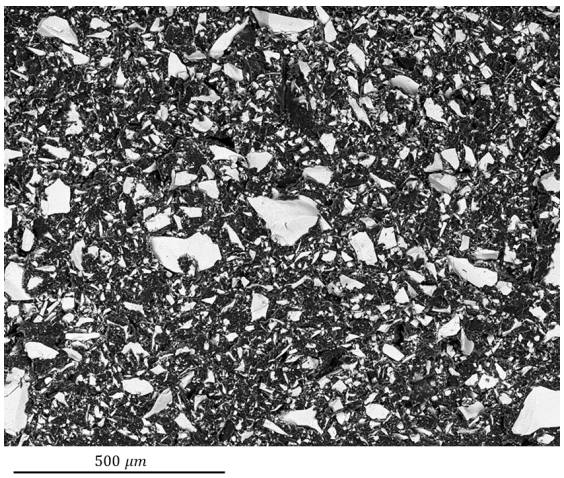

Figure 2.2.3: Scanning electron microscopy of an epoxy sample at scale = 500 μm (magnification = 80x, low vacuum, 15 kV).

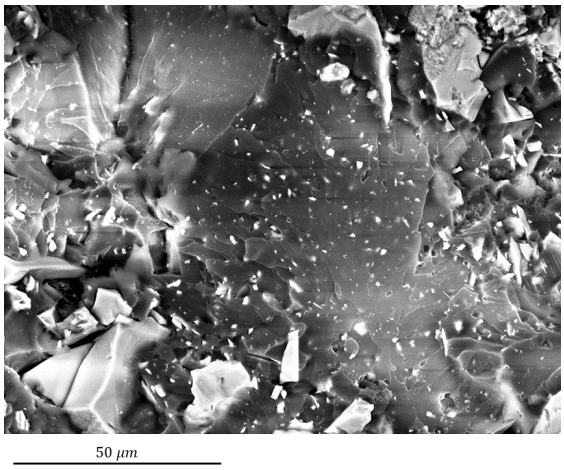

Figure 2.2.4: Scanning electron microscopy of an epoxy sample at scale = 50 μm (magnification = 1000x, low vacuum, 15 kV).

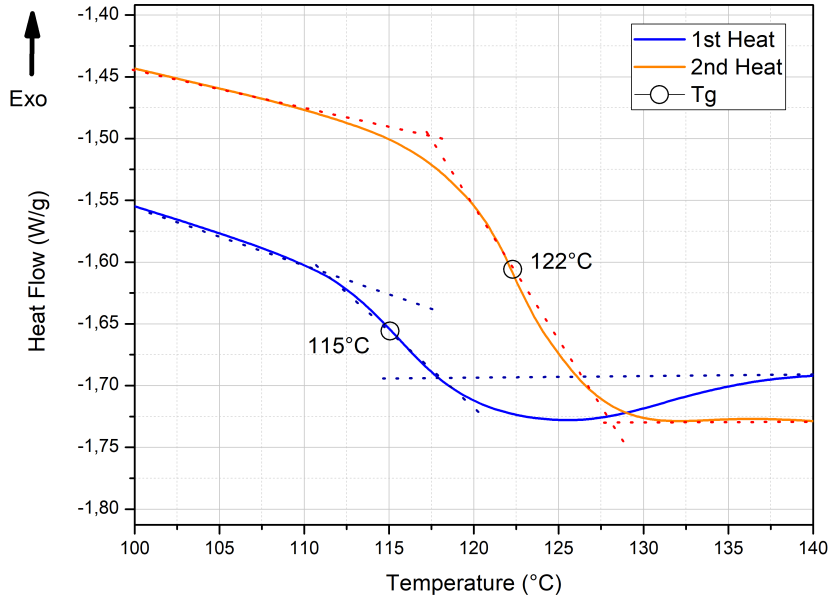

Figure 2.2.5: Thermogram of the epoxy composite after molding.

Functional group	Wave number (cm^{-1})	Vibrational mode
Hydroxyl (-OH)	3500	ν(O-H)
Aromatic (C-H)	3052	ν(C-H)
Aromatic (C-H)	3033	ν(C-H)
Methyl (CH_3)	2966	ν(C-H) asymmetric
Methylene (CH_2)	2931	ν(C-H)
Methyl (CH_3)	2872	ν(C-H) symmetric
Esther (OC=O)	1739	ν(C-O)
Phenylene	1610	Quadrant stretching
Phenylene	1580	ν(C=C) aromatic
Phenylene	1510	Quadrant stretching
Phenyl ortho	1458	Semi circle stretching
Dimethyl $-C(CH_3)_2$	1381	
Dimethyl $-C(CH_3)_2$	1363	
Aromatic ether C-O-C	1240	ν(C-O-C)
Phenyl $-C(CH_3)_2-$Phenyl	1184	ν(C-C)
Esther (O=C-O)	1152	ν(C-O)
Aliphatic ether C-O-C	1042	ν(C-O-C)
p-phenylene	830	Out of place $\delta(C-H)$ arom.
$C(CH_3)_2$	807	$C(CH_3)_2$ skeletal

Table 2.2.1: IR bands and peaks attributions for the epoxy resin.

It provides another tool to verify an incomplete cross-link by the verification of hydroxide peaks, once non reacted hydroxides should intensifies the band around 3500 cm^{-1} [38]. Effectively, a band is identified in this domain, but it is not as intense as literature suggests to reinforce a incomplete cross-link hypothesis.

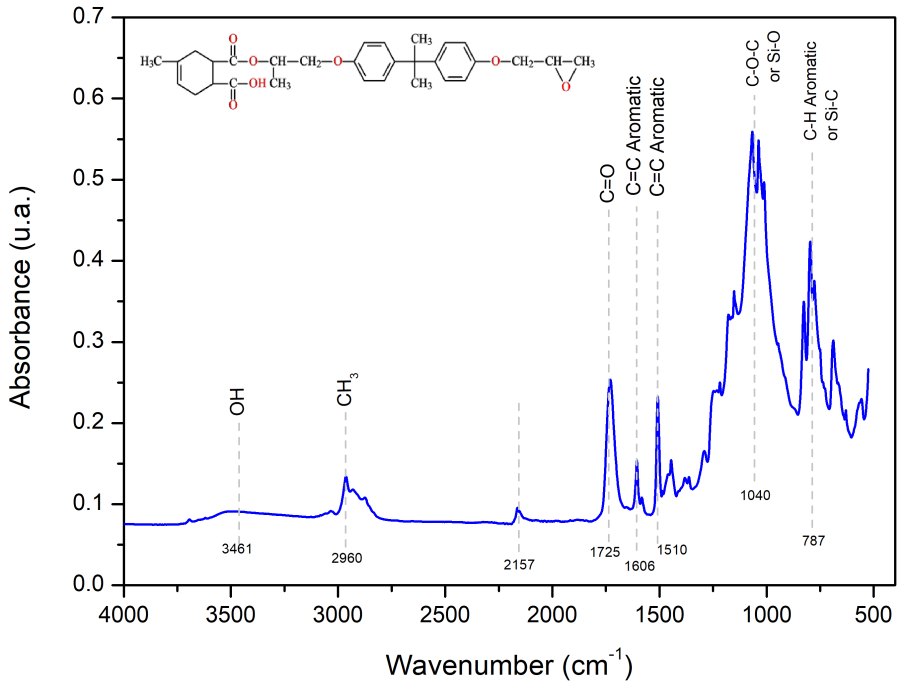

Figure 2.2.6: Infrared spectra for epoxy samples as molded.

Density	1,1 - 1,4 g/cm^3
Volume resistivity (IEC 60093)	$10^{14}\Omega cm$
AC breakdown (IEC 60243-1)	20 kV/mm
Compression set (125°C and 70 hours) with compression rate of 5%	25%
Compression set (125°C and 70 hours) with compression rate of 10%	15%

Table 2.2.2: Summary of main properties of the silicone rubber given by the supplier

2.2.2 Silicone rubber

2.2.2.1 Formulation

The silicone rubber is a MVQ (methyl-vinyl siloxane) provided by [redacted]. The chemical structure is illustrated in figure 2.2.7. It's an HTV (high-temperature vulcanized) silicone cured with peroxides. It is also an HCR.

A summary of the main properties is given in the table 2.2.2. No information about the permittivity is given.

MVQ are supposed to be more flexible than common MQ (methyl-siloxane) silicones, as the PDMS (polydimethylsiloxane). It's commonly found in O-rings, seals, gaskets, tubing, cable insulation, surgical and medical applications. Vinyl content usually ranges up to 4.5%. The supplier informs that this grade has 20-30% of silica content, in addition with carbon black and iron oxide in quantities not declared. It is believed that carbon black and iron oxide are added to give a brown color. Sheets with a thickness of 1 mm were manufactured and supplied directly by the supplier (2.2.8). No further information is given about the fabrication process.

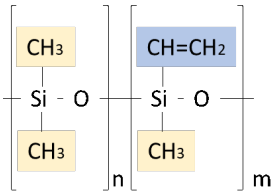

Figure 2.2.7: Chemical structure of a MVQ silicone.

Figure 2.2.8: Single layers of silicone sheets as provided by the supplier.

2.2.2.2 Characterization

The aim of this section is to explore as much as possible the structure and formulation of the silicone plates. It is acknowledged that these techniques may provide somewhat limited information, added to the fact that no information is provided about the fabrication procedure.

One first point of concern about this material is the quantity, the morphology, and the distribution of fillers dispersed in the matrix. The prime attempt was the

visual verification based on SEM micrographs. Both surface and bulk have been explored.

Exploring the polymer morphology, formulation, and fillers: Figures 2.2.9(a) and 2.2.9(b) show examples of two different surfaces spotted by secondary electrons with high vacuum and 1 kV. On both of them, some roughness has been identified by strips everywhere, some of them parallel; it is believed it comes from the molding. Another important feature was the presence of small dots all over the surface; some of them, in Figure 2.2.9(b), having the size of around one micrometer.

Due to the surface perspective, even when samples undergo ethanol cleaning before testing, distinguishing them from dust proves challenging. The EDX spectra within the marked dots exhibit peaks similar to those outside. One example is presented in Figure 2.2.9(e) where silicon, oxygen, carbon, and aluminum have been identified. Initially, the presumption was that this grade contained trihydroxide aluminum ($Al_2(OH)_3$), a common component in many industrial elastomers known for its fire-retardant properties. However, confirmation of the presence of $Al_2(OH)_3$ from the supplier remains elusive, as it will be seen later in Figure 2.2.10. Its origin may be attributed to dust, any impurity, or simply coming from the SEM specimen's stub.

This EDX spectra gives insights about the presence of silica. In the siloxane chain, the atomic ratio of Si and O is 1:1; but in the silica, it is 1:2, if roughly approximated to SiO_2. According to Figure 2.2.9(e), this material has a ratio of around 2:3, which is in the middle of 1:1 and 1:2.

To obtain images that show the bulk, samples have been frozen in liquid nitrogen (77 K, i.e. around -195°C) and broken inside it (cryogenic cut). This temperature is lower than the melting temperature (-40 °C) and Tg (-120 °C); the material being in the glassy state, the rupture is supposed to be fragile. However, during the examination, it has been pointed out that the material charges a lot under high vacuum and high voltages. As a consequence, even if the equipment has a good resolution (some nm), the test was limited to some μm.

In the initial attempt, the morphology appeared unclear, as depicted in Figure 2.2.9(c). A coarse relief seemed to prevail, featuring numerous bright dot structures that could either indicate the presence of silica or silicone asperities. To enhance resolution without significant charging effects, a thin layer of gold (5 nm) was deposited on the surface through sputtering deposition, resulting in the macrograph shown in Figure 2.2.9(d). Once again, the predominant features are round structures, exhibiting an average diameter of 70 nm.

An additional approach to access the silica content involved employing a density method. The weights of six dry samples were measured using a gravimetric method, and considering their respective shapes, a density of $(1.23 \pm 0.02) g/cm^3$ was calculated. Based on the mixing law of Equation 2.2.1, where Φ represents the volume fraction, and d the density, a volume fraction Φ_{SiO_2} of around 14% of silica has been found, with the $d_{SiR} = 1,05 g/cm^3$[2] and $d_{SiO_2} = 2,3 g/cm^3$. This corresponds to 26% in weight. This value is on the range given by the supplier.

[2]Pure silicone rubber without any filler, as the LSR WACKER Lumisil [193]

$$\begin{cases} \Phi_{SiR}.d_{SiR} + \Phi_{SiO_2}.d_{SiO_2} = d_{sample} \\ \Phi_{SiR} + \Phi_{SiO_2} = 1 \end{cases} \tag{2.2.1}$$

TGA measurements were executed according to the description in 2.1.6. The results are depicted in Figure 2.2.9(f). Up to 400°C, a loss of 2.3% of the weight (732 μg) is observed, likely attributed to the release of H_2O. No distinct degradation process is identified before this temperature range, as no CO or CO_2 is detected. Degradation processes are not totally ignored, but it is hypothesized that this weight loss corresponds to water desorption. Subsequently, degradation initiates at 400°C and continues up to 650°C, resulting in a 67.7% loss of weight (21.7 mg). This can be associated with the release of H_2O and CO. The addition of oxygen to the flow does not significantly alter this weight loss. Towards the end of the process, the total amount of inorganic material corresponds to 30% of the initial weight (9.6 mg). It's important to note that this quantity should not be directly linked to the total amount of silica and other minerals in the formula, as amorphous silica is also a by-product of the degradation of siloxane chains, leading to ceramization of the polymer [194]. The fact that this quantity exceeds the estimated 26% for silica concentration is indeed consistent.

The material remained from TGA was not enough to enable further analysis, thus one sheet was cut into pieces and calcinated in a crucible bowl at 900°C for 1 hour in an exploratory experiment. It resulted in a two-phase solid, white on the top and brown/orange in the bottom, as can be seen in Figures 2.2.10(a) and (b). Not all the organic material has been burned, as indicated by the black spots, that can be also carbon. Both solids were fragile and broke easily into small pieces and powder. They both have been analysed in the SEM (Figures2.2.10(c) and (e)).

The white powder appears to be composed of spherical particles with an approximate diameter of 400 nm. The microanalysis generated from Figure 2.2.10(c) is detailed in Figure 2.2.10(d), revealing the identification of only silicon and oxygen elements (with a negligible carbon peak, disregarded in the analysis). The atomic percentage indicates a quantity of oxygen approximately twice that of silicon.

Given that microanalysis provides only an approximation, we infer that the white powder is likely composed of SiO_2, though the potential formation of metallic Si is not entirely ruled out. An additional noteworthy observation is that the morphology and sizes of the particles, as depicted in Figure 2.2.10(c), are unlikely to be encountered in silicone, as highlighted in Figures 2.2.9(a), (b), (c), and (d). This strengthens the hypothesis that the white powder could potentially be a result of the degradation of the silicone backbone.

In the case of the brown material, no such spheres were observed, as seen in Figure 2.2.10(e). The absence of spheres in the image could be attributed to the resolution limit of the SEM analysis, as structures resembling rounds seem to make up the background. Alternatively, metal particles were dispersed in the image, and the corresponding microanalysis (Figure 2.2.10(f)) revealed the presence of iron. Given that the powder shares a brown hue with the original silicone rubber, it is reasonable to conclude that the iron originates from the pigment; it is known that iron oxides are commonly used as red coloring agents. Silicon and oxygen were also identified in the microanalysis, suggesting that the by-product may be composed of SiO_2 as well.

The hypothesis that silica particles in Figure 2.2.10(e) may be too small to be

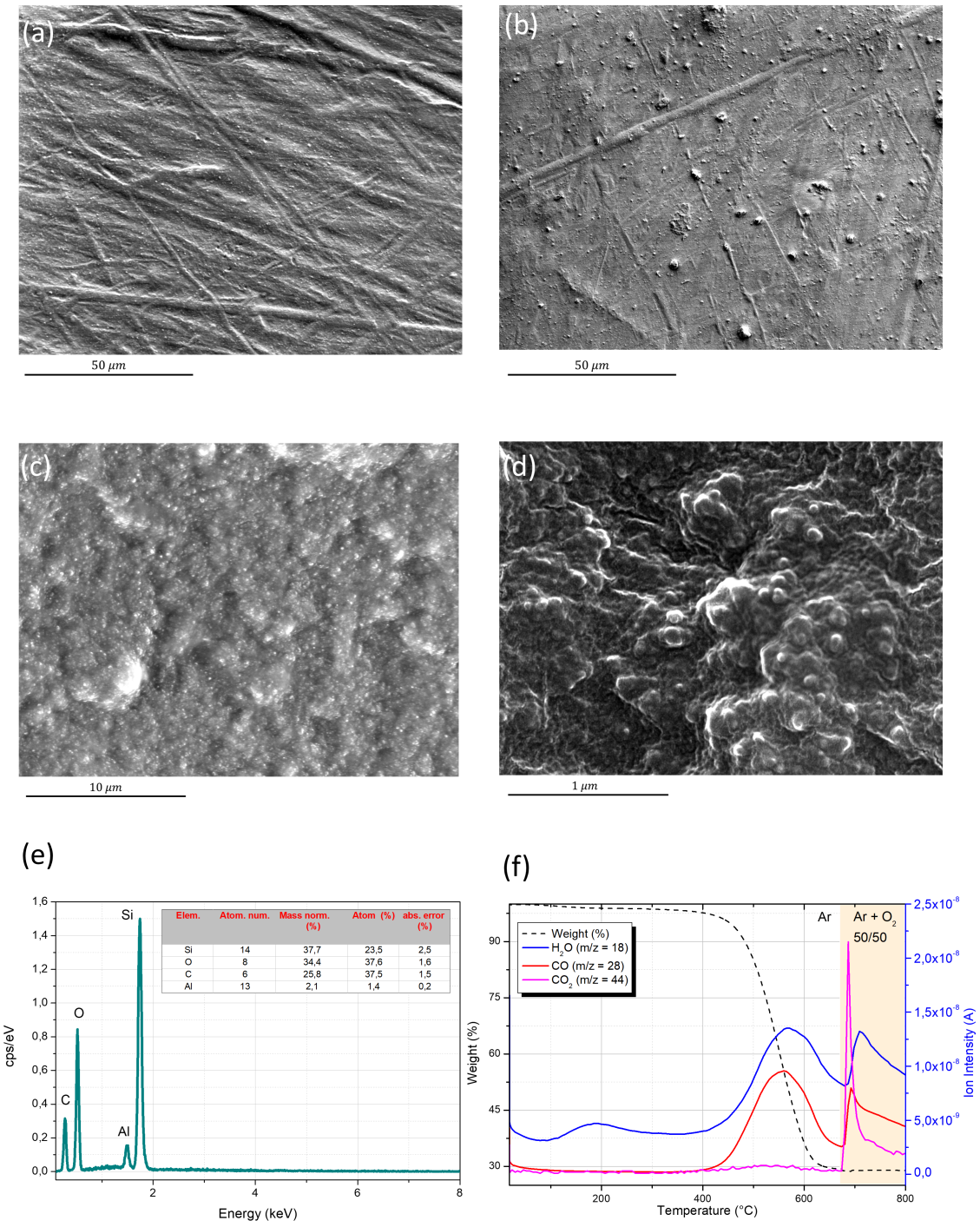

Figure 2.2.9: (a) Scanning electron microscopy of the surface of a sample at scale = 50 μm (magnification = 800x, high vacuum, 1 kV). (b) The same as (a) but for a different sample. (c) Scanning electron microscopy of the cross-sectional surface of a sample at scale = 10 μm (magnification = 4000x, low vacuum, 10 kV, secondary electrons). (d) Scanning electron microscopy of the cross-sectional surface of a sample at scale = 1 μm (magnification = 4000x, low vacuum, 10 kV). (e) EDX spectra of (b). (f) TGA-MS curve of 32 mg of non-conditioned silicone rubber sample.

observed with our SEM, while being distinctly visible in the white powder, suggests their dimensions fall below the detection limit of our SEM, lying in the sub-micron domain. This interpretation gains further support when considering the micrograph in Figure 2.2.9(d). If so, the silicone may be filled with silica nanoparticles, thus classifying the material as a nanocomposite [195]. This morphology looks similar to those found by [196] about an HTV silicone rubber filled with fumed silica, in which the brightness areas of Figure 2.2.9(d) being attributed to fumed silica aggregates. Fumed or pyrolised silica is a common filler for silicone rubbers, it can be a by-product of silicone rubber manufacturing [50] , and usually has sub-micron dimensions.

On the other hand, if this silica is, indeed, nanosized, the concentration of 26% in weight sounds too high, and we can not exclude the possibility of having aggregates. The silica aggregation inputs more complexity to the subject, since there will be non-negligible porosity filled by air and, eventually, by water.

Infrared spectroscopy: IR-ATR analysis was conducted on a freshly non-conditioned plate (Figure 2.2.11), with the majority of the peaks indexed and described in table 2.2.3 [197, 198, 199]. It is noteworthy that there is a systematic absence of characteristic peaks of Aluminum Trihydrate (ATH) in the 3500 cm^{-1} zone [200], indicating the likely absence of this component in the formulation.

The methyl groups surrounding the siloxane chains contribute to their hydrophobicity by virtue of their pronounced non-polarity. One method for assessing hydrophobicity, or indicating degradation, is through the H ratio (equation 2.2.2), representing the relationship between the heights of the absorption peaks of the main chain $Si-O$ (1010 cm^{-1}) and the methyl groups and siloxane, specifically the side $C-H$ (1070 cm^{-1}) [199].

$$H = \frac{A_{Si-C}}{A_{Si-O-Si}} \tag{2.2.2}$$

Based on Figure 2.2.11, it has been found heights of $A_{Si-O-Si} = 0.962$, and $A_{Si-C} = 0.953$, which gives an $H = 0.9905$. This value is the H of reference for this material and is in indicator of the aging characteristics.

Differential scanning calorimetry: In the final check-up, we conducted DSC measurements to verify any potential residual curing processes. Similar to epoxy, silicone vulcanization is characterized by an exothermic process, where the released heat is directly proportional to the formation of cross-linked bonds. In a DSC analysis, cross-link is typically evidenced by an exothermic peak occurring at temperatures exceeding 100°C (with the peak position dependent on the heat rate) [201,

Functional group	**Wave number (cm^{-1})**	**Vibrational mode**
$C-H$ in side chain $Si-(CH_3)_2$	3000	ν(C-H)
Side chain $(Si-(CH_3)_2)$	1260	ν(Si-C)
Side chain $(Si-CH_3)$	1070	ν(Si-C)
Main chain $Si-O-Si$	1010	ν(Si-O)
Vinyl side groups	460	ν(C=C)

Table 2.2.3: IR bands and peaks attributions for the silicone rubber.

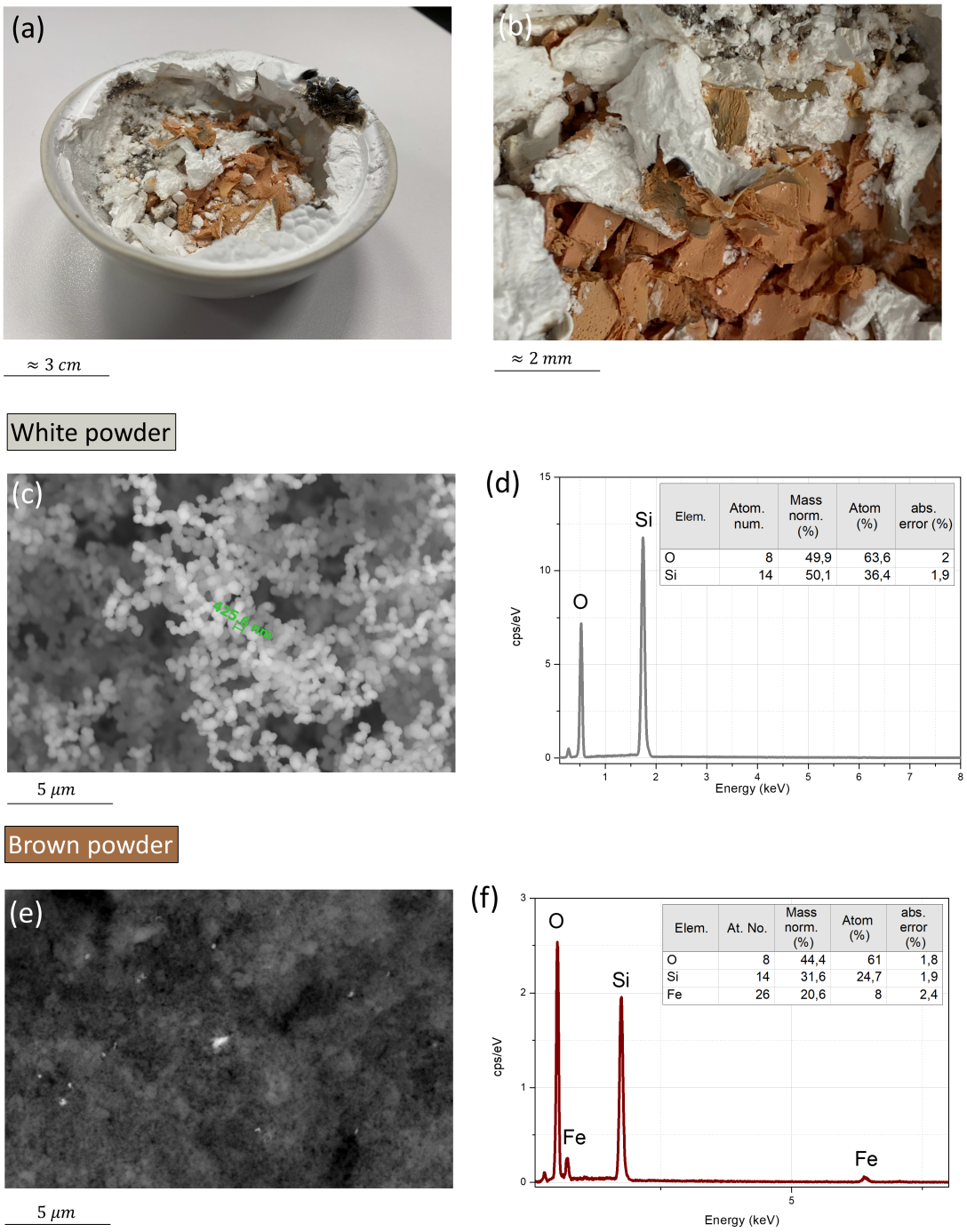

Figure 2.2.10: Investigations about the calcinated silicone rubber. Pictures of the material calcinated in the crucible bowl (a), (b). Micrograph of the white residues (c) and respective micro-analysis by EDX (d). Micrograph of the brown residues (e) and respective micro-analysis by EDX (f). Both (c) and (e) were obtained with Annular Back-Scattered Electron (ABS) detector, at the same magnification (6000 x), same voltage (10 kV), low vacuum, and same scale, thus enabling some comparison.

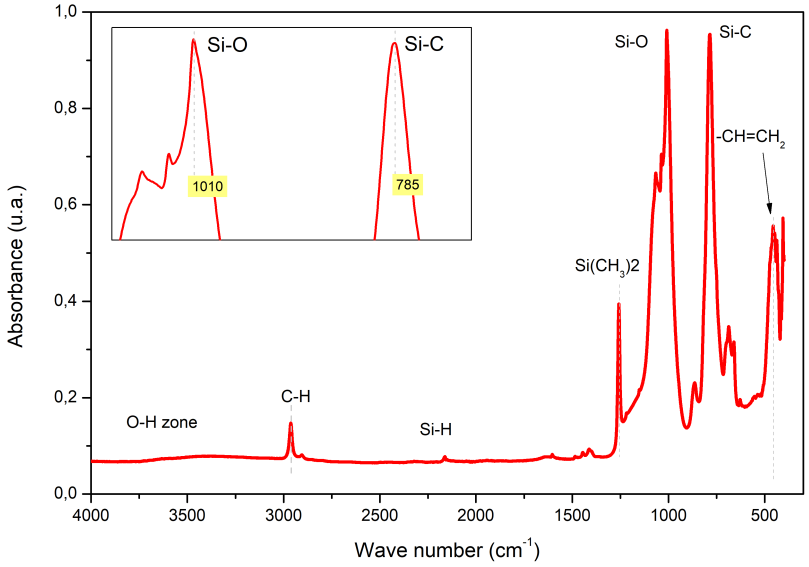

Figure 2.2.11: FT-IR spectroscopy of a silicone rubber plate by means of ATR accessory

202]. However, as illustrated in Figure 2.2.12, no discernible exothermic peak was observed within the temperature range up to 250°C. Additionally, the presence of an endothermic peak at -40°C indicates the melting temperature (Tm) found in the literature for the PDMS [203].

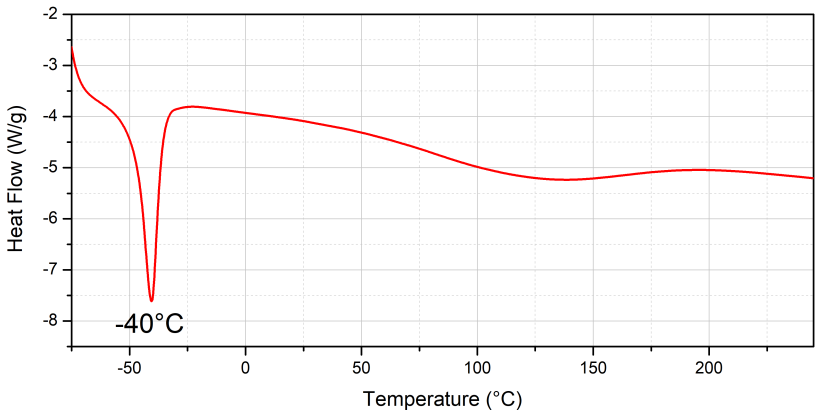

Figure 2.2.12: DSC thermogram of the silicone rubber with heating rate = 10°C/min. The beginning of the curve does no represent any transition, it is merely the thermal equilibrium previously set at -80°C, which is close to the limits of the equipment used.

2.3 Sample preparation and conditioning

Figure 2.3.1 provides an overview of the sample preparation roadmap. Initially, 1-mm thick samples are molded and shaped into 70 mm diameter disks. This shaping step ensures that the samples have compatible dimensions for installation in the electrical test cell.

These samples may initially have varying water contents or specific water-related characteristics due to absorption during fabrication, storage, and shaping. To standardize the water content, they undergo a drying process until all samples reach the same level of water uptake, which is kept as low as possible based on the drying environment. The drying process is considered complete when the samples consistently maintain the same weight over three consecutive measurements. For epoxy resins, this typically involves one measurement per day, while for silicone rubber, it requires one measurement per hour. The drying process is aimed at reducing the water content in the samples to the lowest practical level, but not necessarily to completely eliminate all water uptake. As it will be observed, epoxy resins typically require approximately 14 days to achieve consistent weights during the conditioning process. In contrast, silicone samples, if they absorb water, typically reach equilibrium in as little as 2 days.

Wet samples are fabricated from dry ones inserted in climatic chambers where controlled temperature and relative humidity conditions facilitate water absorption. In this controlled environment, saturation is reached when the sample's weight remains consistent over three consecutive measurements.

Finally, after the preparation process, a 200 nm layer of metal, usually gold, is sputter-deposited onto the samples before they are installed in the test cell.

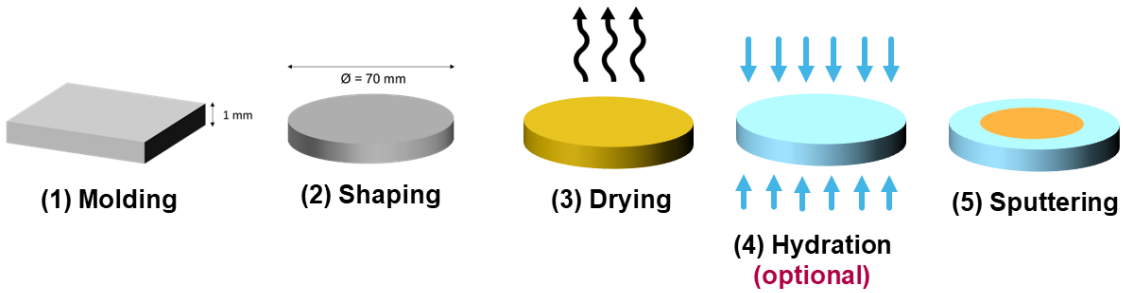

Figure 2.3.1: Sample preparation road map, which consist of molding plates, shaping samples, drying, controlled hydrating, and sputtering.

After the sample is removed from an oven or climatic chamber, it can rapidly gain or lose water depending on the environmental conditions. This water exchange is particularly relevant during subsequent steps, such as the sputtering process (as described in subsection 2.3.4), where a secondary vacuum (5.10^{-4} mbar) is applied for a minimum of 40 minutes. If samples are conditioned with electrodes (by reversing the order of steps 3 and 5) or are already placed in the test cell, there may not be enough surface area available to facilitate water absorption or desorption. This would significantly prolong the process.

Thus, a last conditioning step is added after step 5, the sample being mounted inside the test cell. Both sample and the electrical apparatus are stabilized at the

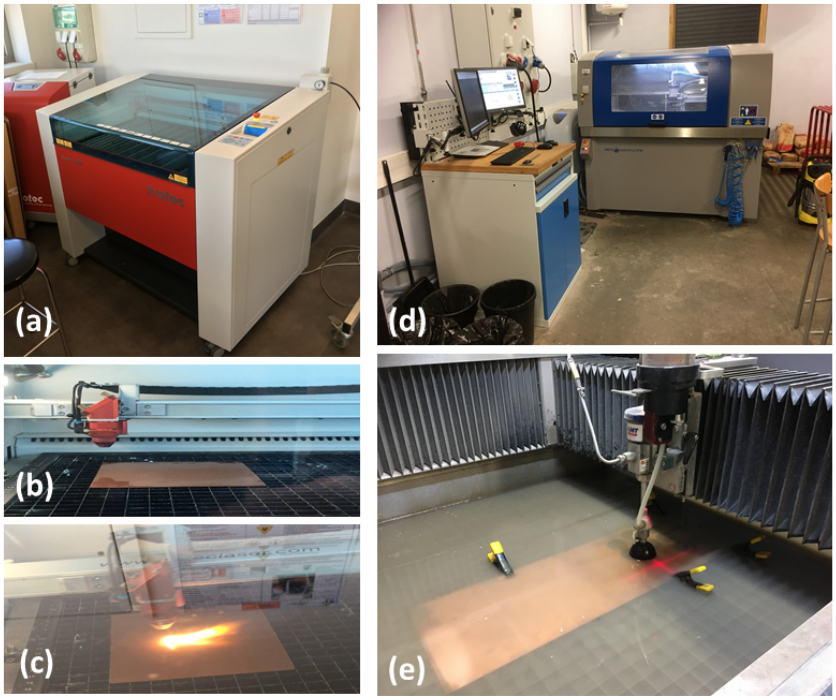

Figure 2.3.2: Shaping machines based on laser-cut (a) which was applied for silicone plates (b and c), and based on water-jet (d) applied to epoxy and metal plates (e).

same temperature and relative humidity conditions as the previous conditioning for at least 4 hours before pursuing the test.

The total process (from obtaining plates to start the electrical measurement) takes in general 1 month.

2.3.1 Shaping

Silicone rubber sheets have been shaped in 70-mm diameter discs with a laser cutting machine (Trotec Speedy 360, Figure 2.3.2-a, b, and c). Since the laser technique is not is suitable for epoxy (toxic material can be projected), epoxy samples are shaped by water jet (Méca Numéric LJ 0710, Figure 2.3.2-d, and e).

As the surface of the plates can have a different microstructure and compactation as the bulk (a *phenonema* often called "skin effect", coming mainly from fabrication) it is not excluded that the shaping will expose the sample's bulk. The author believe that this exposition may interfere in the kinetics of, for example, the water (des)absorption, but not in the general and steady-state properties of the sample.

2.3.2 Drying

The samples are dried in an oven set at 70°C and placed under a primary vacuum. (Figure 2.3.3-a). A temperature of 70°C has been selected to facilitate the removal of water without risking damage to the microstructure, which could potentially occur at higher temperatures. Additionally, a vacuum is employed both to expedite the drying process and to minimize thermo-oxidative degradation by reducing the sample's exposure to oxygen. However, it's important to note that some degree of thermal degradation cannot be entirely ruled out. Aluminum foil supports should

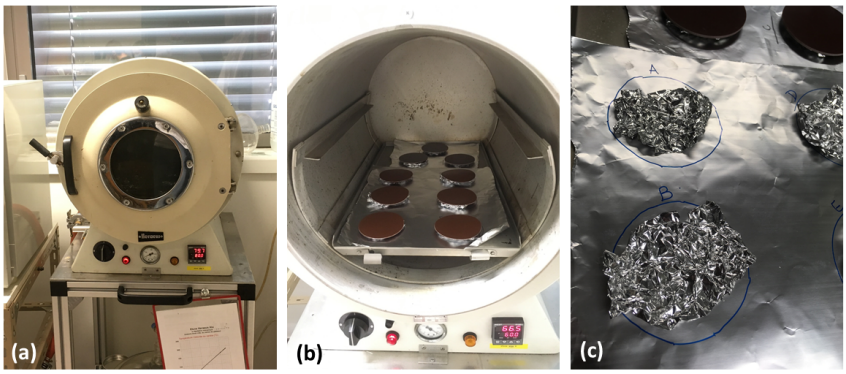

Figure 2.3.3: Drying technique using a vacuum oven (a), in which samples are disposed (b) under aluminum-foil "towels" (c) in order to enable drying on both sides of the sample.

allow for water extraction from both sides of the samples (Figure 2.3.3-a, and b). The samples are left in the oven until their weight stabilizes, which is measured using an analytical balance.

Previous works [132, 113] have indicated that even relatively thin epoxy samples, such as those with a thickness of 1 mm, may require two weeks or more to achieve complete drying, or at least to achieve water stabilisation. This procedure has been adapted from these works, and contrast with the EN ISO 62 standard [204] that suggests a drying at 50°C up to 10 days.

The weight measured at the conclusion of this process provides the initial mass, denoted as m_0, which will be used subsequently to calculate the water uptake. The total quantity of water absorbed is directly linked to this initial mass, and therefore, it is inherently influenced by its accuracy. Hence, the measurement of water uptake is somewhat relative.

Additionally, it is essential to note that this procedure can also extract volatile compounds present in the resins or generated as by-products during cross-linking. These volatiles are felt as a mild odor when the oven is opened during the first days of drying. The impact of these volatiles on electrical measurements, as well as their actual presence in the final products, is a subject of discussion. Nevertheless, the author has deemed the extraction of these volatiles as a necessary trade-off to ensure the uniformity and dryness of the samples.

2.3.3 Hydration

The water uptake experiments are carried out within controlled environments created by climatic chambers, as depicted in Figure 2.3.4-a, and b. In these chambers, both temperature and relative humidity are configured to match the conditions specified for the electrical measurements. For example, if the objective is to conduct tests at 20°C and 90% RH, the climatic chamber is set to this specific temperature and relative humidity combination. The experiment is considered complete when the weight stabilizes over three consecutive measurements.

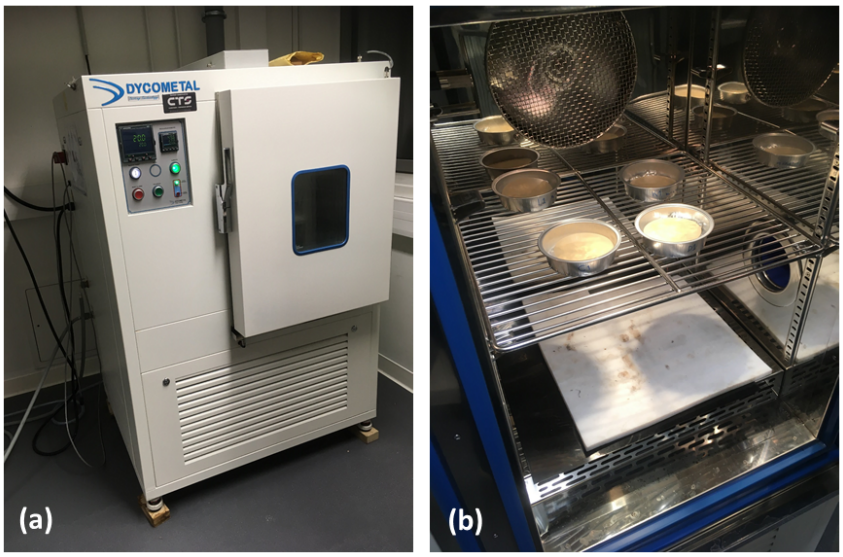

Figure 2.3.4: The conditioning in humidity uses a climatic chamber (a) set at a specific temperature and RH, in which samples are disposed (b) above aluminum-foil structures.

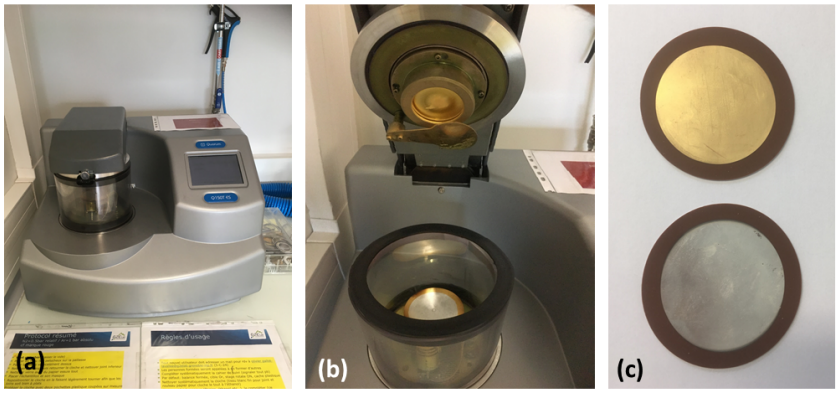

Figure 2.3.5: Turbomolecular pump coater for outside (a) and inside (b); and samples covered with gold and silver (c).

2.3.4 Sputter deposition

Aiming to improve the contact between the samples and the electrodes, samples are covered on both sides by a thin layer of a metal (200 nm on both sides) through sputtering deposition equipped with a turbomolecular pump providing a secondary vacuum (Quorum Q150T ES) (Figure 2.3.5-a, and b). Each side have different dimensions in order to fit the diameters of 50 and 54 mm of the cell electrodes (Figure 2.3.5-c).

The principle, illustrated in Figure 2.3.6, consists of a Physical Vapor Deposition (PVD), more specifically, a cathodic pulverization. Under secondary vacuum conditions (around 3.10^{-2} mbar) a static electric field is applied between the sample and a metal target, which is gold by default, but also silver, platinum, and copper have been tested. A flow of argon is injected in the cell, which will rapidly be energized and create a plasma of Ar^{+}. The ions are accelerated and bombard a target, having momentum enough to extract their atoms and project them to the sample.

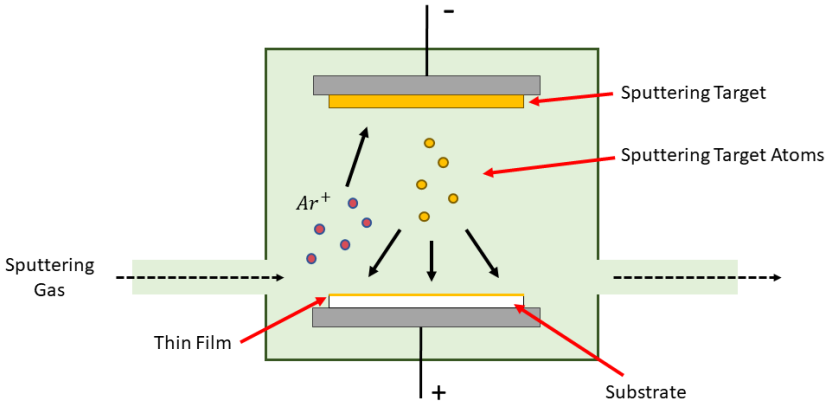

Figure 2.3.6: Scheme of the PVD technique (Adapted from [205])

Metal	Work function (eV)	Thickness (nm)
Platinum	5.6	200
Gold	5.4	200
Copper	4.9	200
Silver	4.7	200

Table 2.3.1: Selected work functions for metallic elements under vacuum [206].

The deposition of each side can stand a couple of minutes to half an hour, depending on the target and the intensity of the field created. A single deposition is finished at the end of 20 minutes. The work functions of these metals are listed in the Table 2.3.1.

2.4 Electrical measurements

2.4.1 Current-voltage measurements

2.4.1.1 Set-up

Two similar custom metallic cells were employed in this study. They had been designed for the Ph. D. of Laetitia Zavattoni [207] and allow pressure or vaccuum application inside (Figure 2.4.1). The cell lid has two threaded openings, useful to screw test probes, but sealed with screw bolts when not used.

The electrodes consisted of a conductive rubber with a 10 Ω transverse resistance, a diameter of 54 mm on the high voltage (HV) side, and 50 mm on the measurement side. The Keithley 6517B Electrometer/High Resistance Meter, equipped with an integrated voltage source, was used to measure the current and apply voltage levels under 1 kV. Beyond this threshold (and systematically thereafter, following the establishment of a testing protocol), the voltage source was replaced by the PS365 SRS High Voltage Power Supply, capable of supplying voltages up to 10 kV.

Since we had a DC power supply of each polarity, tests were conducted in parallel with two different cells. Unless specific electrode arrangements, for example different metals on each side, polarity of the voltage source shall have no effect due to the uniform configuration of the test cell.

To control temperature and relative humidity, both cells were placed inside a climatic chamber (see entire set-up in the Figure 2.4.2). The real-time temperature is measured by three different sources: the climatic chamber own thermocouple, displayed in the chamber digital screen; an external RH test probe (Rotronic xyz) extended externally from the cell and screwed in the cell lid; and an additional thermocouple connected on the top of the cell lid and extended to the mass electrode. The last is connected to the Keithley 6517B Electrometer and all the values are registered at each current datapoint. The RH is equally verified by the chamber's termocouple and the RH test probe, but not recorded.

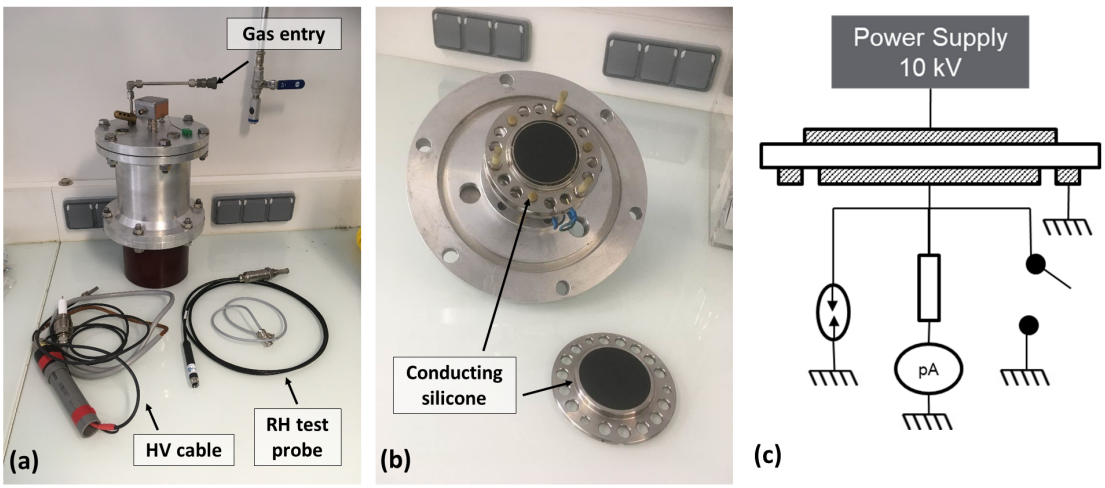

Figure 2.4.1: External view of the test cell (a) and the electrodes (b). Simplified electric scheme (c).

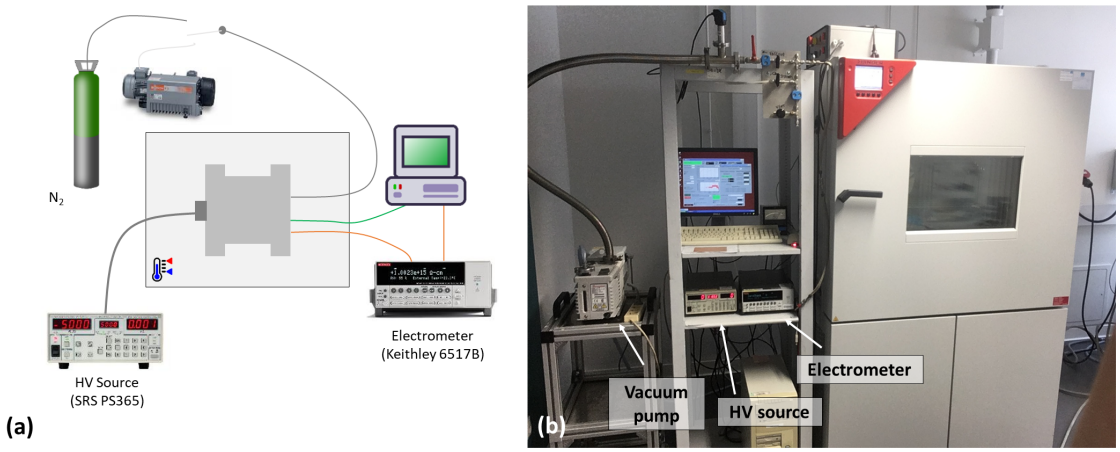

Figure 2.4.2: Scheme (a) and picture (b) of the entire set-up.

2.4.1.2 Installation and cell preparation

Cell preparation: In the case of testing a dry sample, the test cell is tightly sealed, and a purge is carried out using a vacuum pump to lower the internal relative humidity (RH). After each pumping cycle, the cell is then filled with dry nitrogen (N45, $<$ 10 ppm of H_2O). Typically, after three purge cycles, the internal RH stabilizes at 1%, with a potential increase to 3% during the test. Notice that drying concerns not only the sample but also certain insulating parts of the test cell that are made of epoxy screws and bolts. If the test is conducted at elevated temperatures, this purge cycle is repeated once the temperature has stabilized. In the end, a pressure of 2 bars of dry nitrogen is maintained.

When testing a wet sample, one of the cell opening of the lid is left open by the absence of a bolt, allowing for temperature and air exchange between the cell and the climatic chamber, which is set to the same temperature and humidity as the sample conditioning environment. For voltage values up to 3 kV/mm, the test cell remains open. At higher voltage levels, the air breakdown voltage is reached (in accordance with the voltage breakdown estimated by the Paschen curve), so the cell is sealed and directly filled with 2 bars of dry nitrogen, without any prior purge. Given the moist nature of the sample and the dry environment surrounding it, it is anticipated that the sample may lose water to the surroundings, even if a significant portion of its surface is not exposed to surrounding gas. To minimize this effect, after completing each field level above 3 kV/mm, the cell is reopened and reconditioned before moving on to the next voltage level. This is done so that the sample can recover any water it would have lost.

Discharging and stabilization step: Since the beginning of the cell conditioning until 4 hours of temperature and RH stabilisation, the sample is subjected to a short-circuit, and the discharge current is continuously measured. In simpler terms, the sample is discharged before the voltage application begins.

In the initial trial runs, when testing samples at various temperatures, the sample was heated to the highest test temperature, discharged at that temperature, and then cooled down to the lowest temperature at which the voltage program was set to start. However, after conducting several experiments, it was observed that a

Temperature	20°C, 40°C, 60°C, 80°C
Voltage	1 kV to 5 kV
RH	1-3%, 50%, 90%

Table 2.4.1: Design of experiment for electrical test

couple of hours of discharge at the temperature corresponding to the temperature of interest yielded the same results.

Samples are typically kept under discharge for a minimum of 5 hours; i.e. 1 hour for temperature modification, plus 4 hours to ensure the stabilization. Frequently, the stabilization and discharge process extended one overnight.

2.4.1.3 Measurement parameters and program

A resume of the test parameters is found in Table 2.4.1. The chosen voltage program is referred to as "1 hour - 1 hour," which signifies 1 hour under a step voltage followed by 1 hour of short-circuit (where the voltage in the high-voltage source is set to zero). We can also refer to is as Polarization-Depolarization cycles (PDC) of 1 hour each. Only one exception has been made for the dry epoxy composite at 20°C, in which a 8h/8h program was executed (more details in subsection 2.5.6).

The specific voltage level for each sample is adjusted to achieve electric fields ranging from 250 V/mm to 10 kV/mm, with the focus of the thesis relying on the 1-5 kV range, which is the range in which the MVDC insulator is supposed to be applied. Four temperatures were selected: 20°C, 40°C, 60°C, and 80°C. Typically, the test starts at the lowest temperature and the lowest voltage level. Three relative humidity (RH) levels were considered: 1-3% RH, 50%, and 90%. In relevant cases, other temperature and RH values were also examined. In summary: the sample is installed, discharged, possibly re-conditioned, and just then the electrical test starts. Figure 2.4.3 displays an example of a voltage program at four distinct voltage levels.

The Figure 2.4.3 presents an example of signal obtained from a protocol consisting of 2 distinct temperatures, at which 6 voltage levels are tested. The pre-discharge current is not shown, and all the signal is presented in absolute value in order to provide comparable visualization of discharging currents. The conduction current is obtained by the sum of the current at the end of 1 hour of charging, and the end of the following 1-hour discharging. This conduction current is applied to calculate the current density. The entire testing process can be as long as a month, as indicated by the data provided in Table 2.4.2. The most critical step is the sample conditioning prior to the electrical test, varying broadly according to the material's water sorption kinetics. This raises the question of whether our current protocol is excessively stringent and if there is room for reducing the duration of these tests. Some of these questions will be addressed in the section 2.5.

2.4.2 Space charge measurements

2.4.2.1 Set-up

Space charges were quantified through the laser-induced pressure pulse (LIPP) method. It involves the generation of a pressure pulse by a laser source (Nd: YAG laser) with a wavelength of 1064 nm, in the infrared. It emits a 6 ns pulse with energy

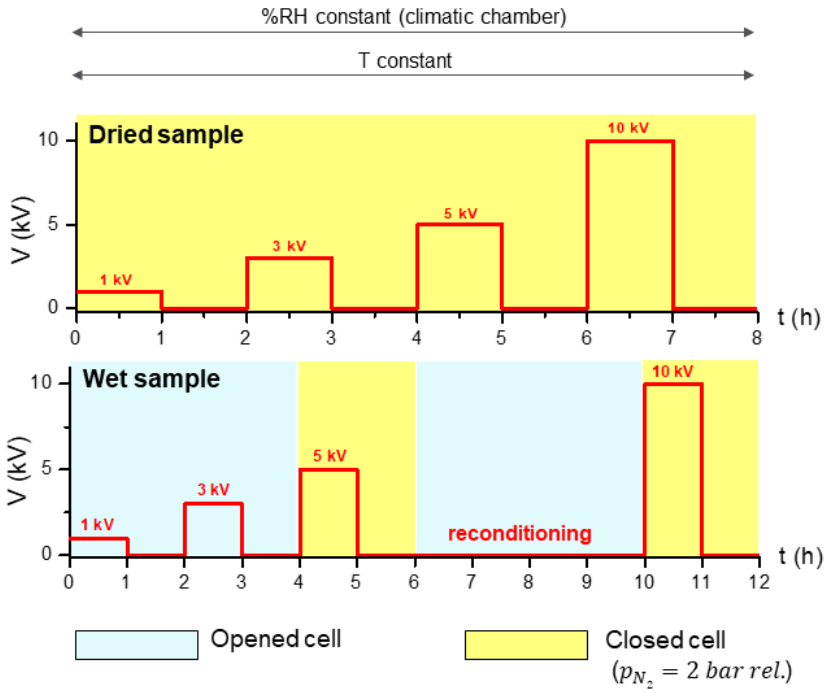

Figure 2.4.3: Examples of voltage programs for dried and wet samples.

of 450 mJ and a beam of 8 mm via a compartment having black ink that absorbs all the energy and propagate the pulse through the counter-electrode, and the sample thickness, as illustrated by Figure 2.4.5. This process results in the generation of a signal, either in voltage or current, that is directly proportional to the accumulated charge, measured with a 50 Ω input impedance of an amplifier (amplification 40 dB, bandwidth 400 MHz) and digitized in an oscilloscope (bandwidth 500 MHz). The limit of the measure is around 0.1 C/m^3. By analyzing this signal over time, we can derive information regarding the charge distribution across the thickness of the sample, ultimately allowing us to infer details about the field distribution. The voltage has been applied with a 20 kV SRS HV source (model PS 375 for positive polarity, and PS 370 for negative one).

The measurements were conducted using samples conditioned similarly to those employed for I-V measurements, with only two distinctions: the size of sputtered electrodes (40 mm and 33 mm in diameter for LIPP measurements) and the lack of relative humidity (RH) control, as the test cell is installed in an oven without such regulation. Potential water losses during the test are minimized by the cell configuration, which seals the sample. All other steps leading up to sample installation remained unchanged, including sample dimensions. The complete experimental setup is illustrated in Figure 2.4.6.

2.4.2.2 Data acquisition and treatment

The calibration, volt-on and volt-off measurements, and all the data treatment strategy is reproduced from the Hoan's work [81] and adapted by the author into a Python code. It can be summarized on the following steps:

1. **Installation:** The conditioned sample is installed in the test cell, which is

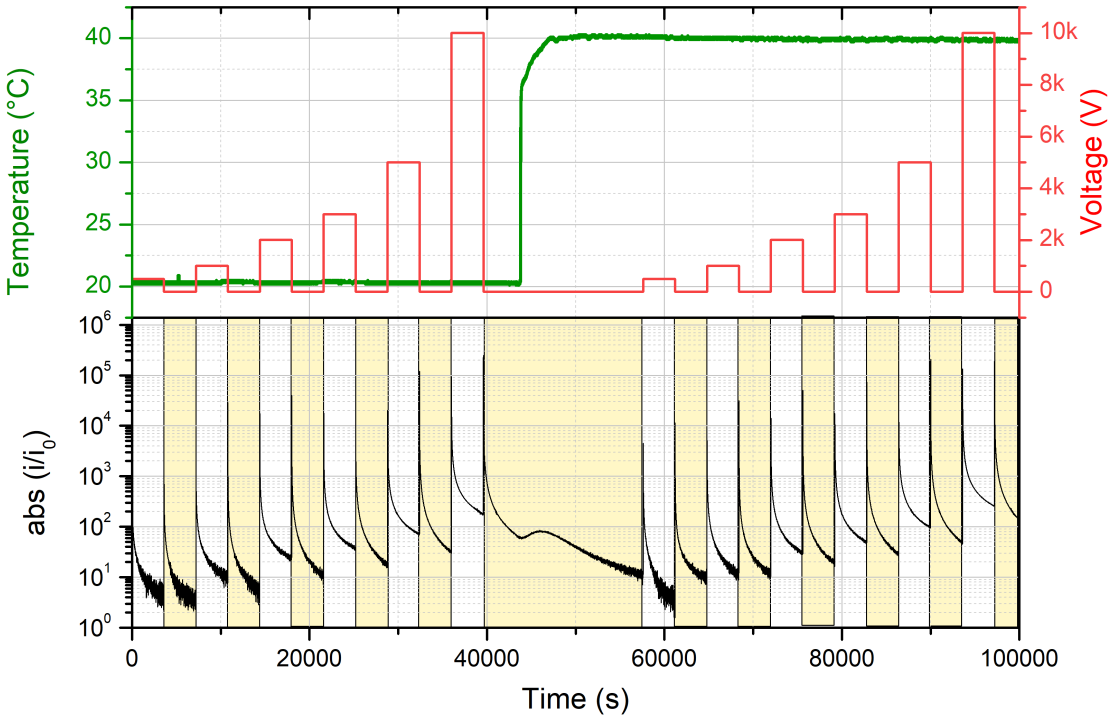

Figure 2.4.4: Example of dry sample of epoxy tested at 6 voltage levels and 2 temperatures.

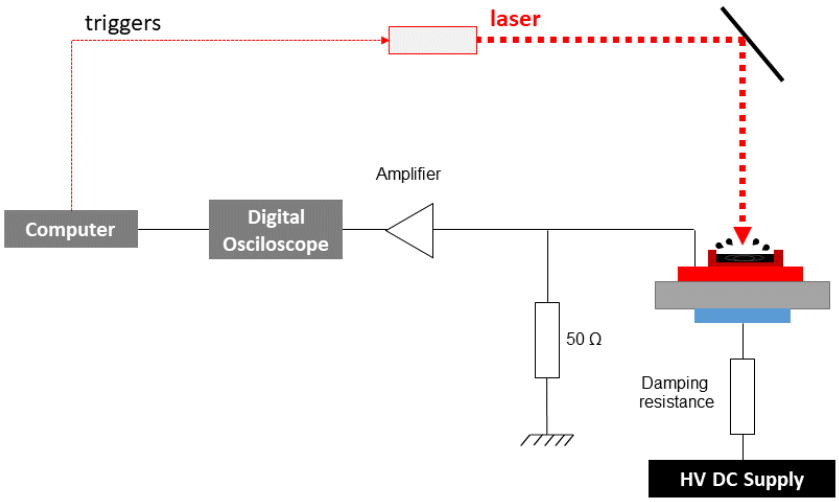

Figure 2.4.5: Scheme of the LIPP method.

Step	**Silicone**	**Epoxy (dry)**	**Epoxy (90% RH)**
Molding	0	72	72
Drying	48	336	336
Hydration	24	0	120
Sputtering	1	1	1
Discharge & Stabilization	5	5	5
Electrical test (5 voltage levels)	10 - 55	10 - 55	18
TOTAL	***88 (≈ 4 days) - 133 (≈ 5,5 days)***	***424 (≈ 18 days) - 469 (≈ 20 days)***	***552 (≈ 23 days)***

Table 2.4.2: Quantity of hours spent in each step of sample preparation, testing, and treatment. The shortest time-length for the electrical test represents 1 temperature, and the broader one, 4 temperatures.

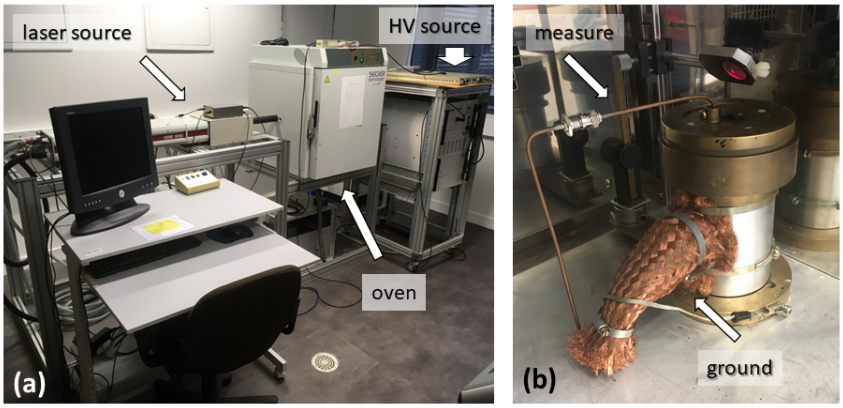

Figure 2.4.6: View of the test apparatus with indication to the laser source, HV source, and oven (a); and view of the oven inside.

inside the oven. The system stays 4 hours in thermal equilibrium prior to the test.

2. **Calibration curve:** A voltage is applied (from the SRS HV source). Immediately after the application, a first signal is acquired. This is the calibration signal. One example of en entire signal for a dry silicone rubber with gold sputerring on both sides is represented in Figure 2.4.7(a). The input and the output can be easily determined. The speed v is calculated considering that the time distance of the maximum of each peak t_{total}, which should be proportional to the sample thickness d_{total}. Thus, the acquisition time (in μs) can be transformed in distance or position d (in mm) with the equation $d_i = v.t_i$. The result can be seen in Figure 2.4.7 (b).

3. **Calculating correction coefficients:** Since the calibration curve is obtained just after the voltage application, we consider that there is no distortions due to charge injection or intrinsic space charges. However, there are distortions coming from the mechanical attenuation of the wave propagation; the cathode and anode peaks have different sizes, so they have to be corrected so as the

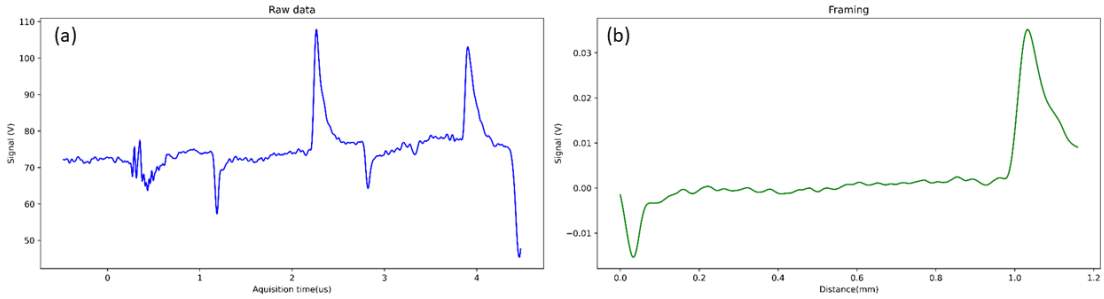

Figure 2.4.7: Signal obtained from the oscilloscope (a), and signal framed, with time converted to distance (b) for a dry silicone rubber with gold sputtering on both sides, at 40°C, and $V_{app} = 5000V$.

integral must be zero. It means that, in our data treatment, the surface areas, or the integral of each calibration peak is corrected in order to have the same value. This is done by two equations: the corrected signal $u(t_i)$, equation 2.4.1, which considers the propagation time t_i and the speed of propagation v, and the attenuation coefficient α_a obtained with equation 2.4.2. The surfaces of input and output peaks S_{input} and S_{output} respectively are obtained from the integration of each peak.

$$u(t_i)_{corrected} = \frac{1}{e^{-\alpha_a.d_i}}.u(t_i) = \frac{1}{e^{-\alpha_a.v.t_i}} \tag{2.4.1}$$

$$\alpha_a = \frac{1}{d} ln \frac{S_{output}}{2.S_{input}} \tag{2.4.2}$$

Remark that in equation 2.4.2 the surface areas are related by a factor equals to 2. The acoustic impedance of the air being much smaller than polymers, it is expected an output peak at least 2 times bigger than the input one. The reason why we are considering mostly the surface area instead of the peak heights is because we know that the output peak will also spread widely due to energy absorption during wave propagation. Taking the surface area instead of the height enable us to consider this distortion. In the case of that silicone rubber of Figure 2.4.7, the speed has been found as $0.928mm/\mu s$ and the attenuation coefficient as $1280m^{-1}$. Indeed, this procedure lead us to convert the original signal of voltage as a function of time, in voltage as a function of distance or position. The corrected signal of Figure 2.4.7 is shown in Figure 2.4.8.

4. **Volt-on and Volt-off measurements:** The sample remains under voltage. Signals obtained under voltage are called "Volt-on measurements". Aiming to make eventual space charges more visible, the sample is put under short-circuit for a short period of time. Measures obtained just after this short-circuit are called "Volt-off measures". If space charges are accumulated in the material, they will create counter-charges (mirror charges) in the electrodes which will be visible in the Volt-off measurement.

5. **Corrections and post-treatment of Volt-on and Volt-off measurements:** Once acquired, all Volt-on and Volt-off measurements are corrected

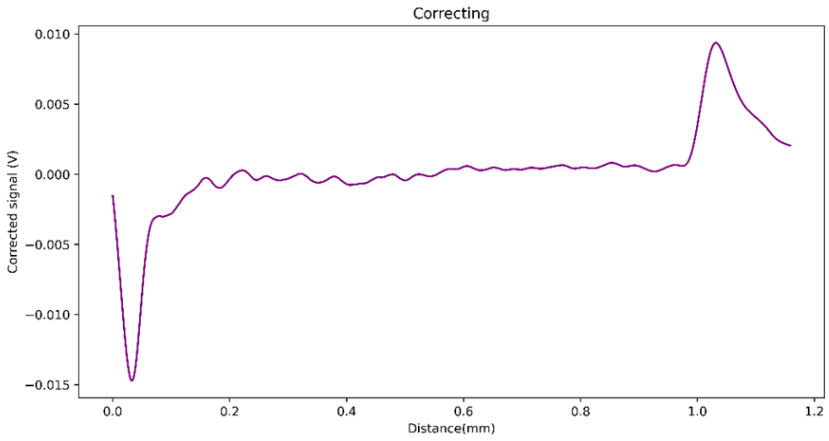

Figure 2.4.8: Corrected signal of calibration measurement for a dry silicone rubber with gold sputtering on both sides, at 40°C, and $V_{app} = 5000V$.

based on Equation 2.4.1 with coefficients coming from the calibration measurement. The voltage is converted in charge density based on equation 2.4.3, which takes into account the signal as a function of the time $u(t)$, the speed v and a factor k. This factor, Equation 2.4.4, considers the surface charge density (σE_{total}) and the surface of the input peak (S_{input}). The equation 2.4.4 is rooted on the first Gauss' law, so as the equation to calculate the electric field through the thickness (the sum of the charge density divided by the permittivity). An example of treated data is shown in Figure 2.4.9.

$$\rho(z) = k.u(t).\frac{dt}{dx} = \frac{k}{v}.u(t) \tag{2.4.3}$$

$$k = \frac{\epsilon.V_{app}}{d_{total}.S_{input}} \tag{2.4.4}$$

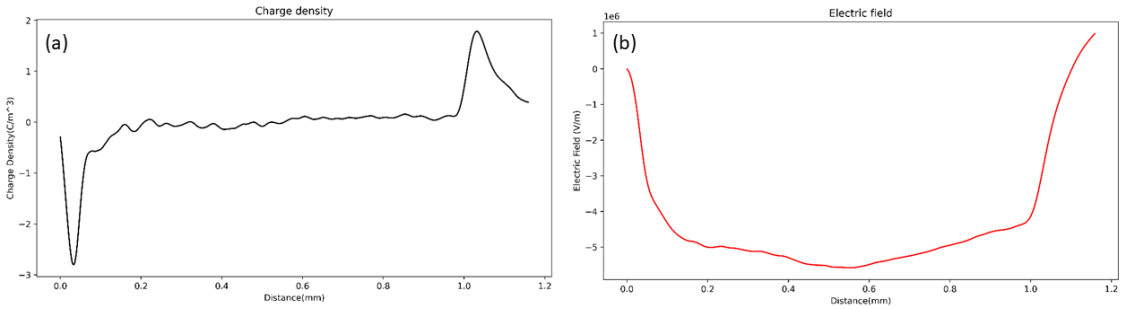

Figure 2.4.9: Example of LIPP signal converted to charge density (a) and electric field distribution (b). The curve is the same obtained from the calibration measurements of a dry silicone rubber with gold sputtering on both sides, at 40°C, and $V_{app} = 5000V$. These figures can be taken as a first "Volt-on measurement", a "photograph" of the sample immediately after the voltage application.

2.5 Questionning sample preparation and measurement protocols: some answers provided by the experiments.

This section will provide some case scenarios that prompted the author to tailor the procedure described in sections 2.3 and 2.4.1.2.

2.5.1 Why should we care about sample fabrication?

Two 1-mm thick plates of pure silicone rubbers, i.e. without any filler, produced from the same raw material, have been fabricated by gravitational molding and curing in oven at 160°C, but with different curing times: sample A has been cured for 1 hour with no post-curing; and sample B, 6 hours with 8 hours of post-curing at 80°C.

These plates have been shaped into disks of 70 mm of diameter. Figure 2.5.1(a) shows the polarization as a function of time for such samples when exposed to 1 kV during 1 hour of test. It can be noted that the current of sample B at the end of 1 hour differs from the current of the sample A by a factor equals to 2.15. In addition, the higher the voltage level, bigger is this difference: when tested at 10 kV/mm, the current of sample B was 10.57 times higher than sample A. This difference is broadening because, as presented in Figure 2.5.1(b), the apparent conductivity of sample A decreases with voltage, almost if the sample A were liquid-like, while sample B has a conductivity that increases with voltage as most of solid dielectrics.

The difference of samples being attributed to the curing time, a first hypothesis concern about different cross-linking degrees, with sample B having a higher cross-linking degree than sample A. A second hypothesis concern about the proportions of raw materials: as it is a bi-component silicone, if the quantity of each raw material is not well dosed, the final product shall deviate from an elastomer and

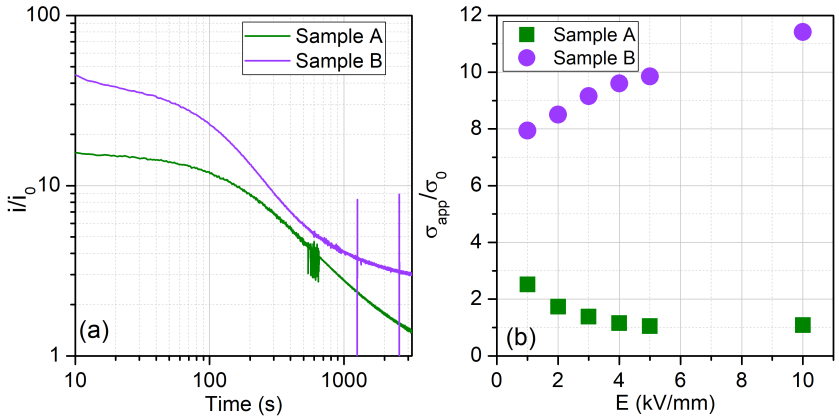

Figure 2.5.1: Relative electric current as a function of time for two samples of silicone rubber at 40°C (a), and the apparent conductivity of such samples as a function of field at 40°C (b). Sample A has been cured at 160°C for 1 hour, and sample B for 8 hours with 6 hours of post-curing at 80°C.

give a gel-like material. A third hypothesis concerns about the demolding: neutral detergent has been applied on the mold, further dried before molding. The presence of detergent in the bulk and the impact of it on surface is unknown. In any event, what has to be pointed out is that the same material can present contrasting results as a consequence of distinct fabrication means. If the fabrication is unknown, the understanding is limited.

If the experimenter has the capability to create its own samples, it is imperative to furnish comprehensive information regarding the fabrication process. This is crucial for ensuring the reproducibility of sample fabrication. Setting aside concerns related to confidentiality, it should be recognized that even minor alterations in the fabrication process can lead to significant variations in results. This variability can contribute to challenges faced by the scientific community in reproducing identical outcomes from "similar" materials.

2.5.2 Why discharge the sample prior to the electrical test?

Some authors, such as Kuchler [208], and Lisowski [209], emphasize the significance of stored charges in current measurements and resistivity. However, it remains unclear why these charges are not neutralized during the test, and their origin is not well-defined. Possible sources could include sample fabrication, charge exchange during contacts, or friction, among other hypotheses.

During first exploratory measurements, it was found that a discharge was about to reduce the conduction current. Still, at that time, precise control over temperature and relative humidity was not well-established. As the experimental protocol took shape, the "pre-discharge step" became an integral part of the process. By any means, the sample - grounded - had to undergo a waiting period of several hours to attain thermal equilibrium. Consequently, we are not able to provide the real impact of such step in the measure without further analysis.

Due to the software's capability to record current only when a voltage is applied, deliberate discharging of the samples was undertaken. In other words, a zero voltage was applied to prompt the software to record data during thermal equilibrium, allowing for the detection and verification of any potential anomalies possibly taking place prior to the test.

2.5.3 Why control the water content?

As detailed in the literature review, some authors showed that the water content could affect drastically the current measured. As a matter of fact, we noticed that the conduction current decreased as the annealing time increased. Heating the samples leads to dry it, and the reduction of current could be related to a reduction of water content.

So, a question raised: what is the impact of water content? As the water content of a fresh sample is unknown, a protocol for conditioning samples has been designed. This is the protocol described in sections 2.3.2 and 2.3.3.

During drying step, the total weight loss will depend on the previous water content, which depends on fabrication and the environment of pre-conditioning. In a preliminary study, three different samples of silicone rubber have been dried and a lost of $0.85 \pm 0.03\%$ in weight had been observed. A similar test was conducted

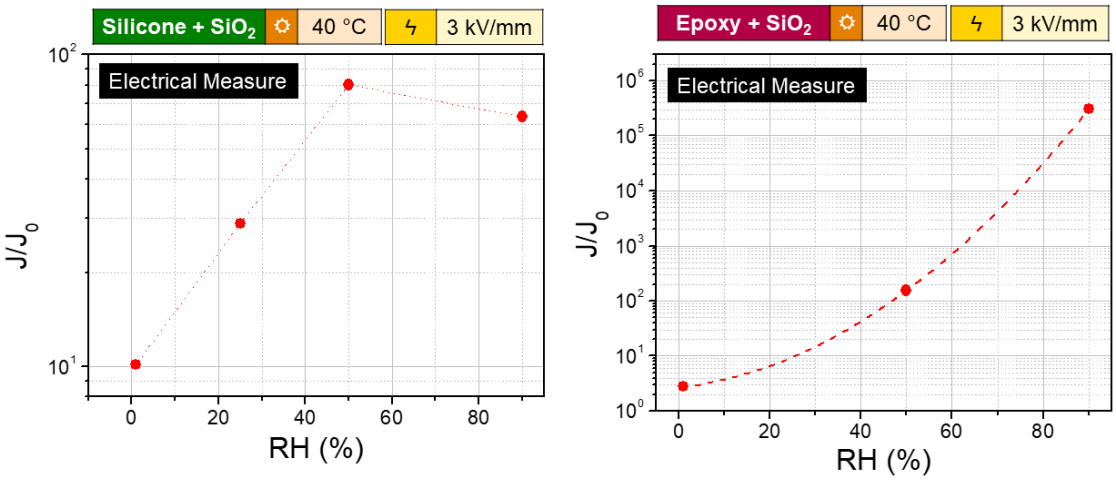

Figure 2.5.2: Relative moisture absorption as a function of the RH of conditioning for a silicone and an epoxy sample, associated with the relative current density as a function of RH of conditioning and testing.

with epoxy samples, and a loss of 0.47 ± 0.01% was identified.

In a second step, samples were humidified in the environment of climatic chambers that were already stabilized at the controlled temperature and relative humidity (RH) of the following electrical test. As it will be explained in details in chapters 3 and 4, at the highest RH of the study (90%), the weight of the silicone composite increased 1.2%, and epoxy (reported to the matrix) 1.1%.

Once the sample dried and humidified, the electrical test are performed at the same conditions to avoid having a new metastable sample. The current density at 90% RH for silicone samples is in average 5.3 ± 1 times larger than the dried sample at 40°C, as it can be seen in Figure 2.5.2. In addition, it looks like the increase in current slows down when 1% of water content is attained. More detail about the water absorption impact of this material will be discussed in chapter 4. In the case of the epoxy composite (Figure 2.5.2), the samples conditioned at 90% RH presented a current density 3-4 orders of magnitude larger for the same voltage level at the same temperature. This huge difference between dried and wet samples underlines the impact of water in the main conduction mechanism. These aspects are explored in chapter 3.

2.5.4 Why care about electrode material?

The Schottky injection considers the contribution of the materials from the contact through their work functions. In many cases, however, the impact of the work function is not clear, but as seen in the literature (section **??**), the nature of the metal and their symmetry remains a key factor on the electrical test.

The impact of the electrode material will be discussed in detail for each dielectric in chapters 3 and 4, but it is worth to anticipate here that, for the case of the epoxy resin, the electrode materiel does not seen to affect the current measured. In contrast, for the silicone composite, there is an impact that ranges by a factor 12 at 1 kV/mm and 3 at 5 kV/mm. Both cases can be seen in Figure 2.5.3.

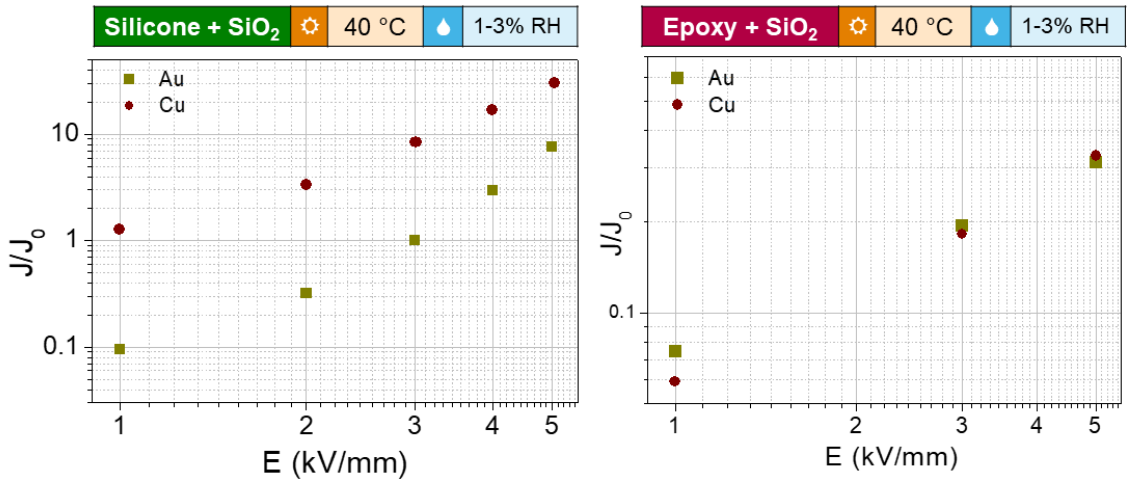

Figure 2.5.3: Relative current density as a function of electric field for a dry silicone and a dry epoxy composite, both coated by 200 nm of gold or copper.

2.5.5 How much strict should we be about temperature and RH control?

The conductivity is very sensitive to the temperature, and temperature changes during the test can drive to misleading results. At the same time, changes in the RH can force the material to loose or gain water, and again, changes during the test can also lead to misleaded results. Two subjects merit attention: the measurement at room condition, and the temperature or RH stabilization itself.

2.5.5.1 The ambiguity of room temperature:

We are always tempted to do experiments at the room temperature (i.e. between 20°C and 25°C). The impact of temperature seems to be well acquired by the scientific community, and the exponential relationship written as an Arrhenius-like equation is widely known. For the epoxy resin of this study, the current densities obtained at 20°C and 25°C under 3 kV/mm differ by a factor 1.9 in dry conditions (1-3% RH), 2.7 at 50% RH, and 3.4 in wet conditions (90% RH), as it will be see in chapter 3.

It also has to be pointed out that the ambient temperature can vary from the room temperature, and that the range of ambient relative humidity can be wide, both of them being continuously unstable along the year. As an example, as showed in Figure 2.5.4, along six months between summer and winter, the conditions of one of the ambient-controlled laboratories where the test has been performed presented a variation of humidity from 14.7%, to 61.7% in summer. If the same epoxy samples were in equilibrium with these coupled values, the current shall differ according to a factor equals to 32. It is worth to mention that climatic chambers and ovens in the room may even decrease the ambiant humidity, and increase the temperature, as recorded in February.

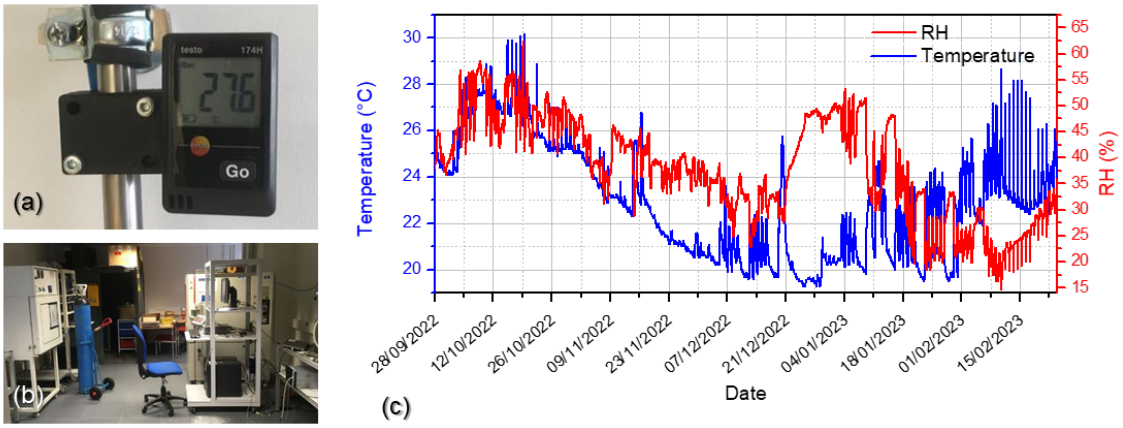

Figure 2.5.4: Photo of the room temperature and RH test probe (a) applied in one of the lab rooms (b) and the result of temperature/RH acquisitions within 6 months (c).

2.5.5.2 The risk of testing a meta stable sample

Samples take time to achieve equilibrium with environmental conditions. As it can be seen in Figure 2.5.5, the water uptake is mostly impacted by RH, with temperature increasing the kinetics of water absorption. When a dry sample is conditioned in a chamber previous stabilized at 30°C and 25% RH, it took 10 days to achieve weight stabilization; the water content did not change when temperature is increased to 40°C, and 60°C, and the weight measured were more unstable because the equipment sensibility when the material is warm (see section 2.1.5). At 60°C, it took 5 days more to achieve a new equilibrium at 50% RH. As will be show in chapter 3, the current density of this epoxy at 60°C varied one order of magnitude between conditioning at 25% RH and 50 % RH.

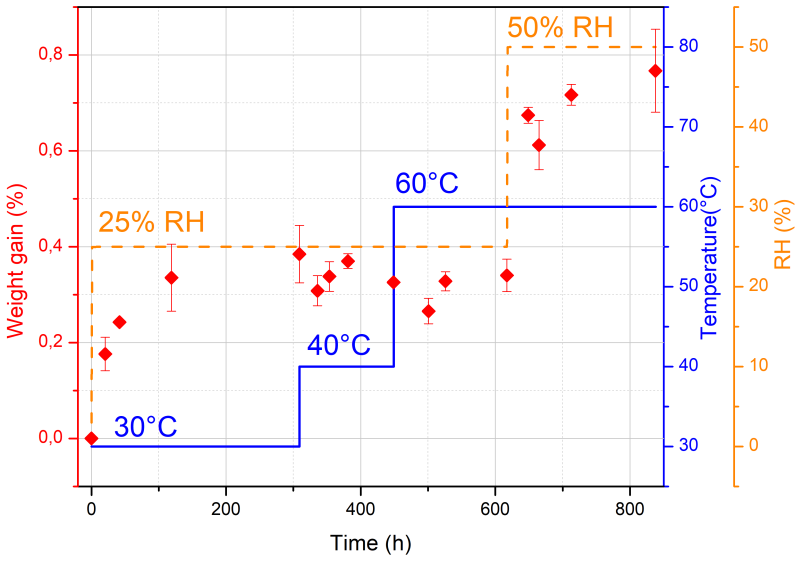

Figure 2.5.5: Weight gain (reported to the matrix) of an epoxy resin under many coupled temperature-RH changes. Samples are dried at the beginning.

If the sample is not properly conditioned and if the RH is not controlled during the electrical test, what is measured can be issued from a metastable material. Samples are continuously losing and reabsorbing water following environmental changes.

An exaggerated illustration: To put this effect on evidence, one epoxy sample conditioned at 40°C and 90% RH was tested at 60°C with no control of RH on purpose. In such conditions, as soon as 60°C was achieved, the Rotronic RH test probe indicated a RH stabilized at 5%. Remark that this RH at 60°C depends on the effective RH of the premises. Since the electrodes are around 10 mm smaller in diameter than the sample, the sample's edge is expected to dry, so as the bulk over time. There will be an heterogenous distribution of moisture inside the sample, with the center being more hydrated than the periphery.

As soon as temperature stabilized, a series of consecutive 10-hour PDC cycles has been performed, all of them with volt-on equals to 3 kV. Figure 2.5.6 shows the continuous decrease of the polarization currents during volt-on steps. If the conduction current or the conductivity were about to be calculated based on the data at the end of each cycle, a variation of 3 decades would be found between the first and sixth cycles.

At the end of cycles, the sample lost 83% of the total amount of water absorbed during conditioning, even if it was covered by the electrodes on the major part of its surface.

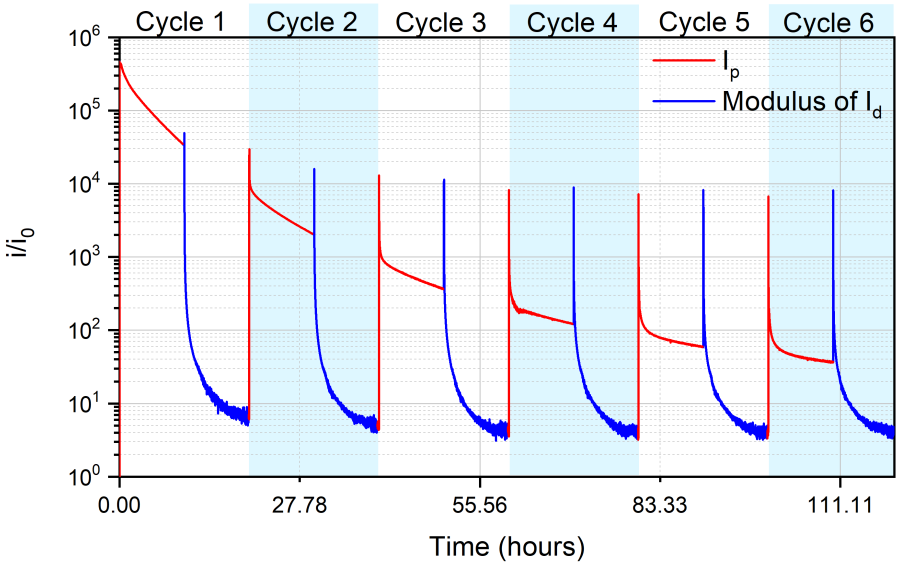

Figure 2.5.6: Relative current as a function of time for an epoxy sample conditioned at 40°C and 90% RH and tested at 60°C, with PDC cycles of 10 hours each, 3 kV/mm at each polarization cycle.

2.5.5.3 The risk of a negative sum of currents

For better thermal control, tests should be performed at isothermal conditions, but sometimes the temperature takes time to stabilize, or it fluctuates around a given value. Figure 2.5.7 shows an experiment that started 2 degrees Celsius before the

desirable 40°C had been achieved. The temperature displayed is the one from the thermocouple that goes inside the cell. We do not know the difference between the temperature in the sample and the one of the thermocouple. Because of the low thermal conduction of the insulator, some delay is expected. The result shows a discharge current (in modulus) higher than the charge one, leading to a counter conduction current; i.e. a conduction current with the opposite signal of the applied voltage.

The authors do not believe that this material has special features leading to the creation of energy during discharge; on the contrary, in a first hypothesis, as the discharge is taking place at a higher temperature, the rate of resorption can be higher than absorption, and space charges (especially if some of them are in deep traps) will be evacuated faster. We remarked that such phenomenon has only been observed at low voltages.

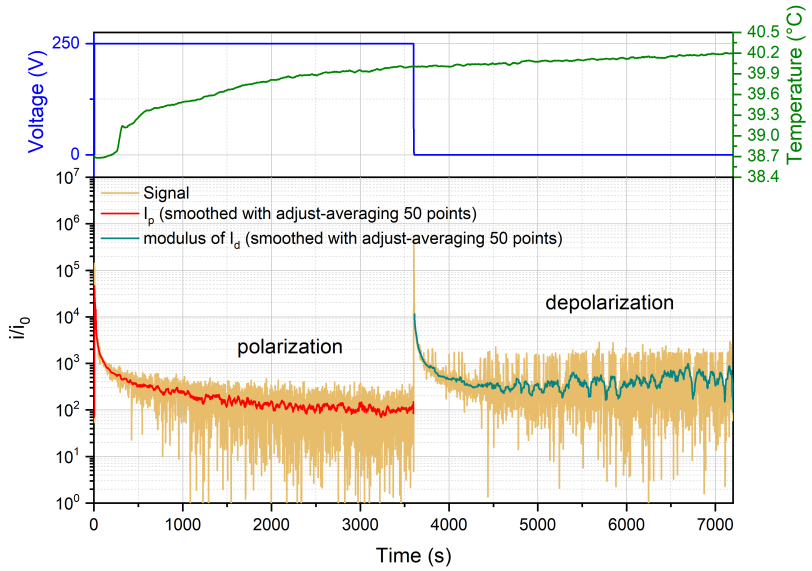

Figure 2.5.7: Relative current as a function of time for a sample tested at 250 V with a PDC cycle of 1 hour. Dried bilayer sample.

2.5.6 Is the 1 hour-1 hour test the best time length?

It depends on what we want. Some works deal with the inaccuracy related to measurement time [210].

For the silicone composite of this study, PDC cycles of 1 hour have been enough to achieve a trustful result (even at 20°C), since values obtained with longer tests remained the same (Figure 2.5.8). Actually, cycles of 30 minutes should be enough to obtain the same result. The additional 30 minutes stressed the material unnecessarily.

That's not the case of the epoxy, as seen in Figure 2.5.9. At the lowest temperature (20°C), humidity (1-3% RH), and voltage (1 kV), the sum appears stable initially but gradually decreases over time (Figure 2.5.9(a)). The current obtained by summing absorption and resorption currents after 8 hours is only half of the value obtained from the 1-hour test and remains unstable. However, the stabilization rate

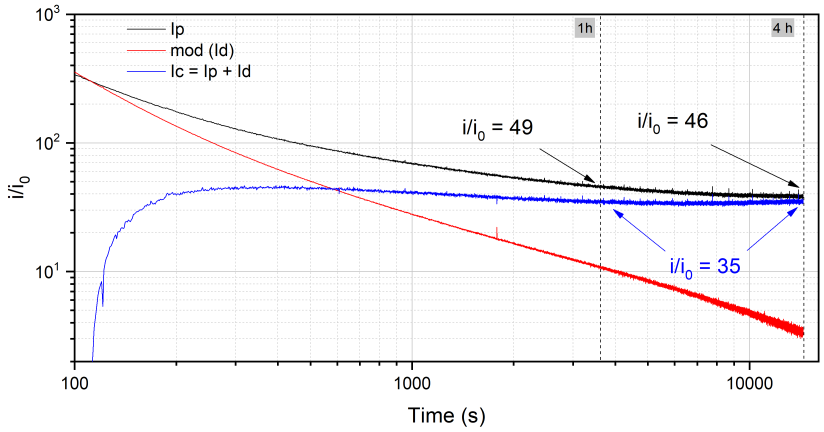

Figure 2.5.8: Relative current as a function of time for a dry silicone composite at 20°C and V = 1 kV. The value obtained with PDC cycles of 30 minutes, 1 hour, and 4 hours are the same.

improves with higher temperatures, electric fields, and water uptake. As shown in Figure 2.5.9(c), at 40°C, the sum decreases by 35% from 1h/1h to 8h/8h. For 20°C and 50% RH (Figure 2.5.9(b)), as well as for 20°C and 90% RH (Figure 2.5.9(d)), the sum current appears stable over 1h/1h and even matches the absorption current.

Contrary to appearances, as suggested in Figure 2.5.9(a), the stability of the sum does not guarantee long-term stability. We acknowledge, however, that tests longer than 1h/1h or 8h/8h might be impractical for comprehensive parameter scanning, and we accept the risk of potential overestimations at lower temperatures/fields/humidity with 8h/8h measurements.

In summary, the 1h/1h test appears suitable for both materials in the study under most test conditions. However, under specific conditions, such as at 20°C and lower fields, the 8h/8h test was employed.

2.5.7 Are the conduction current values repeatable?

Each experiment has been repeated three times with a different sample each time, with them conditioned similarly to each other. The values fluctuates within 1.5 times the average of these 3 measurements. Only the values at lower temperatures and lower voltages (20°C and 1 kV/mm) presented a deviation sometimes equal to 3 times the average, due to a higher noise and the smoothing strategy.

2.5.8 Additional details that has to be highlighted

2.5.8.1 Evaluating the off-set:

Many events coming from the test apparatus can lead to inaccuracies and uncertainties during the measurement. Some authors [210, 163] have pointed out that the DC power supply may produce an offset that would mistakenly increase the value of electrical current. This biased current should then be subtracted to both the polarization and depolarization currents. In this study, no offset has been identified.

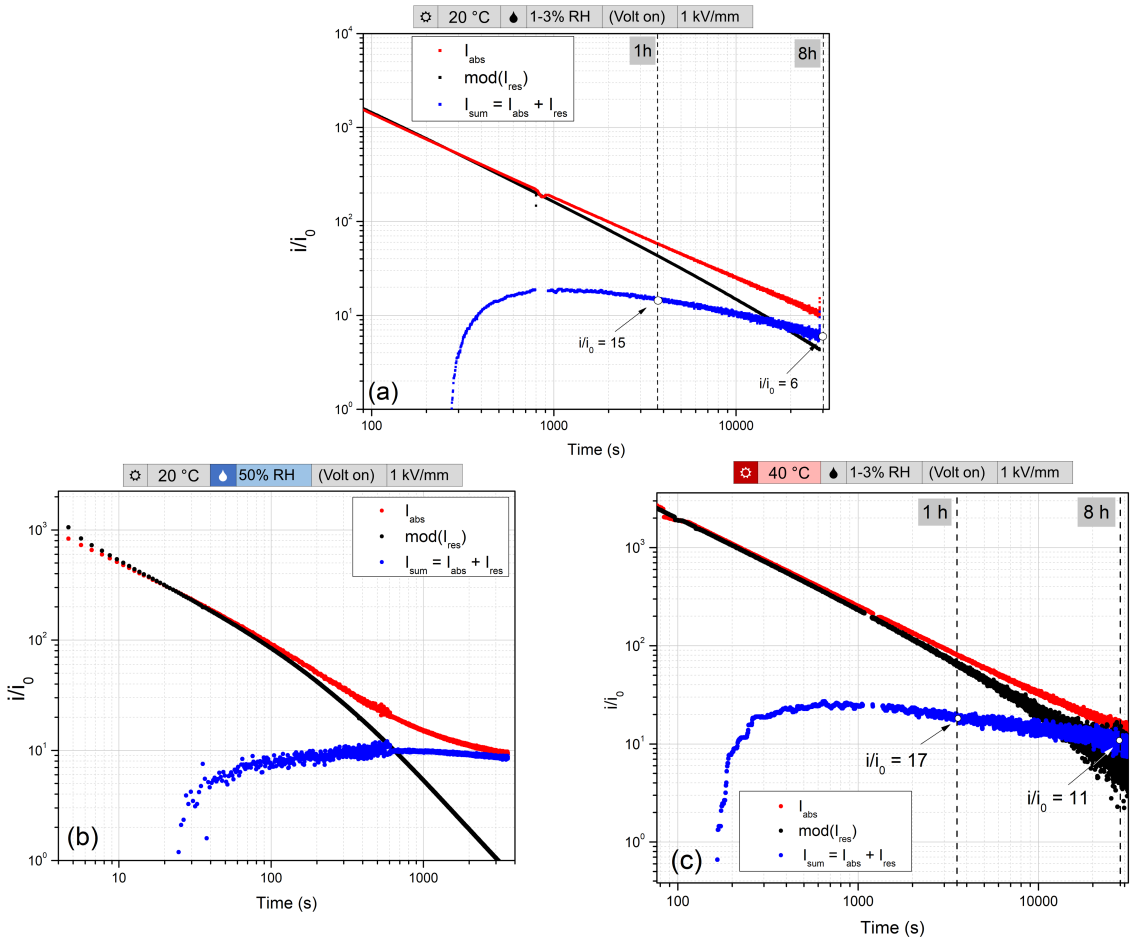

Figure 2.5.9: Relative current as a function of the time for epoxy samples with Volt-on = 1 kV. Parameters: (a) 20°C and 1-3% RH. (b) 20°C and 50% RH. (c) 40°C and 1-3% RH.

2.5.8.2 The discrepancy of digital filtering and smooth:

Kuchler [208] advised about the importance of having a low pass filter to reduce the noise coming from the HV source. At the beginning, there was no filter in the set-up, and the raw data had to be smoothed. But the smooth strategy can change considerably the conduction current value, as illustrated by Figure 2.5.10 that compares a 8h measure (just polarisation or absorption current) with an 1h/1h in which a filter was applied, both cases for a dry silicone rubber sample at 40°C. The 8h/8h measure presented a noise so important that, depending on the smooth strategy, the value of conduction current at the end would change over 1 order of magnitude. It does not happen with the sum of currents with the 1h/1h measure, that was more stable over the time of , even if the sum has been smoothed too (adjacent-average of 50 points). One interesting feature is the fact that the conduction current obtained with the 1h/1h test only matched with the 8h measure if higher values of the noisy signal are considered.

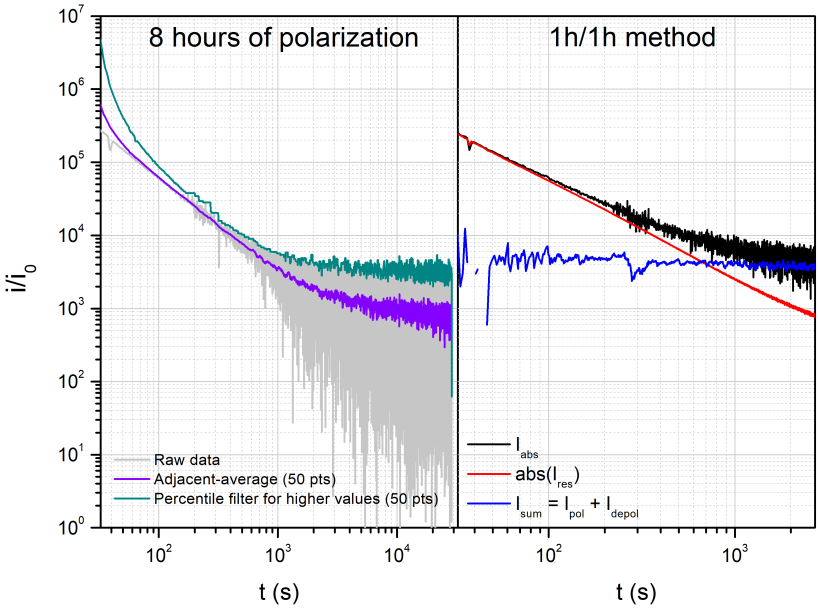

Figure 2.5.10: Smoothed relative current as a function of time for two similar silicone rubber samples measured at 1 kV/mm, 40°C and 1-3% RH.

2.5.8.3 The challenges of testing at extreme conditions:

The health of test apparatus can be out of control at extreme parameters. More than once, when 80°C and 90% RH have been set to the climatic chamber, the RH increased faster than the temperature stabilization, so water has condensed inside the cables connecting the cell to the power supply. Many times the current profiles showed an anomalous behaviour, with a resorption more important, in module, then the absorption. In many cases, the measured failed after some hundreds of seconds. These events being systematic at 80°C and 90% RH, this set of parameters has been excluded from results.

2.6 Partial conclusions & perspectives

The process of electrical measurement, as a means of characterizing a specific material, begins long before voltage is applied. Since conductivity is indicative of a material's structure and microstructure, it is crucial to carefully prepare the sample to gain a clear understanding of what will be tested. Often, more time is devoted to sample preparation than to the actual electrical testing itself. But it gives much more information to build clear structure-property relationships. With their in hand, it becomes easier to interpret the results of real-world components, such as cable and bushing assessments.

For the materials under study, after fabricating and shaping the samples, the following steps were undertaken:

- Drying: to put all the samples on equal footing.
- Hydration at determined temperatures: to control the quantity of water that the sample sorbed prior to the electrical test.
- Sputter deposition under secondary vacuum: to ensure a good contact and avoid large air layers between the electrodes and the insulator.
- Installation and discharging.
- During the electrical test, accurate temperature and RH stabilization.

The selected electrical test involved subjecting the samples to PDC cycles lasting for 1 hour each, with one exception at 20°C and under 1-5 kV/mm for the epoxy resin; for this case, 8 hour cycles were more appropriate. These tests were conducted under the same temperature and relative humidity (RH) conditions as the conditioning process.

These steps have been designed based on learnings gained after many attempts to achieve repeatable current-voltage measurement results of silicone rubbers and epoxy resins. It is noted:

- For elastomers and thermosets, the influence of sample fabrication and potential risks of the completion of curing process during the electrical test. It has a huge impact on the values measured, so as in the conduction mechanisms.
- The importance of having the water sorption controlled, specially for materials with hydrophobic matrix, as the silicone.
- The influence of the electrode material on the injection, and the insights obtained from testing the same material with different electrode systems.
- Verifying the best time-length for each PDC cycle according to the temperature, RH, and material.

Perspectives: Some additional parameters have been ignored or not fully investigated, and authors are not able to conclude about the impact of them.

- The impact of possible charges stored in the sample prior to the test.

- The impact of mechanical pressure made by the electrodes, especially for elastomeric samples, as following changes of the compression set. An attempt to measure the pressure and some clues are detailed in the Annex **??**.
- Possible changes during storage, as degradation or migration.
- The impact of thickness in the J-E plot.

3 The monolayer of epoxy composite

This chapter presents the results and investigations concerning the epoxy composite discussed in Chapter 2, and it is structured into two main sections: water sorption and electrical tests.

3.1 Water Sorption of the Epoxydic System

The objective of this section is to comprehend the process of water sorption over time, and under stabilization. As evidenced in the literature review (Section 1.2.4), valuable insights can be gleaned from measuring water uptake. Furthermore, given the primary goal of controlling water content for electrical tests, it is imperative to demonstrate that the water quantity within the insulation is effectively stabilized at specific temperatures and relative humidity (RH) levels. The estimation of the sorbed quantity is crucial for achieving this goal.

3.1.1 Results

3.1.1.1 Temporal Weight Gain

The water sorption has been accessed with timely-spaced weight measurements of initially dry samples placed inside a climatic chamber. A minimum of three samples have been used to the measurements, with results showing the average and the standard deviation.

Figure 3.1.1 shows the relative water absorption $\Delta m/m_0$ at 40°C and 50% RH as a function of the time. Considering the standard deviation of these measurements, one can say that five days should be enough to achieve a constant weight.

Previous studies have checked that in such unaged epoxy-compound with micro silica fillers, water is absorbed in the matrix (see literature review 1.3.1). Thus, relative water absorbed values are corrected to reflect the water content of the matrix rather than the mass uptake relative to the whole sample. As seen in chapter 2 (2.2.1.1), the compound is molded with 62% of fillers in weight.

3.1.1.2 Steady-state Weight Gain

A qualitative chart of water uptake at equilibrium has been designed based on gravimetric measurements, and presented in Figure 3.1.2. The amount of 1.4% of water

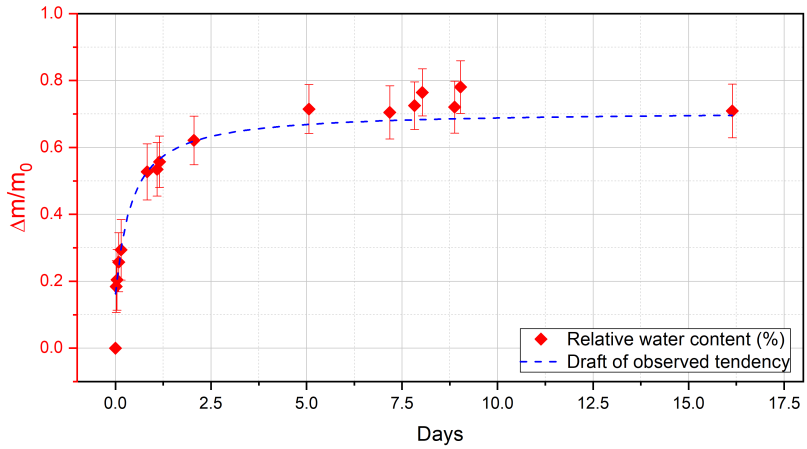

Figure 3.1.1: Water absorption of the epoxy composite as a function of time at 40°C and 50% RH for samples with 1 mm of thickness. The values are corrected to show the matrix content.

has been identified for the highest temperature-RH couple, which corresponds to a raw value of 0.45% of water uptake if the whole system is considered. The same data is re-plot in a 2D graph in Figure 3.1.3, that also let in evidence the increase of uptake with temperature and enables the investigation about the isotherm mechanism.

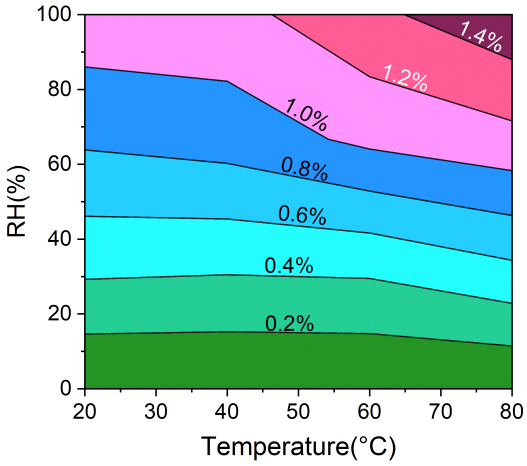

Figure 3.1.2: Chart of water content (%) at equilibrium reported to the matrix as a function of temperature (T) and relative humidity (% RH).

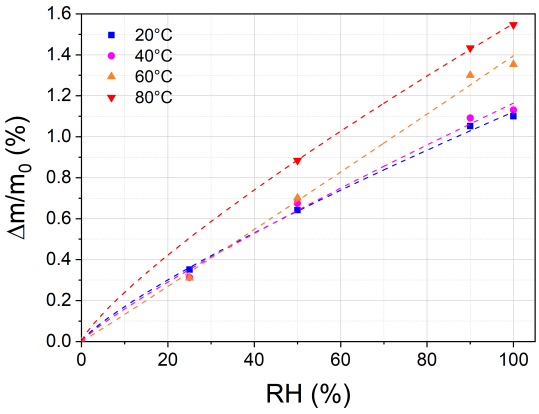

Figure 3.1.3: Water content reported to the matrix as a function of the relative humidity.

3.1.2 Discussion

3.1.2.1 Diffusion mechanisms

The results of Figure 3.1.1 enable us to calculate the diffusion coefficients. Both mechanisms (Fick's and Langmuir's) have been investigated, and both of the models agree with the results of Figure 3.1.1. The fitted curves are presented in Figure 3.1.4, they have been obtained numerically based on the method of the least squares.

Validation with Fick's law: When Fick's law is considered, a diffusion coefficient D_{Fick} equals to $3.10^{-12} m^2/s$ has been found. This value is in the middle of the one obtained by Brun [113] with a microcomposite at 80°C and 80% RH, which is around $1.10^{-11} m^2/s$, and the one calculated by Zou [211] also with a microcomposite, but at 25°C and 75% RH, i.e. $4.10^{-13} m^2/s$. Effectively, the diffusion constant following exclusively an Arrhenius law, it makes sense that at in intermediary temperature, the coefficients reach an intermediary level.

Validation with Langmuir's law: On the other hand, when a Langmuir's model is considered, the diffusion coefficient $D_{Langmuir}$ is around $1.10^{-10} m^2/s$, with α equals to 2.10^{-5} and β equals to 1.10^{-5}. We can not compare directly D_{Fick} and $D_{Langmuir}$, but it is worth to notice that α is the double of β, which suggests a bonding much more important than the debounding. In other words, an important portion of water molecules would remain attached to the matrix.

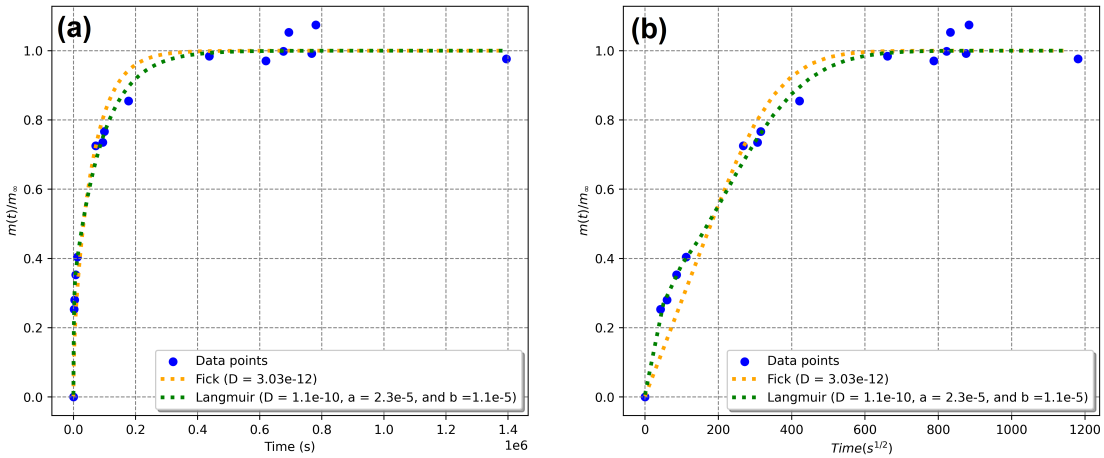

Figure 3.1.4: Water absorption as a function of the time (a) and the square root of the time (b) for an epoxy composite at 40°C and 50% RH.

Where the water can be attached? Remembering the literature review (1.3.1), and looking closely to the matrix structure (Figure 1.2.4), we find electronegative oxygens provided by the carbonyl group $(=O)$, hydroxides $(-OH)$, and some partial electronegativity coming from the oxygens attached to the $carbonyl/CH$, and $phenyl/CH_2$, the last one being less electronegative due to the domination of the non-polar phenyl. There is also the possibility of having hydrogen bridges with the siloxane backbone $(Si-O)$ coming from the silica.

All of these possibilities should make us privilege the Langmuir's model in detriment of the Fick's. As a matter of fact, if we examine the Figure **??**(b), the Lang-

muir's model seems to fit better the increase of water uptake. These conclusions would be in accordance with the epoxy/anhydride studied by Bonniau [212], for example. However, it's important to note that this choice remains somewhat subjective. Upon analyzing the standard deviation calculated using the method of least squares, the deviation for Fick's coefficient is 4.10^{-13}, while for Langmuir's, it is 4.10^{-11}. Both values are accurate enough to yield a deviation one order of magnitude smaller than the respective diffusion coefficient values. In light of this situation, for the sake of parsimony, we advocate for privileging the simpler model with fewer assumptions, which is the Fick's.

3.1.2.2 Water sorption isotherms

The first step to explore the sorption mechanism is to transform the data of Figure 3.1.3 in a curve of the sorption ratio θ as a function of water vapour pressure P. Applying the Equation 1.2.14 as sorption ratio, and extracting the pressure rate from the RH (Equation 1.2.1), the data is plot in Figure 3.1.5. At a first glance, the datapoints look less disperse than in Figure 3.1.3, as the calculus of θ normalize them according to the weight gain at $RH = 100\%$, based on the assumptions made in section 1.2.4.3. Because of this lower dispersion, one would be tempted to fit all the data with a linear equation and resume all the data in one single equation.

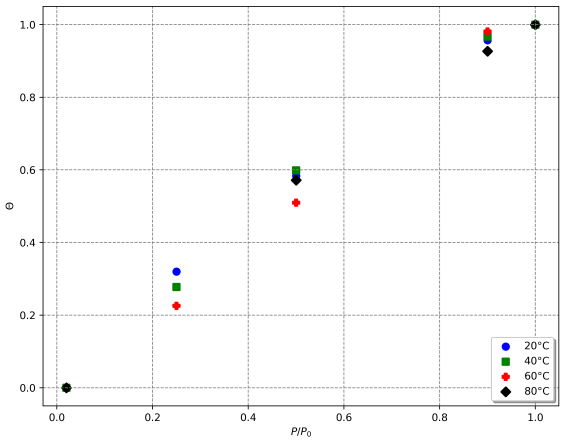

Figure 3.1.5: Isotherm of water sorption rate θ in the epoxy composite at different temperatures as a function of the vapour pressure rate P/P_0.

Firstly, the isotherm models are investigated. Figure 3.1.5 suggests a tendency that bent to a Henry's model, or a Freundlich's model, and eventually a Langmuir's model, since the Freundlich's law is a local Langmuir. The numerical method of least squares has been applied to fit the data with these three models, and the results are illustrated in Figure 3.1.6. Many different iterations and parameter guesses have been tested in order to ensure the convergence. Note that the pressure P was obtained considering the saturation pressure P_0 given in Equation 1.2.2 (see subsection 1.2.4 in chapter 1).

The Langmuir's model does not fit the data, but the others two do. The estimation of the Henry's coefficient presented a standard deviation numerically equals to 0.03, and the Henry's inside the Freundlich's, 0.4. These number are inferior to the respective isotherm constants by a few orders of magnitude. Thus, again, the Henry's law is privileged due to its simplicity. As see in section 1.2.4.3, the Henry's

law, generally describing an ideal case of dilute solution, is interpreted as a penetrant randomly dispersed within the polymer matrix. This random feature is also in accordance with the Fick's diffusion model.

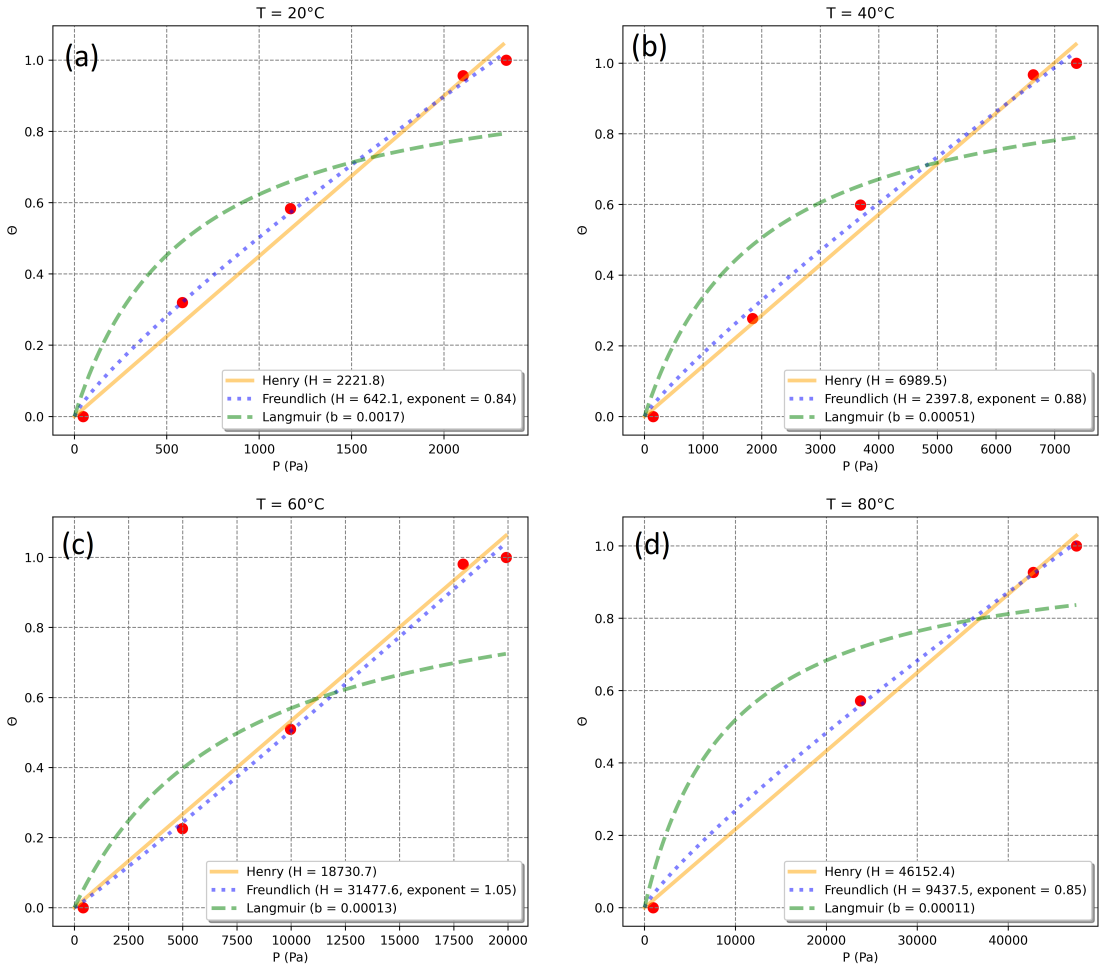

Figure 3.1.6: Correlation of Henry's, Freundlich's, and Langmuir's models to the data of sorption ration θ as a function of the water vapour pressure P for four temperatures: 20°C, 40°C, 60°C, and 80°C.

One can note that the Henry's coefficient is increasing with temperature. One of the simplest extrapolations is the one of Equation 3.1.1 [213] that accounts for the relationships of the H at a reference temperature T_0 and the temperature of interest T as approximately the relation of saturation vapour pressures at the same temperatures.

$$\frac{H(T)}{H(T_0)} \approx \frac{P_0(T)}{P_0(T_0)} \tag{3.1.1}$$

If the T_0=20C is taken as example, with $P_0(20C)$ calculated from Equation 1.2.2 and $H(20C)$ obtained from Figure 3.1.6 (2221), the H at any other temperature T can be calculated, still with $P_0(T)$ obtained from Equation 1.2.2. The values of H showed in Figure 3.1.6 and the extrapolation with $T_0 = 20C$ are illustrated in Figure 3.1.7. It emerges that a good fit is found no matter the value of T_0 is considered, because the relation $H(T_0)/P_0(T_0) \approx 1$ for the four temperatures of the study. Or, more simply, $H(T_0) \approx P_0(T_0)$. What are the mean implications on θ?

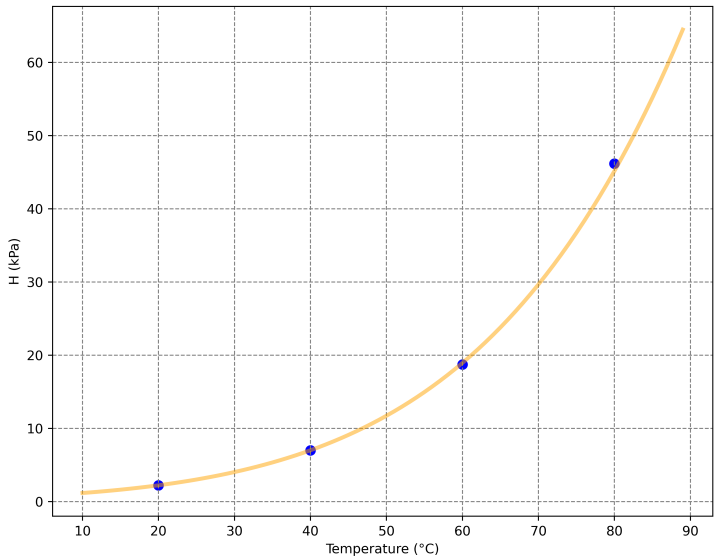

Figure 3.1.7: Vapour-pressure extrapolation technique for Henry's constant of epoxy composite and water

If $H(T)$ of Equation 3.1.1 is substituted in the Henry's law, we could be able to find the temperature-dependent sorption ratio as it follows in Equation 3.1.2:

$$\theta(T) = \frac{P(T)}{H(T)} = \frac{P(T).P_0(T_0)}{H(T_0).P_0(T)} \tag{3.1.2}$$

However, because $H(T_0) \approx P_0(T_0)$, Equation 3.1.2 assumes the form of Equation 3.1.3. This equation says that, for the epoxy composite, Henry's constant represents the saturation vapour pressure ($H = P_0(T)$) and that the sorption ratio is linearly and exclusively proportional to the RH.

$$\theta = \frac{P}{P_0(T)} = \frac{RH}{100} \tag{3.1.3}$$

In other words, we can draw a unique line in the Figure 3.1.5 with a slope equals to 1, with the ratio sorbed θ being the same value as the fractional RH of the environment.

3.1.2.3 Investigating the abnormal increase at higher temperatures

Examining the Figure 3.1.3 give us the impression that higher temperatures enable more water uptake, which is made clear in Figure 3.1.8. At RH = 100%, the water contents are similar at 20 and 40°C, but it increases at 60°C and again at 80°C. As showed in equation 1.3.1, the total amount of water under saturation as function of RH should not depend on the temperature. The temperature should play with the kinetics, but not with the total amount of water under saturation level unless structural or microstructural modification occur. Aiming to collect insights about it, some characterizations as DSC, DMTA, and FT-IR have been executed.

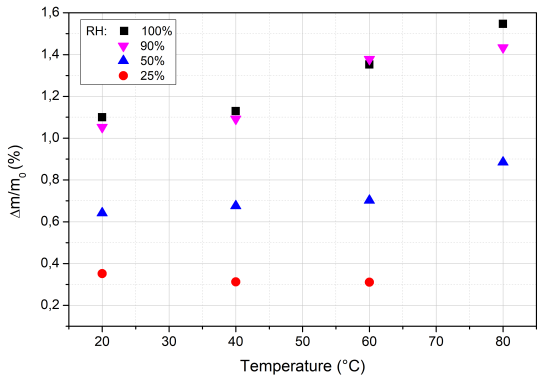

Figure 3.1.8: Relative weight gain as a function of the temperature for samples conditioned at RH = 25%, 50%, 90%, and 100% (liquid water)

Search for phase transitions and plasticization Figure 3.1.3 shows that higher temperatures enable more water uptake. At RH = 100%, the water contents are similar at 20 and 40°C, but it increases at 60°C and again at 80°C. As showed in equation 1.3.1, the total amount of water under saturation should not be a function of temperature. The temperature plays with the kinetics, but not with the total amount of water under saturation level. Before diving into any changes in this equation, it sounds better to verify eventual structural or microstructural modification at these higher temperatures. Aiming to collect insights about it, some characterizations as DSC, DMTA, and FT-IR have been executed.

The DSC thermogram of a dry sample, obtained according the protocol described in section 2.1.1 with rate of 20°C/min, can be seen in Figure 3.1.9(a), and it shows a difference of 7°C in the Tg between the first and second thermal cycles. Additionally, an endothermic peak can be identified in the first cycle, just after the glass transition.

Endothermic peaks at this position are usually associated with physical ageing, i.e. a structural relaxation via segmental motion of amorphous regions [214]. A physical ageing can come from molding process, or conditioning. A reduction in the Tg values, on the other hand, would be in accordance with the hypothesis of polymer plasticizing. The water, as a polar solvent, penetrates the bulk. In thermoplastics, these water molecules will allocate themselves between the chains, increasing the mean free path and giving them additional mobility. In thermosets, this water accommodation would provoke tue same behaviour under a limit after which hydrolysis provides the destruction of elastically active network chains resulting in chain scissions [31]. This *hydrolysis* also results in a Tg reduction and plasticizing, but it's not reversible. A residual cross-link could also explain a Tg difference, but in this case, an exothemic cross-link peak should be identified.

The second heat run in Figure 3.1.9(a) representing a sample fully dried, the Tg in the first heat suggests that the dry DSC sample can yet contain some water absorbed. This should happen if:

- The drying procedure is not efficient enough to expel all the water absorbed.
- During manipulation (taking the sample from the oven, measuring the weight, cutting the DSC sample), the sample has absorbed some water from the environment.

Even if the sample takes time to achieve a steady-state condition, it's known that it will start to uptake moisture as soon as it is taken from the oven. Later, when the sample is already installed in the electrical test cell, under dried N_2 with RH = 1-3%, it can expel some of the water uptaken during manipulation, but there is no evidence to consider that the sample is fully dry. The dry sample, providing the m_0 value in this thesis, represents just the "most dry possible" case.

Aiming to understand the limit of the Tg dislocation, a sample has been immersed in deionized water at room temperature for one month. The thermogram of Figure 3.1.9(b) illustrates this result. A difference of 14°C has been achieved between first and second heat. Besides, no endothermic peak appears at the end of the transitions.

Even so, the second heat still looks similar to the one at Figure 3.1.9(a), with a net second degree transition without any endothermic peak, implying that the first heat could be correlated to the water and the thermal history.

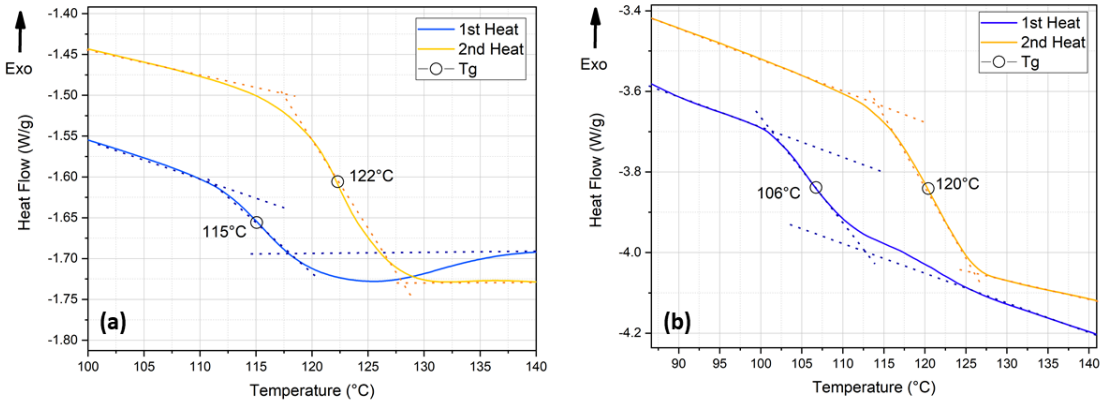

Figure 3.1.9: Thermogram of an epoxy composite previously dried at 70°C under vacuum for at least 2 weeks (a), and a similar epoxy composite immersed in deionized water for 1 month (b).

The Tg decrease due to water absorption raised some questions: at which temperatures the secondary transitions are located and how are they modified with the water uptake? Even importantly: can these transitions be widely or positioned at the temperature range selected for the sample conditioning and electrical test (20-80°C)?

More information have been acquired through thermo-mechanical analysis, which results are illustrated in Figure 3.1.10. At the temperatures of interest (20°C, 40°C, 60°C, and 80°C) wet samples tended to present a higher $tan\delta$, which is related itself to the mechanical viscosity component. In other words, materials presenting higher $tan\delta$ are more rubbery-like. In the case of the sample conditioned under liquid deionized water, the $tan\delta$ is almost one order of magnitude higher than dry samples, and the Tg transition is significantly broadened. At 80°C, this sample is closer to a "leathery" state than the "glassy" state at 20°C. The immediate conclusion is that, at isohydric conditions (at same conditioning), the material will present small changes on its physical state among the temperatures of interest. When wet, these differences are escalated. The driest sample at 20°C and the wettest one at 80°C can be seen as different materials.

As soon as the temperature rises, we get closer to the Tg, and the material before rubbery starts to be leathery. How it helps to increase the total amount of water

absorbed?

Fan et al [215] have found a similar behavior for a die-attach film. According to them, the saturation moisture concentration is dependent to the free volume fraction, which increases when temperature cross the Tg.

We know from literature that the increase of *tanδ* are allowed by the loss of secondary bonds inside the material (intrinsic secondary bonds, as Van der Waals). Water can already break existing Van Der Waals bonds between polymer chains and substitutes molecules on each part of the former bond, increasing the free volume. Evidently, this free volume increase is limited because of the crosslinks. This should contribute to a larger plasticizing anyway (correlated to the Tg shift of DSC thermograms), which itself leads to larger mechanical losses due to the increase of the viscosity component. Put all of this differently, if the secondary bonds are even weaker or nonexistent because of the temperature raise, hydrophilic sites will be more susceptible to water attachment. Another explanation comes from the fact that the temperature can also swell the material, so as there are more space to accommodate water molecules.

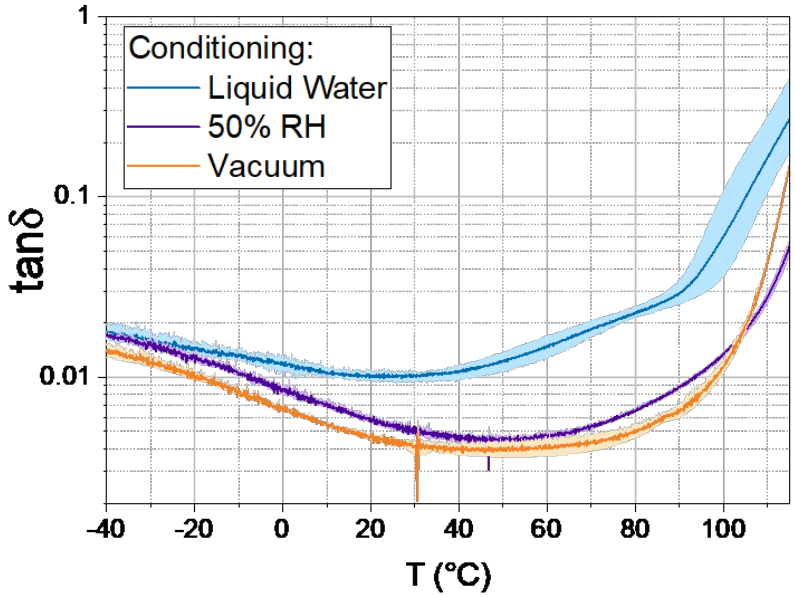

Figure 3.1.10: Isochronal DMA result of mechanical losses *tanδ* with temperature depending on the samples conditioning: liquid deionized water at 40°C (blue line), 50%RH at 40°C (purple, on the middle), drying under vacuum at 70°C (orange).

Chemical degradation evidences: Other non-reversible mechanisms can take place, as thermo-oxidative degradation (hydrolysis). Ultimately, the swelling and hydrolysis can promote micro-cracks and erosion.

A first evidence of a non-reversible process should be seen in the gravimetric measurements: if a degradation mechanism is about to occur, the weight should continue to increase, which is not the case.

A second evidence is the non reversibility of the weight, but these samples were able to dry and achieve the same level of water content of departure.

A third evidence should be assigned by structural modification observed with infrared spectroscopy. Antoon at al [216] observed that, for a DGEBA/anhydride

exposed at 100% RH, and 80°C for a longtime, ester bonds were able to by hydrolyzed and lower absorbance at 3500 cm^{-1} (alcohol groups) and 1720 cm^{-1} (carboxyls) should be found. The infrared spectra of Figure 3.1.11 show no evident peak evolution among the different steps of sample conditioning and electro-thermal history.

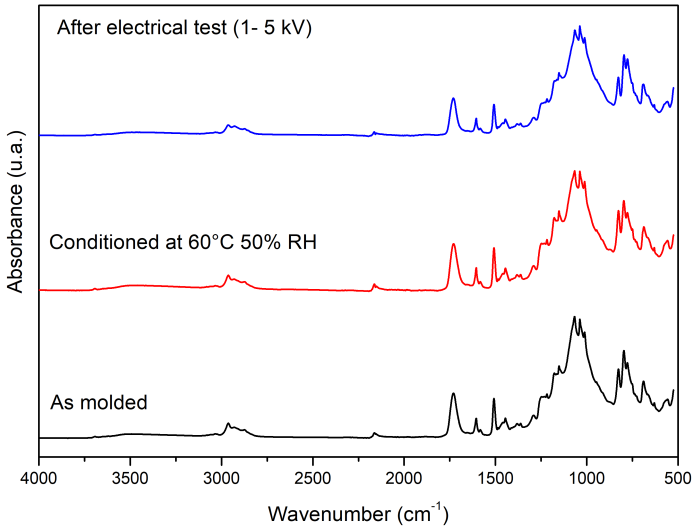

Figure 3.1.11: Infrared spectra of an epoxy sample as molded, after conditioning at 60°C and 50% RH, and after electrical test at 60°C and 50% RH.

3.2 Electrical tests in the Epoxydic System

In this section, the DC current of the epoxy composite is investigated as a function of the electric field, temperature, and water uptake. A punctual complementary space charge measurement of a dry sample is also presented. In the discussion section, we delve into the conduction mechanisms, temperature-dependent mechanisms, and insights about the impact of water absorption.

3.2.1 Results

3.2.1.1 Current-voltage tests

The reference curves: The findings presented in this section serve as reference results, as they incorporate the comprehensive assessment of temperatures and relative humidities applied to the epoxy composite with gold sputtering on both sides; i.e. with electrode systems that are symmetrical in nature and inert.

Figure 3.2.1 displays the current density profiles as a function of electric field for the dry samples sputtered with gold on both sides. Each isotherm exhibits two distinct regions, whose slopes have been traced and calculated. At low voltages, the slope is close to 1, while at higher voltages, the slopes decrease from 2.17 at 80°C, 2.62 at 60°C, to 2.57 at 40°C and 20°C. The electric field threshold (E_{th}) has been identified within the range of 3-6 kV/mm for the temperatures under investigation, and it decreases with the temperature raise.

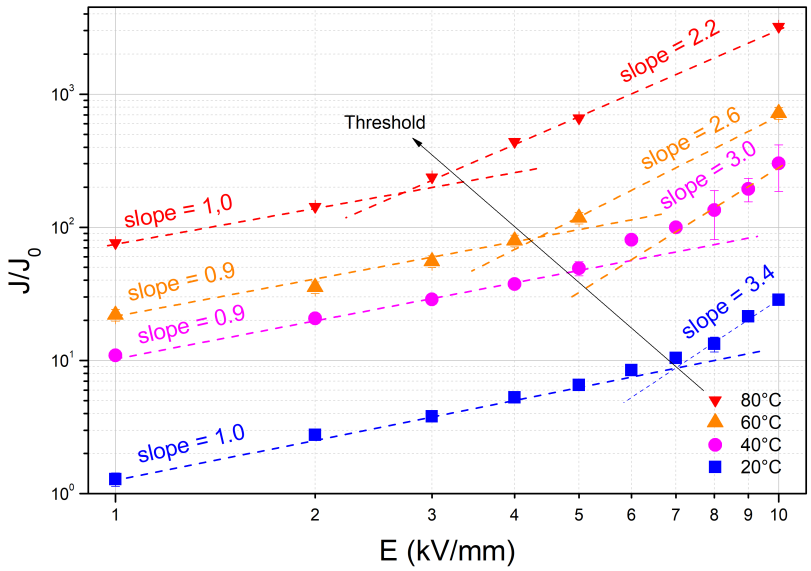

Figure 3.2.1: Current density in a dried epoxy sample as a function of electric field at 4 different temperatures. RH= 1-3%.

For samples conditioned at 50% RH, similar curve profile have been observed (Figure 3.2.2), but three main differences can be noted:

1. The current densities exhibited a significant increase of several orders of magnitude compared to the dried samples.

2. The threshold decreased, appearing between 1-2 kV/mm for measurements conducted at 20-60°C. Consequently, additional measurements were conducted at lower fields.

3. The slopes in the non-ohmic domain are all equal to 2.

4. The conduction profile at 80°C displayed a consistent fit with a slope close to 2 for all data points, even at low fields, indicating the absence of a discernible threshold.

It is worth to remember, as described in 2.4.1.3, that up to 3 kV/mm, the measurement has been conducted with the test cell opened and at equilibrium with the climatic chamber environment. At higher voltages, the vessel has been closed and dry N_2 under 2 relative bars has been injected. No impact of this operation can be noticed from the datapoints.

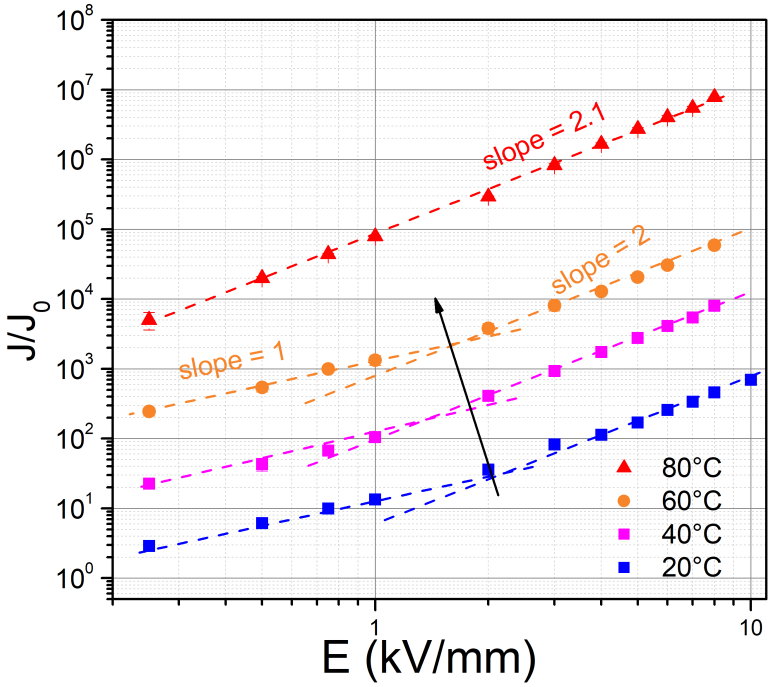

Figure 3.2.2: Current density as a function of electric field for 2-sides gold-sputtered samples conditioned at 70°C under vacuum and tested at 50% RH.

When conditioned at 90% RH, a regime with a slope of 2 is consistently observed across the range of voltages and temperatures (20-60°C) investigated, as depicted in Figure 3.2.3. Only the values at 20°C and 250-500 V suggest an ohmic mechanism. In comparison to the dry samples, the current density (J) here exhibits an even greater increase, with a difference of 5 orders of magnitude. This difference can be observed, for instance, when comparing the values of J at 5 kV/mm and 60°C between the samples conditioned at 1-3% RH and 90% RH. We remember that the measurements at 80°C failed four times, probably due to water condensation in the electrical system and parasite currents.

Influence of the electrode metal: Figure 3.2.4 illustrates the results for dried samples tested at 40°C, covered with gold, copper, silver, platinum, or left without

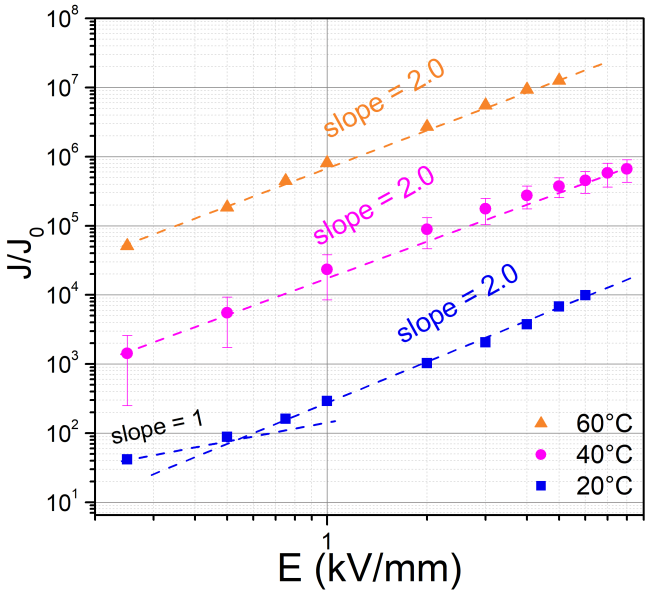

Figure 3.2.3: Current density as a function of electric field for 2-sides gold-sputtered samples conditioned at 70°C under vacuum and tested at 90% RH.

metallization (direct contact with conductive silicone rubber tape). At lower fields, all currents appear to be similar, considering a standard deviation of 1.5 times the calculated values. However, as the field increases, deviations become more noticeable due to varying slopes of the data points. For instance, at 5 kV/mm, the silver-sputtered sample exhibits twice the conductivity compared to the copper or gold-sputtered samples.

Is this difference significant? As discussed in section 2.5.7, a deviation of 2 for this voltage level can be considered significant, indicating that only the silver-sputtered sample at 5 kV/mm (and potentially at 4 kV/mm) differs significantly from the other samples. A slope equals to 1.2 has been found to the silver-sputtered sample between 2 kV/mm to 5 kV/mm.

Regardless the lack of impact from electrode materials, we were also intrigued by the possibility of exploring the influence of dissimilar electrodes, i.e. where the cathode and anode are made of different materials. Figure 3.2.5 illustrates the results of these experiments for copper-sputtered samples, and gold-sputerred ones. When just one side is covered by the metal, the other side has a direct contact with the test cell electrodes, which are made of conductive silicone rubber (carbon black).

If we consider a deviation of 1.5 times the measured value as significant, no significant impact was observed for copper-based electrodes. In the case of gold-based electrodes, although the results appear more scattered, they still do not reach significance, even at 1 kV/mm. It is important to recall (as mentioned in section 2.5.7) that at 1 kV/mm, the deviation can be as high as three times the measured value.

3.2.1.2 Space-charge profile

As presented in the literature review (section 1.3.1), previous studies have warned about the impacts of silica particles on space charge signal obtained through PWP (pressure-wave-propagation) methods, as the LIPP. Commercial silica contain quartz,

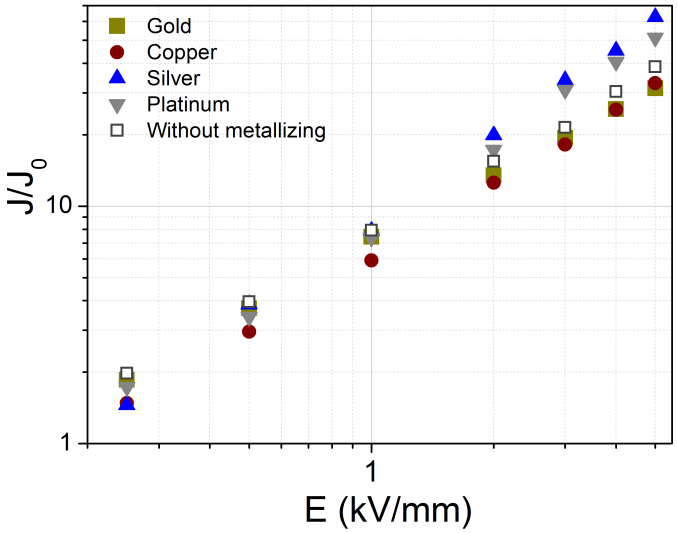

Figure 3.2.4: Relative current densities as a function of electric field for samples conditioned at 70°C under vacuum and tested at 1-3% RH at 40°C. Effect of electrode material.

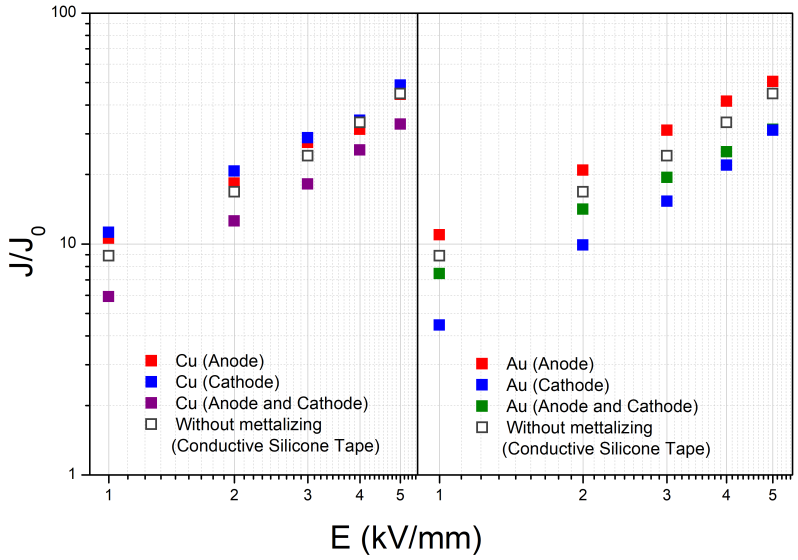

Figure 3.2.5: Relative current densities as a function of electric field for samples conditioned at 70°C under vacuum and tested at 1-3% RH at 40°C. Effect of asymmetric electrodes.

a piezoelectric particle that is able to generate spurious signals detected through wave pressure propagation. Since the size particles are not small enough (some of them have sizes in the micrometers range) multiple reflections should introduce a random component at a frequency associated with the size and distribution of the particles. This random component is observed on measurements, and they have been reduced by post-treatment low pass filtering. The protocol consisted of filter firstly the calibration measurement, and to try to reproduce the same filtering strategy with the same filter parameters on the following measurements of the same sample. An example is illustrated in Figure 3.2.6. The so-called "reference curve" has been applied as the calibration curve.

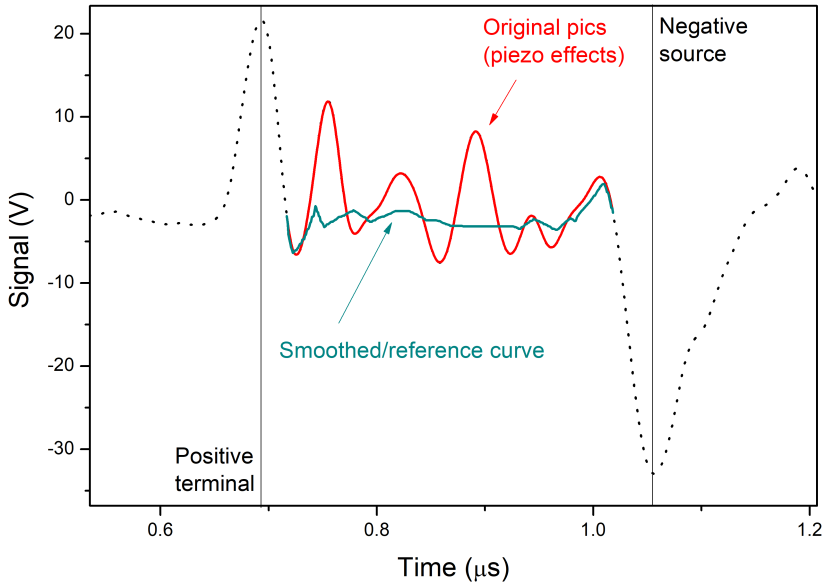

Figure 3.2.6: "Volt-on" space charge measurement obtained at approximated 5 seconds after voltage application. Parameters: Dry epoxy sample, 40°C, V_{app} = - 5000 V, gold sputtering on both sides.

These spurious signals were also present on "Volt-off" measurements, but the low pass filtering strategy has been less efficient. The position of the spurious signal shifted at each measurement, and the author felt less confidence to determine the beginning and the end of the sample during the first hours of polarization.

Figure 3.2.7(a) shows the charge density distribution for polarized samples immediately after the voltage application, after 1 hour, and after 14 hours. It was noted that, after 1 hour of polarization, the spurious signal changed (it was dislocated along the x-axis, and the peaks height also changed), thus the filtering of spurious signal had less efficiency, and it is hard to conclude about the charge accumulation in the volume, so as an apparent alternation of positive and negative charges looks like to be found.

Anyway, the anode peak is more intense than the cathode. A field reinforcement provided by heterocharge accumulation should explain it, suggesting a negative homocharge injection from the cathode, and subsequent accumulation of them as heterocharges in the anode. In addition, the cathode peak is not reinforced. On the contrary, after 14 hours, it has been weakened, and a predominance of negative charges looks to fill the bulk. Considering yet the hypothesis of homocharge injection, it looks like these charges have spread out throughout the thickness, acting as a heterocharge package towards the anode. When the electric field distribution is examined (Figure 3.2.7(b)) a heterocharge accumulation on the anode became evident, providing a field reinforcement on this side.

Figure 3.2.8 present an evolution of charge density as a function of time where we can see the progressive predominance of negative charges in the volume.

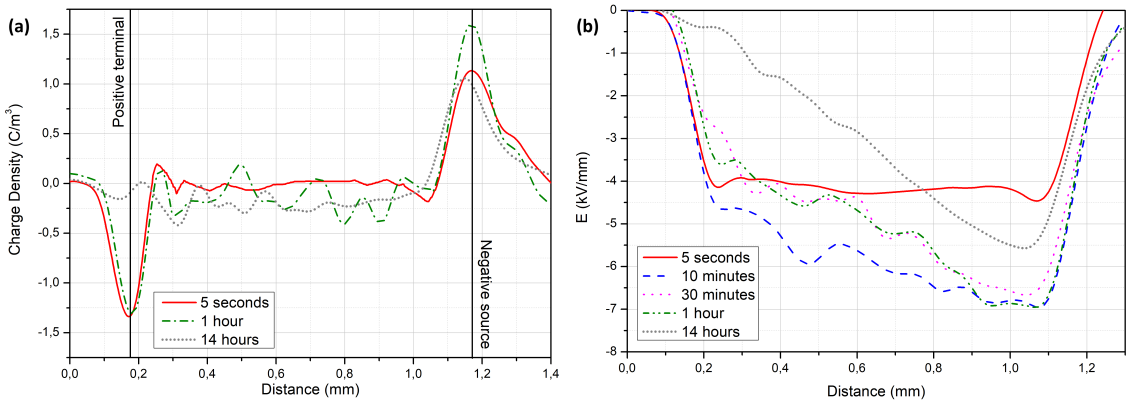

Figure 3.2.7: Charge density distribution as a function of distance or thickness (a) and electric field distribution (b). Parameters: Dry epoxy sample, 40°C, V_{app} = -5000 V, gold sputtering on both sides.

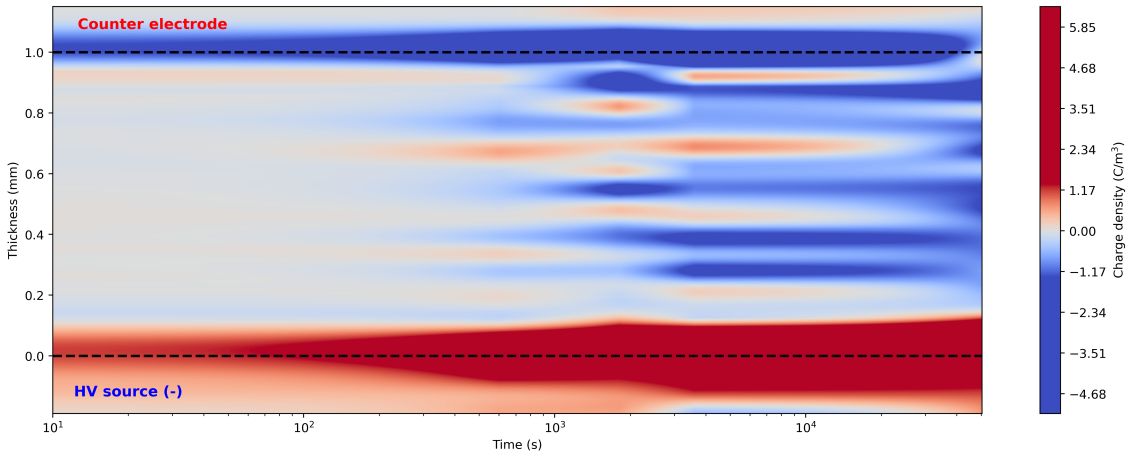

Figure 3.2.8: Volt-on charge density chart as a function of thickness and time for a dry epoxy sample covered with gold on both sides, at 40°C and $V_{app} = -5000V$.

3.2.2 Discussion

The primary objective of this section is to delve into all the data derived from electrical measurements - our focus is not an exhaustive examination of every detail within the data, nor is it an attempt to test all available models. Instead, our approach centers around highlighting specific correlations. We will provide a more in-depth discussion only when pertinent.

Our exploration revolves around key questions:

- Where does the boundary lie between ohmic and super-ohmic conduction? (Section 3.2.2.1)
- What can be stand for the super-ohmic mechanisms? (Section 3.2.2.2)
- How water and temperature impact the value of J? (Sections 3.2.2.2 and 3.2.2.3)
- How asymmetric electrode systems impact what has been stand for the reference measurements? (Section 3.2.2.2)

3.2.2.1 The limits of the ohmic conduction

The space charge accumulation can be considered as a driving force for ageing mechanisms [217]. Since the non-linearity can be related to the accumulation of space charge, considering the non-linear domain as the voltage levels in which the space charge predominates in the charge transport, the identification of the boundary between linear and non-linear domains has technological interest. The visual analysis of the reference curves of section 3.2.1.1 gives an approximation about the voltage threshold V_{th} that characterizes the change from linear to non-linear domain.

The temperature-dependence and RH-dependence of the V_{th}: It has been observed that the threshold voltage (V_{th}) decreases with both temperature and relative humidity (RH). Table 3.2.1 presents the experimental values of V_{th} corresponding to various combinations of these parameters. In the case of samples at 1-3% RH, the decrease in V_{th} with temperature follows a linear trend, with a slope equal to -70. However, for hydrated samples, the relationship does not appear to be linear, though there is an insufficient amount of data for a more in-depth analysis. A similar limitation is encountered in the V_{th} dependence on RH, as only up to 3 data points are available at each temperature. One can conclude that below the

	20°C	40°C	60°C	80°C
1-3% RH	7000	6000	4500	3000
50% RH	2040	1750	1600	≤ 250
90% RH	525	≤ 250	≤ 250	-

Table 3.2.1: Approximate threshold voltages V_{th} between linear and non-linear $J(E)$.

values of V_{th} from Table 3.2.1, the material is under the linear domain, and so the conduction is ohmic, obtained directly from the Ohm's law. However, there are two considerations that merit our attention: (1) the possibility to have space charges in the linear domain, and (2) the distinction between apparent conductivity and real conductivity.

Space charge accumulated in the ohmic domain: The space charge measurements showed in Figures 3.2.7, 3.2.14, and 3.2.8 are performed under a voltage level attributed to the linear domain (5000V).

After 1 hour of polarization, there appears to be an apparent alternation of positive and negative charges, similar to what Gallot-Lavallée observed for filled epoxy at 72°C [142]. However, as emphasized in Section 2.5.6, it is important to note that the material may not be in a steady-state condition after just 1 hour of testing. The result that likely represents a situation closer to stabilization is the one obtained at 14 hours of polarization (Figure 3.2.14). In this result, positive space charges are distributed throughout the volume, leading to field reinforcement in the cathode due to the presence of heterocharges, and field attenuation in the anode. How is it possible that such a material under such a disturbed electric field distribution may still be considered under an ohmic domain?

- Hypothesis 1: the results showed in Figure 3.2.14 are consequences of the measurement artefact or data treatment, even if it was consistent among three different measurements conducted with three different samples. As presented in section 2.4.2, the relative humidity could not be controlled during LIPP measurements, there is a chance that the sample starts to absorb water from the environment around the cell.

- Hypothesis 2: the space charge accumulated is not strong enough to impact considerably the charge transport, or at least, it allows for the assumption of a homogeneous field as a reasonable approximation. However, given that the applied voltage of 5000V is close to the approximated threshold voltage (V_{th}) at 40°C, it is not surprising that a notable charge density has started to manifest. Regrettably, measurements at lower voltages were too noisy to yield reliable information regarding charge density in the linear domain and, therefore, were not included in this study.

Assuming Hypothesis 2 to be valid, the findings in Section 3.2.1.2 indicate that the transient current of the sample at 1-3% RH and 40°C could involve an interplay between space charge accumulation. Such charges may be present in the steady-state condition associated to the linear domain.

The slope of J(E) in the ohmic domain as a fraction of the real conductivity: One can be tempted to calculate the conductivity from the linear regions of the $J(E)$ profiles. However, according to the trapping theory, real insulator like this epoxy must be full of traps, and these traps may lower the current also in the linear domain. As a consequence, the slope does not give σ but $\theta\sigma$ instead, being θ a fraction representing the rate of charge carries available for conduction. Thus, the slope obtained from the Ohm's law in the linear domain provides an apparent conductivity σ_{app}. The intrinsic material conductivity, or real conductivity, or trap free conductivity that is multiplied by θ, is denoted as σ_{real}.

If σ_{app} is linear, is σ_{real} linear too? In the linear domain, there are two occasions in which the resulting σ_{app} is a constant:

- If both σ_{real} and θ are voltage-independent. In this case, the σ_{app} give a fraction of the σ_{real}.

- If σ_{real} and θ are voltage dependent but inversely proportional; i.e. when voltage increases, σ_{real} increases but θ decreases at the same rate. This being true, the relation $\theta\sigma_{real}$ could be a constant over voltages and give an illusion of linearity and independence of the field at the form of a constant σ_{app}. However, intuitively, it make sense to have θ increasing with voltage, because stronger fields increase the probability of charge carriers to hop potential barriers, or crossing them by tunnel effect, ultimately extracting them from their original traps and contributing to conduction. So, this possibility seem unlike to happen.

In technological applications, both the apparent conductivity (σ_{app}) and the real conductivity (σ_{real}) are crucial, as the first provides insights into the current delivered by the insulation system to the measurement electrode.

3.2.2.2 Exploring the super-ohmic mechanisms

As outlined in the literature review (Section 1.2.5.6), we categorize super-ohmic conduction into two groups due to the utilization of two distinct approaches. The first approach involves non-linearity in accordance with the space charge limiting model, while the second approach incorporates non-linearity through traverse barrier mechanisms. Given that the second approach entails a more extensive set of equations, some of which may be conflicting (such as Poole-Frenkel and Schottky, Hopping, and Ionic), the investigation becomes more intricate. Consequently, we give preference to the first approach. Nonetheless, we acknowledge and include considerations about the second approach in our analysis.

Non-linearity according to the space charge limiting models: The interpretation of the non-linearity of the current-voltage profiles with regard to the space charge limiting models is straightforward: if the slope in the log-log graphic is equal to 2, it fits with the SCLC with a single set of shallow traps (J_θ); if it is higher than 2, then it is the SCLC with exponential levels of trapping (J_l). Why bother then?

If these correlations are correct, considering the reference curves (Figures 3.2.1, 3.2.2, and 3.2.3), it means that the water absorbed (and all the followed (micro)structural modification) provides a single privileged set of shallow trap level that becomes predominant for conduction, because all the slopes of the most dried samples are higher than 2, but as soon as the sample is hydrated, all the slopes are exactly or very close to 2. In other words, the water would increase the trapping occurrence of a particular level, and it increases the current.

Water may provide local polarization resulting in local energy-band deformation. The transport may be made by polarons, with the hidrogen bonds providing additional localized (trap) states. But if it is the case, should water be considered a "dopant"?

This reasoning also imply that the increase of temperature, by reducing the slope in the driest sample (Figure 3.2.1), should also provide a single-level trap mechanism at a higher temperature (and the temperature does not have a dopant effect at all, unless it charges the material's structural configuration).

These events could be related with the T_t, which has no clear definition, and is associated by Lambert [91] by a factor merely indicating the trapping distribution (see literature review, section 1.2.5.6). If T_t decreases (as a consequence of water

sorption or thermal vibration[1]) at temperatures below T_{test}, then empty traps at the top of the distribution, near the conduction band, will dominate those near the quasi-Fermi level, reducing the situation to a single set of shallow trap.

Dissado [89] argues that, when voltage increases, more charge is injected so the Fermi level moves up as more and more traps are filled. Thus, another hypothesis to explain the exponential to one single set SCLC shift is that the water absorption and the temperature facilitate the trap filling, moving the Fermi level to levels closer enough to the conduction band that charges between these levels are more easily detrapped to the LUMO. It may explain the increase in current, but not the shift exponential-single set. If the gap between the new Fermi (namely quasi-Fermi) and the conduction band is narrow, there is a chance that the traps within these levels behave like a single-set? It not excludes the possibility of having new shallow traps as a consequence of water sorption. The move of the Fermi level may maximize the impact of such new shallow traps.

The increase of conduction with increasing water content could also be interpreted in terms of ionic conduction due to the migration of ions issued from water dissociation. However, such an ionic conduction constitutes a mass transfer towards the electrode, which naturally cannot be permanent [134, 218]. In this case, we could imagine that electrochemical reactions would occur at the electrodes generating oxygen and hydrogen gases. The water content inside the material could be regenerated by the humid environment. Contrary to usual ionic conduction phenomena, a stabilized situation could be imagined.

Water ions are probably present as space charges but their contribution to the conduction is probably negligible, which can be rather attributed to electron mobility.

Looking closely to the mobility and charge carriers concentration: The correlation of the non-linear datapoints of the dry sample with the SCLC with exponential distribution of traps has been executed through a Python code that applies the least-square method. To let the reasoning more clear, the equation characterizing the mechanism was simplified to the Equation 3.2.1. The M values, the calculation of the effective mobility $\mu_{eff} = L\mu$ and the T_t are all showed in table 3.2.2. In order to obtain the μ_{eff}, it was necessary to define a ϵ_r for the epoxy composite. For instance, the value of 4 is considered, based on the values obtained from the results of Figure C.4.1(a). However, as this figure indicates, at lower frequencies the permittivity increases significantly. If a higher ϵ_r is considered, the values of μ_{eff} are reduced; then the values appearing in table 3.2.2 shall be the highest possible for the range of ϵ_r that can be considered.

$$J_l = L(\epsilon_0\epsilon_r)^l \mu \frac{V^{(l+1)}}{d^{(2l+1)}} = M.V^{(l+1)} \tag{3.2.1}$$

There are two remarks from the data of Table 3.2.2:

- The mobility increases with temperature, which is intuitive. Their range of $10^{-15} - 10^{-13}\ m^2/Vs$ agrees with the range of inter-trap mobility within intermolecular regions cited by Dissado [89].

[1] Can we say "phonon sorption"?

T (°C)	l	M	μ_{eff} (m^2/Vs)	T_t (°C)
20	2,4	7,0E-23	5E-15	430,2
40	2	2,8E-20	3E-14	353
60	1,6	2,6E-18	4E-14	259,8
80	1,2	5,0E-16	1E-13	150,6

Table 3.2.2: Coefficients extract from the fit of SCLC with exponential distribution of traps on the data of current-voltage profiles of the epoxy composite at 1-3% RH.

	50% RH	90% RH
T (°C)	μ_{eff} (m^2/Vs)	μ_{eff} (m^2/Vs)
20	2E-14	7E-13
40	3E-13	6E-11
60	2E-12	1E-09
80	3E-10	-

Table 3.2.3: Coefficients extract from the fit of SCLC with single level of traps on the data of current-voltage profiles of the epoxy composite at 50% RH and 90%RH.

- According to the linear tendency of l as a function of T, the single set SCLC should be achieved when $T = 90C$. At this temperature, $T = T_t$.

The same approach has been conducted for the hydrated samples, but using the SCLC single set of traps (J_θ) as reference. Again, the $\epsilon_r = 4$. The μ_{eff} are found in Table 3.2.3. According to this table and the Table 3.2.2, μ_{eff} decreases exponentially with the increase of water uptake (or RH). Besides, larger water uptakes also increase the rate at which the μ_{eff} decreases among the temperatures at isohydric conditions (for example, for the sample at 1-3% RH, the μ_{eff} at 80°C are 10^2 times bigger than at 20°C; but at 50%, the factor is increased to 10^4). The mobility approaches the model of electronic conduction in solids that ranges of 10^{-5} - 10^{-6} m^2/Vs [89], but they are still below the range, which is consistent with trapping activity. Some insights can still be earned from the analysis of the V_{th}. If, for the sake of simplification, only ohmic and single-level SCLC are considered, the Equation of V_{th} should be stated as the one in Equation 3.2.2. Taking again $\epsilon_r = 4$, values of the volumic concentration n of charge carriers of the order of 10^{18} m^{-3} can be obtained at T = 20°C and RH = 50%.

$$V_{th} = \frac{8nqd^2}{9\epsilon_0\epsilon_r} \tag{3.2.2}$$

According to Table 3.2.1, the V_{th} decreases a few orders of magnitude with the increase of temperature and water uptake. This would be possible if:

- n decreases, but ϵ_r is constant; this leads to admit paradoxically a decrease in charge carriers with increasing temperature and water content. In this situation, θ would also decrease, and μ has to increase much more to give the increase of μ_{eff} seen in Table 3.2.3.

- n is constant, but ϵ_r increases. It is expected that the permittivity increases with the increase of temperature and water uptake, but if n is constant, the

ϵ_r of hydrated epoxy should be at least 10 times higher than the ϵ_r for the driest sample. Again, we face the ambiguity of selecting the good ϵ_r from Figure C.4.1. If we choose values at very lower frequencies and consider them more representative of a DC stress than the values at high frequencies, than an increase of one order of magnitude would be impossible.

- n decreases, and ϵ_r increases at the same time.

The considerations do not explain solely the V_{th} decrease, but the current increase itself, as schematized in Figure 3.2.9. As a matter of fact, Equation 3.2.2 can only be obtained because the ohmic conduction is a function of n, and the single-trap level SCLC depend on ϵ_r. Both currents are proportional to the apparent mobility $\theta\mu$, that increases with temperature and water sorption. So, if only ϵ_r increases, the J_θ increases more than J_Ω, shifting the threshold towards left. The same effect is achieved if n decreases.

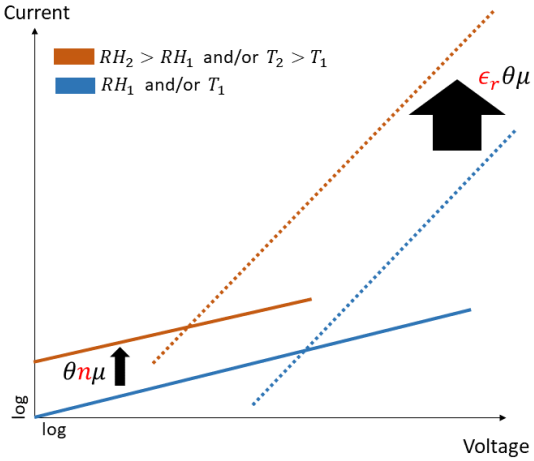

Figure 3.2.9: Scheme illustrating the decrease of V_{th} with the increase of water uptake

Non-linearity according to traverse barrier mechanisms: As presented in chapter 1 (1.2.5.6), the current can be described based on traverse barrier mechanisms. Some correlations are presented first, and then the ambiguity and contradictions are explored at the end.

Evidences of Schottky injection: Figures 3.2.10(a),(b), and (c) show the Schottky plots for the three RH of the study. Both the regions attributed to the ohmic and super-ohmic can be correlated to the Schottky injection, but only those obtained from the super-ohmic region are discussed. An attention has to given to the higher voltage values of the measurement at 90% RH and 40°C (Figure 3.2.10(c)) fitted with green dotted lines: a mechanism change seems to appear. As a matter of fact, this change can also be perceived in the other temperatures represented in this Figure 3.2.10(c). This feature will be discussed in details in subsection **??**, but for now, for exploratory purposes, two correlations will be applied for that measurement.

The values of ϵ_r and ϕ_{eff} extracted from Figure 3.2.10, and the factor λ_E attributed to a field correction necessary to give $\epsilon_r = 4$ (according to Annex C) are organized in the Table 3.2.4.

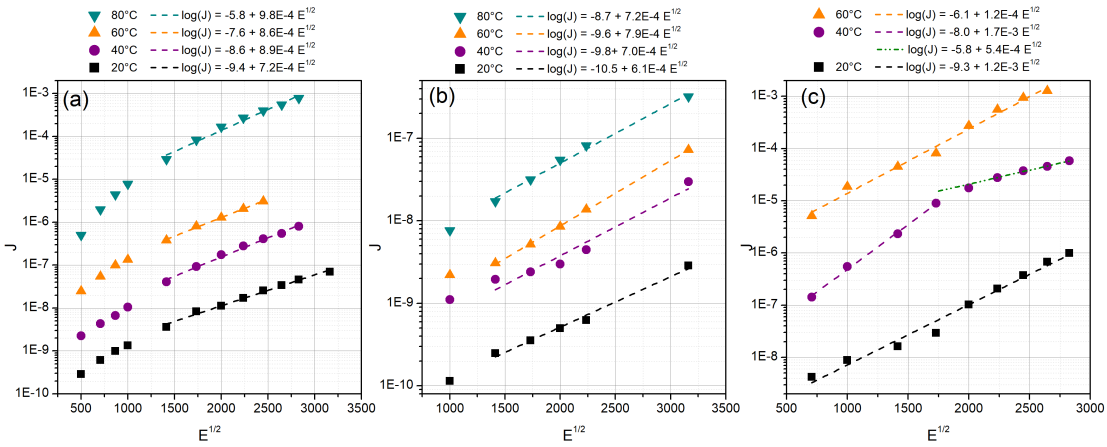

Figure 3.2.10: Shottky correlations for samples conditioned at 1-3% RH (a), 50% RH (b), and 90% RH (c).

	1-3% RH			50% RH			90% RH		
T (°C)	ϵ_r	λ_E	ϕ_{eff} (eV)	ϵ_r	λ_E	ϕ_{eff} (eV)	ϵ_r	λ_E	ϕ_{eff} (eV)
20	6.1	1.5	0.54	4.4	1.1	0.52	1.5	2.7	0.51
40	4.0	1	0.56	2.5	0.6	0.53	0.7 / 6.8	6.0 / 0.6	0.52 / 0.46
50	2.7	0.7	0.60	2.4	0.6	0.54	1.3	3.1	0.49
60	3.0	0.75	0.61	1.6	0.4	0.52	-	-	-

Table 3.2.4: Coefficients extracted from the Schottky correlation.

Globally, the effective work functions were at the same range $(0.5 - 0.6\ eV)$. At lower temperatures and humidity, a field reinforcement is experienced. As temperature increases, there is a turning point at which no reinforcement is found, and after which the field is attenuated. The water ingress looks to support the field attenuation, but the measurement at 90% RH and 40°C should not be considered unless we imagine that, as electrical stresses increase, an attenuation situation would be shifted to a reinforcement.

Tracing back the literature review, a tendency of field attenuation for dry samples as a consequence of homocharge build-up has been encountered many times ([145, 101, 142]) but there is always heterocharge formation mainly close to the cathode when the temperature, electric field, and time increases (as seen, indeed, in Figure 3.2.7), and this is not observed within this Schottky approach. Therefore, or we consider that this fitting represents the pre-heterocharge build up situation, or we consider that this approach is not suitable at all.

Evidences of Poole-Frenkel transport: The Poole-Frenkel correlation is illustrated by the fittings of Figures 3.2.11(a), (b), and (c) for the three RH of the study. Only the correlations at 50% RH are satisfactory. For the sake of our exploration, some attempts at other RH have been executed. The ϵ_r and calculated field attenuation/reinforcement factor λ_E are showed in Table 3.2.5. The first thing to note is that the values of ϵ_r are too high, and because of that, such correlation does not sound to be realistic. Nevertheless, when we look closer to the values at 50% RH, we can see the field reinforcement we were looking for, but the magnitude

	1-3% RH		50% RH		90% RH	
T (°C)	ϵ_r	λ_E	ϵ_r	λ_E	ϵ_r	λ_E
20	-	-	20.7	5.2	10.2	2.6
40	-	-	35.8	9.0	-	-
60	68.3	17.1	36.1	9.0	24.0	6.0
80	22.2	5.6	19.8	5.0	-	-

Table 3.2.5: Coefficients extracted from the Poole-Frenkel correlation

remains, still, unrealistic: it would imply that, when 10 kV/mm is applied, there is a reinforcement raising the field to 90 kV/mm, surely above the voltage breakdown!

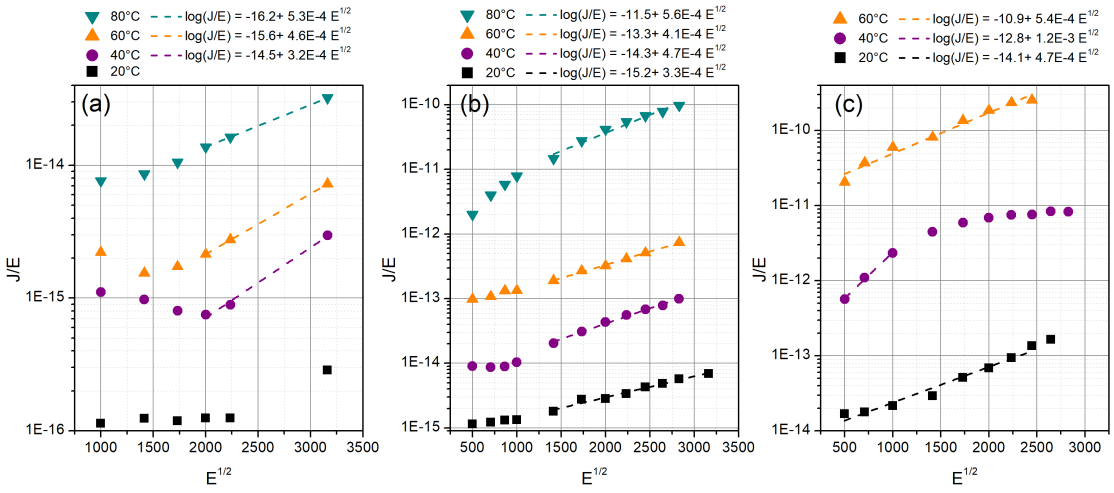

Figure 3.2.11: Poole-Frenkel correlations for samples conditined at 1-3% RH (a), 50% RH (b), and 90% RH (c).

Evidences of Fowler-Nordheim and Hopping: The data were not able to fit the Fowler-Nordheim at any condition. On the other hand, all measurements at all temperatures in all RH were able to fit the Hopping mechanism for the same jump distance of around 16 *nm*. As a matter of fact, if we want to "force" a fitting with lower jump distances, as the 5.7 *nm* found by Guillermin [96] or the 4 *nm* found by [141] and still have reasonable regression coefficients (R^2 close to 1), we can, as seen in Figure 3.2.12 for the driest sample at 40°C. This approach does not seen to give us sufficient insights to pursue the discussion, it only give us an additional evidence to eventually prioritize the hopping conduction in the volume according to the Poole-Frenkel mechanism.

Evidence coming from different electrode materials: Studying Figure 3.2.4 that shows the I-V measurements with different materials at the contact, the electrode system does not seem to interfere in the current measured at the voltages of the study. Such current would not be limited by injection mechanisms because the injection mechanisms focus on metals' work functions, and even when they are different, the current is the same. But injection may occur: the fact that we have

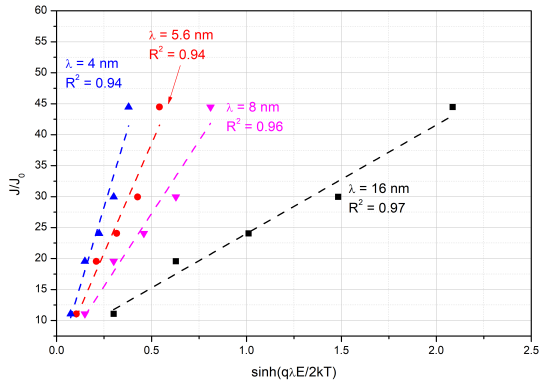

Figure 3.2.12: Hopping plot for samples conditioned at 1-3% RH and tested at 40°C

space charge accumulated is an evidence that charges have been injected, unless all of them have originated from ionisation or dissociation processes.

It contradicts all the discussion about the SCLC mechanism, because we should not have a current limited by the bulk and by the interfaces at the same time, even if we suppose that all the currents are the same at the steady-state condition. However, we can have a bulk-limited conduction as a result of influences coming from the interfaces: One theory that we can present to justify the lack of importance of the electrode materials concerns the composite's Fermi level. As detailed by Simmons on his articles [219, 220, 221] the conduction can be bulk-limited if the bottom of the conduction band is more than 4 kT above the interfacial barrier height. There would be a relatively high concentration of free space charge throughout the dielectric, meaning that the space charge current is relevant. The differences in some 0.2-0.4 eV would not be enough to change this scenario.

Therefore, while Schottky injection and hopping conduction can provide information about the mechanism at the charge carrier level during the steady-state condition, it is the SCLC approach that is allowing us to delve more deeply into the data.

3.2.2.3 The impact of the temperature and its implications

Numerous studies have already highlighted the validity of an Arrhenius-like relationship for this material [96, 141, 222]. The Arrhenius law is described by Equation 3.2.3.

$$J = J_c exp\left(\frac{-E_a}{k}\left(\frac{1}{T_0} - \frac{1}{T}\right)\right) \tag{3.2.3}$$

In this equation, J_c represents the current at an initial temperature T_0, T is the temperature of interest, k is the Boltzmann constant, and E_a is the activation energy. Figure 3.2.13 demonstrates that the data conform to Arrhenius laws regardless of the conditioning parameters. The deduced activation energies are provided in Table 3.2.6.

It is worth noting that these activation energies are primarily dependent on the water content and have a lesser dependence on the electric field. Thus, associating the relative humidity for the equation, a coupled effect temperature-water absorption would be able to describe the increase in the current density when water is absorbed.

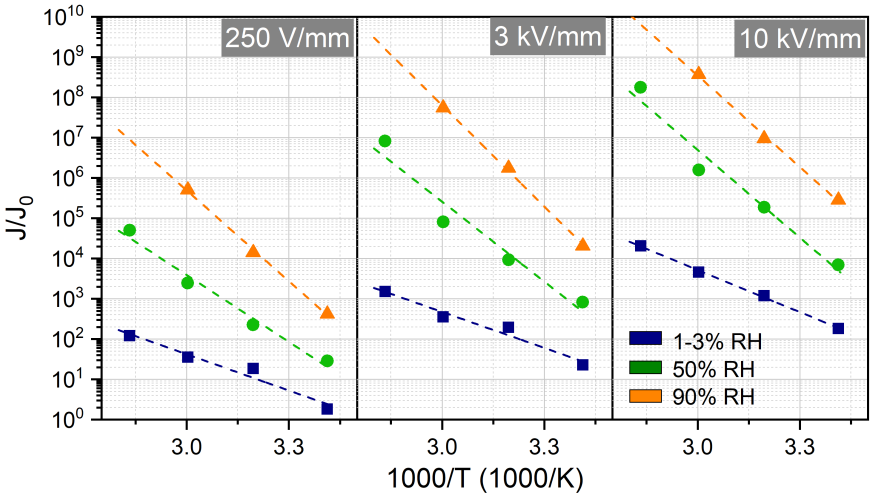

Figure 3.2.13: Current density as a function of the inverse of the temperature in the range of temperature 20-80°C. Current density as a function of the inverse of the temperature in the range of temperature 20 - 80°C.

	0.25 kV/mm	3 kV/mm	10 kV/mm
1-3% RH	0.26	0.26	0.3
50% RH	0.47	0.57	0.62
90% RH	0.65	0.72	0.65

Table 3.2.6: Activation energies E_a calculated from figure 3.2.13.

3.2.2.4 Comment about the space charge measurements

As highlighted in the literature review 1.3.1.2, an overall accumulation of negative homocharge has been found by Guillermin [101] after the same measurement technique in an unfilled epoxy resin. According to him, this could be explained by ionic mobility: a dissociation of organic acids ($R-COOH$) in protons (H^+) and conjugated ions ($R-COO^-$). Water present in the medium can also dissociate ($H_2O \rightarrow H^+ + OH^-$). Protons present higher mobility than conjugated ions or hydroxide, so they will manage to achieve faster the cathode, letting behind plenty of OH^- that account for the negative charge accumulated in the bulk. Once the cathode is injecting nehative homocharges, they will neutralize the positive charge carriers generated by dissociation. The Volt-Off measurement of Figure 3.2.14 at 14 hours of polarization shows the negative charge accumulated in the volume, and the consequently positive induced charge on the electrodes, resulting in field attenuation in the cathode and reinforcement in the anode.

It sounds contradictory to consider dissociation of water if we are analysing a dry sample. However, one has to observe that:

- The samples are not completely dried; as stressed before, we are testing a "most dried possible" sample.
- Contrary to the current measurement, we could not control the humidity around the LIPP's cell. We are not able to guarantee that the sample is not reabsorbing water during the measurement. As a matter of fact, we could

have measured the weight of the sample before and after the measurement, but for it we had to clean the sample from the silicone grease commonly applied at the interfaces, and normally consider that some electrode material had also been detached from the sample and get adhered to the cell's electrodes during the sample removal; in sum, too much uncertainties to measure a quantity that should be too small.

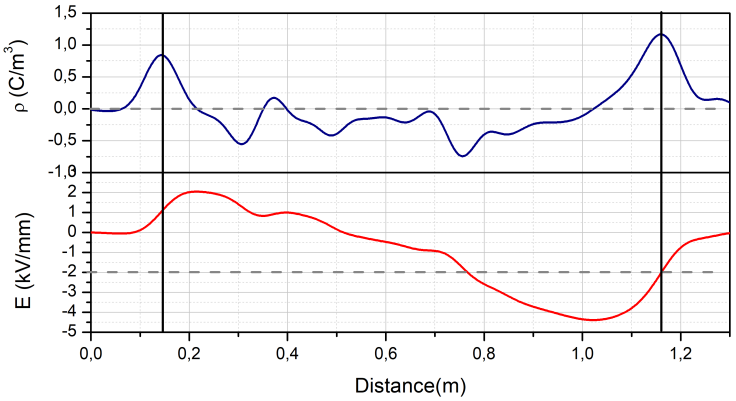

Figure 3.2.14: Volt-off measurement: Space charge density distribution as a function of distance or thickness and electric field distribution created by space charges. Parameters: Dry epoxy sample, 40°C, V_{app} = - 5000 V, gold sputtering on both sides, 14 hours of polarization.

3.3 Partial conclusions and perspectives

This chapter focused on the properties of an industrial epoxy composite, the DGEBA-MTHPA-microsilica system.

First, the water sorption mechanisms were studied.

When as a function of the time, the Fickian diffusion has been identified, which is in accordance with the literature for epoxy composites.

When as a function of the water vapour pressure, or relative humidity, the quantity of water absorbed under equilibrium respected the Henry's law.

The total amount of water absorbed is also impacted by the temperature. This was reversible, and after several investigations, could not be attributed to hydrolysis. We collected evidences that correlate this event to plasticizing.

This has a relevant impact in the electrical current measurements: the sample conditioned at 90% RH presented a conduction current up to four orders of magnitude higher than the sample at 1-3% RH.

The water reduces the voltage threshold, anticipating the non-linear conduction to lower voltages. It also shifts a non-linear mechanism attributed to the SCLC with exponential distribution of traps to a SCLC with a single-level of traps. We consider that the water can increase the quantity of shallow traps, and attenuate the effect of deep traps present in the dry composite.

Space charge measurements were executed for a dry sample at 5 kV/mm for 15 hours at 40°C. Negative charges have been encountered in the volume, producing field attenuation at the cathode and reinforcement at the anode. However, these results have to be analysed with caution because spurious signals coming from the piezo-effects coming from the quartz interfered on the quality of the curves. Besides, we were unable to control the water uptake during space charge measurements.

The so-called "traverse barrier mechanisms" (Schottky, Poole-Frenkel, Fowler-Nordheim, and Hopping) were also investigated, but little insights were obtained from them. A possible correlation with Schottky injection and field attenuation sounded promising, but this goes against the SCLC approach and the space charge measurement results.

The analysis of the current as a function of the temperature let us associate the results with an Arrhenius-like mechanism. The activation energy is dependent of the water absorption.

Pespectives : It is listed below some possibilities of future works resulted from the previous investigations:

- Space charge measurements with controlled water content, under controlled RH environment.
- Investigations at higher or lower temperatures and higher water uptake.
  - More than once, when samples conditioned at 90% RH were tested, the values at higher fields presented a tendency to come back to the ohmic regime, as in Figure 3.3.1. For now, this transition is considered a measurement artefact: the only way to measure at higher voltage levels is by injecting gas under pressure, and the gas is usually very dry, so there is a risk of drying the sample during the measure.

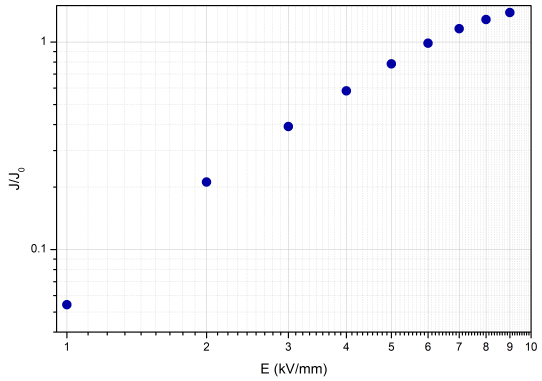

Figure 3.3.1: Relative current density as a function of the field for a sample conditioned at 90% RH. T = 40°C. Gold on both sides.

- The impact of pigments and dyes.
  - Industrial equipment generally has a color. The color is produced by pigments (if inorganic) or dyes (if organic) that are added in the formulation in small quantities (up to 1% in weight). Often, pigments are metallic oxides that can be hydrated. We conducted some investigations about the impact of some pigments presented into the form of a powder, or dispersed in a liquid, with the results of dry samples at 40°C illustrated in the Figure 3.3.2. More investigations were necessary to cross the nature of the pigment, and the combined influence of the pigment and the silica.

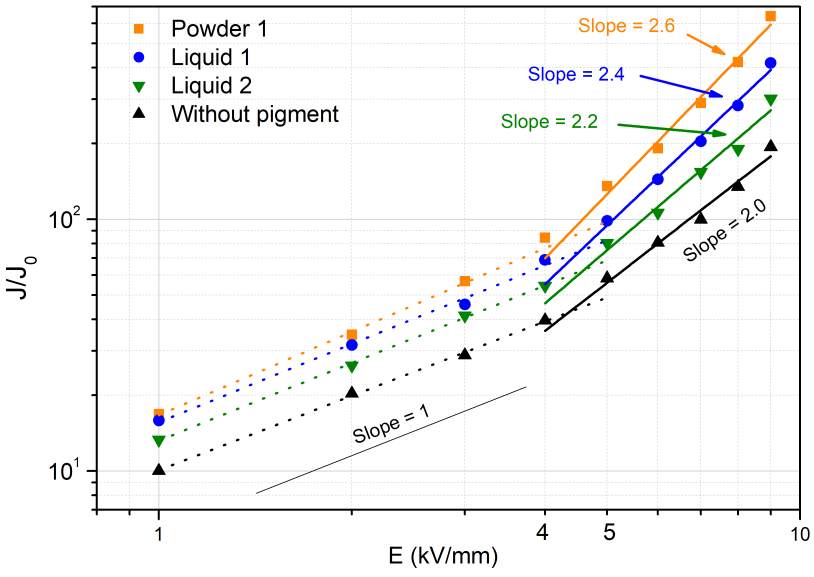

Figure 3.3.2: Relative current density as a function of the electric field for samples at 1-3% RH and different pigments. T = 40°C. Gold sputtering on both sides. Measurements executed and treated by M. Lou Lacquement

4 The monolayer of silicone rubber

This chapter presents the results and investigations concerning the silicone rubber characterized in Chapter 2, and it is structured into two main sections: water sorption (section4.1) and electrical tests 4.2.

Given that the samples were not internally manufactured at Schneider and, being an industrial-grade material with numerous additives, some of which are challenging to identify, we prepared an additional silicone rubber without fillers and dyes. Complementary electrical experiments conducted with this silicone rubber are elaborated upon in the latter part of the electrical test results section. Further information on the fabrication process can be found in Annex B. It's noteworthy that this particular silicone rubber grade is not discussed in the water sorption section (4.1) due to its inherent hydrophobic nature, rendering it incapable of water uptake.

4.1 Water Sorption of the Silicone System

The methodology employed for the epoxy is similarly applied here: initial investigation focuses on the temporal weight gain, followed by examination of the sorption isotherm. In the discussion section, our aim is to ascertain the type of isotherm and subsequently establish a correlation between water sorption and the (micro)structure of this particular grade.

4.1.1 Results

4.1.1.1 Temporal Weight Gain

Silicone rubbers are supposed to be hydrophobic, but the material tested here has absorbed some water from its environment. The water absorption has been followed by more than one temperature and %RH couple, and results are plot in Figure 4.1.1 that shows the average of three measurements of different samples, and the standard deviation. The first difference noticed in comparison with epoxy samples is that the kinetics is faster, with an equilibrium or steady-state condition achieved at around 100 minutes (approximately 1 hour and a half). Because we are not sure about the morphology of the silica, by means of precaution the water uptake has not been reported to the matrix.

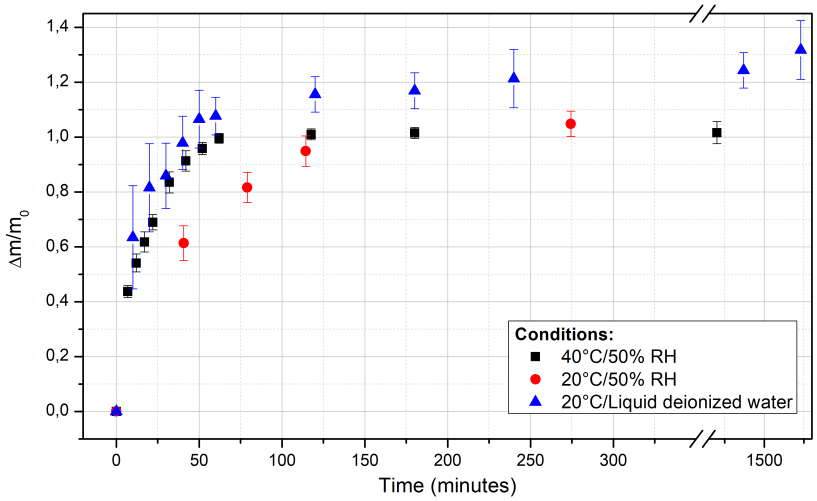

Figure 4.1.1: Water absorption of the silicone rubber as a function of time at 40°C/50% RH, 20°C/50%RH, and 20°C/deionized water for samples with 1 mm of thickness.

Another feature is the impact of the temperature. This is more clear in Figure 4.1.2, in which a sample at equilibrium at 20°C and 50% RH has been heated, and the weight decreases. These values have been corrected according to the air buoyancy effects discussed in the chapter 2 (section 2.1.5).

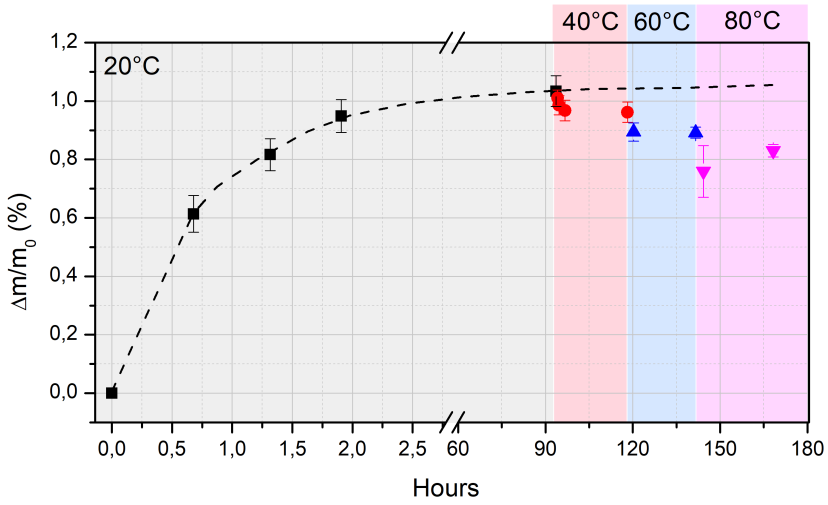

Figure 4.1.2: Water absorption as a function of time at different temperatures and 50% RH.

4.1.1.2 Steady-state Weight Gain

The same procedure of sample moisturising was applied for different values of RH, the weight of specimens tested after 1 day of conditioning is illustrated in Figure 4.1.3. It shows non-linear behavior between weight gain and RH. The specimens were able to absorb up to 1.2% of water at high RH environments. The brackets in the graphic represent the standard deviation obtained from the measurement of

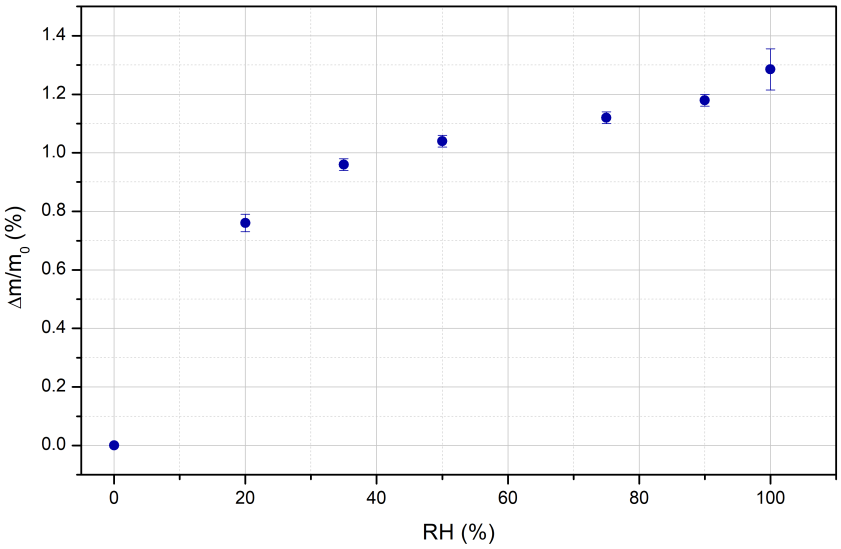

Figure 4.1.3: Saturated moisture concentration as a function of RH at 40°C.

three different samples subjected to the same conditions. It is noticed that the difference of water uptake between the driest sample and 50% RH are much larger than between 50% RH and the saturation under liquid water (100% RH); in the first interval, the weight increases 1.05%, but in the second interval, the increase of around 0.25% is observed.

4.1.1.3 Water absorption in the complementary silicone rubber

As presented in the introduction of this chapter, a second silicone rubber (LSR, without fillers) have been prepared (Details in Annex B).

For the sake of verification, these samples have been dried into an oven under vacuum according to the procedure described in section 2.3.2. No weight difference has been noted before and after the drying. They were conditioned at 40°C and 90% for at least one day, and again no weight gain has been identified: after 6 days of conditioning, a difference of 0.02% was found, which is at the limit of the balance resolution.

4.1.2 Discussion

4.1.2.1 Diffusion mechanisms

The water uptake dynamics are explored with regard to two different mechanisms: Fick's and Langmuir's. Both mechanisms have been communicated [223, 149] and even important quantities for certain silicone rubbers, as RTV and condensation grades, have been reported in other fields [224].

The Fick's approach is illustrated in Figure 4.1.4 as it fits all the curves. At 50% RH, the D_{Fick} increases from $6.10^{-11}m^2/s$ at 20°C to $2.10^{-10}m^2/s$ at 40°C, which is logic since higher temperatures should speed up the mechanism. Under room temperature (around 23°C) in deionized water, $D_{Fick} = 1.10^{-10}m^2/s$. Looking closely the datapoints, this fit looks less evident, but the standard deviation of 8.10^{-12} is considered low. These values are two orders of magnitude higher than those for epoxy.

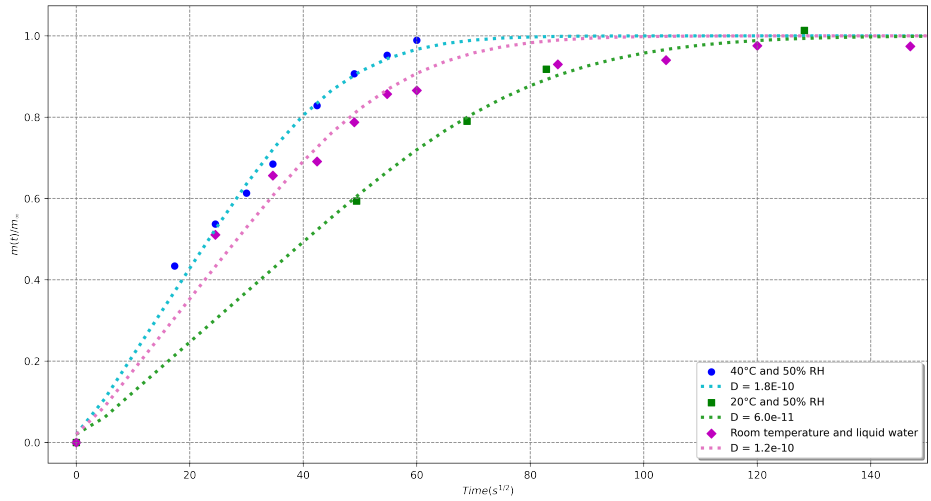

Figure 4.1.4: Water absorption as a function of the square root of the time for many silicone rubber samples, with a fitting corresponding to the Fick's law. Average of three different samples.

	20°C and 50%RH	40°C/50%RH	T_{amb}/ liquid
$D_{Langmuir}$ (m^2/s)	2.10^{-11}	1.10^{-10}	2.10^{-10}
D_{Fick} (m^2/s)	6.10^{-11}	2.10^{-11}	1.10^{-10}
α	2.10^{-4}	2.10^{-4}	5.10^{-5}
β	3.10^{-4}	7.10^{-3}	$1,5.10^{-4}$

Table 4.1.1: Langmuir's coefficients for the water uptake of silicone samples

The same investigation has been conducted for the Langmuir's mechanism, with results shown in Figure 4.1.5. Again, all the datapoints seem to fit, and the diffusion coefficients changed considerably. They are summarised in table 4.1.1.

Even if the diffusion coefficients change from one mechanism to another, they are still at the same orders of magnitudes. Besides, here, the debounding coefficients (β) are higher than the bounding ones (α) leading to the conclusion that the debounding is somewhat favored.

Since both mechanisms seem to describe the kinetics satisfactorily, we believe that the Fick's diffusion, being more simple, should be privileged.

4.1.2.2 Water sorption isotherms

Looking closely to Figure 4.1.3, one can note the similarity between this curve and a traditional isotherm corresponding to the Langmuir's physical adsorption (see literature review, section 1.2.4.3). This model is the simplest mass transfer process of gases and vapors on solid surfaces that physically represents a monotonic approach to an adsorption that corresponds to a monolayer.

If we count with the last datapoints of Figure 4.1.3, i.e. at 95% and 100% RH, in the sense we consider that at higher RH the water absorption should increase, the datapoints fit with the Type II pattern of Brunauer (or the BET model described

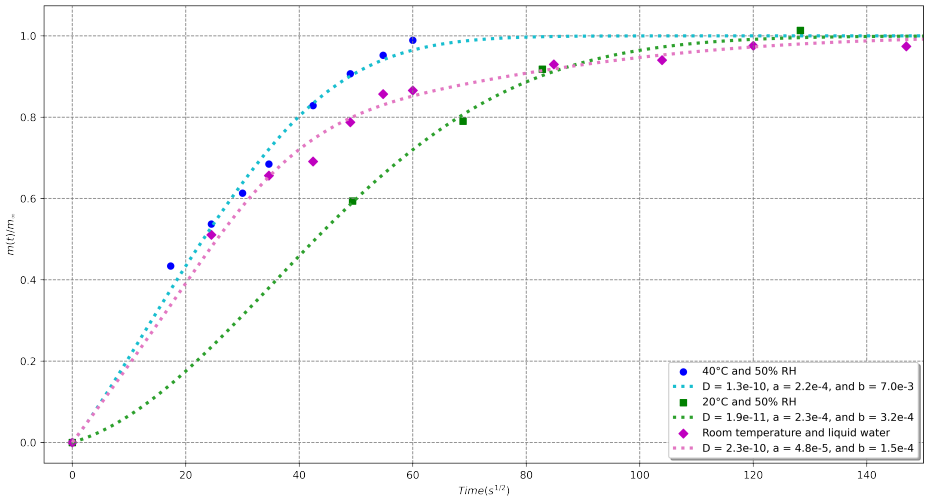

Figure 4.1.5: Water absorption as a function of the square root of the time for many silicone rubber samples, with a fitting corresponding to the Langmuir's law.

in the literature review, section 1.2.4.3). However, for the sake of simplicity, they were neglected in the fitting.

Thus, the correlation with data and Langmuir's model is illustrated in Figure 4.1.6. The coefficient b is equal to 0.001 Pa^{-1}. We recall that the b represents the affinity constant, and tells how strong an adsorbate molecule is attracted onto a surface [70].

Another evidence that reinforces the hypothesis of adsorption is the thermal behaviour. The adsorption is exothermic, then favoured as the temperature decreases [63]. Besides, the parameter b is proportional to $exp(T^{-1/2})$. The data of Figure 4.1.2 of water sorption at 50% RH and additional data obtained at 90% RH are re-plotted into the Figures 4.1.7(a) and (b) to show this effect.

Where and how the water could be adsorbed? If we are measuring a bulk change, how is it possible that we have identified an adsorption pattern? The first hypothesis is that the water vapour will only adsorb onto the sample's surface. Even if it's true (there is no reason to think that the water vapour won't be adsorbed on the sample's surface) the total weight increase looks too high. The water vapour should penetrate the bulk. Considering that this material is a nanocomposite, the extension of the silica's surface may be relevant to justify a water adsorption large enough to be measured by gravimetric measurements. In addition, the fact that the LSR silicone rubber without filler does not uptake any water (Annex B) supports the hypothesis of silica adsorption in the filled-industrial silicone grade.

This feature is not original itselt, and as presented in Chapter 1 (1.3), there are many evidences in the literature about water sorption around nanofillers and microfillers embedded in a polymeric matrix (as in [153, 131, 225, 226, 227]). The novelty here lies on the evidences that, up to 75% RH, the water may not be organized in a core-shell structure, but in a monolayer (it is one of the assumptions of the Langmuir's isotherm model).

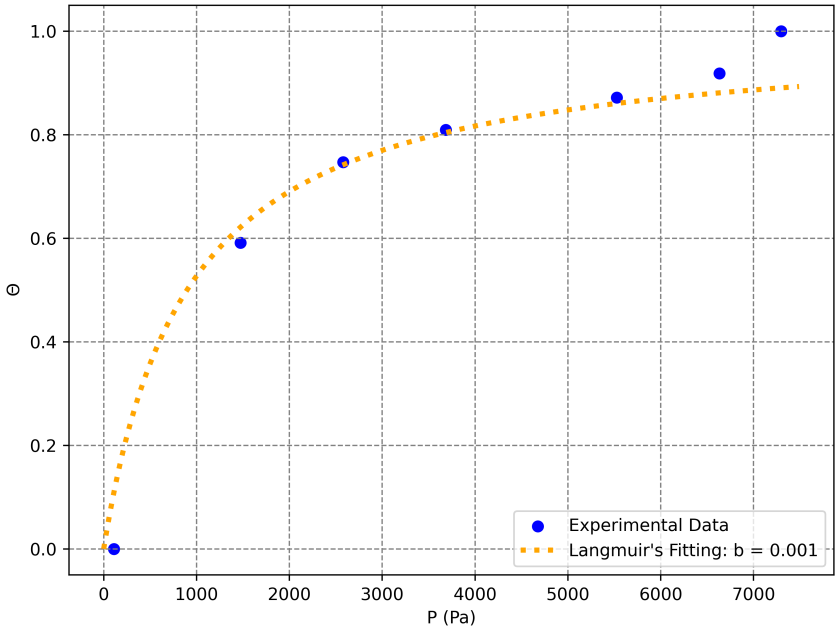

Figure 4.1.6: Rate of sorption as a function of the vapour pressure of water at 40°C for the industrial silicone rubber. Fitting with Langmuir's adsorption model, with b = 0.001.

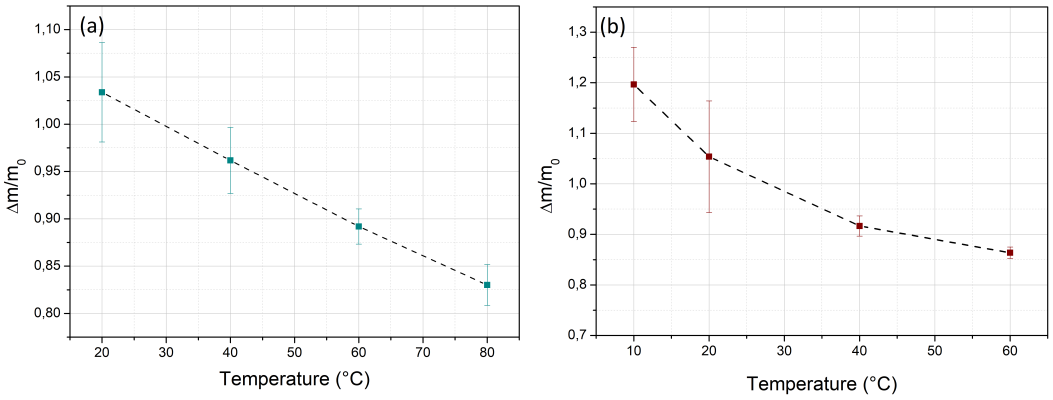

Figure 4.1.7: Water sorption as a function of the temperature at 50% RH (a), and 90% RH (b).

How the water would reach the silica? The water can not only diffuse through the matrix, but also through the filler-matrix interface by capillarity forces, specially if the wetting of the filler's surface by the matrix is incomplete [228]. The high hydrophobicity of the silicone matrix must account for a poor wetting as a result of a poor adhesion of filler-matrix, allowing enough free space for water wicking.

Where exactly the water could be adsorbed? The Langmuir's adsorption model assumes that the adsorbed species are adsorbed at definite, localized sites, each site accommodating (attaching) only one adsorbate species. Lange [74] argues that there would be two types of adsorbed water on the surface of precipitated silica: physically adsorbed water giving a BET isotherm, and a H-bonded to silanol groups ($SiOH$) corresponding to Langmuir's isotherm, requiring 10 kcal activation energy for its remotion. Because both types are not clearly separated, the data suggest the predominance of a monolayer coverage.

Silanols may be present on the surface of amorphous fumed silica [154], and they may be randomly distributed on the outer surface. Caillerie et al [155] investigated commercial pyrogenic silicas and three different types of silanols are proposed: (1) isolated "internal" inaccessible, (2) external "free", and (3) external hydrogen bounded. Yet, the hypothesis of a monolayer is also proposed, with a surface coverage of 4.75 H_2O/nm^2 that starts to be build at RH as low as 3.6%. The ratio of water adsorbed and surface hydroxyl should be 1:1.

Water adsorbed in silica can indeed provide charge carriers. According to Bascom [129], there would be proton and hydronium exchange between adsorbed water and the hydroxyls at the surface, culminating in water dissociation. The rate H^+/H_2O is $10^5 - 10^6$ times higher in the water on silica than in pure water. Similar events should be allowed on the surface of Fe_2O_3 which are acid-like because its crystalline structures provides preferential accommodation of OH^- (remember that this silicone grade has some iron oxide as well coming from the dye).

Prigogine et al. [156] agrees with the idea of a charge transfer, that would be associated with the unsaturated character of silicon atoms. They propose the existence of two adsorption sites: one acting as an electron acceptor (proton donor) and another as an electron donor (proton acceptor), with interdependence between them. In other words, a duality acid-base. When focusing on pure silica powder, they observed that water tends to pair with the $-OH$ groups from the $SiOH$, forming clusters. Due to the slight acidity exhibited by silicon, it redistributes the electronic density and provides protons that are transferred from the $-OH$ to the water cluster. As the $-OH$ loses a proton, the oxygen of the hydroxyl acquires a negative charge, strengthening the π-bond with silicon. This enhances the electronic density around silicon, resulting in the displacement of electrons towards neighboring oxygens, imparting a basic character to them.

All of these possibilities are schematized in Figure 4.1.8: at dry conditions, silanols are available; as the RH increases, water molecules are adsorbed on the surface, and clusters can be formed around them as the RH increases even more.

Our interpretation is that not all of the surface may be available for adsorption due to filler-matrix contact. This contact may limit (but not inhibit) water clustering, especially at higher relative humidity (RH), as illustrated in Figure 4.1.3. The observed increase in water uptake under conditions of RH exceeding 75% (the last 2 datapoints of Figure 4.1.6 or Figure 4.1.3) aligns with the BET model assumption of clustering or multilayer formation when the vapour pressure approaches the

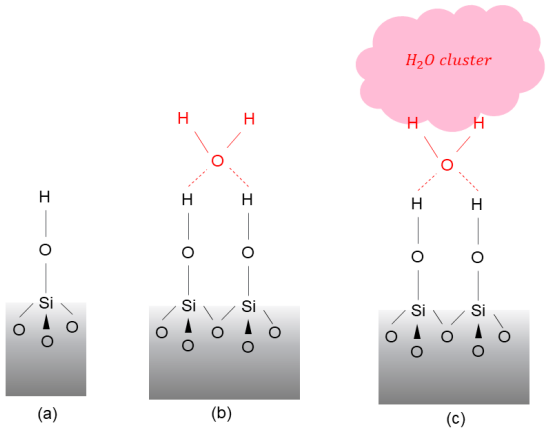

Figure 4.1.8: Simplified scheme of a silanol free to be bounded (a), a bound silanol (b), and a water cluster around a bounded water molecule (c). Adapted from Prigogine [156]

saturation. This notion recalls the idea of core-shell structures and potential water connections between silica particles.

Adsorption onto silica pores should not be excluded as well, but the existence of such pores in the nanosilica of the study was not further investigated.

4.2 Electrical tests in the Silicone System

4.2.1 Results

4.2.1.1 Current-Voltage profiles

Influence of temperature and water content: Figure 4.2.1 presents the isothermal curves of current density as a function of electric field for dried samples. Two distinct domains are proposed:

- In the first one, at lower fields, the dot line with a slope equal to 1 representing a linear relationship matched with measurements. A linear relationship represents an ohmic behavior in which $J = \sigma E$, with σ being the conductivity that doesn't depend on the field.

- In the second one, a non-linear behavior recognized by a line with a slope greater than unity. The slope decreases with temperature from 3.6 at 20 ^{o}C to 2.5 at 80 ^{o}C. The field thresholds separating these domains (the black arrow) also decrease with temperature, suggesting that the mechanism responsible for the non-linearity is also temperature-dependent.

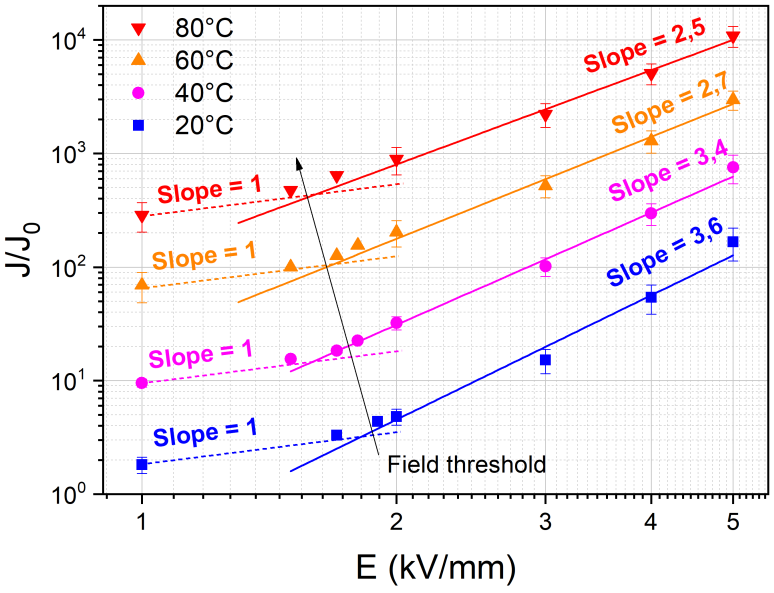

Figure 4.2.1: Relative current density as a function of electric field for dry silicone rubber samples at 20°C, 40°C, 60°C, 80°C.

Figure 4.2.2 shows the results for samples previously conditioned in moist environments (50% RH and 90% RH) and tested at equal conditions at low fields (1-3 kV/mm) or under 2 relative bars of dry air at higher fields (4-5 kV/mm). As for dried samples, two domains (linear and non-linear, or ohmic and non-ohmic) are suggested. As a whole, for 50% RH, current density increased 1 decade in comparison with dried specimens.

For tests done at 50% RH, one can notice that:

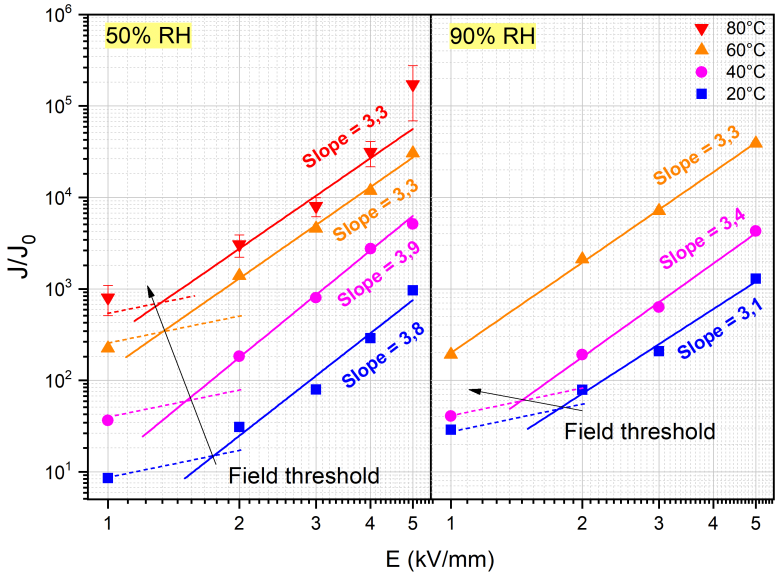

Figure 4.2.2: Relative current density as a function of electric field for hydrated silicone rubber samples at 4 temperatures. RH = 1-3%.

- The field thresholds look similar than for dried samples, despite the increase of current density.
- The slopes are higher than those of dried ones, and they decrease more slowly with temperature.

For tests at 90% RH, it is worth to mention that:

- Most values of current density are similar to those at 50% RH unless values at 20°C for lower fields.
- The black arrow looks more bent, which point out a higher sensibility with field.
- No values at 80°C and 90% RH were measured due to instabilities of measurements at this condition.

Aiming to investigate the influence of electrode materials, measurements similar as those made with gold sputtering were carried with silver or copper metallized electrode and carbon black electrode (without metal sputtering). All results are illustrated in Figure 4.2.3 that highlights the effect of electrode material. In similar conditions, current density can change up to 1 decade from one electrode system to another. Among different temperatures, the hierarchy of electrode systems remained generally the same unless for carbon black that progressed differently than the others.

Influence of electrode metal on current densities: Considering that the electrode material can matter on the measured current, asymmetrical configurations have been tested by current measurements and space charge. By *asymmetrical electrode* we mean electrodes that differs in nature on each side of the insulation. Into

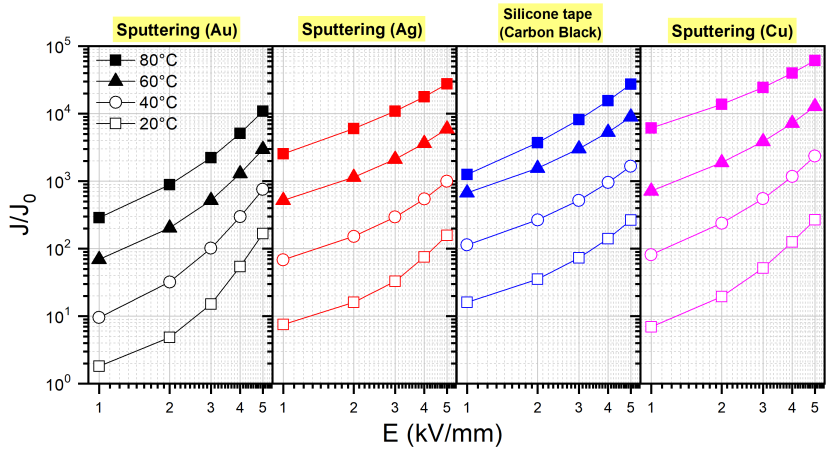

Figure 4.2.3: Influence of the metal electrode on the relative current density as a function of electric field for dry silicone rubber samples at 4 temperatures.

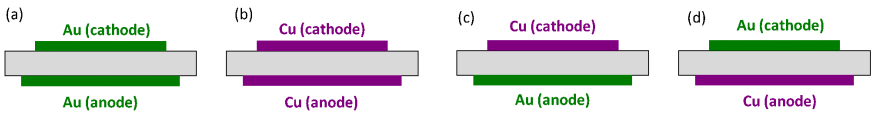

Figure 4.2.4: Electrode designs for symmetrical (a and b) and asymmetrical (c and d) configurations.

bushings, for example, the insulator is associated with the conductor (usually copper or aluminum) in one side and a screen on the other side (potentially some other metal, as steel). Just gold and copper have been applied, in the configurations of Figure 4.2.4.

The current density as a function of the electric field for the anode/cathode couples (Au/Au, Cu/Cu, Au/Cu and Cu/Au) are presented in Figure 4.2.5. The linear domain is suggested by the gray line in which a slope equals to 1 has been extrapolated from data at 1 kV/mm. Some additional datapoints for Au/Au samples have been measured and added to the graph in order to verify this transition. The non-linear region is underlined by a slope higher than the unity, with their values listed in the table.

In general, current density values of symmetric gold electrode samples are one order of magnitude lower than all the other systems of the study. The non-linear region has a slope equals to 3.43.

The current density of symmetric copper electrode samples has a slope in the non-linear region equals to 2.47. The systems with two different electrodes presented a non-linear mechanism with a slope close to 2 (slope = 1.86 and 1.87). Both symmetric copper sputter-coated and asymmetric samples presented close values of J.

It is worth to note that the threshold (represented by the circle) seems to be the same for symmetric samples (E = 1.64 kV/mm), and also the same for asymmetric ones (E = 1.88 kV/mm).

One may ask if a slope of 2 is systematic for asymmetrical systems. Additional measurements have been executed for new samples in which just one side has been sputter-coated. The other side stayed in contact with the conductive silicone tape

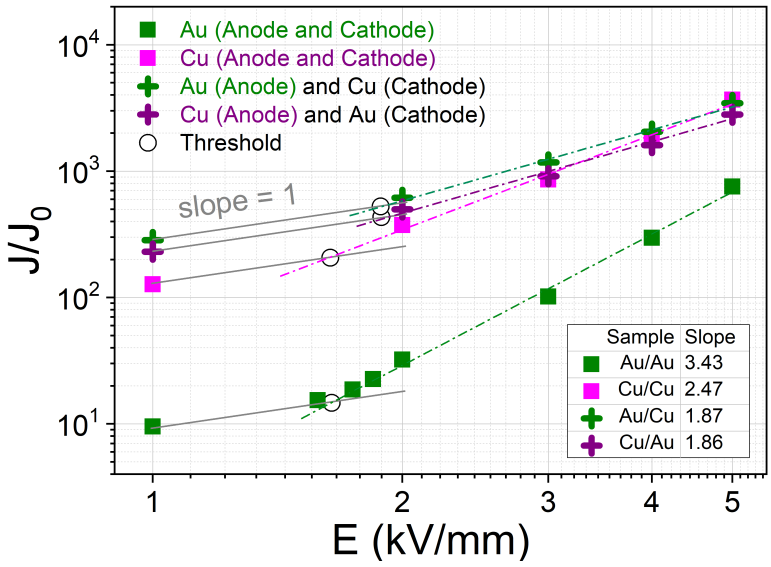

Figure 4.2.5: Relative current density as a function of electric field for dry silicone rubber samples associated with different electrode systems: Au or Cu on both sides, and Au/Cu at both polarities. T= 40°C.

(SiR-C, i.e. filled with carbon black, so as the conductor is made of carbon) that has always been present (Figure 2.4.1). The result, that can be seen in Figure 4.2.6, shows that all the profiles in the non-linear region can be fit with a slope very close to 2 as well, including symmetric SiR-C electrodes (i.e. without any coating).

In Figure 4.2.6, all the asymmetric systems exhibits higher currents than the symmetric one. In addition, the polarity applied to the conductive silicone separates regions of current amplitude with close values for Au/C and Cu/C, or for C/Au and C/Cu. Again, a slope equals to 1 has been extrapolated from 1 kV/mm and presented as the gray line. In this case, the threshold seems to be higher when gold was applied as sputter-coat.

Because the insulator is the same, it leads to conclude that the measurement of the current density (so as the volumetric conductivity itself) cannot be dissociated from the electrode system. In other words, conductivity seems to be a property of the electric insulated system, which includes the metallic contacts.

4.2.1.2 Space-charge profiles

The charge density profile through the symmetric gold-coated sample under voltage (Volt-on) and immediately after short-circuit (Volt-off) is showed in Figure 4.2.7(a). On both curves, the charge distribution seems homogeneous inside the bulk, and the volt-off curve reveals that the material has been slightly negatively charged. The presence of negative charge is confirmed by positive induced charges at the electrodes on both sides of Volt-off measurement.

When the sample is copper-coated on both sides, this profile is altered, as depicted in Figure 4.2.7(b). Induced peaks in Volt-on curves are lower but wider. An accumulation of charges is evidenced by the negative charge-packet located on the cathode side both on Volt-off and Volt-on curve.

Either under volt-on or volt-off, the peaks at the electrodes are broader than for Au/Au sample. Under volt-on, these broad peaks can be attributed to ho-

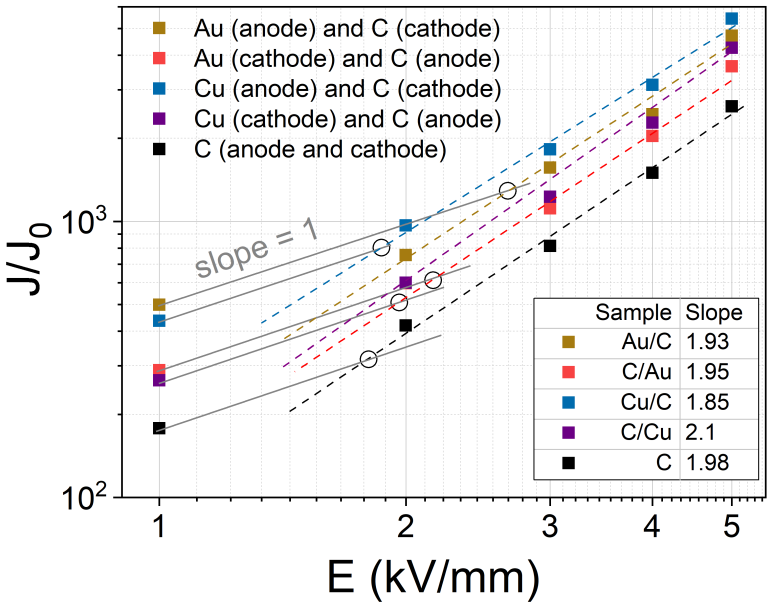

Figure 4.2.6: Relative current density as a function of electric field for samples with electrode systems made of carbon (C) on both sides, or by gold (Au) or copper (Cu) replacing one of the carbon electrodes.

mocharges injected under both polarities. Under volt-off, positive homocharges are still observed but negative homocharges are not. Conversely, a slight concentration of positive heterocharges is detected under volt-off at the cathode.

Anyway, as it will be addressed in the discussion section, it has been observed that the copper in contact with the cathode has been oxidized. The passivation of the copper layer during the measurement has major impacts in the results, and despite many different attempts, there is no simple way to get rid of it as we were enable to perform space charge measurements in inert atmosphere. We insisted in perform and show these measurements because it still has a link with the reality: the atmosphere during application is not inert, and the conductor is not entirely free of corrosion mechanisms.

In the case of the asymmetric electrode system with gold as cathode and copper as anode, qualitative observations are similar as for Figure 4.2.7(b) with slight differences. The negative charge-packet is centred deeper inside the sample, as portrayed in Figure 4.2.7(d). This logically increased the peak induced under volt-off at the cathode which is larger than in Figure 4.2.7(a). The increase of the induced peak at the anode reveals a larger concentration of these negative space charges as a whole with the gold cathode.

The Au/Cu sample has been discharged and tested again at the same voltage level, but with an opposite polarity. Figure 4.2.7(c) shows a similar Volt-on profile as in Figure 4.2.7(d), as if the curve were reflected by the y axis, i.e. an accumulation of positive charges into the bulk instead of negative charges.

4.2.1.3 Complementary results: exploring a second silicone rubber free of fillers

As mentioned in the introduction of this chapter, the silicone rubber primarily selected for investigation is an industrial grade full of additives and fillers. The interest

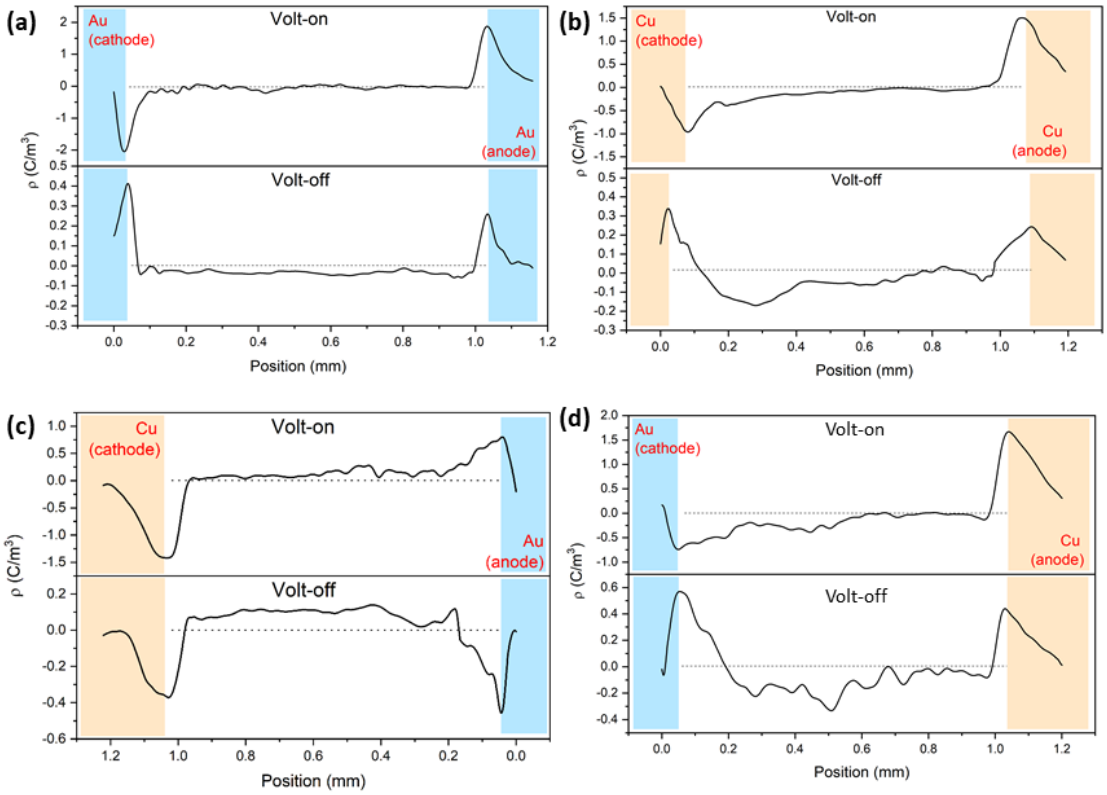

Figure 4.2.7: Charge density profiles as a function of position or distance (mm) for different metal sputtering and polarities: Au/Au + 5000 V (a), Cu/Cu +5000 V (b), Au/Cu - 5000 V (c), and Au/Cu + 5000 V (d).

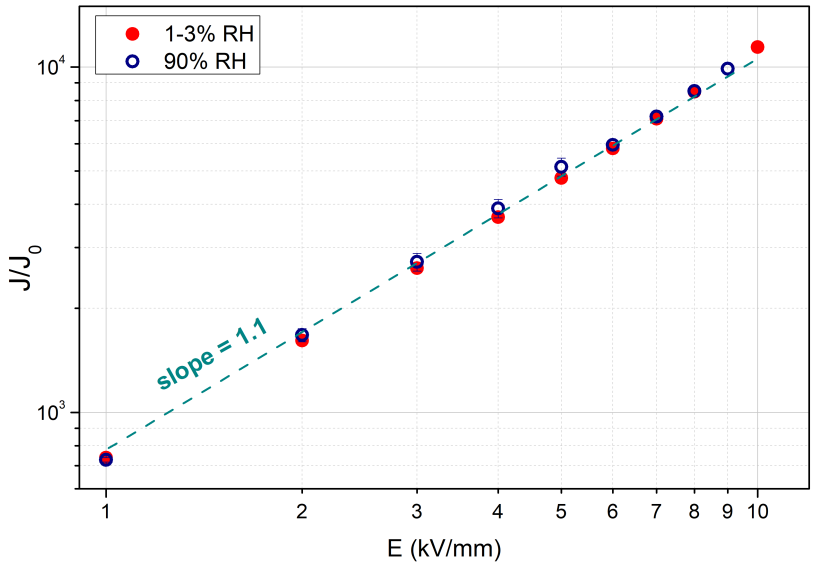

Figure 4.2.8: Relative current density as a function of electric field for LSR Lumisil 7601 A / B ® from Wacker. Proportion of components: 50% A, 50% B. Temperature of electrical test: 40°C. Electrical tests conducted by Lou Lacquement.

of testing another silicone rubber is motivated not just by the seek of any generalization for such materials, but also to the understanding of the role of all these additives and components in the final electrical property. Therefore, another grade free of fillers, with the same matrix, and mold by gravity casting is investigated. Details about this grade and the molding procedure are detailed in the Annex B.

Figure 4.2.8 shows the I-V profiles at 40°C and at 1-3% RH or 90% RH or such silicone.

Because of the impact of water uptake in the electrical properties of the industrial silicone rubber, we insisted in perform electrical tests with controlled relative humidity levels for this grade too.

Some important observations are listed below:

- All measurements presented the same results. As this grade does not uptake moisture, the RH has no impact on the electrical performance.
- The slope is equal to 1.1. This silicone is considered ohmic for all the voltage levels tested, i.e. it has a constant conductivity.
- At 1 kV/mm, the current density is around 500 times higher than the industrial grade, being equivalent to that grade at 80°C.

Two additional samples have been analysed:

- In a first one, the material has been cured for 1 hour at 160°C without post-curing. Not the all the material has been cured, but a portion on the middle of the plate was able to be collected. For this sample, we consider that we have an incomplete cross-linked elastomer.
- In a second one, a mixture of 25% of component A and 75% of component B was prepared following the adjusted procedure (with curing and post-curing). Here, we consider we have an over-crosslinked elastomer.

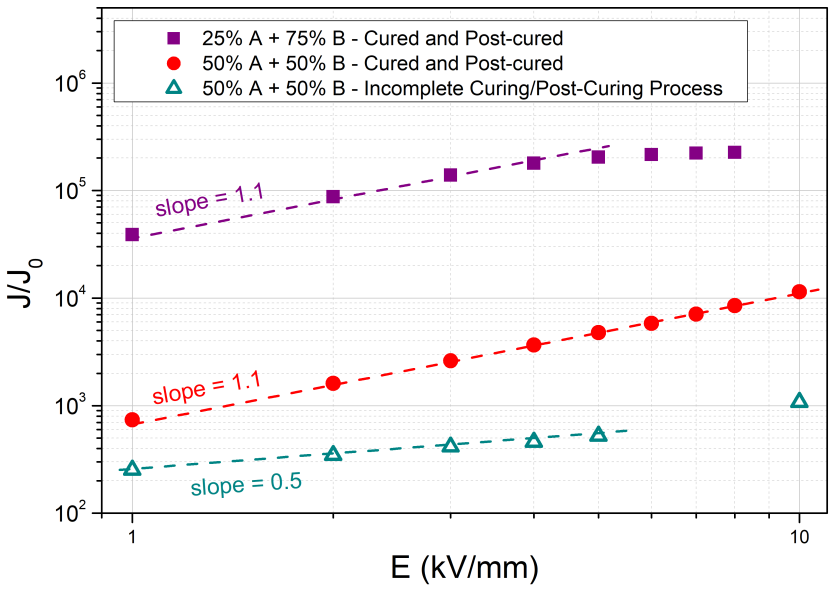

Figure 4.2.9: Relative current density as a function of electric field for three different LSR Lumisil 7601 A/B ® samples. Temperature: 40°C. Electrodes: 200 nm gold sputtering on both sides. Dry N_2 pressure inside the test cell: 2 bar rel. Electrical tests of red circle and purple square data points collected by Mr. Lou Lacquement.

Figure 4.2.9 shows the I-V profiles of these samples. Differing from the reference 50% A 50% B material of Figure 4.2.8, it is worth to note that:

- The sample with uncompleted curing/post-curing process presented a lower current density, with a slope lower than the unity. The apparent conductivity of this material is decreasing with the increase of voltage level.
- The 25% A 75% B mixture present a higher current density, with the same slope at lower fields, but the slope evolves across data points, decreasing at values lower than the unity.

In no case the non linearity of Figures 4.2.1, 4.2.2, 4.2.5, and 4.2.6 has been found.

4.2.2 Discussion

As stated for epoxy in chapter 3, the purpose of the upcoming discussion is not to deliver a comprehensive evaluation of all the data presented in the results section. Instead, the analysis will be centered on addressing the following questions:

- How the current density J is impacted by the water uptake? (4.2.2.1)
- Where does the boundary lie between ohmic and super-ohmic conduction? (Section 4.2.2.2)
- What can stand for the super-ohmic mechanisms? How asymmetric electrode systems impact what has been stand for the reference measurements? (Section 4.2.2.3)
- What can be stated for the filler-free silicone rubber? (Section 4.2.2.5)

4.2.2.1 An electrical conduction model based on water adsorption

The first relevant information from Figure 4.2.2 (the J measured at $RH = 50\%$ and $90\%RH$) is that the electrical conduction does change according to the water adsorption. Thus, one can consequently doubt if the current measured is still a bulk current (through the matrix) or mostly a the interface silica-matrix.

Considering data from Figures 4.1.3 and 4.1.6, it is inferred that the electrical measurements conducted at 1-3% RH and 50% RH are likely ruled under an incompleted monolayer, with measurements at 50% RH approaching monolayer completion. However, at 90% RH, monolayer is supposed to be completed, or at least the presence of water clustering and/or multilayer formation may be anticipated. We stress that there is insufficient evidence of either core-shell structures or clusters substantial enough to bridge silica particles. In addition, tests conducted at RH below 75% are unlikely to be affected by water channels as the monolayer would not be well completed.

Aiming to have more insights about the impact of the RH in the current density, additional electrical measurements with samples conditioned and tested at $RH = 25\%$ were performed. The data of the relative J as a function of RH or water uptake are organized in the graphics of Figures 4.2.10(a) and (b), respectively.

As can be seen, the current increases with the RH until about RH = 50% and then stabilizes. This evolution correlates fairly well with the evolution of the water uptake with the RH as depicted in 4.1.3. Once the monolayer is completed, the J ceases to increase. Hereafter the value of J at $RH = 50\%$ is referred as the saturated current-density (J_s).

The striking resemblance in format between Figure 4.2.10(a) and Langmuir's isotherm has motivated the formulation of an equation that establishes a relationship between the current increase and water vapor pressure resembling a Langmuir isotherm. There are not sufficient data for confirming with precise accuracy any attempt, but a reasoning with a linear relation can be drafted as follows: if we assume that the increase in current is proportional to the water adsorbed on the surface of the silica, as it sounds to be the case, then the relationship of the increase in current with the current at the monolayer completion (J_s) should be proportional to the

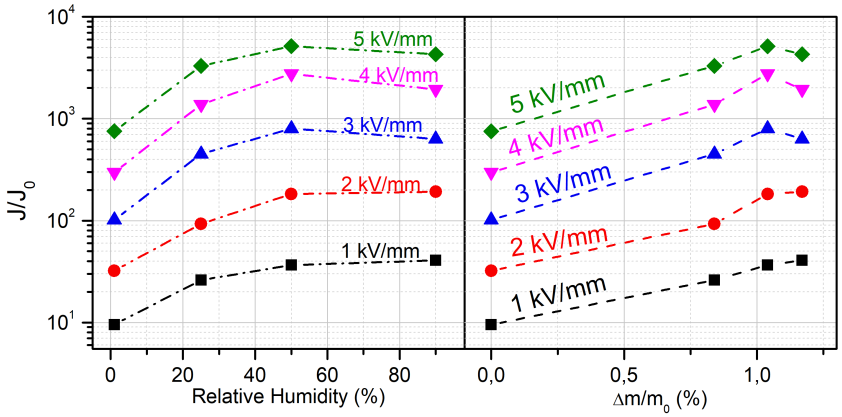

Figure 4.2.10: Current density as a function of the relative humidity (a) and as a function of water uptake (b) for a silicone rubber specimens tested at 40°C.

fractional sorbed water θ by some constant A, as in Equation 4.2.1. In the equation, the b_J has the same unit as the b coming from the Langmuir's isotherm (Pa^{-1})

$$\frac{J - J_0}{J_s} = A.\theta = A.\frac{b_J P}{1 + b_J P} \tag{4.2.1}$$

The equation 4.2.1 fits well for the first three datapoints (Figure 4.2.11) that comprehend the vapour pressure range of monolayer formation, unless at 4 kV in which the fit is not proper (the standard deviation for the coefficients are the double of their values). The last datapoint, at $RH = 90\%$ is generally presented below the fit. According to this model, the curve line at $P = 6635Pa$ corresponding to $RH = 90\%$ represents what the current density value should look like if the monolayer formation was allow to continue. The coefficients A and b_J are listed in Table 4.2.1. It is noted that A is field dependent and decreases when the voltage increases, and b_J trend to behave directly proportional to the field. Should this suggest that the electric field promotes water uptake?

It also may respect all the requirements of the Langmuir's isotherm [70], as so as special requirements for composites that make the current measurement sensible to the adsorption:

- The filler's surface is homogeneous, so the adsorption energy is constant over all sites.
  - The matrix is hydrophobic, so it will not compete on trapping water with the surface.
- Adsorption on surface is localised.
  - The adhesion matrix-filler is poor, otherwise the matrix will occupy the sites possibly occupied by the water.
- Each site will accommodate only one molecule or atom. Modifications of the Langmuir isotherm for multimolecule receptor binding are possible [68].

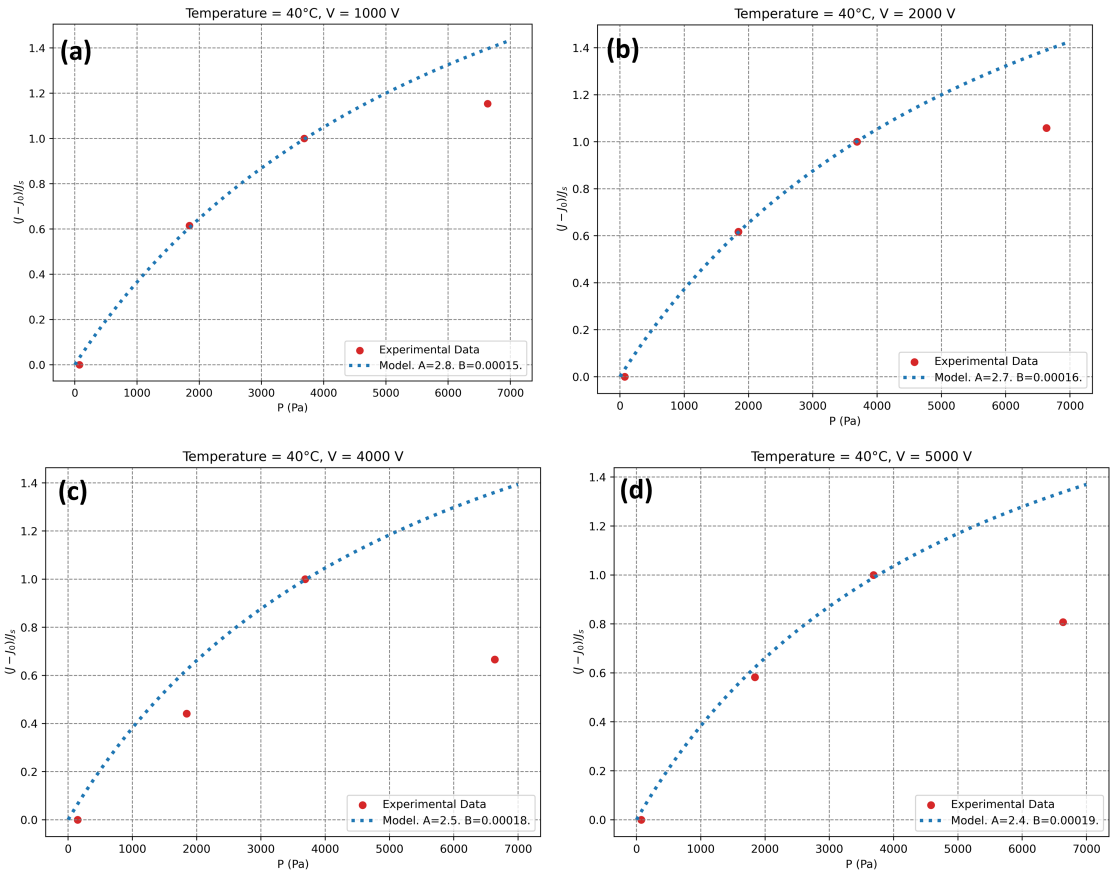

Figure 4.2.11: Relative electrical current density increase as a function of the water vapour preasure and fit with Equation 4.2.1 for silicone rubber samples at 40°C, and different voltage levels (from 1 to 5 kV).

A general equation is proposed (Equation 4.2.2) having a Langmuir-like behavior. More data is necessary to assert about the temperature and field-dependent parameters.

$$J(E,T,P) = J_0 + J_s.A(E,T).\left(\frac{b_J(E,T)P}{1+b_J(E,T)P}\right) \tag{4.2.2}$$

This approach ignored if the conduction mechanism is ohmic or not. Because the voltage threshold (as discussed in the next section, 4.2.2.2) lies in the 1-2 kV/mm interval, no graphic in Figure 4.2.11 shows data extracted from two supposed different mechanisms at the same time.

V_{app} (kV)	A	b (Pa^{-1})
1	2.8	1.5E-04
2	2.7	1.6E-04
3	2.6	1.7E-04
4	2.5	1.8E-04
5	2.4	1.9E-04

Table 4.2.1: Coefficients of Equation 4.2.1 obtained from the fitting of Figure 4.2.11

	20°C	40°C	60°C	80°C
1-3% RH	1950	1760	1600	1500
50% RH	1740	1530	1350	1300
90% RH	1780	1480	$\leq$ 1000	-

Table 4.2.2: Approximate estimated threshold voltages V_{th} between linear and non-linear $J(E)$.

4.2.2.2 Determining the linearity threshold

In the $J-V$ curves of samples with gold symmetric electrodes at different temperatures and humidity (4.2.1, 4.2.2) an attempt to separate the mechanisms in ohmic and non-ohmic is provided, and some additional measurement around the supposed interception for the driest sample also suggests a threshold. The approximate voltage thresholds V_{th} are listed in Table 4.2.2. Their dependencies with temperature and relative humidity merits to be put in contrast of what has been stated for the epoxy:

- As for the epoxy, the V_{th} is reduced with the increase of temperature. But here, this reduction is soft.
- At the same conditions of temperature and humidity, the silicone presented a V_{th} of about 3-4 times smaller than those of the epoxy.
- As for the epoxy, the V_{th} is reduced with the increase of relative humidity. These values are projections based on the graphic of Figure 4.2.2. However, between 50% RH and 90% RH, the difference looks less significant or even indistinguishable (as at 20°C/50% RH compared to 20°C/90%RH).

For dry samples ($RH = 1-3\%$) at 40°C, the change of the metal did not change the V_{th} range. The thresholds for the asymmetric electrodes (Figures 4.2.5 and 4.2.6) are still considered at the same range. As a matter of fact, the V_{th} of the curves of the samples Au/C and C/Au (4.2.6) look higher than 2, but there are not enough datapoints to point accurately the V_{th}.

4.2.2.3 Exploring the current mechanisms and charge transport

The effect of electrodes underlined in the results section is orienting the reasoning onto an injection mechanism since they take into consideration the nature of the electrodes through their respective work functions ϕ. Schottky requires a linear plot of J as a function of the $\sqrt{E}$, and Fowler-Nordheim a linear plot of J/E^2 against E^{-1}. The both attempts are presented in Figure 4.2.12 for the Au/Au silicone rubber at 1-3% RH and 40°C, with the results at higher temperatures and humidity following the same trend: a correlation with Schottky.

The tunnel effect is excluded because the thermal behavior follows an Arrhenius relation between J/T^2 and $1/T$, illustrated in Figure 4.2.13.

The hopping conduction is also thermo-activated, but it does not take into account the nature of the electrodes. The curves can also fit with the SCLC models, and from them the mobilities can be extracted, but again little insight is offered about the electrode material.

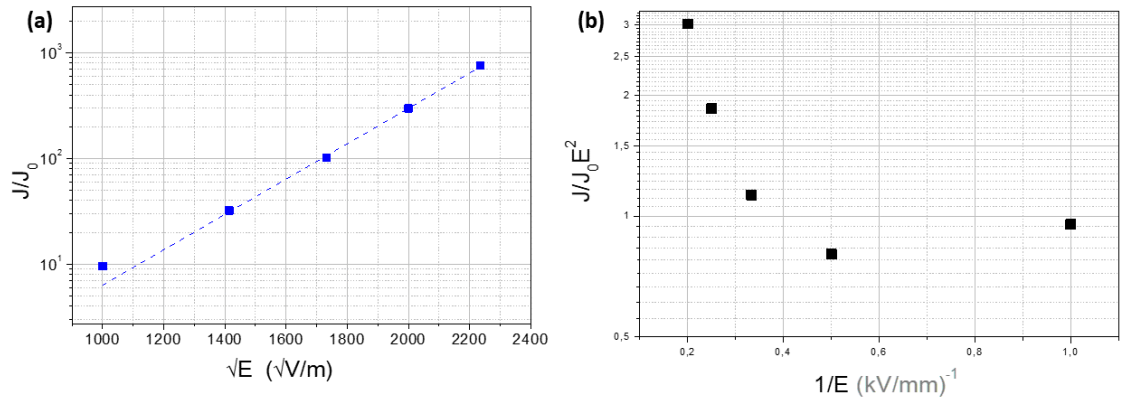

Figure 4.2.12: Verification of the data with Schottky (a), and Fowler-Nordheim (b) injections. The data applied was those from the silicone rubber at 1-3% RH, 40°C, and with symmetric gold sputtering on both sides

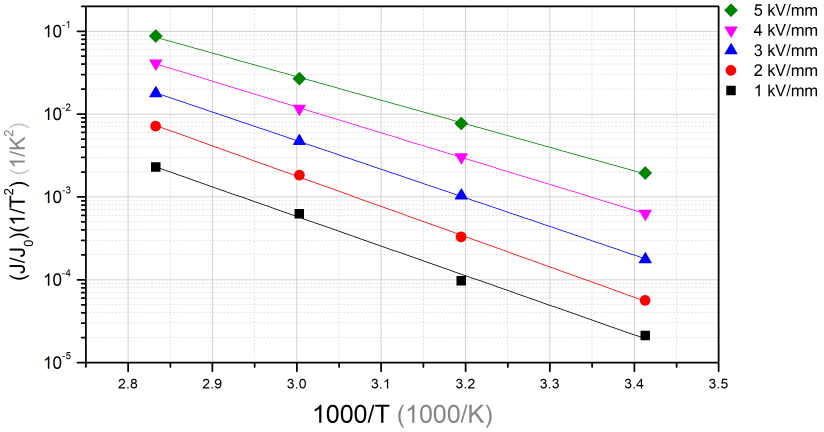

Figure 4.2.13: Relative J/T^2 vs $1000/T$ for 5 electric fields; dried sample with gold sputtering and tested at 1-3% RH and 40°C.

Thus, the mission of the following discussion is to explore how the J can be impacted by the cathode and the anode. The conduction models will be chosen according to the information they are supposed to provide.

We start the discussion with the simplest case: similar electrodes with low water content ("low" because we can not prove that the water content is null). Then, the impact of dissimilar or asymmetric electrodes are considered. In a third moment, the impact of the water uptake will be addressed.

Case 1 - Similar electrodes with low water content: Electrode-limited conduction.

Schottky fitting and assumptions: Figure 4.2.14 underscore the Shottky correlation with all the electrode systems tested for the 1-3% RH condition and electrodes made of the same material. The coefficients have been extracted (Table 4.2.3), with values of ϵ_r and ϕ showed in Table 4.2.4.

It is noted that:

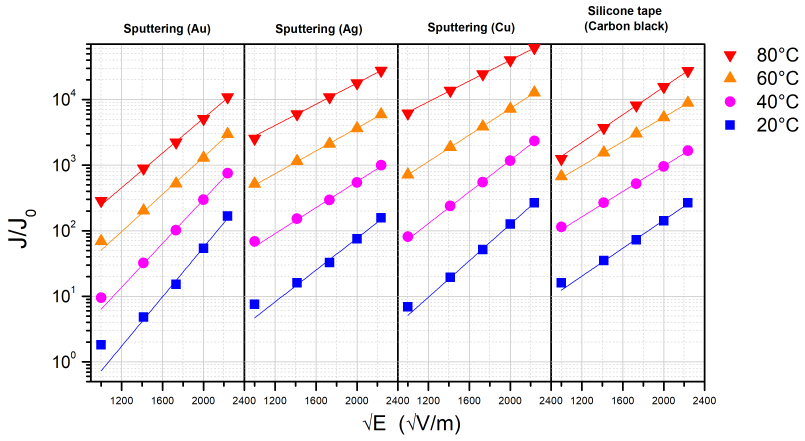

Figure 4.2.14: Current density as function of the square root of electric field for 4 electrode materials at 4 temperatures; dried samples tested at 1-3% RH.

	Gold		Silver		Copper		Carbon black	
	intercept	slope	intercept	slope	intercept	slope	intercept	slope
20°C	-12	1.9e-3	-10	1.2e-3	-10	1e-3	-10	1e-3
40°C	-11	1.7e-3	-9	1e-3	-9	1e-3	-9	9e-4
60°C	-10	1.4e-3	-8	9e-4	-8	1e-3	-8	9e-4
80°C	-9	1.3e-3	-7	8e-4	-7	7e-9	-8	1e-3

Table 4.2.3: Coefficients obtained from the fitting of Figure 4.2.14.

- The ϵ_r are lower than common values (between 3-4) [229] measured with dielectric spectroscopy (see C). This is a strong argument to deny the correlation.
- The correlation should be done with the contact field E_c, and not with the applied fieldE_{app}. For instance, the contact field is $E_c = \lambda_E E_{app}$, λ_E being a parameter representing the field enhancement in the contact.
- The energy barrier ϕ is lower than the work function of each metal under vacuum [206], which is consistent since the energy barrier represents the effective energy barrier representing the metal working function lowered by the insulator affinity χ, i.e. $\phi_{eff} = \phi - \chi - \beta\sqrt{\lambda_E E_{app}}$, with ϕ_{eff} as the effective work function and ϕ as the work function of the metal under vacuum.
- Therefore, if the values of ϕ in Table 4.2.4 are, in reality, $\phi - \chi$, with ϕ being equal to the respective work function earlier presented in Table 2.3.1,

	Gold		Silver		Copper		Carbon black	
	ϵ_r	ϕ (eV)	ϵ_r	ϕ (eV)	ϵ_r	ϕ (eV)	ϵ_r	ϕ (eV)
20°C	0.64	0.93	1.5	0.87	1.2	0.88	2	0.85
40°C	0.71	0.95	2.0	0.88	1.4	0.88	2.1	0.86
60°C	0.87	0.96	2.3	0.89	1.7	0.89	2	0.88
80°C	0.89	0.98	2.4	0.9	2.5	0.88	1.4	0.93

Table 4.2.4: Properties extracted from Schottky coefficients

	Gold	Silver	Copper	Silicone tape
20°C	0.18	0.43	0.34	0.57
40°C	0.20	0.59	0.40	0.59
60°C	0.25	0.67	0.50	0.59
80°C	0.26	0.68	0.71	0.4

Table 4.2.5: Values of field reinforcement λ_E provided by fitting with Schottky injection and by forcing the entry of an $\epsilon_r = 3.5$.

they suggest an insulator affinity too large (of around 4 eV, whereas for other polymers, as polyethylene, the χ turns around 1 eV) [90].

For instance, if we force a fitting that gives a $\epsilon_r = 3.5$, the values of λ_E will be as given in Table 4.2.5. It can be seen that the field is attenuated, with temperature reducing the attenuation. The biggest attenuation is made by the gold electrodes. One can suggest that the gold inject homocharges more easily than the other electrodes.

Because the ϵ_r tends to decrease with the increasing temperature, once the change of ϵ_r was not taken into account to calculate the values of field reinforcement λ_E in 4.2.5, those at higher temperatures can be seen as minimum ones.

Poole-Frenkel fitting and assumptions : The plot of $log(J/E)$ against $\sqrt{E}$ for gold and copper electrode systems are presented in Figure 4.2.15, and the values of permittivity needed for fitting are found in table 4.2.6.

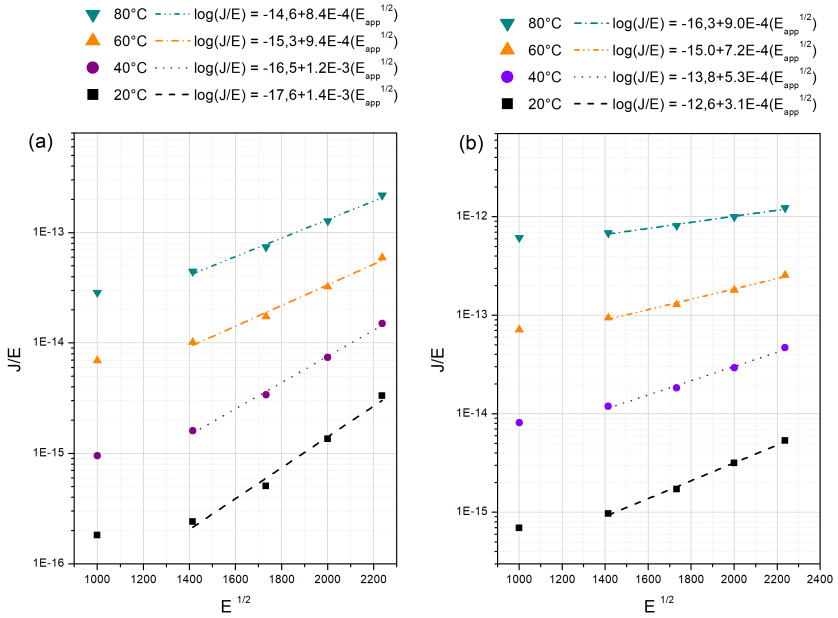

Figure 4.2.15: Poole-Frenkel plot of conduction currents for the silicone rubber at $1-3\%$ RH and gold electrodes on both sides (a), or for copper on both sides (b).

Since the interception of the fitting represents $log(\sigma_0) - E_{T0}$, as the value of σ_0 is unclear, we were unable to proper determine E_{T0}, so for instance no statement will be done for the trap depth E_{T0}. If, again, we suppose that there is a field

	Gold		Copper	
T (°C)	ϵ_r	λ_E ($\epsilon_r = 3.5$)	ϵ_r	λ_E ($\epsilon_r = 3.5$)
20°C	4.6	1.32	11	3.2
40°C	5.6	1.60	15	4.3
60°C	8	2.28	25	7.2
80°C	9	2.53	65	18.7

Table 4.2.6: Coefficients extracted from the fitting with Poole-Frenkel for the Au/Au samples. The values of ϵ_r are obtained directly from the fit, and the values of λ_E are obtained correcting the ϵ_r to be equal to 3.5.

reinforcement λ_E that will compensate the permittivity to give a $\epsilon_r = 3.50$, the values of field reinforcement are calculated and shown in the third column of table 4.2.6. The coefficients suggest an enhancement that increases with the temperature.

The field enhancement for copper is higher than for gold. The values at 60°C and 80°C are too high. So, at these temperatures, we are tempted to conclude that the Poole-Frenkel mechanism is unlikable to be predominant.

Thus, we have this situation in which both of the mechanisms fit, each one suggesting a different thing. An impasse between Schottky and Poole-Frenkel has been encountered many times in the literature for other insulation systems ([221, 230, 231]) and has been called "anomaly Poole-Frenkel" in which the current is bulk limited, but the field dependence is that expected for the electrode-limited Schottky mechanism [230]. For instance, a similar situation has been investigated by Notingher et al [232] for the XLPE, in which field enhancements close to those found for the gold electrodes (1.4 - 1.6) have been found.

The complexity that abounds with the Schottky injection rely on the difficulty to determine ϕ_{eff} without delve into a deeper discussion about the model assumptions: it is not clear if the electron will hop over the barrier, or directly in the forbidden band towards a trap. If it is the case, in addition to the insulator's electronic affinity χ, we should also consider the "trap affinity" E_{T0} that would be the energy necessary to extract a charge from a deep trap to the insulator's conduction band. Complementary, in the steady-state, the band bend should provide a continuity between the contacts and the insulator; the injection and the extraction should be somewhat equivalent because there is no space charge accumulation once steady-state is achieved, and it is not intuitive to conclude that an electron is going to be extracted through a Schottky mechanism.

Case 2 - Dissimilar electrodes with low water content: Shifting to bulk-limited cases? The slopes of the current-voltage profiles for dissimilar electrode systems are all equal or very close to 2, tempting a fit with SCLC, which is a bulk-limited mechanism and contrast with the traversing barrier approach.

The question is: Does it make sense to reduce all the systems (similar and dissimilar) to SCLC-cases, or should we reasoning in terms of a shift from one approach to another?

Ultimately, the SCLC model accounts for space charge in all the sample, bearing indeed for those in the contacts.

If we apply the SCLC model to all these results (similar and dissimilar electrode systems), we find the values for effective mobility ($\mu_{eff} = L\mu$) and the trapping

	μ_{eff} (m^2/Vs)	T_t (°C)	ϕ
Au/Au	1e-12	490	5.1-5.5
Cu/Cu	3e-12	190	4.5-5.1
Ag/Ag	4e-13	160	4.3-4.7
Au/Cu	3e-13	40	-

Table 4.2.7: Coefficients obtained from the fitting with SCLC corresponding to the exponential distribution of traps. All the measurements were conducted at 40°C. Since the Au/Cu system fit with the single-level SCLC case, the T_t = 40°C.

temperature T_t organized in Table 4.2.7. Their work functions ϕ has been added as reference: both mobility and trapping temperature are decreasing with the increase of ϕ.

The effect of dissimilar electrodes would have, for the silicone, the same effect of the water absorption for the epoxy: the increase of traps, and the shift to a single-level SCLC case. But here, because this increase of traps is attributed to the electrode-system, it may be limited to the contact region.

The electrode material is going to change only the trapping structure at the contact, with each metal (nature, structure, and microstructure) producing an unique surface of states. The effective mobility of the Au/Cu system (which is the same for the Cu/Au system) is showed in Table 4.2.7; the trapping temperature is the test temperature because it fits a single-level SCLC case. The μ_{eff} is close to the Ag/Ag system, so as it would be its work function if we average the work functions of the gold and the copper.

Even if the current-voltage profiles of Au/Cu and Cu/Au look similar, the quantity of charge accumulated is not, as denounced by space charge results (Figure 4.2.7). When copper is the cathode, there was accumulation of positive charge in the volume, but when gold is the cathode, the accumulated charge is negative.

Case 3: Similar electrodes with high water content In section 4.2.2.1 it was observed that the water uptake increased the current up to one order of magnitude, following the pattern of water adsorption. When analysing the current-voltage profiles (Figures 4.2.1 and 4.2.2), one can note that the slopes are almost the same, suggesting that the water content is not changing the conduction mechanism.

The Figure 4.2.16 shows the fitting with Schottky and Poole-Frenkel mechanisms. Up to the monolayer formation (50% RH), the data fit with both. For the sample at 90% RH, the last two datapoints deviate.

The same strategy applied for similar and dissimilar electrodes at $1-3\%$ RH can be applied again: the values of ϵ_r were extracted from both mechanisms, and a value of field reinforcement λ has been attributed in order to correct the ϵ_r to 3.5. These parameters are disposed in Table 4.2.8 for the measurements at 40°C with gold electrodes on both sides.

Despite the good fit of Figure 4.2.16, the model coefficients do not change significantly between RH conditions, and do not help to explain the influence of water adsorbed.

A tentative to fit the results with SCLC gives the effective mobility μ_{eff} and the trapping temperature T_t added to Table 4.2.8.

Both of these coefficients follow the trend of adsorption rate θ because the cur-

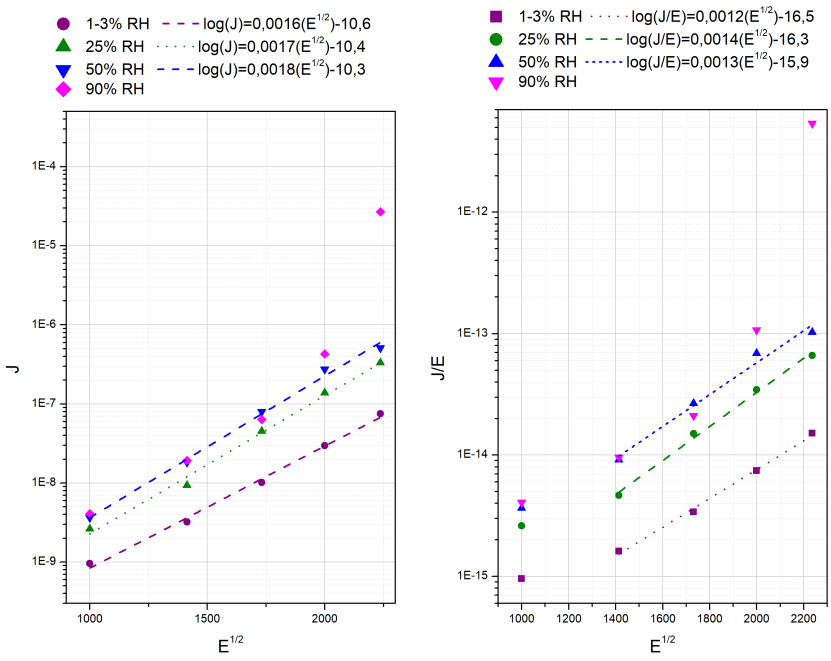

Figure 4.2.16: Schottky (a) and Poole-Frenkel (b) plots of conduction currents for the silicone rubber at $1-3\%$, 25%, 50%, and 90% RH and gold electrodes on both sides.

	Interfaces				Whole system	
	Poole-Frenkel		Schottky		SCLC	
RH (%)	ϵ_r	λ	ϵ_r	λ	μ_{eff} (m^2/Vs)	T_t (°C)
1-3	4.6	1.6	0.7	0.2	1.4e-12	490
25	4.1	1.1	0.6	0.2	1.4e-11	630
50	4.6	1.4	0.6	0.2	2.3e-11	635
90	4.6	1.4	0.6	0.2	7.5e-12	480

Table 4.2.8: Coefficients obtained from fitting with Poole-Frenkel transport, Schottky injection, and SCLC with exponential distribution of traps.

rent value is following such trend. From $1-3\%$ to 50% RH, the T_t is increasing, suggesting that there are more deep trapping activity. On the other hand, the μ_{eff} is increasing too, indicating that increase of traps facilitates the conduction.

It is not clear why μ_{eff} and T_t decreases at 90% RH, but we can explore some hypothesis:

- If the silica surface exhibits acid-like behavior, as asserted by Prigogine[156] and Bascom[129], it implies the generation of H^+ ions, which serve as deep traps (electron acceptors). Once the surface becomes fully saturated, no further H^+ ions are formed, resulting in a cessation of current increase with relative humidity (RH). The contradiction within this hypothesis lies in the expectation of facilitating ionic conduction; the proposition suggests that protons should migrate towards the cathode through electrostatic attraction. In spite of that, in the field of Earth Sciences and Mineralogy, the ionic (protonic) conductivity provided by water dissociation is widely known. It can be related

to the degradation of minerals and therefore depend on the porosity of the material [233, 127, 128]. Anderson [234] measured the conductivity of silica gel in presence of adsorbed water following the BET model, and a three-step model has been proposed: when the adsorption rate θ is low, there is H^+ formation and ionic transport throughout $SiOH$ surface. During monolayer completion, the formation and diffusion of H_3O^+ is favoured, with H^+ transfer to adjacent H_2O molecules. When monolayer is completed, there is an aqueous phase formation under the form of a film in which the H^+ can diffuse.

- Rather than the generation of H^+ ions, a significant alteration in the OH dipole moment can occur by weakening a single $-OH$ bond of the adsorbed water molecule. This highly polarized hydrogen, with a more positive partial charge $(+\delta)$ and reduced electronic density, could serve as a deeper trap.

- If water form clusters at RH above 70%, the water cluster can act as an independent phase in the material. ([235, 236]) Pure water has a conductivity value at the steady-state ($\approx 10^{-6}\ S/m$) higher than the solids of this study ($\approx 10^{-14}\ S/m$). If the field is reinforced in the less conductive phase, the water clustering or multi-layering bounces the field back to the matrix.

4.2.2.4 Exploratory reasoning to explain the conduction mechanisms

In this subsection, we explore two additional non-conventional approaches aimed to understand the results discussed in the previous section.

Approach of the simultaneity of mechanisms: When the steady-state condition is achieved, no space charge is accumulated over time: electrons have to be injected in the cathode and evacuated in the anode, and the rates of electronic injection j_{inj}, transport in the volumej_{vol}, and extraction j_{ext} have to be the same (as in Equation 4.2.3).

$$J_{(steady-state)} = j_{inj} = j_{vol} = j_{ext} \tag{4.2.3}$$

Thus, no matter the mechanism we choose, our hypothesis within this approach is that the fitting with injection models and transport models can be, simultaneously, valid. In this case, the Schottky fitting j_{SCH} is showing the electronic injection at the same time the Poole-Frenkel j_{PF} is showing the electronic transport, which includes the transport at the vicinity of the anode (Equation4.2.4).

$$j_{PF} = j_{SCH} \Rightarrow J_0.exp(\phi_{eff_{PF}}) = A.T^2.exp(\phi_{eff_{SCH}}) \tag{4.2.4}$$

Note that we are considering that we have different field impacts in the cathode λ_c (included in j_{SCH}) and in the volume λ_v (calculated from j_{PF}).

$$\phi_{eff_{PF}} = -E_{T0} + 2\beta_s\sqrt{\lambda_a E_{app}} \tag{4.2.5}$$

$$\phi_{eff_{SCH}} = -\phi_c + \chi + \beta\sqrt{\lambda_c E_{app}} \tag{4.2.6}$$

Depending on the nature and the position of the space charge, the values of λ will change. If there are predominance of negative charges in the volume, $\lambda_c < \lambda_a$. It is what we see in the flat profile of charge density for the gold-sputtered sample in

Figure 4.2.7(a). If the quantity of negative charges is huge, $\lambda_c << \lambda_a$. It corresponds to the space charge accumulated in the copper-sputtered sample of Figure 4.2.7(b). These conclusions are in accordance with the λ values of Tables 4.2.5 and 4.2.6.

Nevertheless, as discussed in section 4.2.2.3, the Schottky correlation is only possible if we consider a field attenuation (in the cathode), whereas the Poole-Frenkel indicated a field reinforcement. The electric field calculated from the space charge measurements of dry similar electrode configurations are pictured in Figure 4.2.17 and it shows a field attenuation near the cathode, and a field reinforced in the volume (with the maximum of reinforcement near the anode) as those conduction models correlations suggested.

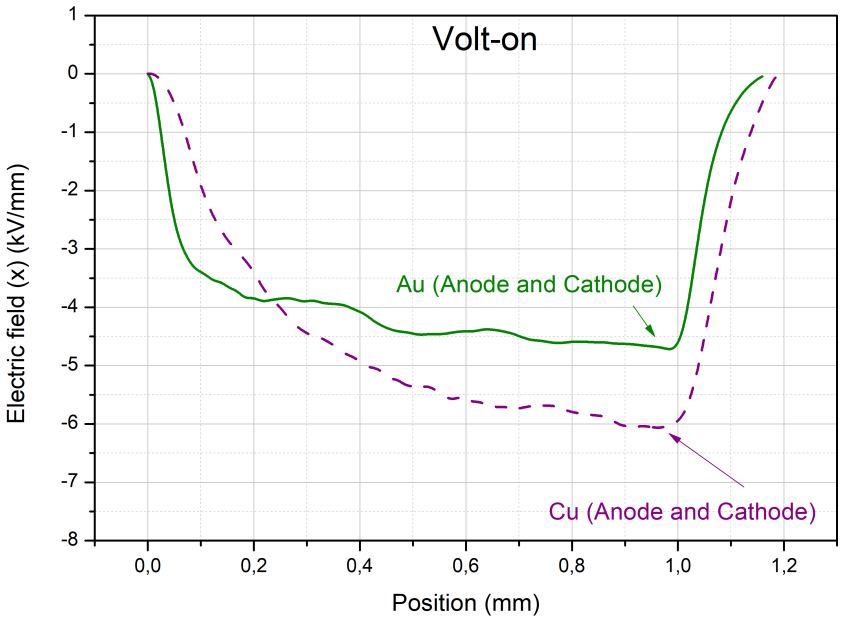

Figure 4.2.17: Electric field distribution throughout the samples' thickness.

It is not clear why the copper-sputtered sample presented a charge density profile (Figure 4.2.7(b)) so different from the gold 4.2.7(a). It is worth noting that the measurement has being affected by oxidation reactions of the copper layer (Figure 4.2.18). This oxidation was particularly observed in the cathode side, shifting this sample to a dissimilar electrode case. Moreover, the sample was adhered to the test cell at the end of the test, suggesting electro-chemical reactions between the copper and the aluminum coming from the native cell electrode. Such oxidation was not seen in the current measurement probably because the test was conducted in inert atmosphere, and because the native electrodes were made of carbon black embedded in a silicone matrix, limiting the possibilities of electro-chemical reactions, but we can not exclude the possibility of copper passivation.

As a matter of fact, there is not a simple way to get rid of this situation: one attempt to perform current measurements with massive copper electrodes roughly smoothed provided the same results as the copper-deposited sample, and another attempt to protect the copper layer by a nickel one has failed: the current profile was the same, but shifted some units to higher values. The nickel was deposited by a sputtering method described in section 2.3.4, but in another sputtering equipment that enabled, under vacuum, the change of metal target. However, bombarding a copper layer with nickel can create a region of cupronickel alloy, and it is not evident

if nickel atoms can diffuse towards the copper layer. In addition, because the silicone sample is very flexible, small deformations can produce microcraks in the metallic layer, ultimately exposing the copper protected by the nickel.

Note that the grease usually applied before the test has disappeared in Figure 4.2.18, probably absorbed by the silicone. This absorption may modify the silicone rubber properties, so as the measurement results.

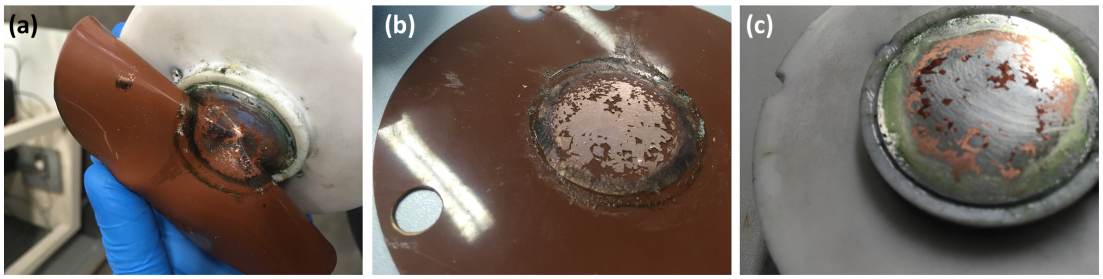

Figure 4.2.18: Photo of the silicone rubber sample with copper electrode oxidized on the cathode side (a). The copper at the cathode adhered to the aluminum of the LIPP cell. It damaged the sample (b) and the cell electrode (c). Note that a grease is applied before the test, and it was absent after it.

Reasoning in terms of energy diagrams as a tool to guide the comprehension: If we come back to the energy diagrams, based mainly on the works of Lampert [91] and Simmons [219, 220, 221] , another approach can be made based on the following assumptions:

- Only extrinsic charges participate in the conduction.
- The cathode should play the role of ohmic contact for electrons, whereas the anode will play the role of ohmic contact for holes. For this statement be true, the metal's Fermi level has to be above the insulator's one. Nevertheless, when voltage is applied, the cathode will act as an electron source, and that is the definition of an ohmic contact.
- If the work function of the insulator ϕ_i is lower than the one of the metal ϕ_m, during the contact there will be electronic transfer from the metal to the insulator. This transfer is responsible for a band bending.
  - It is not evident if barrier at the contact interface will be lowered, but it must produce a counter-field since electrons will be accumulated in the vicinity of the contact, inside the insulator. Additionally, it is not clear if such charge transfer can be directly related to the image charge considered in the demonstration of the Schottky effect [89]. In the demonstration, the reasoning begins considering that a negative charge has departed the contact and has been found in the insulator. How did this charge get here?
- The charge transfer happens on both sides. In the case of similar electrodes, the energy diagram representing the sample should be schematized by the

one in Figure 4.2.19(a) before the contacts, and 4.2.19(b) after the contact; i. e. the edges of the conduction band of the insulator are bent towards the electrode's Fermi levels as a consequence of electronic accumulation.

- If the insulator has trap levels, then the electronic transfer should be higher in average (traps are neutral or positive, thus positive in average).
- The surface has a different structure from the bulk; it must results in more localized states.
- For the sake of simplicity, we are considering that:
  - The working functions are the same in the cathode ϕ_1 and in the anode ϕ_2, for the case of similar electrodes, and
  - That the work function for electrons is similar, in module, for a hole (the energy to extract an electron from the metals' Fermi level and place in the vacuum is, in module, the same to take an electron from the vacuum and put in the metals' Fermi level).

Now, positive voltage is applied in one side, pushing this side upwards, and making it a cathode in which electrons will be injected (Figure 4.2.19(c).).

The insulator polarizes and attenuates the field, but there are already charges at the vicinity of the contacts that will impact the polarization. Besides, if at low field the conduction is ohmic, electrons have to enter and exit the insulator (unless there are field-dependent generation and recombination). Once the insulator is full of traps, those traps will be filled during the passage of the electrons: there will be trapping and detrapping activities. If all the previous statements are true, the sum of all these activities should lead to an attenuation in the cathode and a reinforcement in the anode due to accumulation regions in the contacts, as seen in Figure 4.2.19(c).

The resultant forces points to an alignment of all the Fermi levels with the cost of more band bending, and increase of the accumulation regions described as space charge accumulation in the interface so as in the volume.

Simmons [219] defines the space charge accumulation and field throughout the insulator as an overlapping of accumulation regions, i.e. when the length of both accumulation regions seen in Figure 4.2.19(b) are higher than the sample's thickness. Instead of having a flat level in the center, we must have a distorted band in the middle. This could happen even before voltage application in the case of dissimilar electrodes, as schematized in Figure 4.2.20. This distortion decreases the insulator work function to ϕ_i'. One of the reasons cited by Simmons to justify such configuration is the asymmetry of work functions in the cathode and the anode. Figure 4.2.20(b) also suggests that, no matter which metal represents the cathode and the anode, ϕ_i' will be decreased by the same rate.

The implication of this model is that a space charge mechanism can be, in fact, a consequence of events in the contacts. Therefore, it is not unrealistic to attribute the main conduction mechanism of dissimilar electrode systems, as Au/Cu (Figure 4.2.5) to a bulk limited mechanism, given that a slope equals to 2 tempting the SCLC correlation.

The single-level SCLC can be seen as a limit case of the SCLC with exponential distribution of traps. One hypothesis is that the quantity of charge accumulated

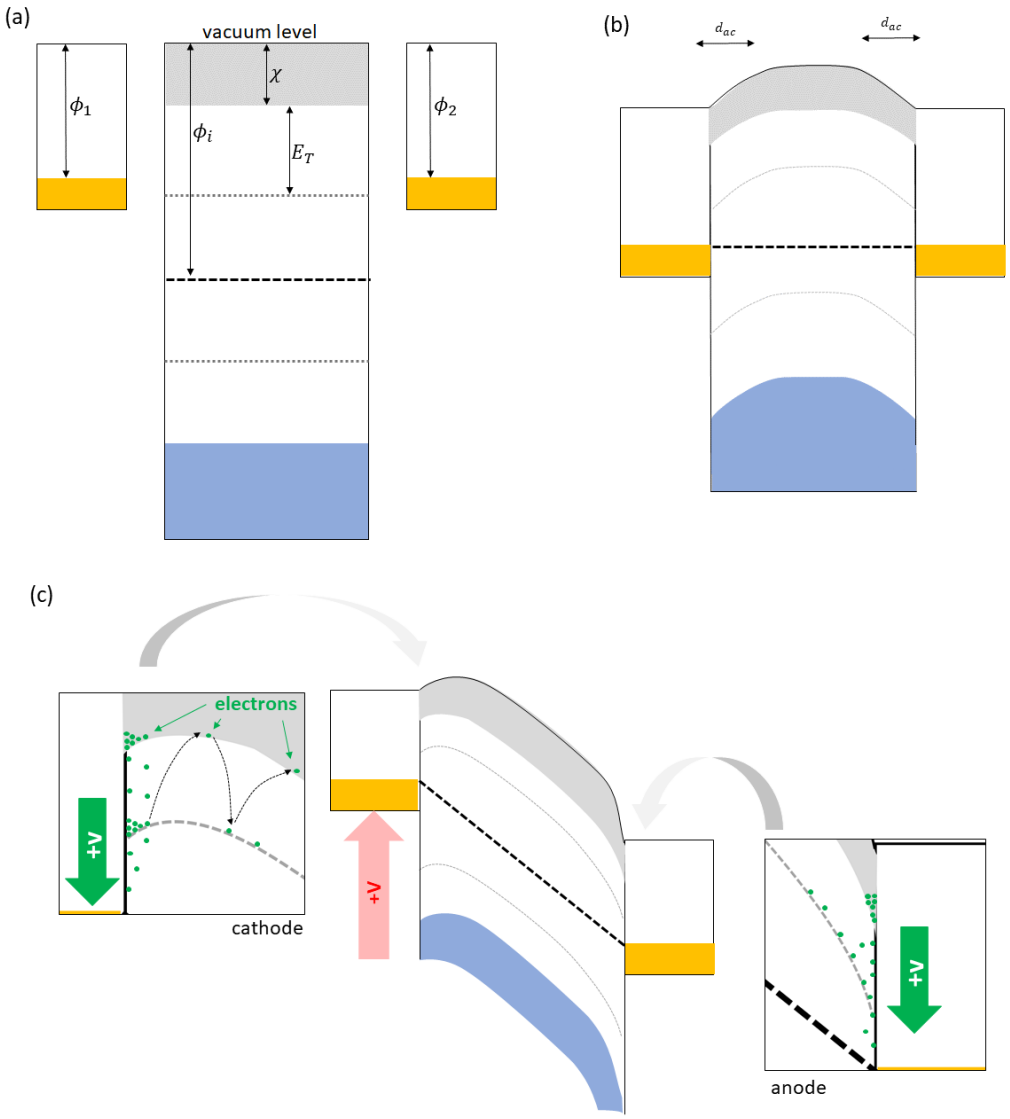

Figure 4.2.19: Energy diagrams of the insulator and similar electrodes before contact (a), after contact (b), and during voltage application (c). The metal work functions are ϕ_1 and ϕ_2, the insulator's affinity is χ, the insulator's work function is ϕ_i, the accumulation regions are d_{ac} for when $\phi_1 = \phi_2$, and the trap depth is E_T considering a simplistic case of one single trap level. Because the density of states at the contact interface has more localized levels, there are more electrons that can be accommodated.

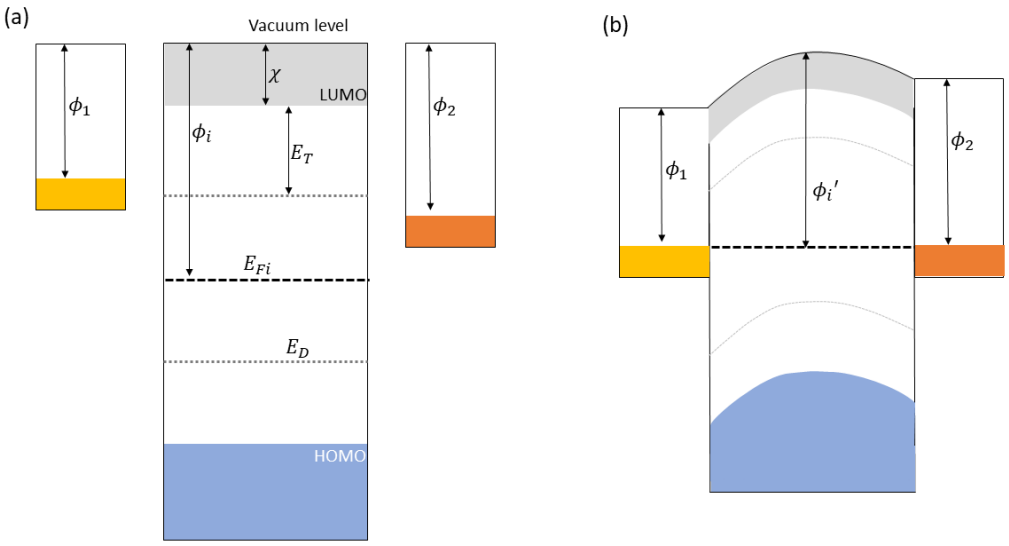

Figure 4.2.20: Energy diagrams of the insulator and dissimilar electrodes before contact (a), after contact (b). The metal work functions are ϕ_1 and ϕ_2, the insulator's affinity is χ, the insulator's work function is ϕ_i, the accumulation regions are d_{ac} for when $\phi_1 = \phi_2$, and the trap depth is E_T considering a simplistic case of one single trap level. A deeper trap level below the Fermi level is also defined as E_D. Because the density of states at the surface has more localized levels, there are more electrons that can be accommodated.

are sufficient to fill the deeper traps. Thus, all the shallow traps very close to the conduction band can be reduced to an averaged single level.

4.2.2.5 Exploring the filler-free silicone rubber

In this section, we dive into the results of the filer-free silicone rubber, which contrasts with those of the industrial grade.

The conduction mechanism attributed to the filler-free grade in Figure 4.2.8 is the ohmic conduction with traps (J_Ω) because we can not make sure that the material is trap-free. The other assumption is that the fillers may reduce the current at low voltages, but because of space charge accumulation and field reinforcement, they increase the current density at higher voltage levels. Figure 4.2.21 put in perspective the filler-free silicone with many conditions of the industrial one, and in all of them, the filler-free presented a larger conduction. For instance, we do not know if the current is electrode-limited as for the industrial grade.

When the curing is not completed, the conduction mechanism is sub-ohmic. As seen in Figure 4.2.22 that illustrates the absorption currents under the first hour of the test for each voltage step, the uncompleted cured sample (Figure 4.2.22(a)) presented a current-time pattern that resembles the charge carrier depletion characteristic of ionic conduction, as found for many dielectric liquids, similarly to the feature reported in other silicone-based solid by Zink [164]. It is not observed in the ohmic sample (4.2.22(b)).

The conduction in dielectric liquids is attributed to the migration of ions coming

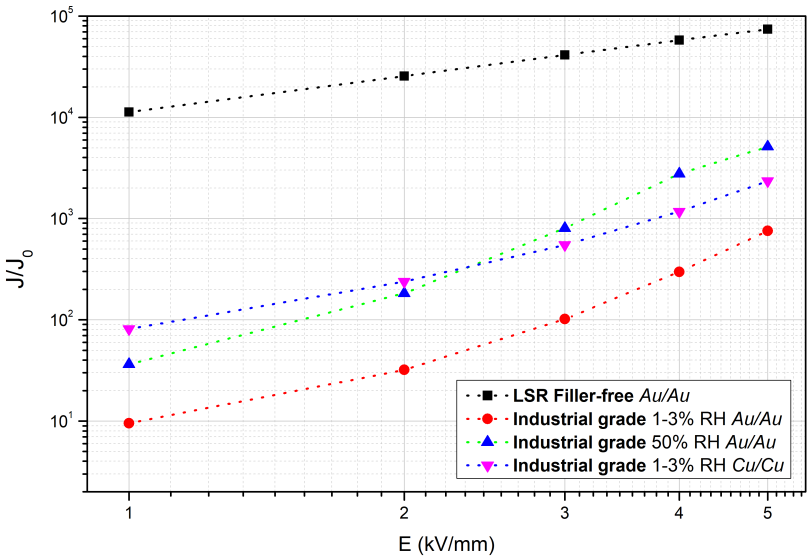

Figure 4.2.21: Comparison between the LSR silicone rubber filler-free with the industrial grade with gold electrodes (1-3% RH and 50% RH) and copper electrodes (1-3% RH).

from impurities.

This diffusion results in a random walk, with the field superimposing to the random path [167].

According to the Stokes–Einstein–Sutherland equation (4.2.7), the diffusion coefficient D_n is a result of the temperature T, the hydrodynamic radius of the liquid r, the Boltzmann constant k, and the viscosity of the liquid η.

$$D_n = \frac{kT}{6\pi r\eta} \tag{4.2.7}$$

Initially, when the raw materials are not cross-linked, the current is ionic due to ionic migrations and therefore not ohmic.

Upon curing of the material, η increases, eventually reaching a theoretically infinite value that characterizes the gelation point. However, incomplete or non-uniform cross-linking throughout the volume can lead to poorly reticulated phase within the bulk, behaving like high-viscosity liquids, even if the sample appears solid at a macroscopic level. Due to potentially lower electrical conduction in this phase compared to the solid incipient matrix, the electric field may strengthen in the viscous phase. Consequently, the current-time and current-voltage patterns exhibit characteristics of a dielectric liquid. However, if the cross-linking process is not completed, it has a risk to complete during the electrical test, as the sample is not stable. Further investigations are required to elucidate how conduction changes around the gelation point and how other factors, such as compression and density, may influence the results.

Additional studies are also essential to elucidate the mechanism with different ratios of A and B components. For instance, given that the B component contains the hardener and short-chain polyorganosiloxane molecules (see 1.2.3), Figure 4.2.9 implies that an increase in cross-linking degree correlates with an increase in current, possibly due to the augmented trap density associated with additional cross-links. If

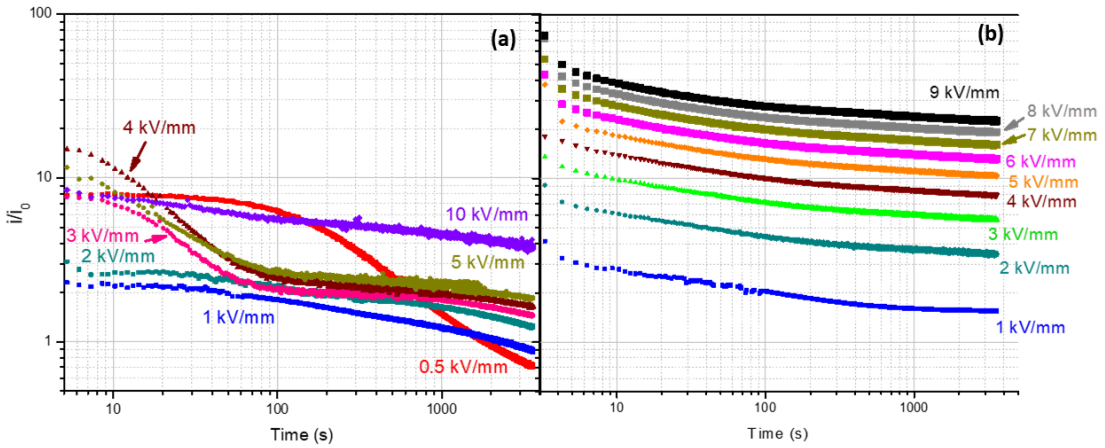

Figure 4.2.22: Absorption current-time profiles of the LSR filler-free with short curing (a), and with long curing (b). In the (a), the first voltage applied was 500V, and in the second, 1 kV. Both graphics are in the same scale.

an excess of polyorganosiloxane leads to the formation of clusters at higher voltages, it could revert to a viscosity-dependent conduction behavior.

4.3 Partial conclusions & perspectives

In this chapter, an industrial HCR silicone rubber applied for MVAC applications have been investigated under DC constraints. The main results are summarized below:

- This silicone grade presented the capability to uptake water from the environment (up to 1.2%).
- The diffusion was fast (1-2 hours to achieve saturation at a given RH) and fits the Fick's law.
- The pattern of water sorbed as a function of the RH followed the Langmuir's isotherm law, which is applied to describe adsorption mechanisms. It is correlated to the formation of a monolayer of water molecules at the fillers surfaces.
- Under DC voltage, the current density increased following the monolayer formation indicated by the Langmuir's isotherm.
- The current density also showed itself dependent on the electrode material (gold, silver, copper, and carbon black) and its configuration (similar or dissimilar).

Many approaches have been tested to determine a conduction mechanism. When traverse barrier mechanisms are investigated, correlations with Schottky injection or Poole-Frenkel transport were possible if we correct the electric field in the models by a reinforcement factor λ_E; the reinforcement or attenuation suggested by these models are in accordance with the field distribution measured by LIPP. Correlations with Space-Charge mechanisms were also explored, but they do not explain alone the impact of the electrode material in the conduction.

One additional LSR silicone rubber with the same matrix but free of silica and manufactured internally at Schneider and G2Elab confirmed that the matrix, being hydrophobic, does not have its electrical conduction affected by the relative humidity. It is, on the other hand, intimately affected by the fabrication procedure. The patterns of current-voltage mechanisms reassembled the sub-ohmic mechanisms commonly found in viscous dielectric liquids.

Perspectives: During the discussion, some ideas of additional measurements and future works are presented. The main topics are listed below:

- Measurements at higher temperatures can be an independent research focus.
- Space charge measurements can be refined to ensure precise control over relative humidity and pressure. This adaptation would facilitate measurements without the concern of encountering a metastable sample that might undergo drying during the process. However, investigations into the compatibility of the silicone gel with the silicone elastomer are imperative to avoid the risk of unintentionally measuring another metastable material. Further research on the effects of different incorporated greases on space charge and conduction transport could also be explored as a subject itself.

- If water adsorbed in the silica impact the conduction transport, changes in the filler material and parameters (sizes, spatial dispersion and distribution) may also affect the water adsorption and the electrical test results, enabling more generalizations about the impact of adsorbed water.

- Comprehending electrochemical reactions in copper-based electrode systems and conducting preparation and measurements on samples with electrodes having controlled oxidation degrees may lead to enhanced correlations and a deep understanding of the mechanisms limiting current in real-world applications.

- The impact of the sample preparation and electrical test on the surface roughness. Figure 4.3.1 shows that after the electrical test, the sample looked more "flat", even in the regions that were covered by the mask during the sputtering process (for those that may correlate it with the metalization). Interestingly, after removing the gold electrodes with ethanol embedded in absorbent paper, the surface that was covered by gold presented concavities in the opposite direction of those observed in the sample's periphery.

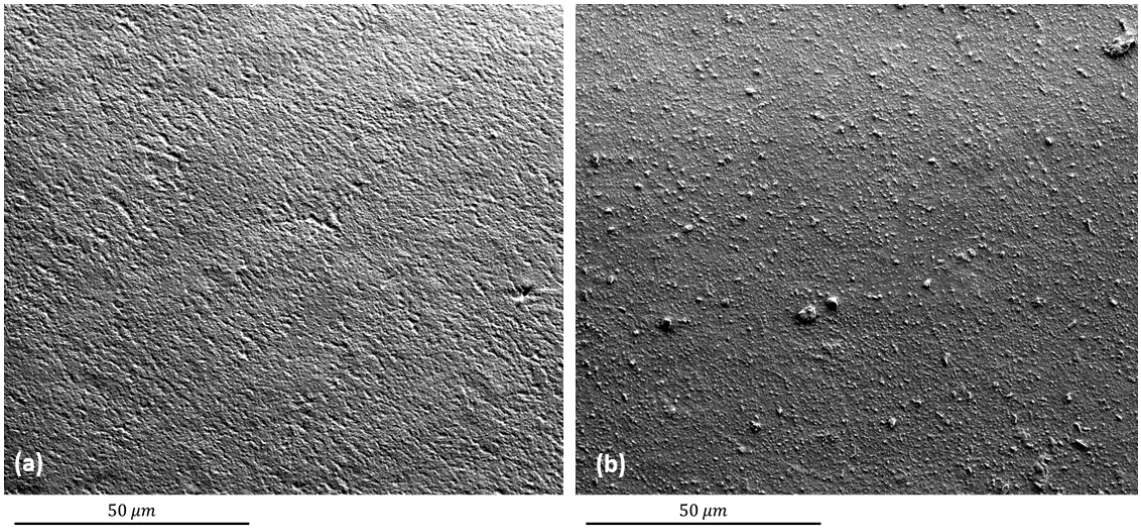

Figure 4.3.1: Scanning electron micrographs of silicone rubber sample after the electrical test. View of the center (a), and the periphery (b) of the sample.

- The transition from a viscous liquid to solid rubber, the presence of "viscous packets" within the bulk, and their influence on the conduction of elastomers present a compelling topic that deserves dedicated exploration in a research project.

5 The multilayer and practical considerations

The access to this chapter is limited.

6

Conclusions & Perspectives

This thesis focused on the DC electrical characterisation of two materials commonly found in MV insulation systems: an epoxy filled with silica, and a silicone rubber. It comprehended physical-chemical characterization to frame their structures and microstructures of departure, current-voltage measurements with punctual additional electrical measurement techniques, as space charge characterization with the laser-pressure pulse method, and dielectric spectroscopy. Exploratory investigations of another silicone rubber without fillers and dyes are also included (filler-free LSR). Specimens have been carefully prepared based on water uptake control, and two configurations were explored: the materials individually (monolayer), and bilayer. The measurements covered a range of temperature between 20°C to 80°C, 250 V/mm to 10 kV/mm, and RH from 1-3% RH to 90%. Gold electrodes were applied as reference.

Many efforts have been done to carefully condition and prepare the specimens before the electrical tests. Learnings have been gained to achieve repeatable current-voltage measurement results. It is required not to:

- Ignore the way the sample has been fabricated, especially as concern cross-linking stabilization.
- Underestimate the impact of electrode material and contacts.
- Underestimate the impact of the water content or the duration of the sample water content stabilization
- Underestimate the duration of the sample temperature stabilization.

The main results concerning the epoxy composites are listed as it follows:

- The rate of water sorbed is directly proportional to the RH, and even the numerical value of such rate is equal to the fractional value of RH, since the sorption mechanism is in accordance with the Henry's sorption model.
- Dry samples presented an ohmic conduction at low voltages, with a voltage threshold ranging from 6 kV/mm at 20°C, and decreasing to 3 kV/mm at 80°C.
- When analysed thorough the optics of space charge limited current (SCLC) mechanisms, the profile of current density as a function of electric field for dry

samples fit with a mechanism of exponential distribution of traps. As soon as the sample gets water, the non-linear mechanism is shifted to a model of one single level of traps.

- Correlations with Schottky injection were possible, but contrast with the theory of SCLC in the bulk, as well the lack of impact of the other electrode materials than the gold.
- The current in relation to temperature fits an Arrhenius law. The activation energy is influenced by the extent of water content.

The main findings about silicone rubbers tests are equally listed below:

- The water sorption was in accordance with the Langmuir's isotherm, that is related to adsorption and preferential sites for sorption. Since the matrix is hydrophobic, the water may be adsorbed on the surface of the silica, and located in the interfaces silica-matrix or agglomerates of silica.
- The water adsorbed impacted the volumic current in the same proportion.
- The current was highly impacted by the electrode system, characterizing this grade as electrode-limited.
- When analysed with the space charge limited mechanism, the profile of current density as a function of electric field for all conditioning fit with a mechanism of exponential distribution of traps.
- When analysed with the traverse barrier mechanisms, the Schottky-injection fitting suggests a field attenuation at the cathode, and the Poole-Frenkel, a field reinforcement at the anode. The field enhancement factors λ_E issued from fit calculations at both electrodes, were in accordance with the field distribution deduced from space charge measurements.

These evidences can not be generalized to all silicone systems. Additional experiments with a filler-free LSR showed that the silicone can be ohmic for all voltages of the study, i.e. until10 kV/mm, and be insensitive to the RH, that is to say with no water ingress. On the other hand, the conduction mechanism is sensible to the material preparation and cross-linking degree: in some circumstances, the apparent conductivity can decreases with the field. Some hypothesis for that has been presented.

The measurements of multi-layers and the respective analysis led to the following conclusions:

- [redacted]
- [redacted]
- [redacted]

- [redacted]
- [redacted]

6.1 Perspectives

Some investigations described in this thesis can still be complemented and merit fully investigations.

The following list summarizes what has been presented in the conclusions of each chapter:

For both epoxy and silicone, mono and bilayer, complementary investigations should be carried out in the following directions:

- Space charge measurements with hydrated samples at stabilized environments.
- Space charge measurements with asymmetric, and/or electrodes that oxidises during the experiment.
- Extending the temperature range of the current-voltage measurements
- Deep investigations about the effect of pigment, dyes, and the silica-matrix interface.
- Impact of temperature and water concentration gradients in the field distribution along the thickness.

Some investigations which have not been considered here would deserve to be studied and the underlying mechanisms clarified. They are:

- Transient currents.
- Surface conduction.
- Impact of degradation/ageing mechanisms.
- Electrical breakdown as function of temperature and water content.

A

Molding procedure of epoxy composite plates

The access to this Annex is limited.

B

Selecting and preparing an alternative LSR silicone rubber

B.1 Motivation

The silicone rubber primarily selected for investigation is a particular industrial grade full of additives and fillers. The interest of testing another silicone rubber is motivated not just by the seek of any generalization for such materials, but also the understanding of the role of all these additives and components in the final electrical property. In particular, we are interested to focus on the non-linearity of current density at relatively low voltage levels as seen in Figure 4.2.1, which is contrasting as from the work of Mourad [163] or even Zink [164]. According to these authors, silicone rubbers should respond as liquids and present a liquid-like pattern conductivity, i.e. a conductivity that decreases with the increase of voltage level or, ultimately, a polarization current comprised of a initial phase of dipole orientation, and a second one related to the space-charge build-up due to intrinsic ionic conduction [3].

One important requirement was the possibility to fabricate the sample internally, for the purpose of having more accurate fabrication parameters control. The LSR Lumisil 7601 A/B ® from Wacker has been chosen. It is an injection-molding high transparent grade developed for optical applications [193]. This grade, as most of LSR, has a similar matrix of the industrial grade for electrical application (which is a MVQ type), but the Lumisil 7601 A/B is free of fillers and dyes, letting us the possibility to eventually add the fillers ourselves if needed, and more primarily, to have reference values of a grade without silica.

B.2 Fabrication procedure

This grade is presented in two components, each containing the base polymer. Component A includes the platinum catalyst, while Component B contains the crosslinker and a catalyst inhibitor [53, 237, 238]. The manufacturer recommends a curing process at 165°C for 15 minutes, followed by post-curing at 200°C for 4 hours for injection and pressure molding. However, due to the simplicity of gravity cast molding in our laboratory, the procedure had to be adjusted as follows:

1. At room temperature, small portions of Components A and B (around 10 g

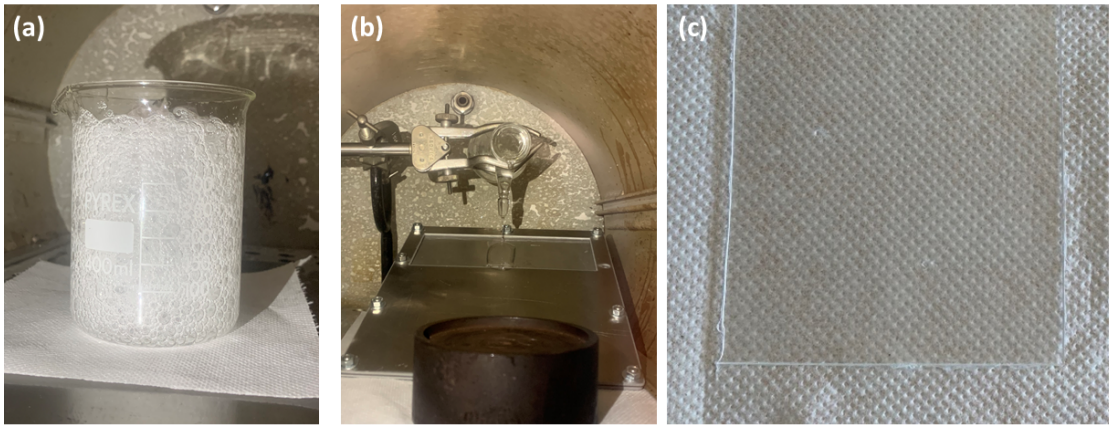

Figure B.2.1: Raw materials mixture under degassing step (a), mixture pouring into the mold under vacuum at room temperature (b), final 1-mm thickness plate without apparent imperfections (c).

each) were dosed at the proportion of 50% each. They were manually mixed in a Becker for 3 minutes.

2. The content in the Becker is degassed in a vacuum chamber (Figure B.2.1(a)) until no bubbles are identified. A minimum of three pourings is required.

3. A small-scale gravity cast funnel is customized as follows: the mixture is transferred to a Kitasato flask, which is bent with the assistance of adapted supports to allow the material to flow through the lateral opening, as illustrated in Figure B.2.1(b). Below the Kitasato, the liquid is directed towards the aperture of a homemade mold, also bent with the help of additional supports. This mold consists of assembled plates and frames, with a frame thickness of 1 millimeter. Prior to use, all mold surfaces are coated with a thin, dry layer of neutral detergent, serving as a demolding agent.

4. As soon as all the apparatus is put on place, primary vacuum is made into the chamber. The mold cavity is filled under vacuum conditions. This step usually last one overnight.

5. After molding, the plates are transferred to an oven previously heat at 165°C. The material is cured for 2 hours. This time-length has been selected to make sure that the material is cured.

6. Outside the oven, the molds are opened. The resulting plate (Figure B.2.1(c)) returns to the oven for the post-curing step, in which it is heat at 200°C for 4 hours. It is expected that all the volatiles are lost in this step.

This procedure is the fruit of many failed attempts with other methods, including tries with the same mold applied for the epoxy plate fabrication.

C

Dielectric spectroscopy: Theory and application in the materials of the study

C.1 Motivation

The relative permittivity ϵ_r is a property commonly associated to AC applications, but it does play a vital role on the understanding of DC current: many events and mechanisms, as Space Charge Limited Current, Schottky injection, and Poole-Frenkel transport depend on the ϵ_r. Besides, the static permittivity ϵ_s, often neglected, can also be an important parameter to evaluate under DC stresses.

This appendix is dedicated to some exploratory experiments with dielectric spectroscopy that enabled the exploration of both permittivity values. These values, associated with those given by suppliers, were used as reference in the thesis.

C.2 Theoretical background

The permittivity from DC measurements: The permittivity ϵ represents the ability of a media to store electrical charges. It is a property of the media; and if embedded of geometry of an object, the permittivity gives raise to the capacitance C of the object. This is illustrated by the two parallel-plate capacitor with surface S and distance d between electrodes: when a DC voltage is applied, the total amount of charges Q stored by the object depend on the C, that is obtained from the ϵ according to equation C.2.1.

$$C = \epsilon \frac{S}{d} \tag{C.2.1}$$

If such experiment is performed under vacuum, the ϵ will be a constant, denoted by ϵ_0 which is equal to $\approx 8.85412.10^{-12} F.m^{-1}$. But if a dielectric material fills the space inter-electrode, the ϵ is increased by a factor (without unity) called relative permittivity ϵ_r which is a characteristic of the dielectric and, as the conductivity, it is constant under some conditions; the reason why ϵ_r is often called "dielectric constant". This increase is due to polarization, that compensate and attenuate the applied field. Since a DC voltage was applied, the ϵ_r is referred to a static permittivity ϵ_s.

Thus, under DC stresses, ϵ_s gives information about the total amount of charge stored Q, and if the amount of charges stored can be measured, the ϵ_s could be

calculated. One example of equation for ϵ_s (C.2.2) is given by Lampert [91] and represents an idealized case of space-charge-limited transient without traps. In such equation, j_0 is the instantaneous current at $t = 0$ just after the voltage application, and the mobility μ is calculated based on the time t_1 which is the time in which a charge, injected from the cathode, takes to achieve the anode.

$$\epsilon_s = 2,25.10^{13}(j_0 d^3/\mu V^2) \tag{C.2.2}$$

The permittivity from AC measurements: The most common technique available to obtain the permittivity is the dielectric spectroscopy, i.e., a technique that measure the impedance as a function of frequency, issued from the interaction between a (dielectric) material with an electromagnetic radiation at frequency ranges below 10^{14} Hz and above 10^{-6} Hz.

Because the dielectric needs a time to complete polarization (relaxation time τ_r), there is a delay between the sinusoidal voltage $V(\omega)$ or field $E(\omega)$, and the material's response (the polarisation $P(\omega)$ and electrical induction $D(\omega)$) that is represented by a phase angle δ_h and results in energy dissipation. By writing these variables in complex notation, the complex permittivity is obtained by equation C.2.3, with ϵ' related to the ability of the material to store charges (ϵ_r) and ϵ'' related to the energy dissipation.

$$\epsilon^* = \frac{D^*}{E^*} = \epsilon' + i\epsilon' \tag{C.2.3}$$

Thus, the relative permittivity ϵ_r and the dissipation factor $tan\delta$ can be found, respectively, by equations C.2.4 and C.2.5. The equation C.2.5 also shows that the $tan\delta$ is related to the ohmic conductivity σ_Ω and the angular moment ω.

$$\epsilon_r = \frac{\text{mod } \epsilon^*}{\epsilon_0} \tag{C.2.4}$$

$$tan\delta = \frac{\epsilon''}{\epsilon'} = tan\delta_h + \frac{\sigma_\Omega}{\omega\epsilon'} \tag{C.2.5}$$

That material's response to the field is due to dipole relaxation arising from orientational motions of molecular dipoles, and electrical conduction from translational motions of electric charges [239].

The polarisation mechanisms: Many polarisation mechanisms can interplay on the final relative permittivity, each one with a particular relaxation time, thus being accessed through different frequencies, as seen in Figure C.2.1. From low frequencies (and longer relaxation times) to higher frequencies:

- **Interfacial polarization:** It comes from interfaces between the sample and the electrodes, or internal material's interface (= *interphase*), as among amorphous and semi-crystalline phases, filler and matrix in composites, polymer A and polymer B in immiscible blends [240]. The Maxwell-Wagner-Sillars (MWS) theory computes the overall permittivity based on each component of a multi-layer, as well as a characteristic relaxation time τ_{MWS} (equation C.2.6) for the interfacial polarization [87].

$$\tau_{MWS} = \frac{(\epsilon_1 d_2 + \epsilon_2 d_1)\epsilon_0}{\sigma_1 d_2 + \sigma_2 d_1} \tag{C.2.6}$$

Therefore, at $\omega = 0$, the statics ϵ_s and σ_s can be found according to the equation system C.2.7.

$$\begin{cases} \epsilon_s = \left(\frac{\sigma_1 \sigma_2 d}{\sigma_1 d_2 + \sigma_2 d_1}\right)\left(\frac{\tau_1 + \tau_2 - \tau}{\epsilon_0}\right) \\ \sigma_s = \frac{\sigma_1 \sigma_2 d}{\sigma_1 d_2 + \sigma_2 d_1} \end{cases} \tag{C.2.7}$$

In addition, as can be seen by equation C.2.5, the ohmic conductivity σ_Ω is proportional to the ϵ' by a factor $1/\omega$; as consequence, if at lower frequencies ϵ' is constant and the slope of -1 is found for ϵ'', we have a purely ohmic conduction. Otherwise, if the slope is higher than -1 and if ϵ' increases, there are charge carriers scattered against the electrodes, characterizing interfacial polarization and space charge accumulation [239].

- **Hoping polarization:** the field reduces the barrier energy between an electron and a neighbor site, therefore promoting a hopping dipole moment which is the moment generated by the transition of a separate charge particle from one potential well to another potential well [87].

- **Orientational/dipolar polarisation:** alignment of permanent dipole moments to the electric field, giving a net polarization in that direction. It comes from the presence of dipoles and asymmetry of atomic groups in the polymer, and it can be related to the molar weight, cross-links, amorphous and crystalline phases.

- **Atomic polarisation:** distortion of the arrangement of atomic nuclei in a polymer molecule.

- **Electronic polarisation:** displacement of the electron cloud of any atom in the polymer macro-molecule relative to its positive nucleus.

The static permittivity ϵ_s from AC measurements: We can extrapolate results to obtain theoretical DC permittivity through Cole-Cole plots, which is an alternative representation to the data of Figure C.2.1, only valid when the material respects the Debye model, i.e., when the *phenomenon* observed is an orientational polarization limited by a relaxation time τ_r according to the equation C.2.8 [242]:

$$P(t) = P_0(1 + exp(-t/\tau_r)) \tag{C.2.8}$$

The ideally Cole-Cole representation, illustrated in Figure C.2.2, plots ϵ'' against ϵ'. As the frequency $\omega = 2\pi f/T$, with T = period, increases from lower to higher values, a perfect circular plot results. The boundaries can be determined, which includes the f = 0 case, or the DC one, giving birth again to the static permittivity ϵ_s [240].

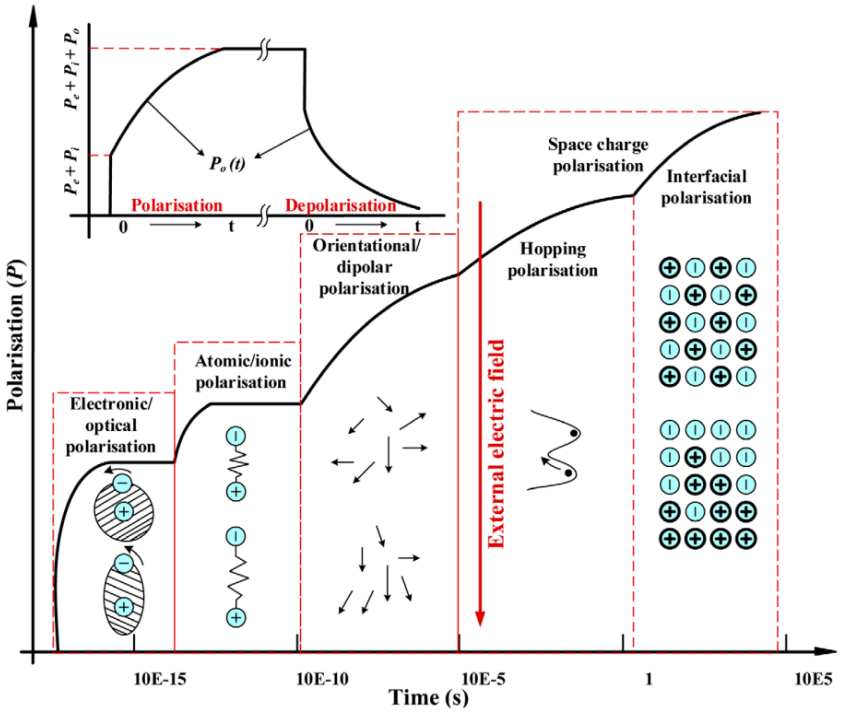

Figure C.2.1: The dielectric permittivity spectrum ranging from higher frequencies, where the electronic polarization occurs, and passing by atomic/ionic polarization, dipolar polarization, and interfacial one. These frequency values are just illustrative, they will change according to the material and operational parameters, notably the temperature [241, 87].

C.3 Materials and methods

C.3.0.1 Set-up

The BDS has been performed with a Novocontrol Alpha-A high resolution dielectric, conductivity, impedance and gain phase modular measurement system (Figure C.3.1(a) having as frequency range $3\mu Hz - 40MHz$, capacity range of $10^{-15}F - 10F$, and impedance range of $0.01\Omega - 2.1014\Omega$. The electrodes have the same format, materials, and dimensions of the electrodes used for current measurements, as seen in Figure C.3.1(b). The test, whose simplified scheme is illustrated in Figure C.3.1(c), consists of the application of a sinusoidal wave voltage $U_1(t)$ by a generator. The material's respond, as electrical current, is converted in voltage $U_2(t)$ by a resistance R. The voltages are are analyzed with respect to the amplitudes and phases of their harmonic Fourier base waves $U_1^*(\omega)$ and $U_2^*(\omega)$. Their relationship give the complex impedance $Z^*(\omega)$ [239].

C.3.0.2 Measurement program

Samples have been conditioned according to the procedure of section 2.3. Once installed in the test cell, at least 4 hours were necessary to achieve temperature equilibrium. The cell does not allow the vacuum pump and the fully control of the RH, which was dependent of the climatic chamber characteristics. Thus, at 20°C, the lowest

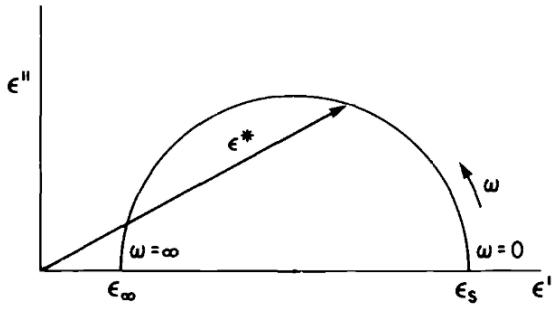

Figure C.2.2: Cole-Cole representation of complex permittivity [240].

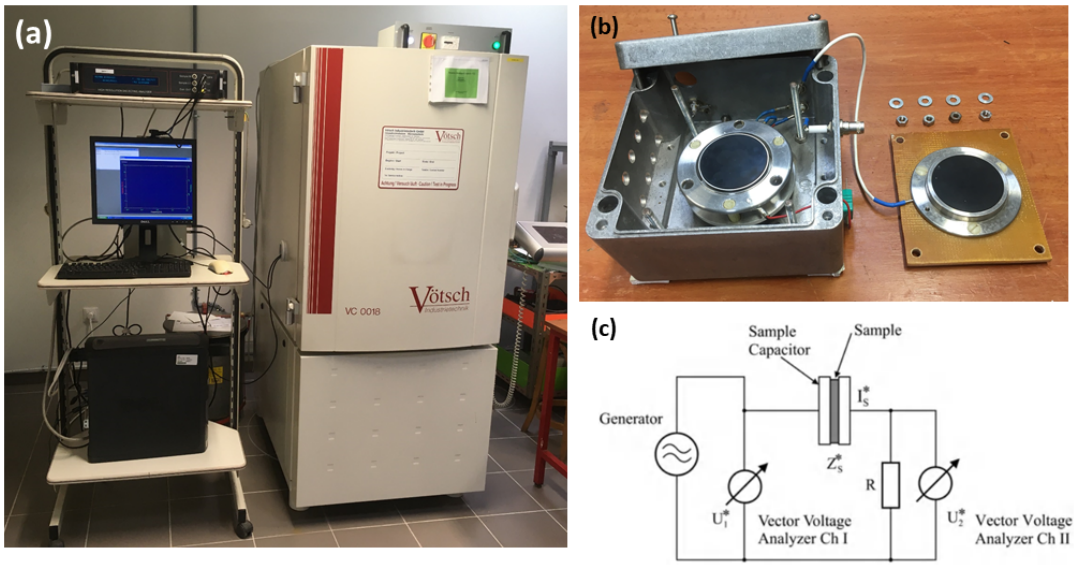

Figure C.3.1: Electrical test apparatus and analyser set-up (a). View of the electrodes (b). Scheme of a simplified Fourier correlation analyser (c) from [239]

C.4 Study case 1: Epoxy composite

The broadband dielectric spectroscopy has been performed for conditioned samples with 2-sides gold sputtering. The data is presented in Figure C.4.1 with regard to the lowest frequencies of the measurement. As we can see, for all measurements, the real components of the permittivity (ϵ') increases as the frequency decreases, all of them having the same values at high frequency. This behaviour is so-called *Low Frequency Dispersion (LFD)*. The relative permittivity also increases with temperature, sometimes somehow linearly (for dry samples, Figure C.4.1(a)) or not linearly (Figures C.4.1(b) and (c)).

The dispersion of permittivity at 10^{-2} Hz is narrow for dry samples (variation of 1.3 units) to very large as the water uptake increases (a variation of 6 units and 370 for samples conditioned at 50% RH and 90% RH respectively). Two remarks have to be made:

1. Measures of wet samples have been reproduced with less accuracy. As we can see for Figure C.4.1(c), more than one try has been made, and the values at low frequency changed considerably. At 80°C, the ϵ' of a first try was equal to 375, and in a second try, 150.

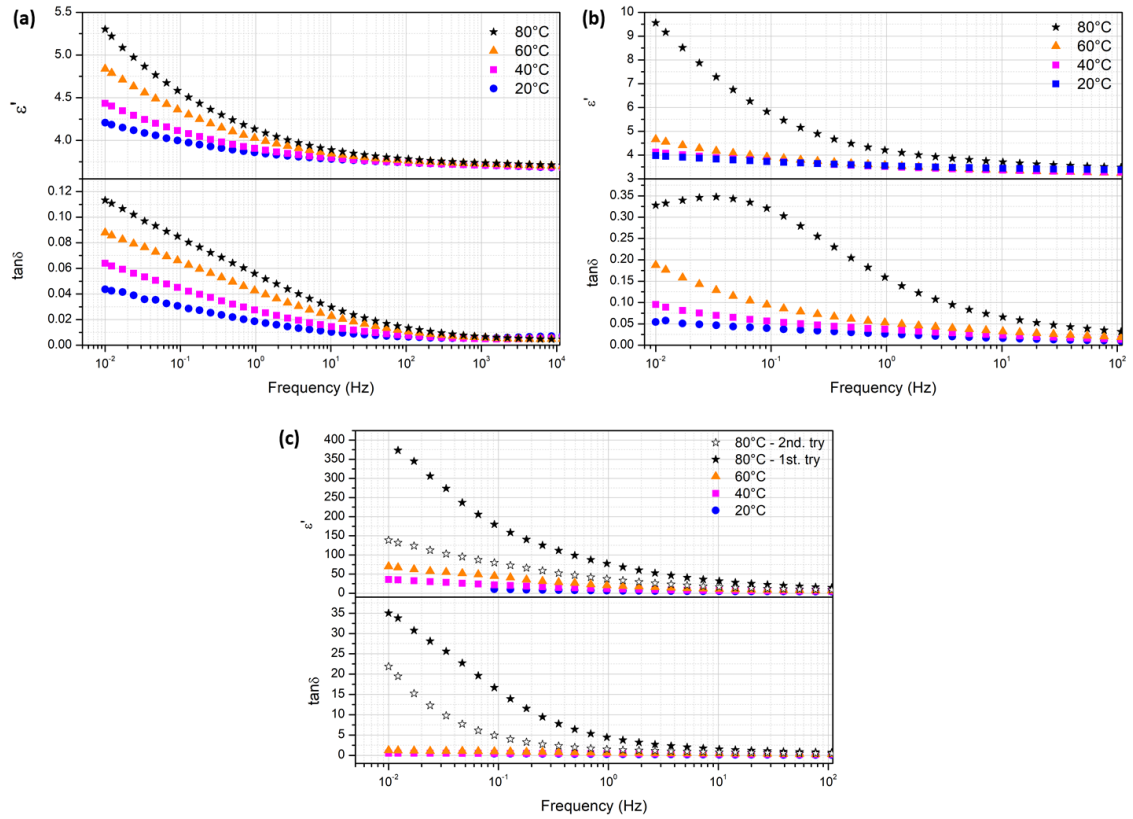

Figure C.4.1: Dielectric spectroscopy of samples conditioned and tested at dry environment (1-3% RH) (a), 50% RH (b), and 90% RH (c).

2. Looking to the $tan\delta$ curves, we can note that they also increase with the decrease of the frequency, and in the particular case of Figure C.4.1(b), at 80°C, the curve appearance suggest that a relaxation time around $3.10^{-2}Hz$ can be set. That's the only curve in which we can make the same consideration, and as Figure C.4.1(c), was not entirely repeatable.

Why do the LFD occur? There are two main trends of thinking: in a first one, more classical, also known as Maxwell-Wagner-Sillars polarization (MWS, [240]), the LFD could be related to an interfacial polarization, so as the polarization between sample and electrodes, or internal interfaces (*interphases*) coming from matrix and filler, also impacted by dispersed macroscopic impurity regions. Because of heterogeneities, space charge build up should occur, as a result of different conductivities and permittivities of the different components of the material. This lead to field distortion and an increase of dielectric loss similarly to ionic and dipole relaxation events. Another trend, developed by Jonscher [243], consider many other different events: a dispersive volume made of a series combination of impedances (not so far from MWS); a conducting volume without any dielectric "signature"; separating injection and removing charge mechanisms, as the Schottky injection, which limits the response as a whole; blocking contacts that limit the response by their geometry or roughness; and electrochemical charge storage as a complement of electrostatics.

By any means, the LFD looks to be general for this sample, and pose concerns about what should be the static permittivity of the material.

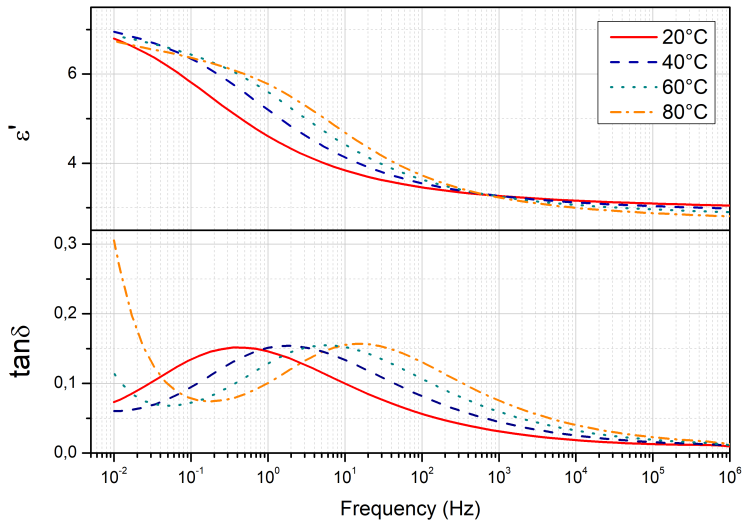

Figure C.5.1: Dielectric properties of the silicone rubber previously dry and measured at isothermal conditions (20°C, 40°C, 60°C, and 80°C) as a function of the frequency. The samples has not been covered by gold.

C.5 Study case 2: Industrial silicone rubber

For exploratory purposes, dielectric spectroscopy was conducted on dry silicone rubber at temperatures of 20°C, 40°C, 60°C, and 80°C, spanning a frequency range from 10^{-2} Hz to 10^{6} Hz. The samples were not sputtered. Each test typically lasted 20 minutes per temperature, with an additional 4 hours allocated to ensure thermal equilibrium.

The results, depicted in Figure C.5.1, illustrate the real component of the permittivity (ϵ') and $tan\delta$. Unlike epoxy samples, there is no dispersion in the low-frequency domain. A relaxation peak is observed at frequencies around 0.5 Hz (20°C), progressing to 50 Hz at 80°C. Additionally, a significant increase in loss is noted at low frequencies for the sample at 80°C.

When plotting the imaginary component of the permittivity against its real component, as suggested by the Cole-Cole plot, a portion of a half-circle can be identified (Figure C.5.2). If we extend the drawing of the half-circle to facilitate the estimation of static permittivities (ϵ_r), the colored values intersecting the x-axis in Figure C.5.2 should represent them.

At 50 Hz, the permittivity of this material would be defined as 3.5, as indicated by the material data sheet. However, the ϵ_0 is approximately 8 at 20°C and decreases with increasing temperature to 6.5 at 80°C.

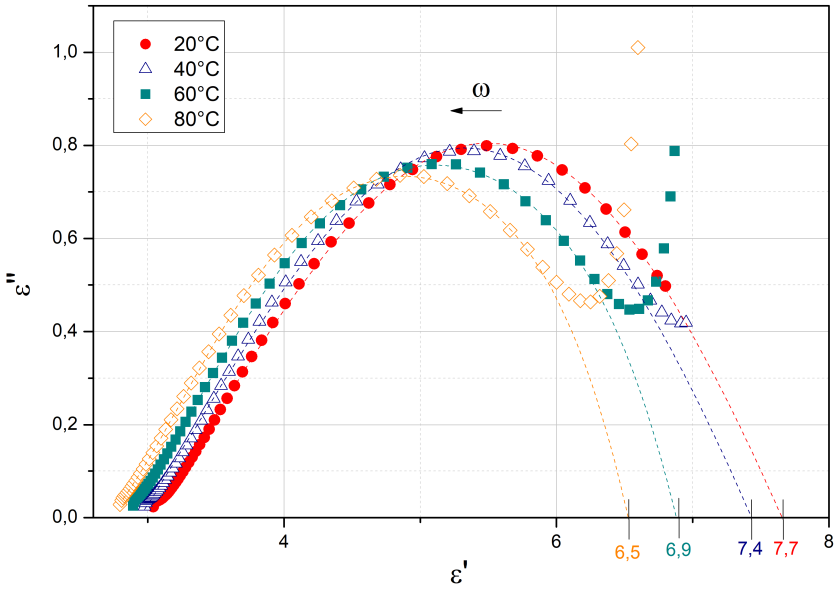

Figure C.5.2: Cole-cole plot of the silicone rubber previously dry and measured at isothermal conditions (20°C, 40°C, 60°C, and 80°C). The samples has not been covered by gold.

Bibliography

[1] Steven W Blume. *Electric power system basics: for the nonelectrical professional*. Piscataway, 2007. ISBN: 9780470129876. DOI: 10.5860/choice.45-4403 (cit. on pp. 2, 7).

[2] Kreuger. *Industrial High DC Voltage*. Delft University Press, 1995. ISBN: 9781626239777 (cit. on p. 2).

[3] Andreas Küchler. *High Voltage Engineering: Fundamentals, technology, applications*. 5th ed. Berlin: Springer Nature, 2018 (cit. on pp. 2, 168).

[4] ABB SACE Devision. *Technical Application Papers No. 24: Medium voltage direct current applications*. Tech. rep. 24. ABB S.p.A., 2017, p. 52. URL: http://search-ext.abb.com/library/Download.aspx?DocumentID=1VCP000681&LanguageCode=en&DocumentPartId=&Action=Launch (cit. on pp. 2, 3).

[5] John Cowdrey. "The War of Currents". In: *Home Power* 111 (2006), pp. 88–92. URL: www.homepower.com (cit. on p. 2).

[6] Clark W Gellings. *The Smart Grid - Enabling energy efficiency and demand response*. 1st ed. Vol. 1. 1. Lilburn, 2009. ISBN: 9781439815748. URL: http://marefateadyan.nashriyat.ir/node/150 (cit. on pp. 2, 5).

[7] Z MA and W. Sheng. *Active distribution systems and distributed energy resources C6: Medium voltage direct current (MVDC) grid feasibility study*. Tech. rep. CIGRE, 2020 (cit. on p. 2).

[8] ENEDIS. *Quels sont les différents types de réseaux électriques ?* URL: https://www.enedis.fr/faq/prevention-du-risque-electrique/quels-sont-les-differents-types-de-reseaux-electriques (cit. on p. 3).

[9] International Electrotechnical Commision. *IEC 60038 - Tensions normales de la CEI*. Tech. rep. 2009 (cit. on p. 3).

[10] Schneider Electric. *Medium Voltage technical guide: Basics for MV design according to IEC standards*. Tech. rep. 2018, p. 136. URL: http://www2.schneider-electric.com/documents/panelbuilders/en/shared/technical-ressources/medium-voltage-design-guide.pdf (cit. on pp. 3, 8).

[11] Schneider Electric Manual. *Guide de conception des réseaux électriques industriels: Les architectures de réseaux*. Tech. rep. 1997, pp. 23–57. URL: https://www.se.com/ww/en/download/document/IENDG_6883427A_chap1/ (cit. on p. 3).

[12] Willis Long. "Evolution of HVdc Links: Mercury-Arc Valves, Thyristors, and More [In My View]". In: *IEEE Power and Energy Magazine* 17.3 (May 2019). ISSN: 15584216. DOI: 10.1109/MPE.2019.2896692 (cit. on p. 4).

[13] International Renewable Energy Agency. *Global energy transformation : a roadmap to 2050*. Tech. rep. 2019 (cit. on p. 5).

[14] Ardelean M and Minnebo P. "A China-EU electricity transmission link: Assessment of potential connecting countries and routes". In: *JRC Science for Policy Report*. Ed. by Jont Research Centre European Comission. 2017. ISBN: 9789279793585. DOI: 10.2760/67516. URL: https://ec.europa.eu/jrc (cit. on p. 5).

[15] Shahid Ullah et al. *The current state of Distributed Renewable Generation, challenges of interconnection and opportunities for energy conversion based DC microgrids*. Nov. 2020. DOI: 10.1016/j.jclepro.2020.122777 (cit. on p. 5).

[16] Gen Li et al. "Frontiers of DC circuit breakers in HVDC and MVDC systems". In: *2017 IEEE Conference on Energy Internet and Energy System Integration (EI2)1*. Beijing, 2017, pp. 1–6. DOI: 10.1109/EI2.2017.8245743. (cit. on p. 6).

[17] Christian M. Franck. "HVDC circuit breakers: A review identifying future research needs". In: *IEEE Transactions on Power Delivery* 26.2 (Apr. 2011), pp. 998–1007. ISSN: 08858977. DOI: 10.1109/TPWRD.2010.2095889 (cit. on pp. 6, 7).

[18] Feng Wang, Lina Bertling, and Tuan Le. *An Overview Introduction of VSC-HVDC: State-of-art and Potential Applications in Electric Power Systems*. Tech. rep. Bologna: CIGRE, 2011. URL: http://www.cigre.org (cit. on p. 6).

[19] D M Larruskain et al. "Transmission and Distribution Networks: AC versus DC". Bilbao, 2003 (cit. on p. 6).

[20] Andreas Giannakis and Dimosthenis Peftitsis. "MVDC distribution grids and potential applications: Future trends and protection challenges". In: *2018 20th European Conference on Power Electronics and Applications (EPE'18 ECCE Europe)* (2018) (cit. on p. 6).

[21] X Pei et al. "A review of technologies for MVDC circuit breakers". In: *IECON 2016 - 42nd Annual Conference of the IEEE Industrial Electronics Society*. 2016, pp. 3799–3805. ISBN: 9781509034741. DOI: 10.1109/IECON.2016.7793492 (cit. on p. 6).

[22] Dragan Jovcic, Guangfu Tang, and Hui Pang. "Adopting Circuit Breakers for High-Voltage dc Networks: Appropriating the Vast Advantages of dc Transmission Grids". In: *IEEE Power and Energy Magazine* 17.3 (May 2019), pp. 82–93. ISSN: 15584216. DOI: 10.1109/MPE.2019.2897408 (cit. on p. 6).

[23] Francisco De Leon. "The future belongs to dc: Edison will beat Tesla after all". In: *IEEE Power and Energy Magazine* 21.2 (Mar. 2023), pp. 78–80. ISSN: 15584216. DOI: 10.1109/MPE.2022.3231000 (cit. on p. 7).

[24] V. K. Mehta and Rohit Mehta. "Introduction to Switchgears". In: *Principles of power system*. Ed. by S. Chand & Company. Vol. 1. New Delhi: Schand, 2006. Chap. 16, pp. 387–395 (cit. on p. 7).

[25] Schneider Electric. *Catalog 2021: Components for Medium Voltage Switchgear*. Tech. rep. 2021 (cit. on pp. 7, 8).

[26] International Electrotechnical Commission. *High-voltage switchgear and controlgear. Part 1: Common specifications for alternating current switchgear and controlgear*. Tech. rep. 2017, p. 256 (cit. on p. 7).

[27] Donald. R. Askeland, Pradeep P. Fulay, and Wendelin J. Wright. *The Science and Engineering of Materials*. 6th. Cencage Learning, 2011 (cit. on p. 9).

[28] L.H. Sperling. *Introduction to physical polymer science*. 4th. Vol. 53. 2. Hoboken, New Jersey, 2006. ISBN: 9780471706069. DOI: 10.1016/0923-0467(93)85007-i (cit. on pp. 9, 10).

[29] A. D. (Aubrey Dennis) Jenkins. *Polymer science. A materials science handbook*. Vol. 1. North-Holland Pub. Co, 1972 (cit. on p. 9).

[30] Sebastião V. Canevarolo Jr. *Ciência de polimeros: Um texto basico para tecnologis e engenheiros*. 2nd. São Paulo: Artliber Editora Ltda., 2006 (cit. on p. 10).

[31] Jean-Pierre Pascault. *Thermosetting polymers*. Marcel Dekker, 2002, p. 477. ISBN: 0824706706 (cit. on pp. 10, 104).

[32] I. Franta. *Elastomers and rubber compounding materials*. Elsevier, 1990. ISBN: 0444429948 (cit. on p. 10).

[33] Sanjay K. Mazumdar. *Composites manufacturing : materials, product, and process engineering*. CRC Press, 2002, p. 392. ISBN: 0849305853 (cit. on p. 10).

[34] B. Ellis. *Chemistry and Technology of Epoxy Resins*. Springer Netherlands, 1993. DOI: 10.1007/978-94-011-2932-9 (cit. on pp. 11, 12).

[35] Clayton May. *Epoxy Resins*. Ed. by Clayton A. May. Routledge, May 1988. ISBN: 9780203756713. DOI: 10.1201/9780203756713 (cit. on pp. 11, 12, 14).

[36] Ansheng Xie et al. "The characteristics of electrical trees in the inner and outer layers of different voltage rating XLPE cable insulation". In: *Journal of Physics D: Applied Physics* 42.12 (2009), p. 10. ISSN: 00223727. DOI: 10.1088/0022-3727/42/12/125106 (cit. on p. 12).

[37] Huong Mai Le Huy. "Vieillissement d'un réseau époxy-anhydride". PhD thesis. Paris: Ecole Nationale Supérieure d'Arts et Métiers, July 1990 (cit. on pp. 12, 13, 62).

[38] Valérie Dureault. "Vieillissement de surfaces d'isolateurs en résine époxy-anhydride : rôles respectifs des UV at du champs électrique". PhD thesis. Grenoble: Université Joseph-Fourier - Grenoble 1, Jan. 1995 (cit. on pp. 12, 62, 65).

[39] C Barrère and F Dal Maso. *Résines époxy réticulées par des polyamines: Structure et propriétés*. Tech. rep. 1997 (cit. on p. 14).

[40] M. K. Antoon and J. L. Koenig. "Crosslinking mechanism of an anhydride-cured epoxy resin as studied by fourier transform infrared spectroscopy". In: *Journal of Polymer Science: Polymer Chemistry Edition* 19.2 (Feb. 1981), pp. 549–570. ISSN: 0360-6376. DOI: 10.1002/pol.1981.170190228. URL: https://onlinelibrary.wiley.com/doi/10.1002/pol.1981.170190228 (cit. on p. 14).

[41] G C Stevens and M J Richardson. *Factors influencing the glass transition of DGEBA-anhydride epoxy resins*. Tech. rep. 1983 (cit. on p. 14).

[42] Alexander J.G. Lunt, Philip Chater, and Alexander M. Korsunsky. "On the origins of strain inhomogeneity in amorphous materials". In: *Scientific Reports* 8.1 (Dec. 2018). ISSN: 20452322. DOI: 10.1038/s41598-018-19900-2 (cit. on p. 15).

[43] Stéphane Holé, Alain Sylvestre, and Stephen Rowe. "The influence of filler particles on space charge measurements". In: *Journal of Physics D: Applied Physics* 37.13 (2004), pp. 1869–1876. ISSN: 00223727. DOI: 10.1088/0022-3727/37/13/022 (cit. on pp. 15, 49).

[44] Maurice et al Morton. *Rubber Technology*. Ed. by Maurice Morton. 1st. Dordrecht: Springer Netherlands, 1999. ISBN: 978-90-481-4010-7. DOI: 10.1007/978-94-017-2925-3. URL: http://link.springer.com/10.1007/978-94-017-2925-3 (cit. on pp. 15, 16).

[45] Wacker AG Chemie. *Solid and liquid silicone rubber: Material and processing guidelines*. Tech. rep. URL: https://www.wacker.com/h/medias/6709-EN.pdf (cit. on pp. 15–17).

[46] Michel Biron. "Silicones ou siloxanes: Structure et propriétés". In: *Techniques de l'ingénieur* N2880.0 (2007), pp. 0–21. URL: http://www.techniques-ingenieur.fr/res/pdf/encyclopedia/42615210-n2880.pdf (cit. on p. 15).

[47] Philip A. Schweitzer. "Standard Practice for Rubber and Rubber Latices—Nomenclature". In: i (2006), pp. 21–23. DOI: 10.1520/D1418-21A.2 (cit. on p. 15).

[48] H. Hillborg and U. W. Gedde. "Hydrophobicity changes in silicone rubbers". In: *IEEE Transactions on Dielectrics and Electrical Insulation* 6.5 (1999), pp. 703–717. ISSN: 10709878. DOI: 10.1109/94.798127 (cit. on pp. 16, 49).

[49] H. Homma et al. "Diffusion of low molecular weight siloxane from bulk to surface". In: *IEEE Transactions on Dielectrics and Electrical Insulation* 6.3 (1999), pp. 370–375. ISSN: 10709878. DOI: 10.1109/94.775625 (cit. on p. 16).

[50] Wahyu S. Putro et al. *From SiO2 to Alkoxysilanes for the Synthesis of Useful Chemicals*. Dec. 2021. DOI: 10.1021/acsomega.1c05138 (cit. on pp. 16, 70).

[51] Theresia Köhler, Andrea Gutacker, and Esteban Mejiá. "Industrial synthesis of reactive silicones: Reaction mechanisms and processes". In: *Organic Chemistry Frontiers* 7.24 (2020), pp. 4108–4120. ISSN: 20524129. DOI: 10.1039/d0qo01075h (cit. on p. 16).

[52] Ján Kruželák, Richard Sýkora, and Ivan Hudec. "Vulcanization of rubber compounds with peroxide curing systems". In: *Rubber Chemistry and Technology* 90.1 (Mar. 2017), pp. 60–88. ISSN: 00359475. DOI: 10.5254/rct.16.83758 (cit. on p. 17).

[53] Matthew Bont, Carol Barry, and Stephen Johnston. *A review of liquid silicone rubber injection molding: Process variables and process modeling*. Feb. 2021. DOI: 10.1002/pen.25618 (cit. on pp. 18, 168).

[54] W. Michel. "Pyrogenic silica as a filler for elastomeric materials". In: *Gummi Fassern Kunststoffe* (2007), pp. 98–105 (cit. on p. 18).

[55] Yang Xue et al. "Comparison of ATH and SiO2 fillers filled silicone rubber composites for HTV insulators". In: *Composites Science and Technology* 155 (Feb. 2018), pp. 137–143. ISSN: 02663538. DOI: 10.1016/j.compscitech.2017.12.006 (cit. on p. 18).

[56] V. M. Gun'ko et al. "Morphology and surface properties of fumed silicas". In: *Journal of Colloid and Interface Science* 289.2 (Sept. 2005), pp. 427–445. ISSN: 00219797. DOI: 10.1016/j.jcis.2005.05.051 (cit. on p. 18).

[57] V M Kopylov et al. "Silica fillers for silicone rubber". In: *Kauchuk i Rezina* 5 (2010), pp. 32–43 (cit. on pp. 18, 50).

[58] Liliane Bokobza. "Elastomeric composites. I. Silicone composites". In: *Journal of Applied Polymer Science* 93.5 (2004), pp. 2095–2104. ISSN: 00218995. DOI: 10.1002/app.20684 (cit. on p. 18).

[59] A Dupont, Dow Corning, and Europe Sa. "Silicones in Industrial Applications". In: *Inorganic Polymers*. Ed. by Roger de Jaeger and Mario Gleria. Vol. 186. 17. 2007, pp. 61–161. ISBN: 1-60021-656-0. URL: https://krayden.com/pdf/xia_tech_paper_characterization_silicones.pdf (cit. on p. 18).

[60] J. Comyn. *Polymer Permeability*. Springer Netherlands, 1985. DOI: 10.1007/978-94-009-4858-7 (cit. on pp. 19, 20, 22, 23).

[61] Gold Book. *The IUPAC Compendium of Chemical Terminology*. Ed. by Victor Gold. Research Triangle Park, NC: International Union of Pure and Applied Chemistry (IUPAC), 2019. DOI: 10.1351/goldbook. URL: https://goldbook.iupac.org/ (cit. on p. 20).

[62] Pavel Veverka and Karel Jeřábek. "Influence of hypercrosslinking on adsorption and absorption on or in styrenic polymers". In: *Reactive and Functional Polymers* 59.1 (Apr. 2004), pp. 71–79. ISSN: 13815148. DOI: 10.1016/j.reactfunctpolym.2003.12.008 (cit. on p. 20).

[63] Arthur W. Adamson and Alice P. Gast. *Physical chemistry of surfaces*. 6th. John Wiley and Sons, 1997 (cit. on pp. 20, 22, 131).

[64] John Crank. *The mathematics of diffusion*. 1956. ISBN: 0198533446 (cit. on pp. 20, 21).

[65] R. Daviaud and C. Filliatre. *Introduction aux matériaux composites. 1 - Matrices organiques*. Vol. 1. CNRS, 1985 (cit. on pp. 20, 45).

[66] Harris G. Carter and Kenneth G. Kibler. "Langmuir-Type Model for Anomalous Moisture Diffusion In Composite Resins". In: *Journal of Composite Materials* 12.2 (1978), pp. 118–131. ISSN: 1530793x. DOI: 10.1177/002199837801200201 (cit. on pp. 22, 25).

[67] Jacques Verdu. *Action de l'eau sur les plastiques*. Tech. rep. Techniques de l'ingénieur, 2000 (cit. on pp. 22, 45, 46).

[68] Hans Swenson and Nicholas P. Stadie. "Langmuir's Theory of Adsorption: A Centennial Review". In: *Langmuir* (2019). ISSN: 15205827. DOI: 10.1021/acs.langmuir.9b00154 (cit. on pp. 22, 24, 144).

[69] Khim Hoong Chu et al. "The Flory-Huggins Isotherm and Water Contaminant Adsorption: Debunking Some Modeling Fallacies". In: *Industrial and Engineering Chemistry Research* 62.2 (2023), pp. 1121–1131. ISSN: 15205045. DOI: 10.1021/acs.iecr.2c03799 (cit. on pp. 22, 25).

[70] Duong Do. *Adsorption analysis: Equilibria and kinetics*. Vol. 2. Imperial College Press, 1998 (cit. on pp. 22, 23, 131, 144).

[71] Peter Atkins, Julio De Paula, and James Keeler. *Physical Chemistry*. 2023 (cit. on p. 24).

[72] Michael J. Adamson. "Thermal expansion and swelling of cured epoxy resin used in graphite/epoxy composite materials". In: *Journal of Materials Science* 15.7 (1980), pp. 1736–1745. ISSN: 00222461. DOI: 10.1007/BF00550593 (cit. on p. 24).

[73] Panaghiotis Nikitas. *Generalized Flory-Huggins Isotherms for Adsorption from Solution*. Tech. rep. 1984, pp. 3315–3329 (cit. on p. 25).

[74] K Robert Lange. "The characterization of molecular water on silica surfaces". In: *Journal of Colloid Science* 20 (1965), pp. 231–240 (cit. on pp. 26, 50, 133).

[75] E. Kuffel, W. S. Zaengl, and J. Kuffel. *High voltage engineering : fundamentals*. Butterworth-Heinemann/Newnes, 2000, p. 239. ISBN: 0750636343 (cit. on p. 26).

[76] Christian Laurent. "D2305 Diélectriques solides et charge d'espace .pdf". In: () (cit. on pp. 30, 31, 39).

[77] N. H. Ahmed and N. N. Srinivas. "Review of space charge measurements in dielectrics". In: *IEEE Transactions on Dielectrics and Electrical Insulation* 4.5 (1997), pp. 644–656. ISSN: 10709878. DOI: 10.1109/94.625650 (cit. on p. 30).

[78] Stéphane Holé, Thierry Ditchi, and Jacques Lewiner. "Non-destructive methods for space charge distribution measurements: What are the differences?" In: *IEEE Transactions on Dielectrics and Electrical Insulation* 10.4 (2003), pp. 670–677. ISSN: 10709878. DOI: 10.1109/TDEI.2003.1219652 (cit. on p. 30).

[79] Petru Notingher. *Characterization methods for dielectrics: Resitivity and conduction currents*. Porquerolles, 2021 (cit. on pp. 30, 37, 42).

[80] P Rain and J L Augé. *Influence of the electrode metal on the injection of space charges in PET and epoxy resin*. Tech. rep. (cit. on p. 30).

[81] Tran Van Hoan. "Injection de charges dans le polyethylene terephtalate à partir de la méthode de l'onde de pression induite par impact laser (LIPP) : modélisation physique et optimisation de la méthode, influence des paramètres de l'inetrface métal-isolant". PhD thesis. Grenoble: Université de Grenoble, June 2010. URL: https://www.theses.fr/2010INPG0050 (cit. on pp. 30, 31, 81).

[82] Duc Hoang Nguyen. "Etude des propriétés électriques des élastomères silicones utilisés pour l'isolation électrique". PhD thesis. 2005 (cit. on pp. 30, 51–53).

[83] S. Holé et al. "Space charge distribution measurement methods and particle loaded insulating materials". In: *Journal of Physics D: Applied Physics* 39.5 (2006), pp. 950–956. ISSN: 00223727. DOI: 10.1088/0022-3727/39/5/009 (cit. on pp. 30, 31).

[84] G. M. Sessler. "Charge distribution and transport in polymers". In: *IEEE Transactions on Dielectrics and Electrical Insulation* 4.5 (1997), pp. 614–628. ISSN: 10709878. DOI: 10.1109/94.625648 (cit. on p. 30).

[85] G M Sessler, J E West, and R Gerhard. *Measurement of Charge Distribution in Polymer Electrets by a New Pressure-Pulse Method*. Tech. rep. 1981, pp. 9–111 (cit. on p. 30).

[86] G. M. Sessler, J. E. West, and G. Gerhard. "High-Resolution Laser-Pulse Method for Measuring Charge Distributions in Dielectrics". In: *Physical Review Letters* 48.8 (1982), pp. 563–566. ISSN: 00319007. DOI: 10.1103/PhysRevLett.48.563 (cit. on p. 30).

[87] K C Kao. *Dielectric phenomena in solids: with emphasis on physical concepts of electronic processes*. Elsevier Academic Press, 2004 (cit. on pp. 31, 33, 40, 41, 43, 171–173).

[88] James F. Shackelford. *Introduction to materials science for engineers*, p. 601. ISBN: 9780133826654 (cit. on pp. 33, 34).

[89] L. A. Dissado and J.C. Fothergill. *Electrical Degradation and Breakdown in Polymers*. Ed. by D.V. Morgan, N. Parkman, and K. Obershott. 1st ed. London: Peter Peregrinus Ltd., 1992, p. 601. ISBN: 0863411967 (cit. on pp. 33, 34, 37, 39, 43, 117, 118, 155).

[90] G Teyssedre and C Laurent. *Charge Transport Modeling in Insulating Polymers: From Molecular to Macroscopic Scale*. Tech. rep. 5. 2005 (cit. on pp. 34, 39, 44, 149).

[91] Murray Lampert and P Mark. *Current injection in solids*. New York: Academic Press, 1970 (cit. on pp. 35, 37, 38, 116, 155, 171).

[92] Roland Coelho and Bernard Aladenize. *Les diélectriques. Propriétés diélectriques des matériaux isolants*. 1st ed. Vol. 1. Lavoisier-Hermès, 1993 (cit. on pp. 35, 39, 43).

[93] H. J. Wintle. "Absorption currents and steady currents in polymer dielectrics". In: *Journal of Non-Crystalline Solids* (1974), pp. 471–486 (cit. on p. 35).

[94] A Manv and G Rakavy. *Theory of Transient Space-Charge-Limited Currents in Solids in the Presence of Trapping*. Tech. rep. 6. 1962 (cit. on p. 37).

[95] Mitsumasa Iwamoto. "Transient current across insulating films with long-range movements of charge carriers". In: *Journal of Applied Physics* 79.10 (May 1996), pp. 7936–7943. ISSN: 00218979. DOI: 10.1063/1.360953 (cit. on p. 37).

[96] Christophe Guillermin. "Vieillissement electrique et thermique d un composite resine epoxy-silice". PhD thesis. Grenoble: Université Joseph Fourier Grenoble I, 2004 (cit. on pp. 43, 121, 122).

[97] N. F. Mott and R. W. Gurney. *Electronic Process in Ionic Crystals*. 2nd ed. Oxford University Press, 1948 (cit. on p. 43).

[98] Yvan Segui. "Courants de conduction". In: *Techniques de l'ingénieur* 33.0 (2014), pp. 1–12 (cit. on p. 43).

[99] W G Lawson. *High-field conduction and breakdown in polythene You may also like High-field conduction and reakdowln in* . Tech. rep. 1965, p. 1805 (cit. on p. 43).

[100] V Griseri et al. "CHARGE INJECTION, ELECTROLUMINESCENCE, AND AGEING OF AN EPOXY RESIN IN HIGH DIVERGENT FIELDS". In: *Dielectric materials, measurements, and applications conference*. 2000 (cit. on p. 43).

[101] C Guillermin, P Rain, and S W Rowe. "Influence of Tg on Space Charge Development in Epoxy Resin". In: *IEEE International Conference on Solid Dielectrics (ICSD)*. 2004 (cit. on pp. 43, 48, 49, 120, 123).

[102] D K Das-Gupta and K Doughty. *DIELECTRIC AND CONDUCTION PROCESSES IN POLYETHERETHER KETONE (PEEK)*. Tech. rep. 1. 1987 (cit. on p. 43).

[103] Alessandro Grillo and Antonio Di Bartolomeo. "A Current–Voltage Model for Double Schottky Barrier Devices". In: *Advanced Electronic Materials* 7.2 (Feb. 2021). ISSN: 2199-160X. DOI: 10.1002/aelm.202000979. URL: https://onlinelibrary.wiley.com/doi/10.1002/aelm.202000979 (cit. on p. 44).

[104] Lars Onsager. "Deviations from Ohm's law in weak electrolytes". In: *The Journal of Chemical Physics* 2.9 (1934), pp. 599–615. ISSN: 00219606. DOI: 10.1063/1.1749541 (cit. on p. 44).

[105] Markus Zahn and Jorge Mescua. "Bipolar charge transport analysis in high voltage stressed dielectrics". In: *Conference on Electrical Insulation & Dielectric Phenomena - Annual Report*. 1985 (cit. on p. 44).

[106] J M Alison and R M Hill. *A model for bipolar charge transport, trapping and recombination in degassed crosslinked polyethene A model for bipolar charge transport, 1 trapping and recombination in degassed crosslinked polyethene*. Tech. rep. 1994, pp. 1291–1299. URL: http://iopscience.iop.org/0022-3727/27/6/029 (cit. on p. 44).

[107] S Le Roy, G Teyssèdre, and C Laurent. "Modelling Space Charge in a Cable Geometry". In: *IEEE Transactions on Dielectrics and Electrical Insulation* 23.4 (2016), pp. 2361–2367. DOI: 10.1109/TDEI.2016.005805 (cit. on p. 44).

[108] Hucheng Liang et al. "Improved space charge transport model in bilayer dielectrics-considering carrier dynamic equilibrium". In: *High Voltage* 5.2 (Apr. 2020), pp. 176–183. ISSN: 23977264. DOI: 10.1049/hve.2019.0193 (cit. on p. 44).

[109] M. Q. Hoang et al. "Modelling the impact of electrode roughness on net charge density in polyethylene". In: *Journal of Physics D: Applied Physics* 54.30 (July 2021). ISSN: 13616463. DOI: 10.1088/1361-6463/abfc8a (cit. on p. 44).

[110] Raphaël Guffond. "Characterization and modeling of microstructure evolution of cable insulation system under high continuous electric field". PhD thesis. Université de Sorbonne, 2019 (cit. on p. 44).

[111] C Laurent et al. *Charge Dynamics and its Energetic Features in Polymeric Materials*. Tech. rep. 2. 2013, p. 357 (cit. on p. 44).

[112] Severine Le Roy et al. "Analysis of Current-Voltage Characteristics in Insulating Polymers Using a Bipolar Charge Transport Model". In: *IEEE Transactions on Dielectrics and Electrical Insulation* 29.6 (Dec. 2022), pp. 2101–2109. ISSN: 15584135. DOI: 10.1109/TDEI.2022.3217429 (cit. on p. 44).

[113] Emilie Brun. "Vieillissement hygrothermique d'un composite resine epoxyde silice et impact sur sa rigidite dielectrique". PhD thesis. 2009, pp. 59–60. URL: https://tel.archives-ouvertes.fr/tel-00440812 (cit. on pp. 45, 46, 62, 75, 100).

[114] T Pham Hong, O Lesaint, and P Gonon. *Water Absorption in a Glass-Mica-Epoxy Composite I: Influence on Electrical Properties*. Tech. rep. 1. 2009 (cit. on pp. 45, 47).

[115] Antonio Apicella et al. "Hygrothermal history dependence of equilibrium moisture sorption in epoxy resins". In: *POLYMER* (1980) (cit. on p. 45).

[116] Antonio Apicella et al. "Effect of thermal history on water sorption, elastic properties and the glass transition of epoxy resins". In: *POLYMER* 20 (1979) (cit. on p. 45).

[117] Antonio Apicella et al. "The effect of water sorption on electrical, mechanical and thermal properties of organic insulating materials". In: *IEEE International Symposium on Electrical Insulation*. 1984 (cit. on pp. 45, 47).

[118] M Reference: Woo and M R Piggott. *Water Absorption of Resins and Composites: I. Epoxy Homopolymers and Copolymers*. Tech. rep. 3. 1987, pp. 101–107 (cit. on p. 46).

[119] Jean Debord et al. "Yesterday, Today, and Tomorrow. Evolution of a Sleeping Beauty: The Freundlich Isotherm". In: *Langmuir* 39.8 (Feb. 2023), pp. 3062–3071. ISSN: 15205827. DOI: 10.1021/acs.langmuir.2c03105 (cit. on p. 46).

[120] B. Lutz and J. Kindersberger. "Influence of absorbed water on volume resistivity of epoxy resin insulators". In: *Proceedings of the 2010 IEEE International Conference on Solid Dielectrics, ICSD 2010*. IEEE, 2010. ISBN: 9781424479443. DOI: 10.1109/ICSD.2010.5568218 (cit. on pp. 46, 47).

[121] B. Lutz and J. Kindersberger. "Influence of relative humidity on surface charge decay on epoxy resin insulators". In: *Proceedings of the IEEE International Conference on Properties and Applications of Dielectric Materials*. I E E E, 2009, pp. 883–886. ISBN: 9781424443680. DOI: 10.1109/ICPADM.2009.5252237 (cit. on p. 46).

[122] Manfred Beyer. "Effect of moisture on dielectric properties". In: *Electrical and dielectric behaviour of cast epoxy resins*. Schering Institute for High-Voltage Engineering and High-Voltage Equipment, 1991. Chap. 1 (cit. on p. 46).

[123] W. Hertl and M. L. Hair. "Adsorption of water on silica". In: *Nature* 223 (1969), pp. 1150–1151 (cit. on p. 46).

[124] Takahiro Imai et al. *Effects of Epoxy/Filler Interface on Properties of Nano- or Micro-composites*. Tech. rep. 2. 2006 (cit. on p. 46).

[125] C. Zou, J. C. Fothergill, and S. W. Rowe. "A "water shell" model for the dielectric properties of hydrated silica-filled epoxy nano-composites". In: *2007 International Conference on Solid Dielectrics, ICSD* (2007), pp. 389–392. DOI: 10.1109/ICSD.2007.4290834 (cit. on pp. 46, 50).

[126] Jian Chen et al. "A review of moisture migration in bulk material". In: *Particulate Science and Technology* 38.2 (Feb. 2020), pp. 247–260. ISSN: 15480046. DOI: 10.1080/02726351.2018.1504152 (cit. on p. 46).

[127] Yongwei Fu et al. "A general form of Archie's model for estimating bulk soil electrical conductivity". In: *Journal of Hydrology* 597 (June 2021). ISSN: 00221694. DOI: 10.1016/j.jhydrol.2021.126160 (cit. on pp. 46, 153).

[128] J. D. Rhoades, P. A. C. Raats, and R. J. Prather. "Effects of Liquid-phase Electrical Conductivity, Water Content, and Surface Conductivity on Bulk Soil Electrical Conductivity". In: *Soil Science Society of America Journal* 40.5 (Sept. 1976), pp. 651–655. ISSN: 0361-5995. DOI: 10.2136/sssaj1976.03615995004000050017x (cit. on pp. 46, 153).

[129] Williard D. Bascom. "Water at the Interface". In: *Journal of Adhesion* 2 (1970) (cit. on pp. 46, 50, 133, 152).

[130] Chen Zou et al. "DC conduction mechanisms in epoxy nanocomposites under the humid environment". In: *Proceedings of the 2010 IEEE International Conference on Solid Dielectrics, ICSD 2010*. 2010. ISBN: 9781424479443. DOI: 10.1109/ICSD.2010.5568060 (cit. on p. 46).

[131] P. Gonon et al. "Influence of high levels of water absorption on the resistivity and dielectric permittivity of epoxy composites". In: *Polymer Testing* 24.6 (Sept. 2005), pp. 799–804. ISSN: 01429418. DOI: 10.1016/j.polymertesting.2005.02.001 (cit. on pp. 46, 47, 50, 131).

[132] L. Zavattoni et al. "Influence of water content and temperature on conduction and field on an Alumina/epoxy insulator". In: *Proceedings of IEEE International Conference on Solid Dielectrics, ICSD*. 2013, pp. 246–249. ISBN: 9781479908073. DOI: 10.1109/ICSD.2013.6619898 (cit. on pp. 46, 75).

[133] R. Lovell. "Decaying and steady currents in an epoxy polymer at high electric fields". In: *Journal of Physics D: Applied Physics* 7.11 (1974), pp. 1518–1530. ISSN: 00223727. DOI: 10.1088/0022-3727/7/11/313 (cit. on p. 47).

[134] M. Ieda. "Electrical Conduction and Carrier Traps in Polymeric Materials". In: *IEEE Transactions on Electrical Insulation* EI-19.3 (June 1984), pp. 162–178. ISSN: 0018-9367. DOI: 10.1109/TEI.1984.298741. URL: http://ieeexplore.ieee.org/document/4081224/ (cit. on pp. 47, 117).

[135] Christophe Guillermin, Pascal Rain, and Stephen W. Rowe. "Transient and steady-state currents in epoxy resin". In: *Journal of Physics D: Applied Physics* 39.3 (2006), pp. 515–524. ISSN: 00223727. DOI: 10.1088/0022-3727/39/3/015 (cit. on pp. 47, 48).

[136] J. Castellon et al. "Electrical properties analysis of micro and nano composite epoxy resin materials". In: *IEEE Transactions on Dielectrics and Electrical Insulation* 18.3 (2011), pp. 651–658. ISSN: 10709878. DOI: 10.1109/TDEI.2011.5931049 (cit. on pp. 47, 48).

[137] J W Mackersie et al. "The electrical properties of filled epoxy resin systems - A comparison". In: *IEEE International Conference on Conduction and Breakdown in Solid Dielectrics*. 2001, pp. 125–128. DOI: 10.1109/icsd.2001.955538 (cit. on p. 47).

[138] Apoorva K. Parmar and R. R. Patel. "Dielectric properties of alumina based epoxy composites for electrical insulation". In: *2018 2nd International Conference on Electronics, Materials Engineering and Nano-Technology, IEMENTech 2018*. Institute of Electrical and Electronics Engineers Inc., Sept. 2018. ISBN: 9781538655498. DOI: 10.1109/IEMENTECH.2018.8465221 (cit. on p. 47).

[139] Yahyaoui. "Matériaux isolants pour appareillages haute tension dans le domaine du courant continu Comportement et vieillissement". In: (2015) (cit. on p. 48).

[140] Loriane DESMARS et al. "High Voltage Electrical Properties of Epoxy / h-BN Microcomposites". In: *2018 IEEE 2nd International Conference on Dielectrics (ICD)*. IEEE, July 2018, pp. 1–5. ISBN: 978-1-5386-6389-9. DOI: 10.1109/ICD.2018.8514777. URL: https://ieeexplore.ieee.org/document/8514777/ (cit. on p. 48).

[141] H. Yahyaoui et al. "Analysis of conduction mechanisms in alumina-filled epoxy resin under dc field and temperature". In: *Annual Report - Conference on Electrical Insulation and Dielectric Phenomena, CEIDP*. 2013, pp. 667–670. ISBN: 9781479925964. DOI: 10.1109/CEIDP.2013.6748181 (cit. on pp. 48, 121, 122).

[142] O. Gallot-Lavallée et al. "Space charge behaviour in an epoxy resin: The influence of fillers, temperature and electrode material". In: *Journal of Physics D: Applied Physics* 38.12 (2005), pp. 2017–2025. ISSN: 00223727. DOI: 10.1088/0022-3727/38/12/025 (cit. on pp. 49, 115, 120).

[143] V. Griseri et al. "Electroluminescence excitation mechanisms in an epoxy resin under divergent and uniform field". In: *IEEE Transactions on Dielectrics and Electrical Insulation* 9.1 (2002), pp. 150–160. ISSN: 10709878. DOI: 10.1109/94.983899. URL: http://ieeexplore.ieee.org/document/983899/ (cit. on p. 49).

[144] Peng Liu et al. "Space Charge Behavior in Epoxy-Based Dielectrics: Progress and Perspective". In: *Advanced Electronic Materials* 8.10 (Oct. 2022). ISSN: 2199160X. DOI: 10.1002/aelm.202200259 (cit. on p. 49).

[145] Peng Liu et al. "Effect of temperature on space charge characteristics in epoxy resin". In: *IEEE Transactions on Dielectrics and Electrical Insulation* 22.1 (Feb. 2015), pp. 65–71. ISSN: 10709878. DOI: 10.1109/TDEI.2014.004518 (cit. on pp. 49, 120).

[146] Jin Li et al. "Effects of high temperature and high electric field on the space charge behavior in epoxy resin for power modules". In: *IEEE Transactions on Dielectrics and Electrical Insulation* 27.3 (June 2020), pp. 882–890. ISSN: 15584135. DOI: 10.1109/TDEI.2020.008737 (cit. on p. 49).

[147] Frederic Gubbels. "Silicones in the Electronics Industries". In: *Inorganic Polymers*. Ed. by Roger de Jaeger and Mario Gleria. 1st ed. Vol. 1. Nova, 2007. Chap. 11. ISBN: 9781600216565. URL: https://www.researchgate.net/publication/238728358 (cit. on p. 49).

[148] Li Cheng et al. "Method for Predicting the Water Absorption of External Insulating Silicone Rubber". In: *IEEE Transactions on Dielectrics and Electrical Insulation* 29.4 (Aug. 2022), pp. 1242–1250. ISSN: 15584135. DOI: 10.1109/TDEI.2022.3183653 (cit. on p. 50).

[149] Yanfeng Gao et al. "A capacitance study of anomalous diffusion of water into HTV silicone rubber materials". In: *IEEE Transactions on Dielectrics and Electrical Insulation* 23.1 (Feb. 2016), pp. 368–376. ISSN: 10709878. DOI: 10.1109/TDEI.2015.005291 (cit. on pp. 50, 129).

[150] K. Y. Lau, A. S. Vaughan, and G. Chen. "Nanodielectrics: opportunities and challenges". In: *IEEE Electrical Insulation Magazine* 31.4 (July 2015), pp. 45–54. ISSN: 0883-7554. DOI: 10.1109/MEI.2015.7126073. URL: http://ieeexplore.ieee.org/document/7126073/ (cit. on p. 50).

[151] Toshikatsu Tanaka. "Dielectric Nanocomposites with Insulating Properties". In: *IEEE Transactions on Dielectrics and Electrical Insulation* 12.5 (2005), pp. 914–928 (cit. on p. 50).

[152] Toshikatsu Tanaka et al. *Proposal of a Multi-core Model for Polymer Nanocomposite Dielectrics*. Tech. rep. 4. 2005, pp. 669–681 (cit. on p. 50).

[153] Chen Zou, J. C. Fothergill, and S. W. Rowe. "The effect of water absorption on the dielectric properties of epoxy nanocomposites". In: *IEEE Transactions on Dielectrics and Electrical Insulation* 15.1 (Feb. 2008), pp. 106–117. ISSN: 10709878. DOI: 10.1109/T-DEI.2008.4446741 (cit. on pp. 50, 131).

[154] A Burneau et al. *Comparative Study of the Surface Hydroxyl Groups of Characterization of Grafted n-Hexadecyl Chains*. Tech. rep. 1990, pp. 1389–1395. URL: https://pubs.acs.org/sharingguidelines (cit. on pp. 50, 133).

[155] Jean Baptiste D'Espinose De La Caillerie et al. *Water Adsorption on Pyrogenic Silica Followed by 1 H MAS NMR*. Tech. rep. 1997, pp. 434–439 (cit. on pp. 50, 133).

[156] Maryna Prigogine and José J. Fripiat. “La réactivité des surfaces de silice”. In: *Journal de Chimie Physique* 76 (May 1979), pp. 26–34. ISSN: 0021-7689. DOI: 10.1051/jcp/1979760026. URL: http://jcp.edpsciences.org/10.1051/jcp/1979760026 (cit. on pp. 50, 133, 134, 152).

[157] Christoph Felix Niedik et al. “Investigation on the electrical characterization of silicone rubber using DC conductivity measurement”. In: *Proceedings of the 2016 IEEE International Conference on Dielectrics, ICD 2016* 2 (2016), pp. 1114–1118. DOI: 10.1109/ICD.2016.7547814 (cit. on pp. 51, 52).

[158] Claudius Freye and Frank Jenau. “DC Conductivity Measurements of Liquid Silicone Rubber: Influence Analysis and Repeatability”. In: *Proceedings - 2018 IEEE International Conference on Environment and Electrical Engineering and 2018 IEEE Industrial and Commercial Power Systems Europe, EEEIC/I and CPS Europe 2018* (2018), pp. 1–6. DOI: 10.1109/EEEIC.2018.8494016 (cit. on pp. 51, 52).

[159] Dominik Haring and Frank Jenau. “Apparent DC conductivity of silicone rubber compounds”. In: *Proceedings of the 2020 IEEE 3rd International Conference on Dielectrics, ICD 2020* 2 (2020). DOI: 10.1109/ICD46958.2020.9341914 (cit. on p. 51).

[160] Shahid Alam, Yuriy V. Serdyuk, and Stanislaw M. Gubanski. “Field-dependent electric conductivities of silicone rubbers deduced from measured currents and surface potential decay characteristics”. In: *International Journal of Polymer Analysis and Characterization* 24.1 (2019), pp. 54–62. ISSN: 15635341. DOI: 10.1080/1023666X.2018.1516369. URL: https://doi.org/10.1080/1023666X.2018.1516369 (cit. on p. 51).

[161] D. K. Das Gupta and K. Joyner. “A study of absorption currents in polypropylene”. In: *Journal of Physics D: Applied Physics* 9.14 (1976), pp. 2041–2048. ISSN: 00223727. DOI: 10.1088/0022-3727/9/14/013 (cit. on pp. 51, 52).

[162] C.G. Garton. “Dielectric loss in thin films of insulating liquids”. In: *Journal of the Institution of Electrical Engineers - Part III: Communication Engineering, including the Proceedings of the Wireless Section of the Institution* 88.1 (Mar. 1941), pp. 23–40. ISSN: 2054-0647. DOI: 10.1049/ji-3-1.1941.0006. URL: https://digital-library.theiet.org/content/journals/10.1049/ji-3-1.1941.0006 (cit. on p. 51).

[163] Maya Mourad et al. “Study of the electrical properties of HVAC EPDM and HVAC silicone rubber under DC constraint”. In: *Jicable HVDC*. 2021 (cit. on pp. 52, 53, 93, 168).

[164] Markus H Zink. “Dielectric conductivity measurements as a central tool to qualify HVDC insulation materials”. In: *8th Conference on Silicone Insulation*. Burghausen: WACKER, July 2022 (cit. on pp. 52, 158, 168).

[165] Claudius Freye, Christoph Felix Niedik, and Frank Jenau. “Investigation on DC conductivity of elastomeric insulating materials considering and reducing influences caused by DC test voltage generation”. In: *Proceedings - 2016 51st International Universities Power Engineering Conference, UPEC 2016* 2017-Janua (2016), pp. 1–6. DOI: 10.1109/UPEC.2016.8114030 (cit. on p. 52).

[166] G.C. Montanari et al. “An investigation of conduction mechanisms at high-field in PET”. In: *IEEE 1997 Annual Report Conference on Electrical Insulation and Dielectric Phenomena*. Vol. 2. IEEE, 1997, pp. 451–454. ISBN: 0-7803-3851-0. DOI: 10.1109/CEIDP.1997.641109. URL: http://ieeexplore.ieee.org/document/641109/ (cit. on p. 52).

[167] E.E. Kunhardt, L. G. Christophorou, and L. H. Luessen. *The Liquid State and Its Electrical Properties*. Ed. by E. E. Kunhardt, L. G. Christophorou, and L. H. Luessen. Vol. 193. NATO ASI Series. Boston, MA: Springer US, 1988. ISBN: 978-1-4684-8025-2. DOI: 10.1007/978-1-4684-8023-8. URL: http://link.springer.com/10.1007/978-1-4684-8023-8 (cit. on pp. 52, 159).

[168] P. Rain et al. “Field and temperature dependence of space charge injection in a silicone rubber”. In: *Journal of Physics D: Applied Physics* 42.23 (2009). ISSN: 00223727. DOI: 10.1088/0022-3727/42/23/235404 (cit. on pp. 52, 53).

[169] Xinyue Zhang et al. “Study on Space Charge Accumulation in Silicone Rubber Encapsulant Under DC Voltage”. In: *2023 IEEE Conference on Electrical Insulation and Dielectric Phenomena (CEIDP)*. IEEE, 2023, pp. 1–4. DOI: 10.1109/CEIDP51414.2023.10410472 (cit. on pp. 52, 53).

[170] D H Nguyen, A Sylvestre, and S Rowe. “Influence of space charges in the dielectric response measurement of silicone rubber”. In: (2004), pp. 149–152 (cit. on pp. 52, 53).

[171] X. Wang et al. “Formation mechanism of space charge in silicone rubber insulation under low DC stress”. In: *Proceedings of the IEEE International Conference on Properties and Applications of Dielectric Materials* 2015-Octob (2015), pp. 116–119. DOI: 10.1109/ICPADM.2015.7295222 (cit. on pp. 52, 53).

[172] Lu Liang et al. “Space charge formation in silicone rubber”. In: *Proceedings of the 7th International Conference on Properties and Applications of Dielectric Materials (Cat. No.03CH37417)*. Vol. 2. IEEE, 2003, pp. 669–672. DOI: 10.1109/ICPADM.2003.1218506 (cit. on pp. 52, 53).

[173] Shahid Alam, Yuriy V. Serdyuk, and Stanislaw M. Gubanski. “Temperature and field induced variations of electric conductivities of HTV silicone rubbers derived from measured currents and surface potential decay characteristics”. In: *Energies* 13.11 (June 2020). ISSN: 19961073. DOI: 10.3390/en13112982 (cit. on p. 52).

[174] Shahid Alam, Yuriy V Serdyuk, and Stanislaw M Gubanski. “Potential Decay on Silicone Rubber Surfaces Affected by Bulk and Surface Conductivities”. In: (). DOI: 10.1109/TDEI.2014.004560 (cit. on p. 53).

[175] Johan Andersson, Henrik Hillborg, and Stanislaw M. Gubanski. “Deterioration of internal interfaces between silicone and epoxy resin”. In: *IEEE International Symposium on Electrical Insulation Deterioration*. 2006, pp. 527–530. ISBN: 1424403332. DOI: 10.1109/elinsl.2006.1665372 (cit. on p. 53).

[176] Juliana Beca et al. “Electrical Tracking and Tree Formation From a Void at a Silicone Rubber - Epoxy Resin Interface”. In: *2023 IEEE Conference on Electrical Insulation and Dielectric Phenomena (CEIDP)*. IEEE, Oct. 2023, pp. 1–4. ISBN: 979-8-3503-3562-0. DOI: 10.1109/CEIDP51414.2023.10410567. URL: https://ieeexplore.ieee.org/document/10410567/ (cit. on p. 53).

[177] Johan Andersson, Stanislaw M. Gubanski, and Henrik Hillborg. “Properties of interfaces between silicone rubber and epoxy”. In: *IEEE Transactions on Dielectrics and Electrical Insulation* 15.5 (2008), pp. 1360–1367. ISSN: 10709878. DOI: 10.1109/TDEI.2008.4656245 (cit. on p. 53).

[178] R Bodega et al. “Space Charge and Electric Field Characteristics of Polymeric-type MV-size DC Cable Joint Models”. In: *Annual Report Conference on Electrical Insulation and Dielectric Phenomena Space*. 2005, pp. 507–510. ISBN: 0780392574 (cit. on p. 54).

[179] R. Bodega and J. J. Smit. “Space charge measurements on multi-dielectrics by means of the pulsed electroacoustic method”. In: *IEEE Transactions on Dielectrics and Electrical Insulation* 13.2 (2006), pp. 272–281. ISSN: 10709878. DOI: 10.1109/TDEI.2006.1624272 (cit. on p. 54).

[180] Riccardo Bodega, G. C. Montanari, and P. H.F. Morshuis. “Conduction current measurements on XLPE and EPR insulation”. In: *Annual Report Conference on Electrical Insulation and Dielectric Phenomena*. 2004, pp. 101–105. DOI: 10.1109/ceidp.2004.1364199 (cit. on p. 54).

[181] Thi Thu Nga Vu. “Étude des phénomènes de charges d’espace dans des matériaux de câbles et câbles modèles destinés à des applications au transport d’énergie en Haute Tension Continue (HVDC)”. PhD thesis. l’Université Toulouse III – Paul Sabatier, 2014 (cit. on p. 54).

[182] T. T.N. Vu et al. “Correlating conductivity and space charge measurements in multi-dielectrics under various electrical and thermal stresses”. In: *IEEE Transactions on Dielectrics and Electrical Insulation* 22.1 (2015), pp. 117–127. ISSN: 10709878. DOI: 10.1109/TDEI.2014.004507 (cit. on p. 54).

[183] Thi Thu Nga Vu et al. “Maxwell–Wagner Effect in Multi-Layered Dielectrics: Interfacial Charge Measurement and Modelling”. In: *Technologies* 5.2 (2017), p. 27. ISSN: 2227-7080. DOI: 10.3390/technologies5020027 (cit. on p. 54).

[184] C. Stancu et al. “Space charge and electric field in thermally aged multilayer joints model”. In: *IEEE Transactions on Dielectrics and Electrical Insulation* 23.2 (Apr. 2016), pp. 633–644. ISSN: 10709878. DOI: 10.1109/TDEI.2015.005363 (cit. on p. 54).

[185] Sebastião V. et al Canevarolo Jr. *Técnicas de caracterização de polimeros*. 1st ed. São Paulo: Artliber, 2017 (cit. on p. 58).

[186] Joseph Menczel and R. Bruce Prime. *Thermal Analysis of Polymers - Fundamentals and Applications*. 1st ed. Wiley, 2009 (cit. on pp. 58, 59).

[187] John M. Chalmers. “Infrared Spectroscopy in Analysis of Polymers and Rubbers”. In: *Encyclopedia of Analytical Chemistry*. Wiley, Oct. 2000. DOI: 10.1002/9780470027318.a2015 (cit. on p. 59).

[188] Lucica Barbes et al. *ATR-FTIR spectrometry characterisation of polymeric materials*. Tech. rep. 3. 2014, pp. 765–777. URL: https://www.researchgate.net/publication/256297992 (cit. on p. 59).

[189] Enrique Saldívar-Guerra and Eduardo Vivaldo-Lima. *Handbook of polymer synthesis, characterization, and processing*. Wiley, 2013. ISBN: 9780470630327 (cit. on p. 60).

[190] Paul Peter Urone and Roger Hinrichs. *Heat, Specific Heat, and Heat Transfer*. Mar. 2020. URL: https://openstax.org/books/physics/pages/11-2-heat-specific-heat-and-heat-transfer (cit. on p. 60).

[191] Georgia L Harris. *Selected Laboratoryand measurement practices and procedures to support basic mass calibrations:* tech. rep. Gaithersburg, MD: National Institute of Standards and Technology, May 2019. DOI: 10.6028/NIST.IR.6969-2019. URL: https://nvlpubs.nist.gov/nistpubs/ir/2019/NIST.IR.6969-2019.pdf (cit. on p. 60).

[192] G Szekely, M Nebuloni, and L F Zerilli. *Thermal analysis-mass spectrometry and its applications*. Tech. rep. 1992, pp. 511–532 (cit. on p. 60).

[193] Wacker Chemie AG. *LUMISIL ® LR 7601/70 A/B Liquid Silicone Rubber (LSR)*. 2022. URL: https://www.wacker.com/h/en-us/medias/LUMISIL-LR-760170-AB-en-2022.06.28.pdf (cit. on pp. 67, 168).

[194] Jinhe Wang et al. "Mechanical and ceramifiable properties of silicone rubber filled with different inorganic fillers". In: *Polymer Degradation and Stability* 121 (2015), pp. 149–156 (cit. on p. 68).

[195] Shaoyun Fu et al. "Some basic aspects of polymer nanocomposites: A critical review". In: *Nano Materials Science* 1.1 (Mar. 2019), pp. 2–30. ISSN: 25899651. DOI: 10.1016/j.nanoms.2019.02.006 (cit. on p. 70).

[196] Yuejing Tong et al. "Effect of surface chemistry and morphology of silica on the thermal and mechanical properties of silicone elastomers". In: *Journal of Applied Polymer Science* 135.35 (Sept. 2018). ISSN: 10974628. DOI: 10.1002/app.46646 (cit. on p. 70).

[197] S. I. Salih, J. K. Oleiwi, and H. M. Ali. "Study the Mechanical Properties of Polymeric Blends (SR/PMMA) Using for Maxillofacial Prosthesis Application". In: *IOP Conference Series: Materials Science and Engineering*. Vol. 454. 1. Institute of Physics Publishing, Dec. 2018. DOI: 10.1088/1757-899X/454/1/012086 (cit. on p. 70).

[198] Can Chen et al. "Micro characterization and degradation mechanism of liquid silicone rubber used for external insulation". In: *IEEE Transactions on Dielectrics and Electrical Insulation* 22.1 (Feb. 2015), pp. 313–321. ISSN: 10709878. DOI: 10.1109/TDEI.2014.004188 (cit. on p. 70).

[199] Zhijin Zhang et al. "Application of Infrared Spectroscopy in Research on Aging of Silicone Rubber in Harsh Environment". In: *Polymers* 14.21 (Nov. 2022). ISSN: 20734360. DOI: 10.3390/polym14214728 (cit. on p. 70).

[200] Heping Liu et al. “Characterization of a severely degraded silicone elastomer HV insulator - An aid to development of lifetime assessment techniques”. In: *IEEE Transactions on Dielectrics and Electrical Insulation* 12.3 (June 2005), pp. 478–486. ISSN: 10709878. DOI: 10.1109/TDEI.2005.1453452 (cit. on p. 70).

[201] S. P. Vasilakos and P. A. Tarantili. “In situ monitoring by DSC and modeling of curing of vinyl polysiloxanes in layered silicate nanocomposites”. In: *Journal of Thermal Analysis and Calorimetry* 127.3 (Mar. 2017), pp. 2049–2058. ISSN: 15882926. DOI: 10.1007/s10973-016-5821-z (cit. on p. 70).

[202] L. M. Lopez et al. “Modeling the vulcanization reaction of silicone rubber”. In: *Polymer Engineering and Science* 47.5 (May 2007), pp. 675–683. ISSN: 00323888. DOI: 10.1002/pen.20698 (cit. on p. 72).

[203] N A Perez. “Etude Calorimétrique et Diélectrique de Nanocomposites Silicones”. PhD thesis. Grenoble: Institut National Polytechnique de Grenoble, Nov. 2008. URL: https://theses.hal.science/tel-00351850 (cit. on p. 72).

[204] ISO. *Plastics-Determination of water absorption Plastiques-Détermination de l’absorption d’eau*. Tech. rep. 2008, p. 2008. URL: https://asrecomposite.comWebwww.iso.orghttps://asrecomposite.com (cit. on p. 75).

[205] Andresa Baptista et al. *Sputtering physical vapour deposition (PVD) coatings: A critical review on process improvement andmarket trend demands*. 2018. DOI: 10.3390/COATINGS8110402 (cit. on p. 77).

[206] W. M. Haynes. *CRC Handbook of Chemistry and Physics*. Ed. by W. M. Haynes, David R. Lide, and Thomas J. Bruno. 95th ed. Boca Raton: CRC Press, 2015 (cit. on pp. 77, 148).

[207] Laetitia Zavattoni. “Conduction phenomena through gas and insulating solids in HVDC Gas Insulated Substations, and consequences on electric field distribution”. PhD thesis. 2014. URL: https://tel.archives-ouvertes.fr/tel-01305949%20https://tel.archives-ouvertes.fr/tel-01121096/ (cit. on p. 78).

[208] F. Kuchler et al. “Polarization-Depolarization Current (PDC) Measurements for Volume and Surface Resistivity Analysis of Polymeric Materials”. In: *Annual Report - Conference on Electrical Insulation and Dielectric Phenomena, CEIDP*. Vol. 2021-December. Institute of Electrical and Electronics Engineers Inc., 2021, pp. 17–22. ISBN: 9781665419079. DOI: 10.1109/CEIDP50766.2021.9705340 (cit. on pp. 87, 94).

[209] Michał Lisowski et al. “Space charge influence on the results of volume resistivity measurements in solid dielectrics”. In: *XVII IMEKOWorld Congress Metrology in the 3rd Millennium*. Dubrovnik, 2003 (cit. on p. 87).

[210] A Perez et al. *Influence of Stabilization Time and Post Processing Methods on the Accuracy of DC Conductivity Measurements*. ISBN: 9781665407502 (cit. on pp. 92, 93).

[211] Zou Chen. “The effect of humidity and surface functionalisation on the dielectric properties of nanocomposites”. PhD thesis. 2007. URL: http://hdl.handle.net/2381/859 (cit. on p. 100).

[212] P Bonniau and R Bunsell. "A Comparative Study of Water Absorption theories Applied to Glass Epoxy Composites". In: *Journal of Composite Materials* 15 (1981) (cit. on p. 101).

[213] Allan Harvey and Francis Smith. "Avoid Common Pitfalls when using Henry's Law". In: *Chemical Engineering Progress* (2007). URL: https://tsapps.nist.gov/publication/get_pdf.cfm?pub_id=50449 (cit. on p. 102).

[214] Bruno Fayolle and Jacques Verdu. *Vieillissement physique des matériaux polymères*. Tech. rep. Techniques de l'ingénieur, 2005 (cit. on p. 104).

[215] X. J. Fan, S. W.R. Lee, and Q. Han. "Experimental investigations and model study of moisture behaviors in polymeric materials". In: *Microelectronics Reliability* 49.8 (Aug. 2009), pp. 861–871. ISSN: 00262714. DOI: 10.1016/j.microrel.2009.03.006 (cit. on p. 106).

[216] M. K. Antoon, J. L. Koenig, and T. Serafini. "FOURIER-TRANSFORM INFRARED STUDY OF THE REVERSIBLE INTERACTION OF WATER AND A CROSSLINKED EPOXY MATRIX." In: *Journal of polymer science. Part A-2, Polymer physics* 19.10 (1981), pp. 1567–1575. ISSN: 04492978. DOI: 10.1002/pol.1981.180191007 (cit. on p. 106).

[217] G. Mazzanti, G. C. Montanari, and L. A. Dissado. "Electrical aging and life models: The role of space charge". In: *IEEE Transactions on Dielectrics and Electrical Insulation* 12.5 (Oct. 2005), pp. 876–890. ISSN: 10709878. DOI: 10.1109/TDEI.2005.1522183 (cit. on p. 114).

[218] M. Ieda and Y. Suzuoki. "Space charge and solid insulating materials-in pursuit of space-charge control by molecular design". In: *Proceedings of 5th International Conference on Properties and Applications of Dielectric Materials*. Vol. 1. IEEE, pp. 16–23. ISBN: 0-7803-2651-2. DOI: 10.1109/ICPADM.1997.617517. URL: http://ieeexplore.ieee.org/document/617517/ (cit. on p. 117).

[219] J G Simmons. *THEORY OF METALLIC CONTACTS ON HIGH RESISTIVITY SOLIDS (II) DEEP TRAPS*. Tech. rep. 1971, pp. 2581–2591 (cit. on pp. 122, 155, 156).

[220] J G Simmons. *THEORY OF METALLIC CONTACTS ON HIGH RESISTIVITY SOLIDS-I. SHALLOW TRAPS*. Tech. rep. 1971, pp. 1987–1999 (cit. on pp. 122, 155).

[221] John G Simmons et al. *Poole-Frenkel Effect and Schottky Effect in Metal-Insulator-Metal Systems*. Tech. rep. 1938, p. 499 (cit. on pp. 122, 150, 155).

[222] Wissal Jilani et al. "Dielectric relaxations investigation of a synthesized epoxy resin polymer". In: *European Physical Journal Plus* 130.4 (2015), pp. 1–10. ISSN: 21905444. DOI: 10.1140/epjp/i2015-15076-6 (cit. on p. 122).

[223] Bo Gong et al. "Moisture Absorption Characteristics of Silicone Rubber and Its Effect on Dielectric Properties". In: *Conference on Electrical Insulation and Dielectric Phenomena*. 2013, pp. 430–433. ISBN: 9781479925971 (cit. on p. 129).

[224] Anna Karin Hulterström, Anders Berglund, and I. Eystein Ruyter. "Wettability, water sorption and water solubility of seven silicone elastomers used for maxillofacial prostheses". In: *Journal of Materials Science: Materials in Medicine* 19.1 (Jan. 2008), pp. 225–231. ISSN: 09574530. DOI: 10.1007/s10856-006-0027-8 (cit. on p. 129).

[225] Anindita Bhuyan and Md Ahmaruzzaman. *Recent advances in new generation nanocomposite materials for adsorption of pharmaceuticals from aqueous environment*. Mar. 2023. DOI: 10.1007/s11356-023-25707-0 (cit. on p. 131).

[226] Csaba Kenyó et al. "Functional packaging materials: Factors affecting the capacity and rate of water adsorption in desiccant composites". In: *Journal of Polymer Research* 20.11 (2013). ISSN: 10229760. DOI: 10.1007/s10965-013-0294-2 (cit. on p. 131).

[227] Yaolin Zhang, S. Y. Zhang, and Ying Hei Chui. "Water vapor adsorption and volumetric swelling of melt-impregnated wood-polymer composites". In: *Journal of Applied Polymer Science* 102.3 (Nov. 2006), pp. 2668–2676. ISSN: 00218995. DOI: 10.1002/app.24092 (cit. on p. 131).

[228] Christos J. Tsenoglou, Sylvia Pavlidou, and Constantine D. Papaspyrides. "Evaluation of interfacial relaxation due to water absorption in fiber-polymer composites". In: *Composites Science and Technology* 66.15 (Dec. 2006), pp. 2855–2864. ISSN: 02663538. DOI: 10.1016/j.compscitech.2006.02.022 (cit. on p. 133).

[229] Michel Biron. "Silicones ou siloxanes: Applications". In: *Techniques de l'ingénieur, Matériaux à propriétés mécaniques* 33.n2882 (2007). URL: http://www.techniques-ingenieur.fr/base-documentaire/materiaux-th11/materiaux-a-proprietes-mecaniques-42535210/silicones-ou-siloxanes-n2882/ (cit. on p. 148).

[230] J. R. Yeargan and H. L. Taylor. "The Poole-Frenkel effect with compensation present". In: *Journal of Applied Physics* 39.12 (1968), pp. 5600–5604. ISSN: 00218979. DOI: 10.1063/1.1656022 (cit. on p. 150).

[231] Herbert Schroeder. "Poole-Frenkel-effect as dominating current mechanism in thin oxide films - An illusion?!" In: *Journal of Applied Physics* 117.21 (June 2015). ISSN: 10897550. DOI: 10.1063/1.4921949 (cit. on p. 150).

[232] P Notingher et al. "Study of Space Charge Accumulation in Polyolefins Submitted to ac Stress". In: *IEEE Transactions on Dielectrics and Electrical Insulation* 8.6 (2001) (cit. on p. 150).

[233] Takashi Yoshino and Tomoo Katsura. "Electrical conductivity of mantle minerals: Role of water in conductivity anomalies". In: *Annual Review of Earth and Planetary Sciences* 41 (May 2013), pp. 605–628. ISSN: 00846597. DOI: 10.1146/annurev-earth-050212-124022 (cit. on p. 153).

[234] James Hunter Anderson and George A. Parks. "Electrical conductivity of silica gel in the presence of adsorbed water". In: *The Journal of Physical Chemistry* 72.10 (Oct. 1968), pp. 3662–3668. ISSN: 0022-3654. DOI: 10.1021/j100856a051. URL: https://pubs.acs.org/doi/abs/10.1021/j100856a051 (cit. on p. 153).

[235] Jerry Goodisman and Rick Blades. "Conductivity of irradiated pure water". In: *Journal of Physical Chemistry A* 104.51 (Dec. 2000), pp. 12029–12044. ISSN: 10895639. DOI: 10.1021/jp001755v (cit. on p. 153).

[236] H Golnabi et al. *Investigation of electrical conductivity of different water liquids and electrolyte solutions*. Tech. rep. 2009, pp. 24–28. URL: www.SID.ir (cit. on p. 153).

[237] Wacker Chemie AG. *Safety Data Sheet Material: 60099952 LUMISIL® LR 7601/70 A*. 2022. URL: blob:https://www.wacker.com/e94f6579-143e-49a3-89a7-2f3fe6e5a188 (cit. on p. 168).

[238] Wacker Chemie AG. *Safety Data Sheet Material: 60099955 LUMISIL® LR 7601/70 B*. 2022. URL: blob:https://www.wacker.com/d9a7abe6-03d4-4e25-a9ad-4e300b71ddb7 (cit. on p. 168).

[239] Andreas . Kremer Friedrich ; Schönhals. *Broadband Dielectric Spectroscopy*. Berlin: Springer-Verlag Berlin Heidelberg, 2003. ISBN: 978-3-642-62809-2. DOI: https://doi.org/10.1007/978-3-642-56120-7 (cit. on pp. 171–174).

[240] R. Bartnikas and R. M. Eichhorn. *Engineering Dielectrics Volume IIA Electrical Properties of Solid Insulating Materials: Molecular Structure and Electrical Behavior*. 1st ed. Baltimore: ASTM International, 1983. ISBN: 978-0-8031-5557-2. DOI: 10.1520/STP783-EB (cit. on pp. 171, 172, 174, 175).

[241] J. Guo et al. "Optimization and experimental verification of coplanar interdigital electroadhesives". In: *Journal of Physics D: Applied Physics* 49.41 (Sept. 2016). ISSN: 13616463. DOI: 10.1088/0022-3727/49/41/415304 (cit. on p. 173).

[242] James D. LIVINGSTON. *Electronic Properties of Engineering Materials*. 1st. New York, United States: John Wiley & Sons Inc, 1998, p. 336. ISBN: 9780471316275 (cit. on p. 172).

[243] A. K. Jonscher. "Low-frequency dispersion in volume and interfacial situations". In: *Journal of Materials Science* 26.6 (1991), pp. 1618–1626. ISSN: 00222461. DOI: 10.1007/BF00544672 (cit. on p. 175).